AN INVESTIGATION INTO THE DIMERISATION OF THE SODIUM-IODIDE SYMPORTER

by

REBECCA JANE THOMPSON

A thesis submitted to

The University of Birmingham

for the degree of

DOCTOR OF PHILOSOPHY

Insitute of Metabolism and Systems Research

College of Medical and Dental Sciences

University of Birmingham

August 2018

Abstract

The active accumulation of iodide into the thyroid, mediated by the sodium-iodide symporter (NIS), is vital for thyroid hormone production, which is essential for neurological development and metabolism throughout life. This system is the target of thyroid cancer treatment post-surgery, as NIS facilitates radioiodide uptake into, and subsequent ablation of, cancer cells. While this is a largely successful therapy, it is ineffective in patients with radioiodide-refractory thyroid cancers due to the loss of functional NIS. Unfortunately, the lack of alternative treatment options for these patients results in an extremely poor prognosis. Consequently, it is of great interest to improve our understanding of NIS regulation, with the ultimate clinical aim of re-introducing functional NIS expression in such patients to enable successful treatment with radioiodide. Since dimerisation is important for the function of many membrane proteins, it is significant that NIS has been suggested to exist at higher molecular weights indicative of dimerisation, although this has not been explored in depth. This thesis demonstrated the occurrence of NIS dimerisation using three distinct methodologies. Although investigations revealed that previously proposed motifs are unlikely to be involved in NIS dimerisation, an alternative role in protein folding was offered for these motifs. Consequently, a novel homology model of NIS dimerisation was created based on the dimeric crystal structure of the family member protein vSGLT, which revealed a putative dimerisation interface. Mutational studies demonstrated that interactions between residues Q471, Y242 and T243 mediate NIS dimerisation and suggested that dimerisation might be involved in protein trafficking.

Dedication

For William.

Acknowledgments

I would like to thank my supervisors Professor Chris McCabe and Dr Vicki Smith for their guidance and support during this PhD. My thanks also go to fellow members of the group, past and present, particularly Vikki Poole, Bhav Modasia and Waraporn Imruetaicharoenchoke for taking the time to show me the ways of the lab, and to Kate Baker for her invaluable help with the final experiments. I would like to express thanks to Dr Jon Mueller for all of his help with the homology modelling and support, and to Professor David Hodson and Nick Fine for their help with the FRET studies and allowing me to use their microscope system. I would particularly like to thank Nick for being my sounding board when we had no idea what to do next! I would also like to acknowledge the MRC for funding this PhD, and Sense for funding me during my write-up.

I am extremely grateful for all of the personal support I have received from my family and friends throughout this PhD. It has been a pretty rough ride and I deeply appreciate all of your perseverance and encouragement. I would especially like to thank my incredible parents for everything you have done and continue to do for us. Finally, I would like to thank Nick for not just being my sounding board for FRET, but for life. Thank you for being there for me at my Te Kā, not just my Te Fiti.

Table of Contents

List of Figures

List of Tables

List of Abbreviations

µCi	microCurie
^{125}I	Iodine radioisotope 125
^{131}I	Iodine radioisotope 131
Å	Angstrom (1Å = 0.1nm)
AEs	Adverse events
ANOVA	Analysis of variance
ATC	Anaplastic thyroid cancer
BCA	Bicinchoninic acid assay
BiFC	Bimolecular fluorescence complementation
BLAST	Basic local alignment search tool
BRAF	Rapidly accelerated fibrosarcoma type-B
BSA	Bovine serum albumin
cAMP	Cyclic adenosine monophosphate
Cer	Cerulean
CFP	Cyan fluorescent protein
Cit	Citrine
CMV	Cytomegalovirus
Co-IP	Co-immunoprecipitation
DNA	Deoxyribonucleic acid
dNTP	Deoxyribonucleotide triphosphate
DTC	Differentiated thyroid cancer
DUOX	Dual oxidase
E. coli	*Escherichia coli*
EDTA	Ethylenediaminetetraacetic acid
EGFR	Epidermal growth factor receptor
Epac2	Exchange protein directly activated by cAMP
ER	Endoplasmic reticulum
FBS	Foetal bovine serum
FGFR	Fibroblast growth factor receptor
FTC	Follicular thyroid cancer

GFP	Green fluorescent protein
GPCR	G-protein coupled receptor
GZM	Glycine zipper motif
HA	Haemagglutinin
I^-	Iodide
IgG	Immunoglobulin G
ITD	Iodide transport defect
kDa	kiloDaltons
LB	Lysogeny broth
LZM	Leucine zipper motif
mA	milliAmps
MAPK	Mitogen-activated protein kinase
mCi	milliCurie
MCT8	Monocarboxylate transporter 8
Na^+	Sodium
Na^+/K^+ ATPase	Sodium-potassium ATPase
$NaClO_4$	Sodium perchlorate
NCS	Newborn calf serum
NIS	Sodium-iodide symporter
p53	Tumour protein 53
PAX8/PPARγ	Paired box gene 8/peroxisome proliferator-activated receptor gamma
PBF	Pituitary tumor transforming gene (PTTG)-binding factor
PBS	Phosphate-buffered saline
pcDNA	Plasmid control deoxyribo-nucleic acid 3.1
PCR	Polymerase chain reaction
PDB	Protein Data Bank
PFS	Progression free survival
Phyre2	Protein Homology/analogY Recognition Engine v 2.0
PI3K	Phosphoinositide 3-kinase
PLA	Proximity ligation assay
PTC	Papillary thyroid cancer
RAI	Radioiodide

RAI-R	Radioiodide-refractory
RAS	Rat sarcoma
RET/PTC	Rearranged during transfection proto-oncogene in PTC
RIPA	Radioimmunoprecipitation assay
RMSD	Root-mean-square deviation
ROS	Reactive oxygen species
RPM	Revolutions per minute
RR	Response rate
RTK	Receptor tyrosine kinase
SDS-PAGE	Sodium dodecyl sulfate polyacrylamide gel electrophoresis
SEM	Standard error of the mean
SSS	Sodium-solute symporter
T3	Triiodothyronine
T4	Tetraiodothyronine (thyroxine)
TBST	Tris-buffered saline containing Tween
TERT	telomerase reverse transcriptase
Tg	Thyroglobulin
TH	Thyroid hormone
TKI	Tyrosine kinase inhibitor
TMD	Transmembrane domain
TPO	Thyroid peroxidase
TSH	Thyroid stimulating hormone
U/L	Units per litre
v/v	Volume to volume ratio
VO	Empty vector only
vSGLT	*Vibrio parahaemolyticus* sodium-galactose transporter
w/v	Weight to volume ratio
WT	Wild-type
YASARA	Yet Another Scientific Artificial Reality Application
YFP	Yellow fluorescent protein

CHAPTER 1 – GENERAL INTRODUCTION

1.1 Normal thyroid function

1.1.1 The thyroid gland

The thyroid is a bi-lobed endocrine gland, normally 50-60mm in length and weighing 25-30g, located in the anterior of the lower neck inferior to the larynx. It is primarily composed of thyroid follicles, spherical structures comprising a monolayer of polarised epithelial cells, known as follicular cells, and a lumen filled with colloid (Figure 1-1). Colloid predominantly consists of the protein thyroglobulin (Tg), from which the thyroid hormones (THs) T_3 (3,5,3'-tri-iodo-L-thyronine) and T_4 (3,5,3',5'-tetra-iodo-L-thyronine or thyroxine) are produced (Dorion, 2017). THs are essential for the pre- and post-natal development of the central nervous system, skeletal muscle and lungs, and also for regulating metabolism in all cells throughout life (Ortiga-Carvalho et al., 2016).

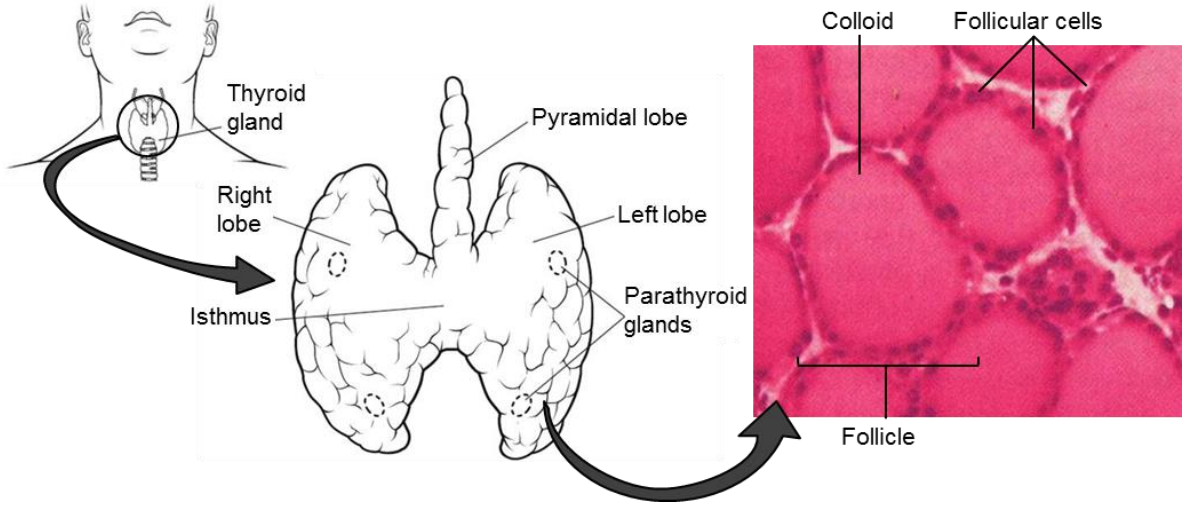

Figure 1-1 – Anatomy and histology of the thyroid gland. Located in the anterior of the lower neck, the thyroid gland has two lateral lobes connected by the isthmus and anchored to the hyoid bone by the pyramidal lobe. Histologically, the thyroid is composed of follicles, spherical monolayers of epithelial (follicular) cells which surround a lumen filled with colloid. The four parathyroid glands, located posterior to the thyroid gland, are not involved in thyroid function. Image adapted from Dorion, 2017.

Dispersed amongst the follicular cells are parafollicular (C)-cells. These cells produce calcitonin in response to high serum calcium (Ca^{2+}) levels to inhibit bone resorption, intestinal Ca^{2+} absorption and renal Ca^{2+} reabsorption. As C-cells comprise only 2-4% of

thyroid cells, this is a minor secondary role of the thyroid (Cote et al., 2015). Although the four parathyroid glands are located posterior to the thyroid (Figure 1-1), they are devoid of influence from or to the thyroid gland, as their role is to produce parathyroid hormone in response to low serum Ca^{2+} levels to oppose the actions of calcitonin (Lee and Anzai, 2013).

1.1.2 Thyroid hormones

1.1.2.1 Regulation of thyroid hormone production

Production of the THs is under the control of the hypothalamus-pituitary-thyroid (HPT) axis. When serum TH levels fall below the normal range (9.0-25.0pmol/l for T_4; 3.5-7.8pmol/l for T_3 (British Thyroid Foundation, 2015)), thyrotrophin-releasing hormone (TRH) is released from hypophysiotrophic neurons of the paraventricular nucleus in the hypothalamus. TRH stimulates the thyrotroph cells of the anterior pituitary gland to release thyroid-stimulating hormone (TSH), which acts on the thyroid to stimulate all of the steps in the TH synthesis pathway (described in section 1.1.2.2) to increase the production and release of THs. Excess THs act on both the hypothalamus and pituitary in a negative feedback loop to switch off the HPT axis, thereby maintaining physiological levels of THs (Ortiga-Carvalho et al., 2016).

1.1.2.2 Molecular mechanism of thyroid hormone synthesis

Figure 1-2 depicts the molecular mechanism of TH synthesis. The first step in the process, the accumulation of iodide (I^-) from the blood into the thyroid follicles, is the most critical as I^- is key component of THs and a lack of I^- prevents TH synthesis. This step is mediated by the sodium-iodide symporter (NIS) expressed on the basolateral membrane of the follicular cells. NIS transports sodium (Na^+) and I^- ions into the follicular cells in a 2:1 stoichiometry by utilising the Na^+ gradient generated by the sodium-potassium ATPase (Na^+/K^+-ATPase). This protein is also expressed on the follicular cell basolateral membrane and actively

transports three Na^+ ions out and two K^+ ions in to the cell (Eskandari et al., 1997, Dohan et al., 2007). I^- is then transported into the follicle lumen by various anion transporters and channels expressed on the apical membrane of the follicular cells, including pendrin (PDS; (Scott et al., 1999)), apical I^- transporter (AIT; (Rodriguez et al., 2002)), cystic fibrosis transmembrane conductance regulator (CFTR; (Devuyst et al., 1997)) and anoctamin 1 (ANO1; (Twyffels et al., 2014)).

Once inside the lumen, I^- is oxidised to iodine and then incorporated onto tyrosine residues of Tg in the colloid which fills the follicular lumen. This I^- organification process produces mono-iodotyrosine (MIT) and di-iodotyrosine (DIT), which are then conjugated to form the THs T_4 and T_3. These steps are all catalysed by thyroid peroxidase (TPO), an enzyme expressed on the apical membrane of the follicular cells, which utilises the hydrogen peroxide (H_2O_2) produced by the dual oxidase proteins (DUOX1 and 2) also expressed on the follicular cell apical membrane (Di Jeso and Arvan, 2016).

Iodinated Tg is then taken into the follicular cells via endocytosis or micropinocytosis, where it undergoes proteolysis in lysosomes to release the THs, which are transported out of the cells mainly via monocarboxylate transporter 8 MCT8 (Visser et al., 2011). MIT and DIT also released during proteolysis are subsequently deiodinated by the iodotyrosine deiodinase enzyme DEHAL1, thus recycling I^- back into the lumen (Moreno and Visser, 2010).

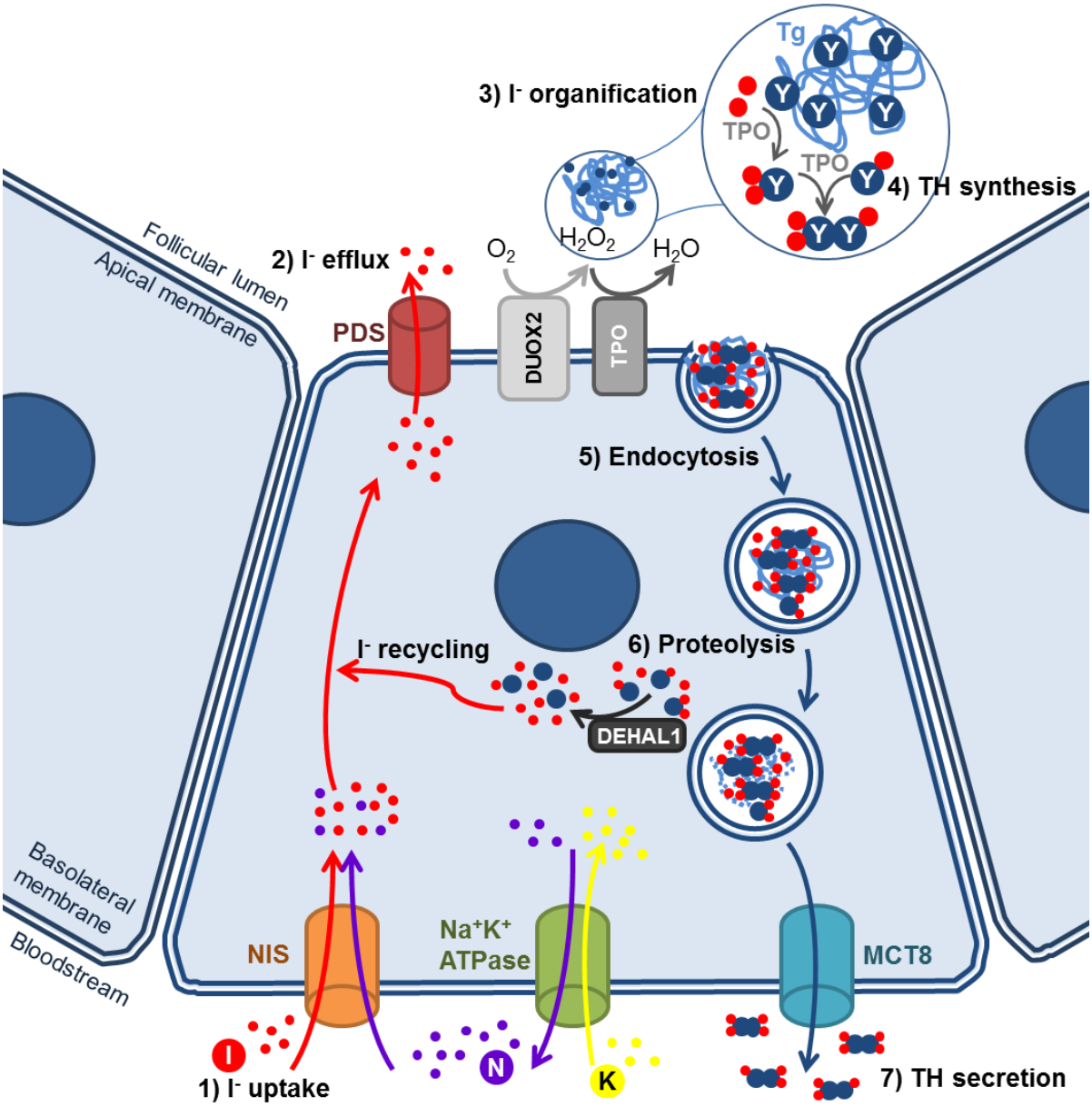

Figure 1-2 – Molecular mechanism of thyroid hormone synthesis. The sodium-potassium ATPase (Na^+K^+ATPase, green cylinder; Na^+, purple dots; K^+, yellow dots) in the basolateral membrane of the thyroid follicular cell maintains a Na^+ gradient across the cells whereby there is a lower Na^+ concentration inside the cell. 1) This Na^+ gradient drives the sodium-iodide symporter (NIS, orange cylinder) to accumulate iodide (I^-, red dots) in the cell. 2) I^- is transported into the follicular lumen by anion transporters, such as pendrin (PDS, dark red cylinder), located on the apical membrane. 3) Here, I^- is oxidised and organified onto tyrosine residues (Y, dark blue circles) of thyroglobulin (Tg, in light blue). 4) This produces mono- and di-iodotyrosines (MIT and DIT), which conjugate to form the thyroid hormones (TH) T_3 and T_4. These I^- organification and TH synthesis steps are catalysed by thyroid peroxidase (TPO, medium grey rectangle) using the hydrogen peroxidase (H_2O_2) produced by dual oxidase 2 (DUOX2, light grey rectangle). 5) Iodinated Tg is endocytosed by the cell. 6) Proteolysis then occurs to release the THs from Tg. MITs and DITs also released during proteolysis are deiodinated by DEHAL1 (dark grey rectangle), thereby enabling unused I^- to be recycled back into the colloid. 7) THs are transported out into the blood by monocarboxylate transporter 8 (MCT8, bright blue cylinder). Image adapted from Ortiga-Carvalho et al., 2016.

1.2 Thyroid cancer

1.2.1 Incidence

Thyroid cancer is the most prevalent endocrine cancer worldwide, with rapidly rising incidence. It is the 20th most common cancer in the UK, with 3,528 new cases diagnosed in 2015. It affects predominantly women (73% cases in the UK are in females) and incidence correlates strongly with increased age. The age-standardised incidence rate has increased by 148% in the past decade alone to 5.6 cases per 100,000 in 2015, and is predicted to rise by 74% to 11 cases per 100,000 population by 2035 (Cancer Research UK, 2016).

1.2.2 Subtypes: prevalence, prognosis and associated genetic abnormalities

Thyroid cancer is subdivided into four main types: papillary thyroid carcinoma (PTC), follicular thyroid carcinoma (FTC), anaplastic thyroid carcinoma (ATC) and medullary thyroid carcinoma (MTC). Unlike the other subtypes which arise from the follicular cells, MTC originates from the calcitonin-producing C-cells, and accounts for 2-4% of thyroid cancers. As these cells are a minority in the thyroid (see section 1.1.1), and MTC tumour initiation, progression and treatment differs from the other subtypes, it is not included in this thesis (Cote et al., 2015, Raue and Frank-Raue, 2016). The prevalence, prognosis and genetic features of the remaining subtypes are summarised in Table 1-1 and described below.

	Prevalence	Prognosis	Adverse clinical features	Oncogenic drivers
Papillary thyroid carcinoma (PTC)	80-85%	Good (95%)	Local spreading Lymph node metastases	*BRAF* (40-50%) *RET/PTC* (20-40%) *RAS* (15%)
Follicular thyroid carcinoma (FTC)	10-15%	Good (91%)	Haematological spreading Bone and/or lung metastases	*RAS* (25-40%) *PAX8/PPARγ* (30-35%)
Anaplastic thyroid carcinoma (ATC)	1-2%	Poor (<1%)	Locoregional invasion Bone and/or lung metastases Dedifferentiation	Multiple genetic abnormalities *BRAF* (56%) *p53* (60%) *TERT* (33%)

Table 1-1 – Clinicopathological and genetic features of thyroid cancer subtypes. Prevalence (relative percentage of thyroid cancer cases) and prognosis (5-year overall survival rate) are shown for papillary thyroid carcinoma (PTC), follicular thyroid carcinoma (FTC) and anaplastic thyroid carcinoma (ATC), alongside the clinical features corresponding to a poorer prognosis and prevalence of the different driving genetic abnormalities associated with each subtype. Table adapted from Zaballos and Santisteban, 2017, and Raue and Frank-Raue, 2016.

PTC is the most frequent type of thyroid cancer, representing 80-85% of cases, and is largely driven by genetic abnormalities which constitutively activate the mitogen-activated protein kinase (MAPK) signalling pathway (Zaballos and Santisteban, 2017), predominantly rapidly accelerated fibrosarcoma type-B (*BRAF*; (Nikiforova et al., 2003, Kimura et al., 2003)) or rat sarcoma (*RAS*; (Esapa et al., 1999, Zhu et al., 2003)) gene mutations, or rearrangements of the rearranged during transfection proto-oncogene in PTC (*RET/PTC*; (Nikiforov et al., 1997, Elisei et al., 2001)). Around 10-15% of thyroid cancer cases are FTC, which is mainly driven by constitutive activation of the phosphatidylinositol 3-kinase (PI3K) pathway (Zaballos and Santisteban, 2017), primarily via *RAS* gene mutations or paired box gene 8/peroxisome proliferator-activated receptor gamma (*PAX8/PPARγ*) gene rearrangements (Kroll et al., 2000, Placzkowski et al., 2008). Prognosis for PTC and FTC is generally good, with a 5-year overall survival rate of 95% and 91%, respectively, due to the high response rate to therapy. However, worse prognoses are attributed to patients with lung and/or bone

metastases, as metastatic disease is the leading cause of thyroid cancer-related deaths (discussed further in section 1.2.3; (Zaballos and Santisteban, 2017)).

In contrast to PTC and FTC, which are termed well-differentiated cancers (DTC), ATC is poorly-differentiated as expression of thyroid-specific genes, such as NIS and TPO (see section 1.1.2.2), is lost due to increased frequency of genetic abnormalities in these tumours (Landa et al., 2016). Alongside mutations which cause constitutive activation of MAPK and PI3K signalling in ATC, additional mutations are commonly seen, such as in the telomerase reverse transcriptase (*TERT*) promoter (Landa et al., 2013, Liu et al., 2013) and tumour protein 53 (*p53*) gene (Landa et al., 2016, Fagin et al., 1993). These additional mutations increase tumour aggressiveness, with locoregional spreading and metastases in the bone and/or lungs often occurring. Although ATC is rare (1-2% of cases), this increased frequency of genetic abnormalities results in an extremely poor prognosis, with a 5-year overall survival rate of less than 1% and mean survival time of 0.5 years from diagnosis. This is largely down to the aggressiveness of the disease and the lack of treatment options for these patients, as the methods which successfully treat the majority of PTC and FTC patients are ineffective in ATC (Zaballos and Santisteban, 2017, Landa et al., 2016).

1.2.3 Treatment

Once a thyroid nodule has been identified as malignant, a total thyroidectomy is usually performed. Following surgery, adjuvant radioiodine (RAI) therapy is administered to patients with DTC to ablate residual thyroid tissue and cancer cells to reduce the risk of recurrence and increase survival. Follow-up treatment involves whole-body RAI uptake scans and measuring serum Tg levels to detect metastatic or recurrent disease. Patients with DTC generally have an excellent response to RAI therapy, resulting in the high survival rates observed in these patients, as these cancer cells retain the ability to uptake and organify I^- (as

described in section 1.1.2.2 (Raue and Frank-Raue, 2016, Viola et al., 2016)). However, RAI therapy can be much less effective in patients with metastatic disease, and its efficacy varies greatly depending on the clinical characteristics.

Although metastases only occur in approximately 10% of patients, metastatic disease is the leading cause of death from thyroid cancer. Distant metastases are most frequently found in the lungs (50%), bones (26%) or both lungs and bone (18%; (Durante et al., 2006)). Approximately two-thirds of patients with metastatic disease retain the ability to uptake RAI, and therefore have the potential to respond to RAI therapy. While 43% of these patients can be successfully treated with RAI therapy, resulting in a 10-year survival rate of 92% and recurrence rate of just 7%, patients who did not achieve remission with RAI therapy have a much worse outcome, with a 10-year survival of 29%. An even poorer outcome is observed in the approximately one-third of patients with metastatic disease who lose the ability to uptake RAI (termed radioiodide-refractory (RAI-R) thyroid cancers), with a 10-year survival of just 10% (Durante et al., 2006). Patients who do not achieve remission after RAI therapy or who have RAI-R disease are usually older with poorly-differentiated tumours and more extensive metastatic disease compared to those who achieve remission with RAI therapy (Durante et al., 2006). Similarly, the cellular dedifferentiation associated with ATC renders these tumours RAI-R, and as such RAI therapy is not administered to these patients. Instead, conventional chemotherapy is given in cases of RAI-R thyroid cancers, although this is predominantly palliative as chemotherapy has very little therapeutic benefit. Unfortunately, there is no successful alternative treatment option, resulting in a very poor prognosis for these patients (Durante et al., 2006, Landa et al., 2016). Evidently there is great clinical need for novel therapeutics for advanced thyroid cancers. Fortunately, our improved understanding of the molecular mechanisms behind the progression to advanced thyroid

cancer is currently enabling the development and clinical trials of potential alternative therapies which are required for these patients.

1.2.3.1 Alternative treatment options currently under investigation for advanced thyroid cancer

1.2.3.1.1 Targeted therapy

Study of the genetic abnormalities observed in thyroid carcinomas have revealed two key signalling pathways which are often constitutively activated: MAPK and PI3K (see section 1.2.2). In normal physiology, these pathways propagate signals from receptor tyrosine kinases (RTKs) at the plasma membrane, such as RET, to alter protein expression at the genomic level by inducing or inhibiting transcription (Figure 1-3). As such, small molecule inhibitors of RTKs (TKIs) and other components of these signalling pathways are currently being explored for the treatment of RAI-R thyroid cancers (Raue and Frank-Raue, 2016, Zaballos and Santisteban, 2017).

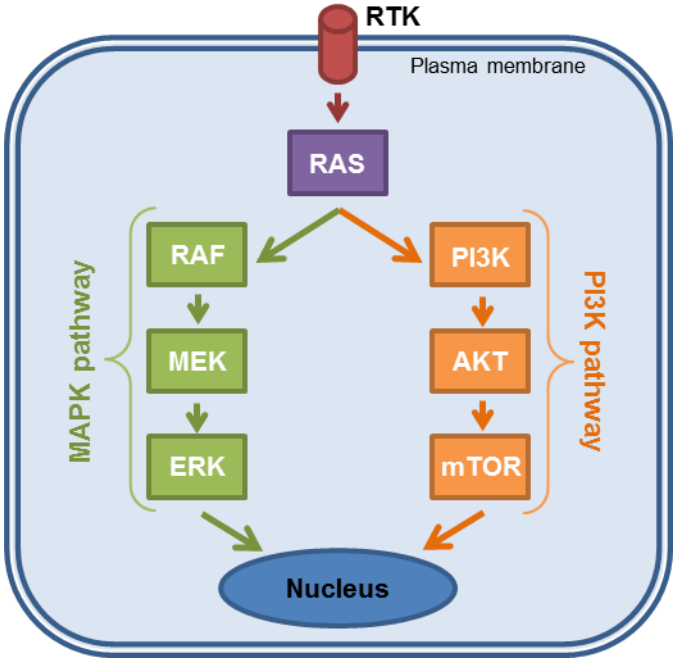

Figure 1-3 – Aberrant signalling pathways in thyroid cancer have led to potential therapeutic targets. The mitogen-activated protein kinase (MAPK; in green) and phosphatidylinositol 3-kinase (PI3K-AKT; in orange) signalling pathways propagate signals from receptor tyrosine kinases (RTKs, red cylinder) at the plasma membrane to the nucleus and result in modulated gene expression. Thyroid cancers are usually initiated by single genetic mutations which result in the constitutive activation of these signalling pathways, while accumulation of genetic mutations in these pathways often leads to cancer progression. Consequently, novel therapeutics designed to inhibit these pathways are currently being explored for the treatment of advanced thyroid cancer. Image adapted from Raue and Frank-Raue, 2016.

While there have been several clinical trials investigating the ability of many different TKIs to treat progressive RAI-R DTC (Viola et al., 2016, Berdelou et al., 2018), only two have been approved by the United States Food and Drug Administration (FDA) and European Medicines Agency (EMA) for this use. During its phase 3 clinical trial (DECISION), sorafinib significantly improved progression free survival (PFS, median PFS 10.8 vs. 5.8 months, with hazard ratio for progression or death at 0.59, 95% confidence interval 0.45-0.76; $p<0.0001$) and partial response rate (RR, 12.2% vs. 0.5% with placebo, $p<0.0001$) compared to control, although there was no statistically significant improvement in overall survival (Brose et al., 2014). Lenvatinib also demonstrated significantly improved PFS (median PFS 18.3 vs. 3.6 months, hazard ratio 0.21, 95% confidence interval 0.14-0.31; $p<0.0001$) and RR (overall RR 64.8%, with 63.2% achieving partial response and 1.5%

achieving complete response, vs. 1.5% with placebo; $p<0.0001$) compared to control in its phase 3 clinical trial (SELECT), but significant improvement in overall survival was not achieved (Schlumberger et al., 2015).

However, TKI therapy is not without its problems. Adverse events (AEs) are frequently experienced, particularly fatigue, nausea, diarrhoea, anorexia, skin rash and hypertension, with more serious AEs often experienced, such as hepatic or renal failure, QT prolongation, venous thromboembolic events, dyspnoea and plural effusion. Experiencing AEs led to dose reduction, interruption or withdrawal for a large portion of patients in all clinical trials involving TKIs (Viola et al., 2016). In the DECISION trial, 98.6% patients treated with sorafinib experienced AEs of any grade (vs. 87.6% for placebo), with 37.2% patients experiencing serious AEs (vs. 26.3% for placebo). This led to dose reduction, interruption and withdrawal in 64.3%, 66.2% and 18.8% patients, respectively (vs. 9.1%, 25.8% and 3.8% for placebo, respectively (Brose et al., 2014)). Treatment with lenvatinib during the SELECT trial resulted in 97.3% patients experiencing AEs of any grade (vs. 59.5% for placebo), with serious AEs experienced by 75.9% patients (vs. 9.9% for placebo). This resulted in dose reduction, interruption and withdrawal in 67.8%, 82.4% and 14.2% patients respectively (vs. 4.6%, 18.3% and 2.3%, respectively, for placebo (Schlumberger et al., 2015). Additionally, TKIs are cytostatic agents, rather than cytotoxic, meaning that complete response is rarely achieved and, once initiated, patients are required to remain on TKIs indefinitely as disease progression occurs rapidly upon cessation. Furthermore, cancer cells often develop an as yet unidentified ‘escape mechanism’ to overcome TKIs. Although clearly promising agents, these complications coupled with a lack of statistically significant improvement in overall survival rates with use of TKIs indicate that further work is required before they can be used as a widely-effective treatment option (Viola et al., 2016).

1.2.3.1.2 Redifferentiation therapy

RAI-R thyroid cancers lose susceptibility to RAI therapy due to cellular dedifferentiation. Thus, it is hypothesised that redifferentiation of these cells, through inducing transcription of thyroid-specific genes, might enable these cancers to respond to RAI therapy. A variety of different agents have been demonstrated to increase RAI uptake in RAI-R thyroid cancers *in vitro* and in clinical trials. Retinoic acid (RA), a vitamin A metabolite, binds to the nuclear RA or retinoid X receptors (RAR or RXR) and the RA-receptor complexes bind to the appropriate response element in the target gene promoter to initiate its transcription. RA has been shown to induce expression of NIS and Tg and resulted in I^- uptake in patients with RAI-R thyroid cancer (Simon et al., 1998, Schmutzler et al., 2002, Kim et al., 2009). Additionally, agonists of the nuclear receptor PPARγ, which heterodimerises with RXR to regulate gene transcription, have shown potential for use as redifferentiation agents in RAI-R thyroid cancer. Treatment with thiazolinediones, specifically troglitazone, induced NIS expression and I^- uptake in transformed thyroid cells (Frohlich et al., 2005).

Another class of agents under investigation for redifferentiation therapy in RAI-R thyroid cancer are histone deacetylase (HDAC) inhibitors. Gene expression can be epigenetically regulated through histone acetylation, which renders histones less condensed and enables gene transcription. This process is catalysed by histone acetyltransferase enzymes and reversed by HDAC enzymes; therefore treatment with HDAC inhibitors can increase gene transcription. A number of HDAC inhibitors have demonstrated increased NIS expression and subsequent I^- uptake in preclinical studies, such as sodium butyrate (Puppin et al., 2005), trichostatin A (Zarnegar et al., 2002), valproic acid (Fortunati et al., 2004), depsipeptide (Kitazono et al., 2001) and suberoylanilide hydroxamic acid (SAHA (Hou et al., 2010)).

Unfortunately, results from clinical trials using these redifferentiation agents have been inconsistent, with some trials showing very little increase in RAI uptake following treatment. However, these trials often had small sample numbers and did not account for the heterogeneity and mutational status of the tumours, which may help explain the lack of conclusive results. Consequently, further work is required to elucidate the circumstances in which redifferentiation agents can be effective treatment options for RAI-R thyroid cancers (Hong and Ahn, 2017). As NIS is the protein responsible for I^- uptake by thyroid follicular cells, it is widely believed that improved understanding of its regulation, with particular focus on its expression at the plasma membrane, could lead to the development of novel therapeutics that boost membranous NIS expression in RAI-R thyroid cancers, thereby facilitating the use of RAI as a successful treatment option for these patients.

1.3 The sodium-iodide symporter (NIS)

1.3.1 Identification, structure and characterisation

Although the ability of the thyroid to accumulate I^- was first described over a century ago (Baumann, 1896) and RAI has been used to treat thyroid disease, including cancer, for over 70 years (Hertz and Roberts, 1942, Seidlin et al., 1948), the mechanism of thyroidal I^- uptake remained elusive until the cloning of rat NIS in 1996 (Dai et al., 1996) and human NIS shortly after (Smanik et al., 1996). NIS is a member of the solute carrier 5A (SLC5A) protein family, a sub-group of the sodium-solute symporter (SSS) superfamily which utilises the Na^+ gradient to transport a wide variety of substrates (Wright and Turk, 2004, Jung, 2002). The human NIS gene (*SLC5A5*), located on chromosome 19p12-13.2, contains an open reading frame of 1929 nucleotides comprising 15 exons and 14 introns which encode a 643 amino acid protein (see section 1.1) with a predicted molecular mass of 68.7 kiloDaltons (kDa) and 84% identity (92% similarity) to rat NIS (Smanik et al., 1996).

The NIS protein was originally thought to have 12 transmembrane domains (TMDs) with intracellular amino- (N) and carboxyl- (C) termini, (Smanik et al., 1996, Levy et al., 1997). However, NIS was experimentally confirmed to have 13 TMDs, with an extracellular N-terminus and a long intracellular C-terminus, through mutation analysis of the sites of glycosylation (see Figure 1-4). NIS has 3 N-linked glycosylation sites: asparagine residues 225, 489 and 502. This increases the molecular weight of the mature, fully-glycosylated NIS protein to ~87kDa. As Asn225 was predicted to be intracellular in the original 12 TMD structure, a 13 TMD structure devised to enable all glycosylation sites to be extracellular is now widely accepted. Mutants with partial or complete abrogation of these glycosylation sites retained 50-90% function compared to wild-type, signifying that glycosylation is important for NIS function, but not vital (Levy et al., 1998a, De La Vieja et al., 2000).

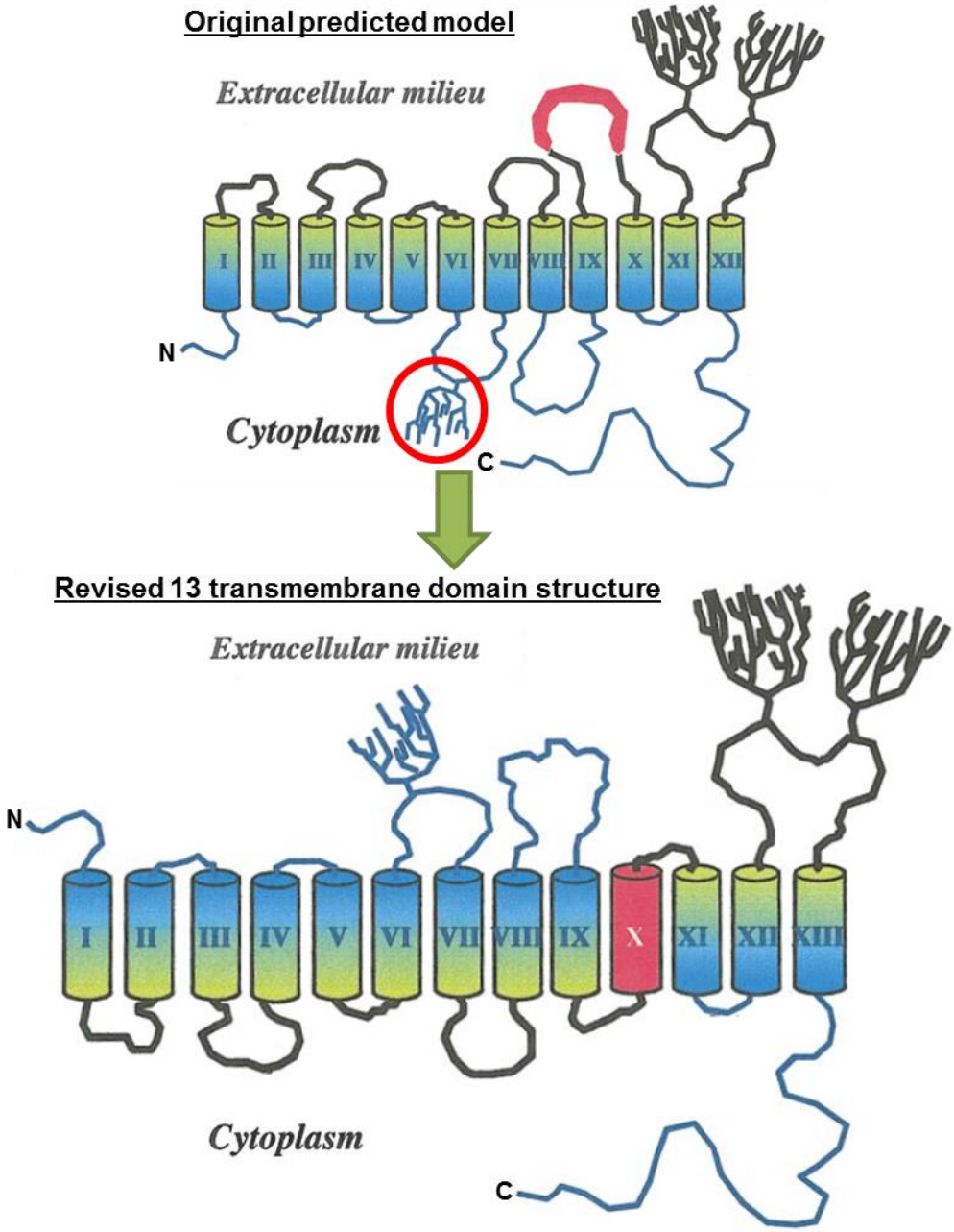

Figure 1-4 – NIS secondary structure. NIS has 13 transmembrane domains (TMDs, depicted as cylinders), with an extracellular amino (N)-terminus and long intracellular carboxyl (C)-terminus (bottom panel). NIS was experimentally proven to have 3 sites of N-linked glycosylation (branched structures) at N225, N489 and N502. As N225 was predicted to be intracellular in the original 12 TMD model (top panel, circled), this led to the development of the 13 TMD structure, whereby a section of the 5th extracellular loop in the 12 TMD model forms the 10th helix of the 13 TMD structure (shown in red). Image adapted from De La Vieja et al., 2000.

1.3.1.1 Analysis of clinically relevant mutations has revealed residues important for NIS structure and function

Mutations in the NIS gene cause I^- transport defect (ITD), a rare autosomal recessive condition where diminished I^- uptake results in congenital hypothyroidism, which can lead to severe impairment of physical and mental development if it is not diagnosed and treated soon after birth. Fourteen different mutations have been identified from ITD patients, and experimental studies on nine of these have provided valuable information on NIS structure and function (shown in Figure 1-5 and summarised in Table 1-2, (Ravera et al., 2017)).

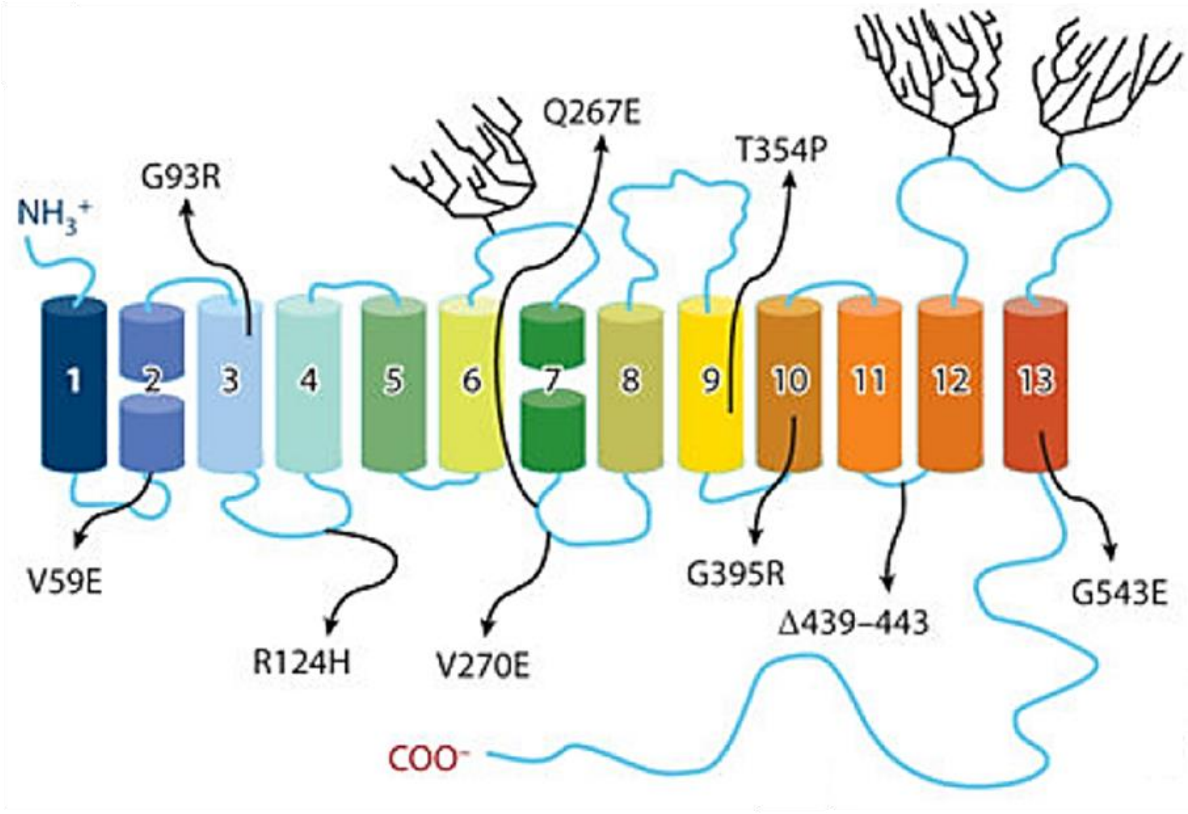

Figure 1-5 – Locations of iodide transport defect-causing mutants on the NIS secondary structure. The experimentally validated NIS secondary structure has 13 transmembrane domains (depicted as cylinders) with an extracellular amino- (NH_3^+, in blue) and intracellular carboxyl- (COO^-, in red) terminus. The 3 glycosylation sites are shown as branched structures. NIS mutations (named using the single-letter amino acid code (Δ represents deletions)) found to cause iodide transport defect in patients are depicted on the secondary structure model. Image taken from Ravera et al., 2017.

Mutant	Location	Effect of mutation	Residue function at relevant position	Molecular requirement at relevant position
V59E	TMD 9	Inactive; expressed at PM	Intramembrane helix-helix interaction	Neutral residue (except proline)
G93R	TMD 3	Inactive; expressed at PM	Pivot point for conformational change (interaction with W255)	Residue side chain affects anion selectivity and stoichiometry
R124H	IL 2	Active; not expressed at PM	Protein folding (interaction with C440)	δ-amino group on residue side chain
Q267E	IL 4	Partial activity; expressed at PM	Intramembrane helix-helix interaction	Neutral residue
V270E	IL 4	Active; not expressed at PM	Interaction with proteins involved in protein trafficking	Neutral residue
T354P	TMD 9	Inactive; expressed at PM	Involved in Na^+ binding	β-OH group on residue side chain
G395R	TMD 10	Inactive; expressed at PM	Intramembrane helix-helix interaction	Small, neutral residue
Δ439-443	IL 6	Inactive; not expressed at PM	Stabilises structure by α-helix N-capping of TMD 12	Asparagine or glutamine required at 441 for N-capping
G543E	TMD 13	Inactive; not expressed at PM	Protein folding	Small, neutral residue side chain

Table 1-2 – Properties of iodide transport defect-causing mutations and their effect on NIS structure and function. NIS mutations (named using the single-letter amino acid code (Δ represents deletions)) found to cause iodide transport defect in patients were experimentally characterised to determine their effect on NIS function and trafficking to the plasma membrane and subsequently elucidate the function and molecular requirements of the residues at the relevant positions. TMD, transmembrane domain; IL, intracellular loop. Table adapted from Ravera et al., 2017.

Studies of mutants which are still expressed at the plasma membrane but either partially or completely inactive have revealed structural information on NIS function. Valine to glutamic acid substitution at position 59 (V59E) results in an inactive protein which is correctly

targeted to the membrane, with function also inhibited by substitution with other charged residues and proline. This highlighted the need for a neutral, helix-promoting residue at this position for intramembrane helix-helix contact (Reed-Tsur et al., 2008). Glycine to arginine substitution at position 93 (G93R) generates an inactive but properly targeted protein. It was shown that different substitutions at this position altered I^- transport kinetics, as well as anion selectivity and stoichiometry (discussed in section 1.3.2.2). The proposed explanation for this was that G93 interacts with residue W255 on TMD 7, forming a 'ball-and socket joint' which acts as a pivot for conformational changes during transport (Paroder-Belenitsky et al., 2011). Substitution of glutamine with glutamic acid at position 267 (Q267E) results in a partially active protein expressed at the membrane. Experimental analyses showed this mutation resulted in a lower catalytic rate without affecting Na^+ or I^- binding and demonstrated that a neutral residue is required at this position for intramembrane helix-helix contact (De La Vieja et al., 2004). Threonine substitution to proline at position 354 (T354P) produces a correctly targeted but non-functional protein. Function was only rescued when substituted with serine, indicating the requirement for a β-OH group at this position, which is believed to be important for Na^+ binding (Levy et al., 1998b). Glycine to arginine substitution at position 395 (G395R) results in a non-functional protein expressed at the membrane. Similar to V59E, there is a requirement for a small, neutral residue at this position for correct intramembrane helix-helix interaction (Dohan et al., 2002).

Mutants with partial or total inhibition of trafficking to the plasma membrane have yielded important information on NIS folding. Arginine to histidine substitution at position 124 (R124H) produces an active protein which cannot be translocated to the membrane. A δ-amino group at this position was demonstrated to be required for correct membrane targeting, as it is believed to interact with residue C440 on IL 6 in order to achieve correct

NIS folding and targeting (Paroder et al., 2013). Substitution of valine with glutamic acid at position 270 (V270E) resulted in an active protein with significant inhibition of trafficking to the membrane. It is thought that this mutation disrupts an area of positive charge within IL 4, which consequently affects interactions with proteins involved in trafficking NIS to the membrane (Nicola et al., 2015). Deletion of residues 439-443 (Δ439-443) generates a non-functional protein which cannot be trafficked to the membrane. Experimental analysis of these five residues revealed that residue N441 was crucial for NIS function. The proposed explanation for this is that N441 mediates α-helix N-capping of TMD 12 which stabilises NIS structure (Li et al., 2013). Substitution of glycine with glutamic acid at position 543 (G543E) resulted in an inactive protein which cannot be targeted to the membrane. This mutant only partially matures, indicating the importance of a small, neutral residue at this position for correct protein folding (De la Vieja et al., 2005).

1.3.1.2 Extrathyroidal NIS expression

Although first identified for its role in I^- accumulation in the thyroid (see section 1.1.2.2), NIS expression has since been identified in a variety of tissues, thereby elucidating how I^- is used and cycled by the body (see Figure 1-6). Circulating I^- which has not been accumulated by the thyroid can be transported into the saliva via NIS expressed on the basolateral membrane of the ductal epithelial cells in the salivary glands (Spitzweg et al., 1999b, La Perle et al., 2013), or into the gastric juice via NIS localised on the basolateral membrane of the mucin-secreting and parietal cells in the stomach (Altorjay et al., 2007). This I^- is absorbed alongside ingested I^- via NIS expressed on the apical membrane of enterocyte cells of microvilli throughout the small intestine (Nicola et al., 2009), forming an I^- recycling mechanism. I^- is eliminated by the kidneys via NIS expressed on the basolateral membrane of distal tubular cells (Spitzweg et al., 2001b), but NIS expression has also been detected on

the apical membrane of cells in the proximal and cortical collecting tubes, suggesting that I^- may also be reabsorbed by the collecting tubes as a final recycling mechanism (Wapnir et al., 2003). Additional I^- transport mechanisms arise during pregnancy. NIS is expressed on the apical membrane of villous syncytiotrophoblast cells in the placenta at a constant level throughout pregnancy, thus enabling I^- to cross the placenta from the mother to the foetus for foetal TH synthesis (Bidart et al., 2000). During lactation, I^- is able to pass from the maternal bloodstream into her milk to provide the newborn with I^- for TH synthesis (see Figure 1-6). NIS is only expressed in the basolateral membrane of alveolar epithelial cells during lactation, and is not present in normal breast cells (Tazebay et al., 2000).

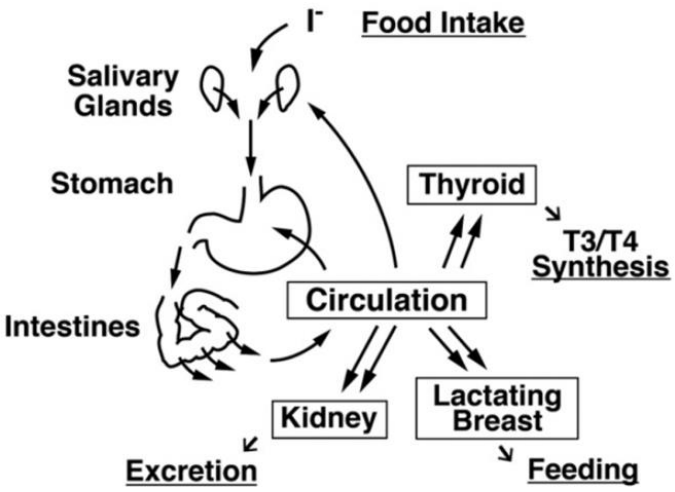

Figure 1-6 – Cycle of iodide uptake, utilisation and excretion in the human body. Ingested iodide (I^-) is absorbed into the circulation in the intestine, and predominantly taken up by the thyroid for thyroid hormone (T3/T4) synthesis, or the lactating breast to provide the newborn with I^-. Remaining circulating I^- can be recycled (i.e. released back into the gastrointestinal system via the saliva or gastric juices to be reabsorbed) or excreted by the kidneys. Image adapted from Kogai and Brent, 2012.

1.3.1.2.1 Additional roles for iodide

I^- is proposed to have additional actions in many non-thyroidal tissues. Reactive oxygen species (ROS) can be detoxified by I^- oxidation, and oxidised I^- has anti-microbial properties. This concept is strengthened by the co-expression of peroxidase systems in many NIS-expressing non-thyroidal tissues, including salivary glands, stomach, intestine, placenta

and lactating breast (De la Vieja and Santisteban, 2018). Additionally, NIS expression in the basolateral membrane of ovarian surface epithelial cells and secretory cells of the fallopian fimbriae implicates I^- as an anti-microbial agent in the female reproductive tract (Riesco-Eizaguirre et al., 2014). Similarly, expression of NIS in the ciliated columnar cells of the bronchial mucosa alongside DUOX and lactoperoxidase enzymes suggests a role for I^- in the anti-pathogen defensive mechanisms in the airways (Kang et al., 2009, Fischer et al., 2011). These additional roles emphasise the importance of I^-, and hence NIS, in physiology.

1.3.2 Potential clinical applications for NIS

1.3.2.1 NIS expression in non-thyroidal cancers

NIS expression has also been shown to be aberrant in a wide variety of non-thyroidal cancers. Like in thyroid cancers (see section 1.2), tumours of tissues which constitutively express NIS tend to lose this expression, such as salivary gland tumours (La Perle et al., 2013), gastric cancers and intestinal metaplasia (Altorjay et al., 2007). In contrast, NIS is often overexpressed in tumours of tissues where NIS expression is inducible, such as breast cancer (Tazebay et al., 2000) and ovarian cancer (Riesco-Eizaguirre et al., 2014), and in tissues with low physiological NIS expression, such as prostate, lung, colon and endometrial cancers (Wapnir et al., 2003). Consequently, it is of great importance to improve our understanding of the regulation of NIS localisation in order to potentially increase functional expression in NIS-expressing non-thyroidal cancers, which could enable the successful treatment of such cancers with RAI.

1.3.2.2 NIS and gene therapy

In addition to I^-, NIS has been demonstrated to transport several other anions with different selectivities and stoichiometries, as described in Figure 1-7 (Eskandari et al., 1997, Dohan et

al., 2007). This knowledge has been widely exploited, with perchlorate (ClO_4^-) commonly used experimentally as a NIS inhibitor and a variety of different radioisotopes of NIS substrates used clinically: I^- (^{123}I, ^{124}I, ^{125}I and ^{131}I), perrhenate (^{188}Re) and pertechnetate ($^{99m}TcO_4^-$), which only exists as a radioisotope (Dohan et al., 2007).

Perchlorate >	Perrhenate >	Iodide ≥	Selenocyanate ≥	Thiocynate >	Chlorate >	Nitrate
ClO_4^-	ReO_4^-	I^-	$SeCN^-$	SCN^-	ClO_3^-	NO_3^-
1:1	1:1	2:1	2:1	2:1	2:1	2:1

Figure 1-7 – Anion selectivities and stoichiometries of NIS. NIS can transport several anions with different selectivities (shown left to right in descending order of selectivity) and stoichiometries (either one or two sodium ions are transported per anion). Image adapted from Dohan et al., 2007.

Radioisotopes of an element arise when there is deviation from the usual number of protons and neutrons within the atomic nucleus, resulting in excess nuclear energy. This unstable atom undergoes radioactive decay to release this excess energy by emitting particulate (e.g. beta, β) and/or electromagnetic (e.g. gamma, γ) radiation, with different radioisotopes undergoing a specific type of decay (Hingorani et al., 2010). For instance, the stable iodine atom has a molecular weight of 127 (^{127}I), comprising 53 protons and 74 neutrons, while loss or gain of neutrons results in radioisotopes of iodine with different molecular weights (e.g. loss of two neutrons results in ^{125}I (WebElements, 2018)). As NIS is able to transport various radioisotopes with different types of decay, and therefore diverse clinical uses (Table 1-3), NIS is able to function both as a reporter (i.e. diagnostic) and therapeutic gene (Hingorani et al., 2010, Ravera et al., 2017).

Radioisotope	Radioactive decay	Clinical use
^{123}I	γ	SPECT
^{124}I	β^+	PET
^{125}I	γ	SPECT
^{131}I	β^-	Cytotoxic agent
^{99m}Tc	γ	SPECT
^{188}Re	β^-	Cytotoxic agent

Table 1-3 – Properties of radioisotopes transported by NIS. Radioisotopes have unstable atomic nuclei and undergo radioactive decay to release this excess nuclear energy. The different types of decay (gamma, γ, or beta, β) confer a different clinical use on the radioisotope, thus enabling NIS to function as a reporter and therapeutic agent for gene therapy. (SPECT, single-photon emission computed tomography; PET, positron emission tomography). Table adapted from Ravera, 2017.

The γ-radiation from ^{123}I, ^{125}I and ^{99m}Tc can be imaged using single-photon emission computed tomography (SPECT), while β^+-radiation from ^{124}I can be imaged using positron emission tomography (PET). The β^--radiation from ^{131}I and ^{188}Re is used therapeutically to deliver cytotoxic levels of radiation to cells directly and to neighbouring cells indirectly via cross-fire of β^--radiation from the affected cells (Hingorani et al., 2010, Ravera et al., 2017). There is increasing evidence to suggest that further indirect cytotoxic effects of β-radiation on neighbouring cells can be induced by the radiation-induced bystander effect, whereby cytotoxic chemicals, such as ROS or cytokines, released from affected cells mediate genomic instability and cell death of neighbouring cells (Mothersill and Seymour, 2004).

It is because NIS has dual reporter and therapeutic function that it has gained significant interest in the field of gene therapy. However, the therapeutic role of NIS in gene therapy was initially questioned, as it was thought that the absence of I^- organification in non-thyroidal tissues would prevent any therapeutic effect (Hingorani et al., 2010). These concerns were alleviated when NIS gene therapy was shown to have a therapeutic response *in vivo* using xenograft tumours of androgen-sensitive human prostate adenocarcinoma (LNCaP) cells stably transfected with human NIS under the control of a prostate-specific antigen promoter (NP-1 cells). Treatment of these NP-1 xenograft tumours with a single

therapeutic dose of ^{131}I (3 millicuries (mCi)) resulted in a significant reduction (>50%) in the volume of all tumours compared to controls (Spitzweg et al., 2000, Spitzweg et al., 1999c). Similar results were achieved using a more clinically relevant method of gene delivery, whereby LNCaP cells were infected with a replication-deficient human adenovirus containing the human NIS gene linked to the constitutive cytomegalovirus (CMV) promoter (Ad5-CMV-NIS). Treatment of Ad5-CMV-NIS infected LNCaP xenograft tumours with a single therapeutic dose of ^{131}I (3mCi) resulted in a mean reduction in tumour volume of 84±12% compared to controls (Spitzweg et al., 2001a). Since these studies, there have been a number of other pre-clinical studies investigating the efficacy of NIS gene therapy in a variety of cancers, such as liver (Sieger et al., 2003, Faivre et al., 2004), breast (Dwyer et al., 2005) and medullary thyroid carcinomas (Cengic et al., 2005), and using a range of gene delivery methods, from transfection plasmids with NIS expression regulated by the CMV promoter (Faivre et al., 2004) to complex viral vectors designed to express NIS using a range of tumour-specific promoters (Sieger et al., 2003, Dwyer et al., 2005, Cengic et al., 2005). I^- uptake was demonstrated in all studies both *in vitro* and *in vivo* using rodent models, and therapeutic response was promising, thus indicating the feasibility of NIS gene therapy (Hingorani et al., 2010).

However, further work still needs to be done before NIS gene therapy can be used clinically, as clinical study has not yielded a therapeutic response. Six males with localised prostate cancer were given an intraprostatic injection of adenovirus expressing human NIS alongside two suicide genes, yeast cytosine deaminase (y-CD) and mutant SR39 herpes simplex virus thymidine kinase (*mut*TK_{SR39}). All six prostates expressed NIS, but with distinct variability of prostate volume expressing NIS (mean 45% volume, range 18-83%). Furthermore, it was calculated that from an administered dose of 200mCi ^{131}I, the mean absorbed dose in these

prostates would have been far below that required to sterilise the prostate (Barton et al., 2011). Improved understanding of how to increase and retain NIS expression at the plasma membrane could be of great benefit to improve the efficacy of NIS gene therapy.

1.3.3 NIS regulation

1.3.3.1 TSH

Despite such wide potential for clinical applications, the mechanisms by which NIS is regulated are not fully understood. However, it is well established that TSH stimulates TH production (see section 1.1.2.1), largely via transcriptional regulation of NIS as TSH has been shown to increase NIS mRNA and protein expression (Kogai et al., 1997). The human NIS proximal promoter, located between nucleotides -478 and -389 relative to the transcription start site, contains a TATA box (AATAAAT), but this promoter does not mediate thyroid-specific NIS expression (Ryu et al., 1998). Instead, the human NIS upstream enhancer (hNUE), located between nucleotides -9847 and -8968 relative to the transcription start site, contains a binding site for the thyroid-specific transcription factor Pax8 and a cAMP response element (CRE)-like sequence, which enable transcriptional regulation of NIS in a thyroid-specific and cAMP-dependent manner, and activation of hNUE results in 15-fold higher NIS expression compared to the proximal promoter alone. Binding of TSH to its receptor, a guanine nucleotide-binding protein (G-protein) coupled receptor (GPCR), causes the trimeric G protein to dissociate into G_{α} and $G_{\beta\gamma}$ subunits which trigger various signalling cascades. It is well established that the G_{α} subunit stimulates adenylyl cyclase to produce cAMP, which then activates protein kinase A (PKA)-dependent and PKA-independent signalling pathways. These pathways trigger the binding of PAX8 to the NIS promoter to increase NIS transcription (Taki et al., 2002, Zaballos et al., 2008). However, the $G_{\beta\gamma}$ subunit stimulates the PI3K pathway to phosphorylate Akt independently of cAMP,

which has been shown to impair PAX8 binding to the NIS promoter and subsequently reduce NIS transcription. This contradictory effect on NIS transcription of the two G protein subunits has been postulated to form part of an autoregulatory system to maintain control of NIS expression, and subsequently iodide uptake, in the thyroid (Zaballos et al., 2008). TSH also post-translationally regulates NIS expression, as it has been shown to increase expression of NIS at the plasma membrane and to extend the half-life of the NIS protein from 3 days in the absence of TSH to 5 days. However, the molecular mechanisms of this post-translational regulation remain elusive (Riedel et al., 2001).

1.3.3.2 Iodide

Conversely, it has been known for over 70 years that excess I^- suppresses TH synthesis, yet the mechanisms for this remain to be fully elucidated. High serum I^- levels were shown to block I^- uptake in rat thyroid and subsequently reduce TH production, which was termed the Wolff-Chaikoff effect (Wolff and Chaikoff, 1948). However, inhibition of TH synthesis was shown to be temporary, with restoration of TH production after approximately 2 days, even in the continued presence of high I^- levels. This is known as the escape from the Wolff-Chaikoff effect (Wolff et al., 1949). Since the first suggestion that this escape mechanism was due to reduced I^- transport, thus reducing the I^- concentration within the thyroid follicles and enabling the resumption of TH synthesis (Braverman and Ingbar, 1963), several studies have investigated the regulatory effect of I^- on NIS expression. It has been demonstrated that high I^- resulted in lower levels of NIS mRNA in dog thyroid *in vivo* (Uyttersprot et al., 1997), reduced NIS mRNA and subsequent I^- transport in rat thyroid cells *in vitro* (Spitzweg et al., 1999a), and decreased NIS mRNA and protein expression in rat thyroid *in vivo* (Eng et al., 1999). Further investigation suggested that NIS mRNA levels were lowered by excess I^- through increased instability of NIS mRNA (Serrano-Nascimento et al., 2010) and/or

reduced transcription due to altered promoter activity (Serrano-Nascimento et al., 2016). Others demonstrated post-translational effects of I^- on NIS, with one study showing that high I^- decreased NIS protein expression in rat thyroid cells *in vitro*, without altering NIS mRNA levels, due to increased protein turnover (Eng et al., 2001), while another study proposed that the increased ROS production associated with excess I^- might be involved in NIS inactivation at the plasma membrane (Leoni et al., 2011). The results of these studies highlight that NIS regulation by I^- is complex, with transcriptional, post-transcriptional and post-translational mechanisms all potentially involved.

1.3.3.3 Other regulators of NIS: IGF1, TGFβ and Retinoic Acid

Although mechanisms of NIS regulation remain poorly understood, other regulators of NIS have been identified which shed new light in this area. Insulin-like growth factor 1 (IGF-1) has been shown to inhibit TSH-induced stimulation of NIS transcription in the stable rat thyroid cell line, FRTL-5 cells. Treatment with a specific inhibitor of phosphatidylinositol-3-kinase (PI3K), LY294002, prevented this inhibition, thereby indicating that this action of IGF-1 is mediated by PI3K. It was also demonstrated that IGF-1 also disrupts cAMP signalling, as IGF-1 prevented increased NIS expression in response to forskolin, thereby suggesting that cross-talk occurs between the PI3K and cAMP signalling pathways (Garcia and Santisteban, 2002). Similarly, transforming growth factor β (TGFβ) has also been shown to interfere with the TSH-mediated stimulation of NIS expression. TGFβ signalling causes increased expression of Smad3, which was shown via GST pull-down assays to physically interact with Pax8. This interaction was subsequently demonstrated to impede binding of Pax8 to the NIS hNUE, thus impairing NIS transcription (Costamagna et al., 2004). Since novel therapeutics for advanced thyroid cancers aim to increase NIS expression, improved

knowledge on negative regulators of NIS expression could also have important clinical relevance.

Conversely, retinoic acid has been shown to induce NIS expression in RAI-R thyroid cancers (as described in section 1.2.3.1.2), although significantly less in known about the mechanisms involved. All-trans-retinoic acid (ATRA) was recently demonstrated to simultaneously enhance ^{131}I uptake and reduce proliferation and invasion of SW1736 cells, an anaplastic thyroid carcinoma cell line. Since similar results were observed in SW1736 cells stably expressing β-catenin shRNA, the authors proposed that ATRA decreases the transcriptional activity of β-catenin, which mediated the effects observed (Lan et al., 2017). Although further study is required to confirm this pathway, this study has revealed another potential target for novel therapeutics to boost NIS expression in advanced thyroid cancers.

1.3.3.4 Protein-protein interactions

Regulation of protein expression and subcellular localisation is often mediated by interactions with other proteins, which can often be altered during disease. However, only two proteins have been shown to bind to NIS: pituitary tumor transforming gene (PTTG)-binding factor (PBF) and the leukaemia-associated RhoA guanine exchange factor (LARG).

1.3.3.4.1 PBF

PBF is the only protein known to directly modulate NIS expression. Co-immunoprecipitation studies have demonstrated direct binding between PBF and NIS, while immunofluorescence and cell-surface biotinylation assays revealed that PBF causes the internalisation of NIS from the plasma membrane, thus reducing I- uptake (Figure 1 8). As PBF is often overexpressed in thyroid and other cancers, this will impede the effectiveness of RAI therapy in such tumours (Smith et al., 2009).

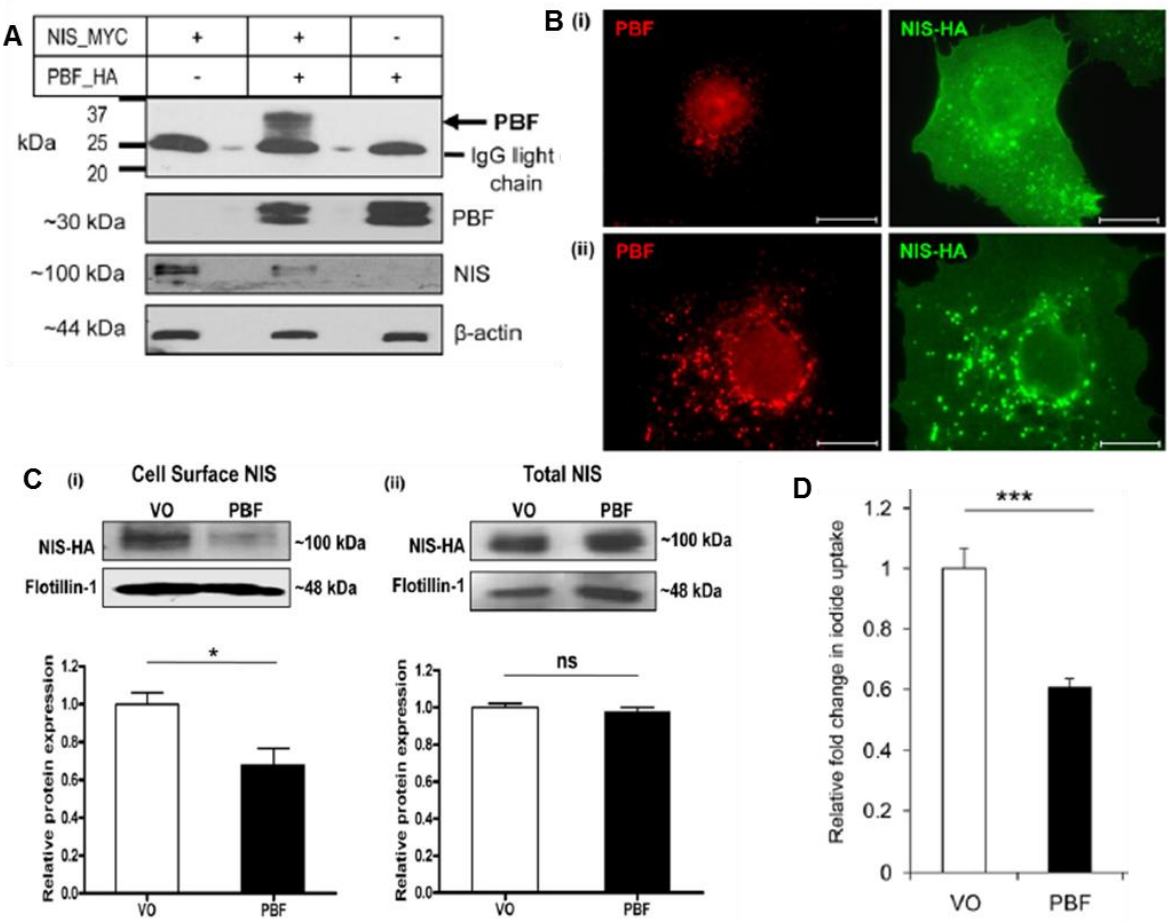

Figure 1-8 – PBF binds NIS and alters its subcellular localisation. A) Co-immunoprecipitation assay gave a 30kDA band representing PBF (arrow) only when NIS and PBF were co-transfected into COS7 cells, demonstrating direct binding between NIS and PBF. Analysis of total protein lysate (lower blots) confirms protein transfection and even protein loading (β-actin). B) Immunofluorescence in COS7 cells shows largely membranous NIS expression in the presence of endogenous PBF (i), while exogenous PBF results in NIS expression largely within intracellular vesicles (ii). C) Cell-surface biotinylation assays in COS7 cells demonstrated that PBF resulted in reduced NIS expression at the cell surface (i) without affecting total NIS expression (ii). D) PBF expression resulted in significantly reduced iodide uptake in FRTL5 cells. Images taken from Smith et al., 2009.

1.3.3.4.2 LARG

LARG was identified as a putative binding protein of NIS based on yeast two-hybrid screenings with the NIS C-terminus, and immunoprecipitation and pull-down assays confirmed that direct interaction between the two proteins occurs via PDZ domains located on the NIS C-terminus and the LARG N-terminus. Interaction between NIS and LARG was shown to stimulate RhoA activation, resulting in increased cell migration and invasion. Furthermore, use of the intracellularly-retained NIS mutant G543E revealed a higher rate of

cell migration compared to WT NIS, demonstrating that intracellular NIS is responsible for these effects. This is of particular interest since intracellular NIS expression is often associated with more advanced thyroid cancers (Lacoste et al., 2012), so further research into this interaction may help provide novel therapeutic targets for such cancers.

1.4 Dimerisation

1.4.1 Dimerisation is a form of protein-protein interaction which can modulate function

While protein-protein interactions which modulate protein function are often considered to take place between different proteins, a large number of proteins are also regulated by interactions with other monomers of themselves in a process known as dimerisation. This can have a wide range of direct and indirect implications for protein function which vary greatly depending on the proteins involved.

1.4.1.1 Dimerisation is required for the function of receptor tyrosine kinases

Dimerisation has been extensively shown to be directly important for the function of RTKs, a large superfamily comprising 58 proteins divided into 20 sub-families, including epidermal growth factor receptors (EGFRs or ErbBs), fibroblast growth factor receptors (FGFRs) and vascular endothelial growth factor receptors (VEGFRs; (Robinson et al., 2000)). RTKs are comprised of an extracellular ligand-binding domain, a single TMD and an intracellular tyrosine kinase catalytic domain (Figure 1-9) and, as such, are involved in the propagation of signals across the plasma membrane (Hubbard and Till, 2000). It has long been established that RTKs exist in the membrane as inactive monomers which then form stable dimers upon ligand binding. Dimerisation activates the RTK by enabling autophosphorylation of the catalytic domains, which mediates signal transduction (Figure 1-9; (Schlessinger, 2000)).

However, there is growing evidence to suggest that a number of RTKs can exist in the membrane as inactive dimers, with ligand binding inducing a conformational change within the dimer which activates the RTK (Figure 1-9; (Maruyama, 2015)). This is particularly pertinent to the insulin receptor (IR), as this receptor is a pre-formed dimer covalently linked via disulphide bonds between the two extracellular domains (Sparrow et al., 1997), but is believed to also occur in monomeric RTKs (Li and Hristova, 2010).

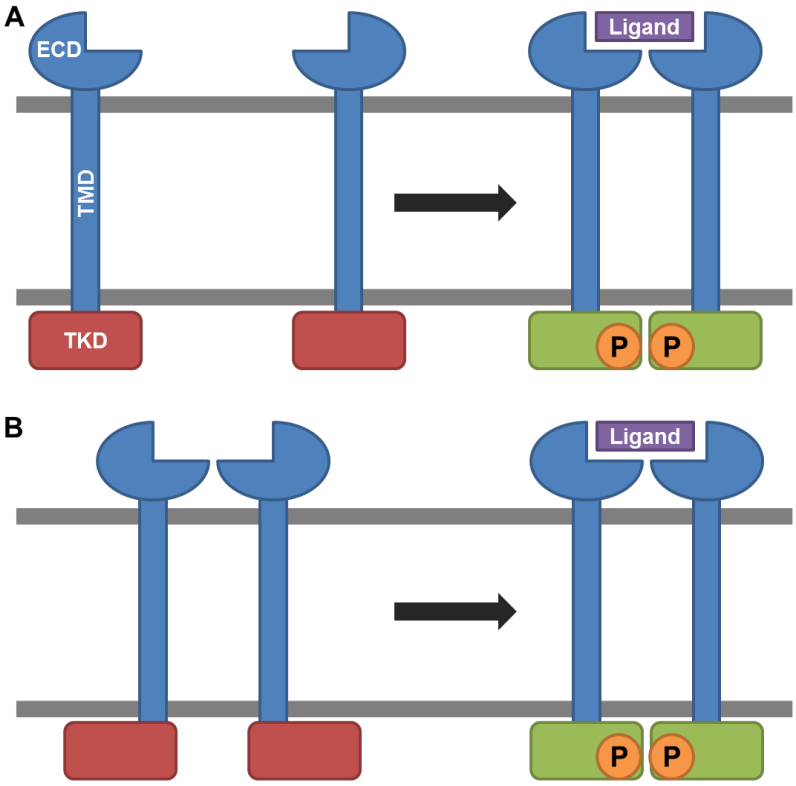

Figure 1-9 - Dimerisation is required for the activation of receptor tyrosine kinases, but it may occur prior to ligand binding. Receptor tyrosine kinases (RTKs) comprise three domains: the extracellular domain (ECD), transmembrane domain (TMD) and the intracellular tyrosine kinase domain (TKD). A) In the traditional method of RTK activation, RTKs exist as inactive monomers within the membrane (red TKD). Binding of the ligand (purple rectangle) induces RTK dimerisation, which facilitates autophosphorylation of the TKDs (orange circles) and results in RTK activation (green TKD). B) In the alternative method of RTK activation, RTKs are believed to be able to exist within the membrane as non-functional dimers. Ligand binding induces a conformational change within the dimer which brings the TKDs into close enough proximity to allow autophosphorylation and RTK activation. Image adapted from Schlessinger, 2000 and Maruyama, 2015.

Although all three RTK domains have been shown to play a role in the dimerisation process, the evidence suggests that the TMD portion is likely the most significant contributor,

although this remains to be fully elucidated (Li and Hristova, 2006). Studies revealed that isolated TMDs from EGFRs were able to dimerise within a bacterial membrane using the TOXCAT assay (Mendrola et al., 2002). In this assay, chimeric proteins were created which fused the TMD of the protein of interest to the DNA-binding domain of the transcriptional activator ToxR and the maltose binding protein, which anchors the chimeric protein to the plasma membrane. As ToxR is required to dimerise in order to function, transcription of the reporter gene, chloramphenicol acetyltransferase (CAT), can only occur if the TMD dimerises within the membrane. Furthermore, the extent of CAT expression is a measure of the strength of dimerisation (Russ and Engelman, 1999). Further studies utilising sodium dodecyl sulphate-polyacrylamide gel electrophoresis (SDS-PAGE) and Förster resonance energy transfer (FRET) techniques demonstrated that isolated TMDs from FGFR3 could also interact within lipid bilayers. Although these interactions were weaker than those observed for glycophorin A (GpA), a well-established dimeric membrane protein, this was deemed physiologically relevant due to the requirement for transient dimerisation of RTKs in order to control the subsequent signalling cascades (Li et al., 2005).

While this is promising data to suggest a pivotal role for TMDs in RTK dimerisation, it is important to note that formation of dimers is predicted to be 10^6-fold higher when proteins are expressed in a membrane due to the relative increase in protein concentration within the membrane environment (Grasberger et al., 1986). Consequently, a more physiologically relevant understanding of RTK dimerisation could be achieved by performing structural and biophysical analysis of the interactions between full-length RTKs. Unfortunately, it remains challenging to resolve high-resolution structures of full-length RTK dimers, which hinders such studies being carried out, and there are additional concerns over the ability to determine dimeric RTK structures, given that the dimeric interactions are relatively weak due to their

transient nature for function (Li and Hristova, 2010). However, the structures of two distinct RTK TMD dimers have been solved, which has shed more light on RTK TMD dimerisation.

The spatial structure of the ErbB2 TMD dimer within lipid bicelles mimicking the membrane was determined by solution nuclear magnetic resonance (NMR) and molecular dynamics relaxation (Figure 1-10). The two TMDs intersect at a -42^{o} angle, thus forming a right-handed symmetrical dimer, and the key residues interacting at the dimer interface were identified as T652, S656 and G660, with transient hydrogen bonds between the side chains of residues T652 and S656 thought to be involved in the dimerisation process (Bocharov et al., 2008b). These residues also form part of a GG_4-like dimerisation motif, a consensus sequence comprising two glycine residues (G) separated by three non-specific residues (X). This sequence facilitates tight helix packing and is strongly over-represented in TM helices compared to random expectation, indicating that this is a significant contributor to TM dimerisation (discussed further in Chapter 4; (Russ and Engelman, 2000)). However, this is not the only GG_4-like motif in the ErbB2 TMD sequence. While this motif is at the N-terminal end of the TMD, another GG_4-like motif exists between G668 and G672 towards the C-terminal end (Figure 1-10). The authors suggest that this structure utilising the N-terminal GG_4-like motif may reflect the active form of the dimer, while dimerisation at the C-terminal GG_4-like motif may correspond to the inactive dimer, suggesting that ErbB2 is capable of forming inactive dimers in the membrane which become activated due to ligand binding causing a conformational change within the structure. Furthermore, the presence of another motif known to be frequently associated with dimerisation, a leucine zipper motif (discussed further in Chapter 4), was described which may participate in additional interactions for the formation of heterodimers or oligomers (Bocharov et al., 2008b).

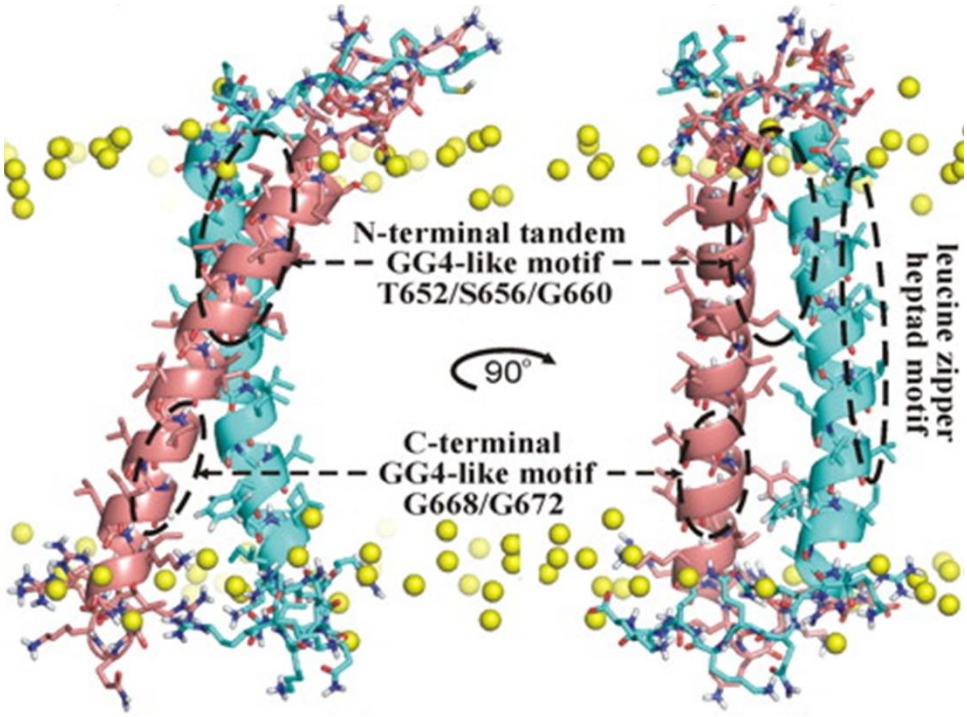

Figure 1-10 - The spatial structure of the ErbB2 transmembrane domain dimer demonstrates the importance of the domains for dimerisation and support the alternative model of receptor tyrosine kinase activation. Ribbons illustrate the backbone of the two transmembrane domains (TMDs) of the ErbB2 TMD dimer (in pink and blue) in two orientations within the lipid bicelle membrane (yellow circles represent the phospholipid heads) and residue side chains are shown in stick form. Dashed ovals highlight the spatial locations of the three dimerisation motifs believed to be involved in ErbB2 dimerisation: the N-terminal and C-terminal GG_4-like motifs are thought to correspond to the active and inactive dimer, respectively, while interactions between the leucine zipper motifs are thought to form heterodimers or oligomers. Image taken from Bocharov 2008b.

Interestingly, a very similar structure was observed for the TMD dimer of the erythropoietin-producing A1 (EphA1) receptor, which was also solved in lipid bicelles. The EphA1 structure was also a right-handed symmetrical dimer, with the two TMDs intersecting at a -44^o angle, and residues A550, G554 and G558 shown to be the key residues interacting at the dimer interface. Again, these residues form the N-terminal GG_4-like motif and this is believed to be the active form of the dimer. However, a second conformation was also observed for EphA1 in these studies, which was deemed to correspond to the inactive dimer. Although a high resolution structure of this minor conformation could not be resolved, the associated chemical shifts predicted that this structure would be a left-handed dimer with an intersection angle of approximately 30^o, likely mediated by interactions between residues

L557, A560, G564 and V567 which form a C-terminal GG_4-like motif (Bocharov et al., 2008a). Altogether, these data indicate a critical role for TMDs in the dimerisation of RTKs.

1.4.1.2 Roles for dimerisation in protein trafficking

Conversely, dimerisation is not thought to be required for the basic function of GPCRs, as a number of monomeric GPCRs expressed in membrane-mimicking lipid vesicles have been shown to mediate their signal transduction upon ligand binding, including β_2-adrenergic receptors (Whorton et al., 2007) and μ-opioid receptors (Kuszak et al., 2009). However, there is mounting evidence suggesting that GPCRs form dimers and oligomers (Hebert and Bouvier, 1998, Fuxe et al., 2010), and dimerisation is believed to be involved in the trafficking of GPCRs to the plasma membrane where they are functional. Figure 1-11 illustrates an overview of the trafficking pathway, in which proteins are synthesised and folded in the rough endoplasmic reticulum (ER), and then processed (e.g. glycosylated) in the Golgi network prior to being trafficked in secretory vesicles to the plasma membrane. Once at the membrane, proteins can be internalised into endosomes and either recycled back to the membrane or targeted to lysosomes for degradation (Peer, 2011).

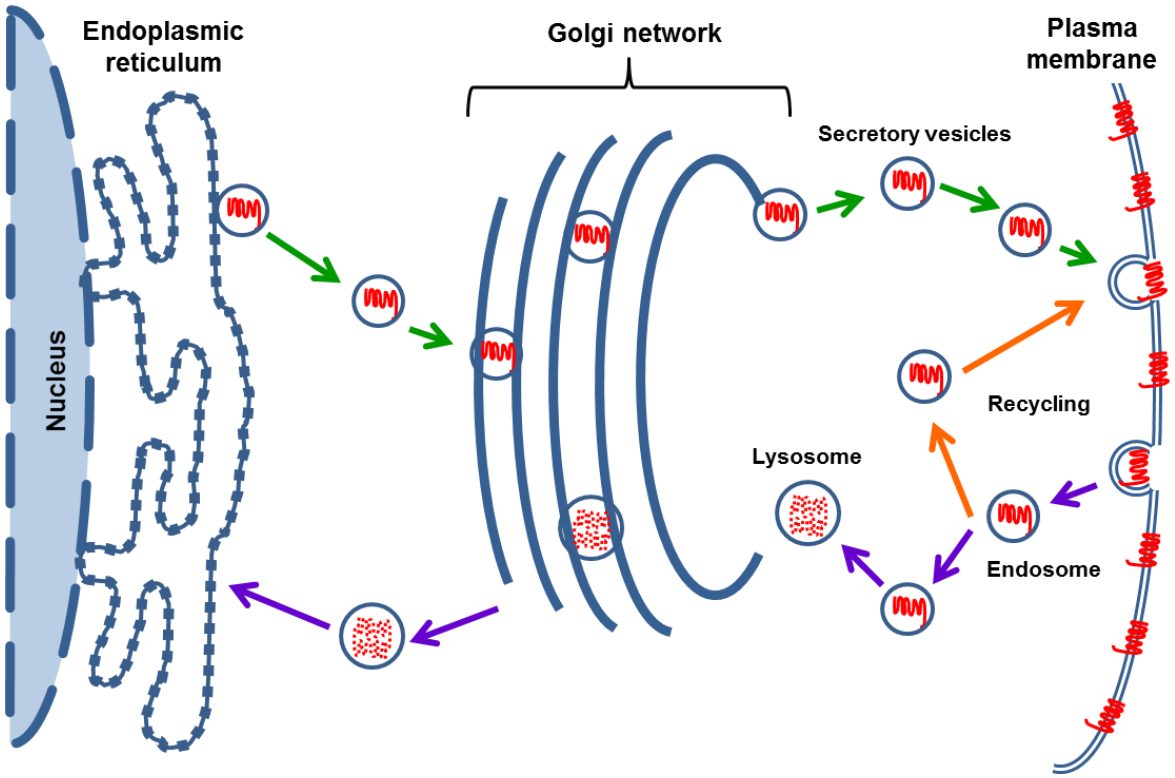

Figure 1-11 – An overview of the membrane protein trafficking pathway. Membrane proteins are synthesised and folded in the rough endoplasmic reticulum (ER) and transported to the Golgi network, where protein processing and maturation occurs. Proteins are then trafficked to the plasma membrane in secretory vesicles (green arrows). Proteins at the plasma membrane can then be internalised into endosomes and either recycled back to the membrane (orange arrows) or targeted to the lysosome for degradation (purple arrows). Degraded proteins are then recycled back through the Golgi network to the ER to enable continued protein synthesis. Image adapted from Peer, 2001.

Dimerisation between the two distinct subunits of the $GABA_B$ receptor has been demonstrated to be required for its function and cell surface expression. The $GABA_{B1}$ subunit is able to bind the agonist but cannot activate G proteins for the subsequent signalling cascades, whereas $GABA_{B2}$ is the opposite. Not only does dimerisation bring the two subunits together to form a functional unit, it also masks an endoplasmic reticulum (ER)-retention sequence on the $GABA_{B1}$ intracellular C-terminus, thus enabling the dimer to be trafficked to the membrane and demonstrating a crucial role for dimerisation in GPCR trafficking (Maurel et al., 2008). Additional studies have also shown that GPCR dimerisation occurs within the ER, and mutated GPCRs which are retained in the ER affect the expression of wild-type receptors at the membrane, thus further supporting a role for dimerisation in the

cellular trafficking of GPCRs to the membrane. Experiments in which the β_2-adrenergic receptor C-terminus was replaced with that of the $GABA_{B1}$ subunit resulted in both the mutant and wild-type receptors being retained within the ER. This not only demonstrated that β_2-adrenergic receptors dimerise within the ER, but also that, unlike the $GABA_B$ receptor, dimerisation of the β_2-adrenergic receptor does not involve the C-terminus (Salahpour et al., 2004). Similar results have been observed with other GPCRs. The addition of an ER-retention sequence to the C-terminus of the chemokine receptor CXCR1 resulted in reduced expression of the wild-type receptor at the membrane (Wilson et al., 2005), while a mutant α_{2B}-adrenoceptor which is retained in the ER caused the ER-retention of not only the wild-type α_{2B}-adrenoceptor, but also the α_{2A}- and α_{2C}-adrenoceptors (Zhou et al., 2006). Furthermore, expression levels of the ER chaperone protein calreticulin are believed to be important for dimerisation to occur between the angiotensin AT_1 and the mature, properly-folded bradykinin B2 receptors, indicating that GPCR dimerisation may be regulated by other proteins, particularly within the ER, as only correctly folded proteins may undergo dimerisation (Abd Alla et al., 2009).

It has been demonstrated that A_2-adenosine receptors are synthesised and trafficked to the membrane as dimers, but assemble into higher order oligomers within the plasma membrane (Vidi et al., 2008), and this is likely to be the case for other GPCRs. Investigations into assessing the dynamics of interactions between β-adrenergic receptors at the plasma membrane were carried out using fluorescence recovery after photobleaching (FRAP), whereby receptors were tagged with yellow fluorescent protein (YFP) at the extracellular N-terminus or with cyan fluorescent protein (CFP) at the intracellular C-terminus. A portion of the membrane of cells expressing both constructs is then photobleached and the time taken for fluorescent receptors to migrate into this area is indicative of the mobility of the receptors

within the membrane. The use of anti-YFP antibodies elucidates the dynamics of receptor dimerisation, as binding of the antibody to YFP significantly hinders the migration of itself and any bound proteins within the membrane (Dorsch et al., 2009). These experiments revealed very little recovery with CFP-tagged β_2-adrenergic receptors, demonstrating the presence of strong interactions between CFP- and YFP-tagged receptors. However, the migration of CFP-tagged β_1-adrenergic receptors was only modestly inhibited by the YFP antibody, indicating that these receptors only transiently interacted with the immobilised YFP-tagged variants, thus demonstrating dynamic dimerisation of β_1-adrenergic receptors (Dorsch et al., 2009). Similar experiments were carried out on D_2-dopamine receptors and also demonstrated dynamic dimerisation of these receptors (Fotiadis et al., 2006).

In summary, although dimerisation has been demonstrated to play important roles in a wide variety of different proteins, these effects appear to be specific to the protein involved. Consequently, no definitive assumptions can be made on how dimerisation affects a protein, as this will need to be determined for individual proteins.

1.4.2 NIS and dimerisation

Interestingly, there is some evidence to suggest that NIS is able to dimerise. Insertion of NIS into the plasma membrane of *Xenopus laevis* oocytes was observed as intramembrane particles (IMPs) of around 9nm diameter during freeze-fracture electron microscopy (Eskandari et al., 1997). As this is a similar size to the IMPs of proteins with comparable molecular weights (~65kDa) that are known to dimerise, such as the *Shaker* K^+ channel (70kDa, 10.7nm IMPs), it suggests that NIS is present in the membrane in a dimeric form (Figure 1-12B (Eskandari et al., 1997)). Nevertheless, this is not conclusive as it does not indicate if direct interactions are occurring between NIS monomers. Furthermore, the effect of glycosylation on NIS molecular weight is not taken into account, which would affect the

size of the IMPs, as mature, fully glycosylated NIS is ~87kDa (see section 1.3.1). Furthermore, size exclusion chromatography (SEC) and light scattering analysis of purified NIS protein isolated from mammalian cells revealed different molecular weights of NIS, indicating that NIS exists in various oligomeric states. This was verified via Western blotting of each fraction from SEC (Figure 1-12C (Huc-Brandt et al., 2011)), and is supported by similar findings from other Western blot analyses on mammalian cells exogenously expressing NIS (Levy et al., 1997, Castro et al., 1999, Dayem et al., 2008). However, these experiments only use extracted protein, so it cannot be determined if these dimeric complexes actually exist, or if this is merely protein aggregation in the lysate.

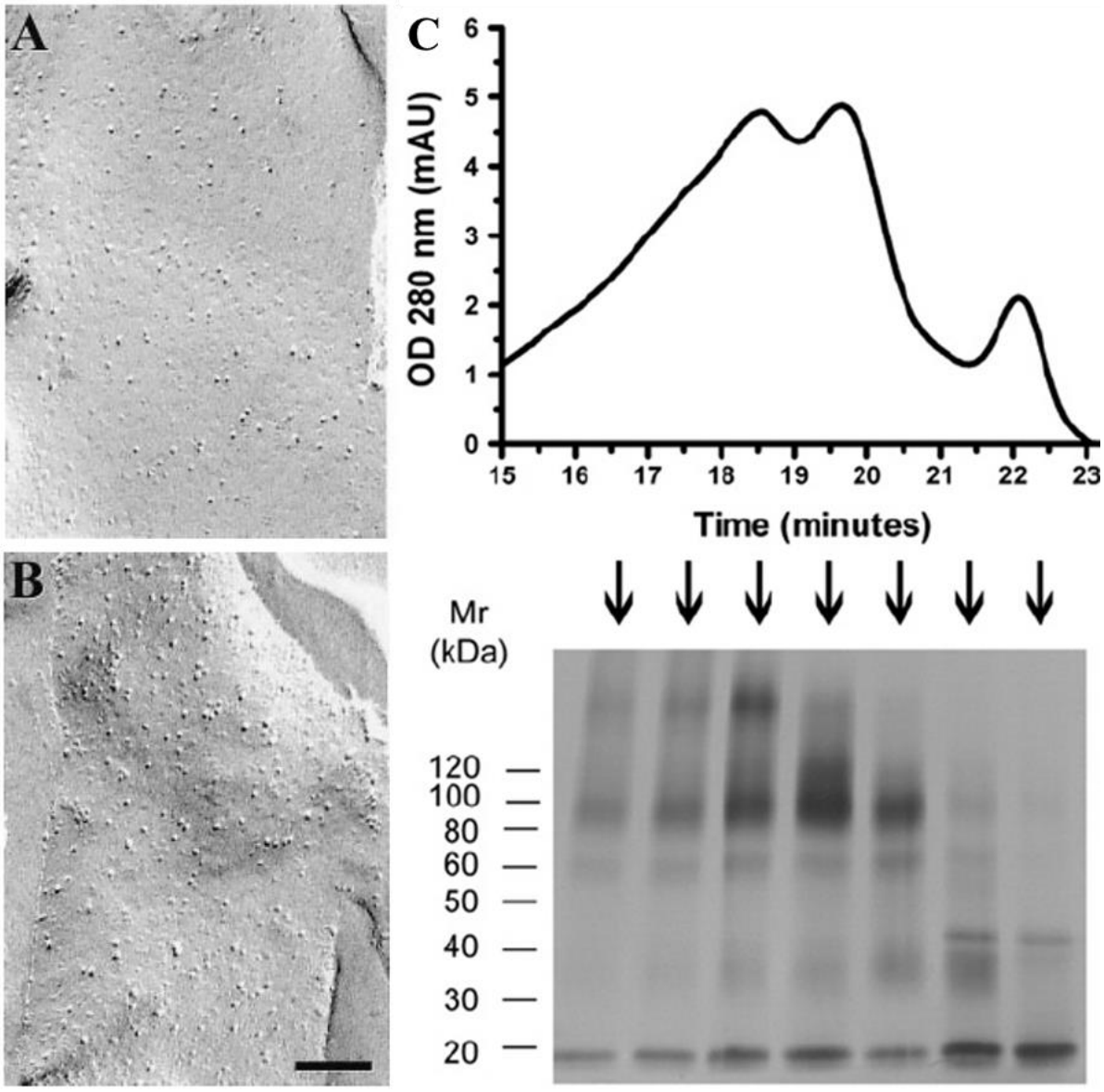

Figure 1-12 – Current evidence suggesting NIS forms dimers. Freeze-fracture electron micrographs of the plasma membrane of a control (A) and NIS-expressing (B) *Xenopus laevis* oocyte reveal increased density of intramembrane particles (IMP) with NIS expression, indicating insertion of NIS into the membrane. NIS IMPs were around 9nm in diameter, which is comparable to that of other proteins with similar molecular weight and that are known to dimerise. (C) Representative profile of size exclusion chromatography and light scattering analysis of purified NIS protein (top panel) and Western blot analysis of the indicated fractions (bottom panel). Bands between the 80-100kDa markers and at ~60kDa represent mature, fully glycosylated NIS and immature, partially glycosylated NIS, respectively, while the 20kDa band represents NIS C-terminal fragments. Higher molecular weight bands are indicative of NIS dimerisation. Images taken from Eskandari et al., 1997 (A and B) and Huc-Brandt et al., 2011 (C).

Critically, it still remains uncertain whether NIS intrinsically forms dimers, as neither study demonstrates direct interaction of NIS monomers in isolated protein or *in vitro*. Moreover, these studies do not consider the potential implications of dimerisation on NIS function,

despite the importance of dimerisation for many proteins. Consequently, further work is required to (i) investigate whether direct interactions between NIS monomers can be detected, (ii) establish the subcellular localisation of NIS dimerisation, and (iii) elucidate the regions of the protein involved in NIS dimerisation.

1.4.3 Methods for investigating protein dimerisation

The methods used to investigate protein dimerisation are based on those widely used for the detection of protein-protein interactions; however, there must first be a way of distinguishing between the two protein monomers in order to confirm that the detected interaction is occurring between two distinct monomers. One commonly used way is to have two variants of the protein, each with a different tag. There is a vast range of methodologies that could be applied (a small number of which are described below); some investigate protein-protein interactions within the whole cell, while others use isolated proteins. As each methodology has its own advantages and disadvantages, employing several such methods is required to validate any observed dimeric interactions, as this will provide a wealth of data to support the conclusions and help to offset the drawbacks associated with individual techniques.

1.4.3.1 Methods using isolated proteins

There are many methods which investigate protein-protein interactions using isolated proteins. One such technique which is widely used is co-immunoprecipitation (co-IP, Figure 1-13). Cells expressing the proteins(s) of interest are lysed and primary antibody associated (either covalently or non-covalently) with sepharose beads is added to precipitate one of the proteins of interest. The precipitate is then washed to remove non-specifically bound protein prior to elution from the beads and analysis to detect the presence of the second protein of interest. This is usually via SDS-PAGE (Western blotting), probing with a primary antibody

to the second protein (Lee, 2007). Provided that the antibodies used do not cross-react between the two proteins, this is a robust way of detecting protein-protein interactions.

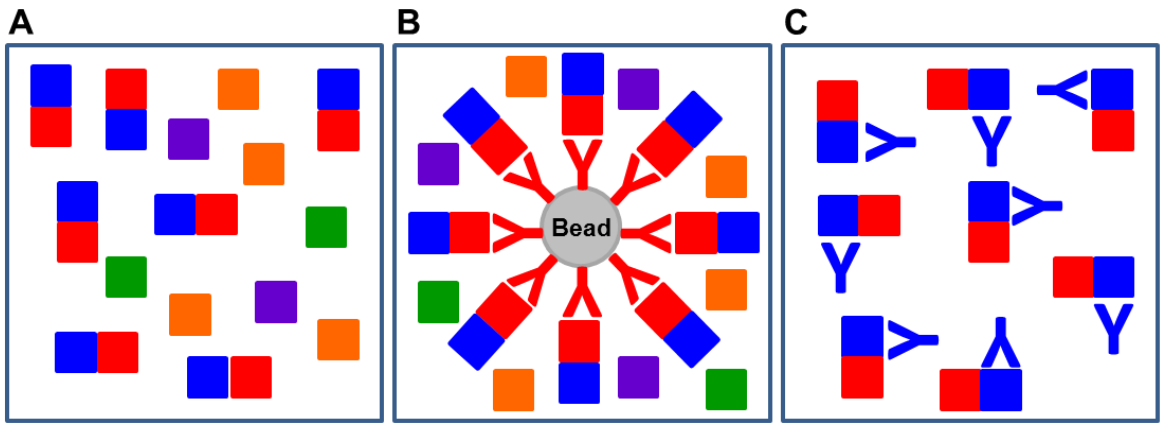

Figure 1-13 – Co-immunoprecipitation is a method for detecting protein-protein interactions using isolated proteins. In order to isolate the protein of interest (in red) from the protein lysate (A), lysates are incubated with sepharose beads associated with primary antibodies (in red) against the protein of interest (B). C) This purifies the protein of interest and any other proteins directly bound to it (in blue). Primary antibodies against the secondary protein (in blue) are then used to detect the presence of this protein and therefore establish an interaction between the two proteins. Image adapted from Lee, 2007.

However, there are some disadvantages to this technique. It is possible to detect interactions between two proteins that do not directly interact but form part of a larger protein complex (Phizicky and Fields, 1995). Conversely, there are several reasons why direct protein-protein interactions may not be observed by co-IP. Firstly, the conditions of lysis may disrupt the interaction, particularly if ionic detergents such as SDS are used. Modifying the lysis buffer to contain low concentrations of non-ionic detergents may alleviate this problem. Secondly, interactions may not be detected due to weak interactions, or the interaction may only be transient and therefore only a small portion of the total proteins are interacting, or the concentrations of the proteins themselves may be too low for detection (van der Geer, 2014).

While this last reason is unlikely to occur in an exogenous system, it may arise when investigating endogenous protein interactions. In such cases, it may be more advantageous to use a more sensitive method, such as protein affinity chromatography. This technique

involves covalently coupling one protein of interest to a column lined with a matrix, such as sepharose, and passing through protein lysates containing the first protein of interest. Proteins which do not interact with the immobilised protein will pass through the column or be easily washed away, whereas proteins which do interact with the immobilised protein will be retained. The proteins are then eluted from the column and analysed to detect the presence of the second protein of interest. The main advantage of this method is its sensitivity, as increasing the concentration of immobilised protein can result in the detection of interactions which are weak or between proteins of low concentration. However, this sensitivity can also be disadvantageous, as this increases the probability of detecting false-positives, so results require extensive validation (van der Geer, 2014).

An alternative method for investigating protein interactions is a variation of an enzyme-linked immunosorbent assay (ELISA), termed sandwich ELISA. Here, one of the proteins of interest is adsorbed onto a plate, either directly or indirectly via binding to an antibody which is already adsorbed onto the plate. Protein lysates are then added to the plates to allow these proteins to interact with the adsorbed protein and any non-specifically bound proteins are washed away. An antibody to the second protein of interest is then added, and a detection method applied to confirm an interaction between the two proteins. Major advantages of ELISAs are their sensitivity and suitability for incubation with complex lysates containing multiple proteins; however, they have similar disadvantages to the co-IP and affinity chromatography techniques above, whereby the physiological relevance of detected interactions cannot be confirmed (GenScript, 2018).

In summary, methods using isolated proteins are valuable for detecting interactions between two proteins. However, the main over-arching disadvantages are the potential to detect interactions which do not physiologically occur within the cell, and the lack of indication on

the implications of dimerisation for protein function. Fortunately, there is a wide variety of methods which investigate protein-protein interactions within the whole cell.

1.4.3.2 Methods using the whole cell

One method commonly employed to investigate protein dimerisation in the whole cell is proximity ligation assay (PLA, (Fredriksson et al., 2002)), which uses a specific kit, such as the Duolink® PLA Technology (Sigma-Aldrich, 2018a). Cells co-expressing the proteins of interest are fixed and permeabilised (Figure 1-14A) prior to incubation with a primary antibody to each protein of interest (Figure 1-14B). PLA probes are then added, which comprise a secondary antibody and an oligonucleotide (Figure 1-14C). In order for the PLA to work, the two primary antibodies must be raised in different species (e.g. mouse and rabbit), thus enabling the two proteins to be distinguished by using complementary PLA probes (e.g. PLUS and MINUS) conjugated to appropriate secondary antibodies (e.g. anti-mouse and anti-rabbit). These complementary PLA probes can then be ligated together, provided they are in close enough proximity. This ligated sequence is then amplified and fluorescently labelled in the next stage of the protocol (Figure 1-14D), which can then be visualised using confocal microscopy (Sigma-Aldrich, 2018a).

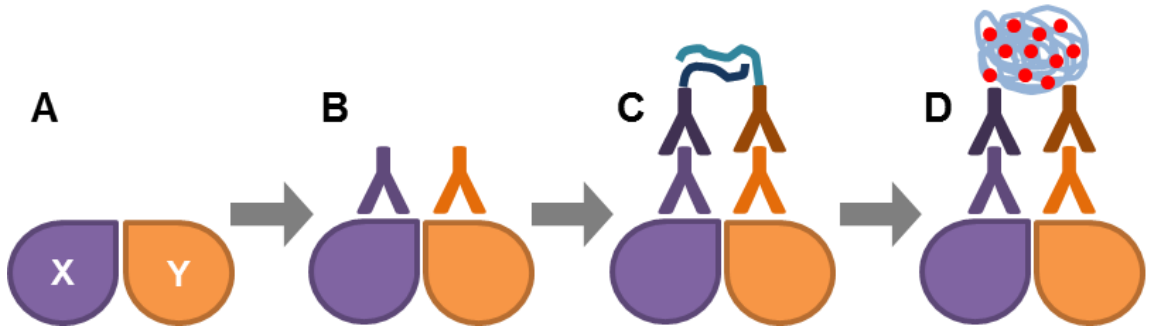

Figure 1-14 – Proximity ligation assay is a method for detecting protein-protein interactions within the whole cell. A) Proximity ligation assay (PLA) is used to detect whether two proteins (protein X in purple and protein Y in orange) are interacting within the cell. Fixed cells are incubated with primary antibodies to the two proteins (B), followed by incubation with secondary antibodies to the two primary antibodies (in darker purple and orange, respectively) which are conjugated to one of two complementary PLA probes (PLUS and MINUS), represented by the dark- and mid-blue lines, respectively (C). D) If the two proteins (X and Y) are in close enough proximity (<40nm) within the cell, the complementary probes can then be ligated together and amplified (shown in light blue) and fluorescently labelled (red dots), which enables visualisation of the interaction using a confocal microscope. Image adapted from Sigma-Aldrich, 2018a.

The main advantages of PLA are its sensitivity and specificity for protein interactions, and that these interactions can be observed within the whole cell, thus confirming both the physiological relevance and subcellular localisation of an interaction (Fredriksson et al., 2002, Weibrecht et al., 2010). However, this assay can only be carried out on fixed cells, meaning that the dynamics of interactions cannot be evaluated. Furthermore, it is possible that the PLA may pick up proteins which are not directly interacting, as PLA signal can still arise from epitopes which are 40nm apart (Sigma-Aldrich, 2018b). Accordingly, this may result in the detection of proteins within the same complex but not directly interacting (similar to the techniques described above), or of proteins within the same secretory vesicles during trafficking, as these vesicles vary greatly in size, from 30-50nm to 200-1200nm (Jena, 2008). Consequently, it could be more advantageous to utilise methods which have a much smaller detection limit in order to detect direct interactions between proteins.

The most commonly used way of achieving this is to utilise fluorescent proteins to demonstrate extremely close proximity between proteins in live cells based on Förster resonance energy transfer (FRET). This involves non-radiative energy transfer from one

excited donor fluorophore to a nearby acceptor fluorophore, thereby resulting in excitation of the acceptor. However, this energy transfer can only occur if the two fluorophores are less than 10nm apart, which is a similar spatial scale to protein-protein interactions (Stanley, 2003, Piston and Kremers, 2007). Utilising FRET to study such interactions it is not without its challenges; however, if these are accounted for by using appropriate controls, experimental approaches and data analysis, such experiments are reliable and informative.

First, the protein(s) of interest need to be labelled with a suitable fluorophore pair which is able to undergo FRET. One of the most commonly used FRET fluorophore pairs is cyan fluorescent protein (CFP) as the donor fluorophore and yellow fluorescent protein (YFP) as the acceptor fluorophore. These are both derivatives of green fluorescent protein (GFP) which have undergone mutation to alter the spectral characteristics of the fluorophore, resulting in a change in colour due to a shift in the emission wavelength (Figure 1-15; (Day and Davidson, 2009)). This is a suitable pairing because the emission wavelength of CFP overlaps with the excitation wavelength of YFP, which is required in order for FRET to occur. Accordingly, a suitable wavelength is used to excite CFP, resulting in subsequent CFP emission, which can then cause excitation of YFP (providing it is within close enough proximity to CFP), thereby generating YFP emission (Figure 1-16). However, this spectral overlap also results in significant spectral bleed-through, or crosstalk, whereby a portion of the excited CFP can be detected by the YFP emission filter (termed CFP crosstalk, Figure 1-17A), while some YFP can be directly excited by the wavelength used to excite CFP (termed YFP crosstalk, Figure 1-17B). This crosstalk contaminates the FRET signal and therefore must be corrected for during data analysis in order to accurately measure FRET (Stanley, 2003, Piston and Kremers, 2007, Day and Davidson, 2009).

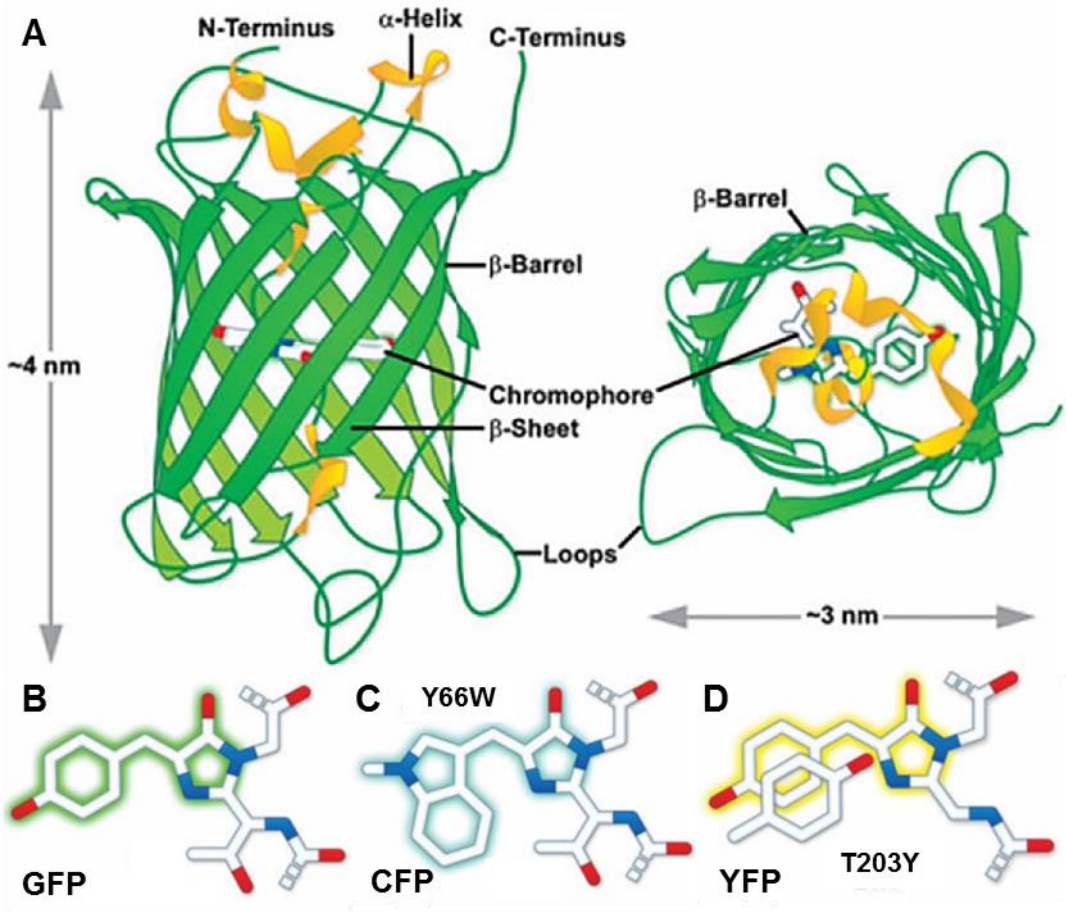

Figure 1-15 – Structures of fluorophores used in FRET. The crystal structure of green fluorescent protein (GFP) revealed that the chromophore is buried within a β-barrel structure (A). The structure of the GFP chromophore is shown in B. Mutations of certain residues in the GFP structure have given rise to fluorophores with an altered emission wavelength which fluoresce a different colour, such as cyan fluorescent protein (CFP, C) and yellow fluorescent protein (YFP, D). The parts of the structure which fluoresce are shaded in the appropriate colour, and key mutations are noted. Image adapted from Day and Davidson, 2009.

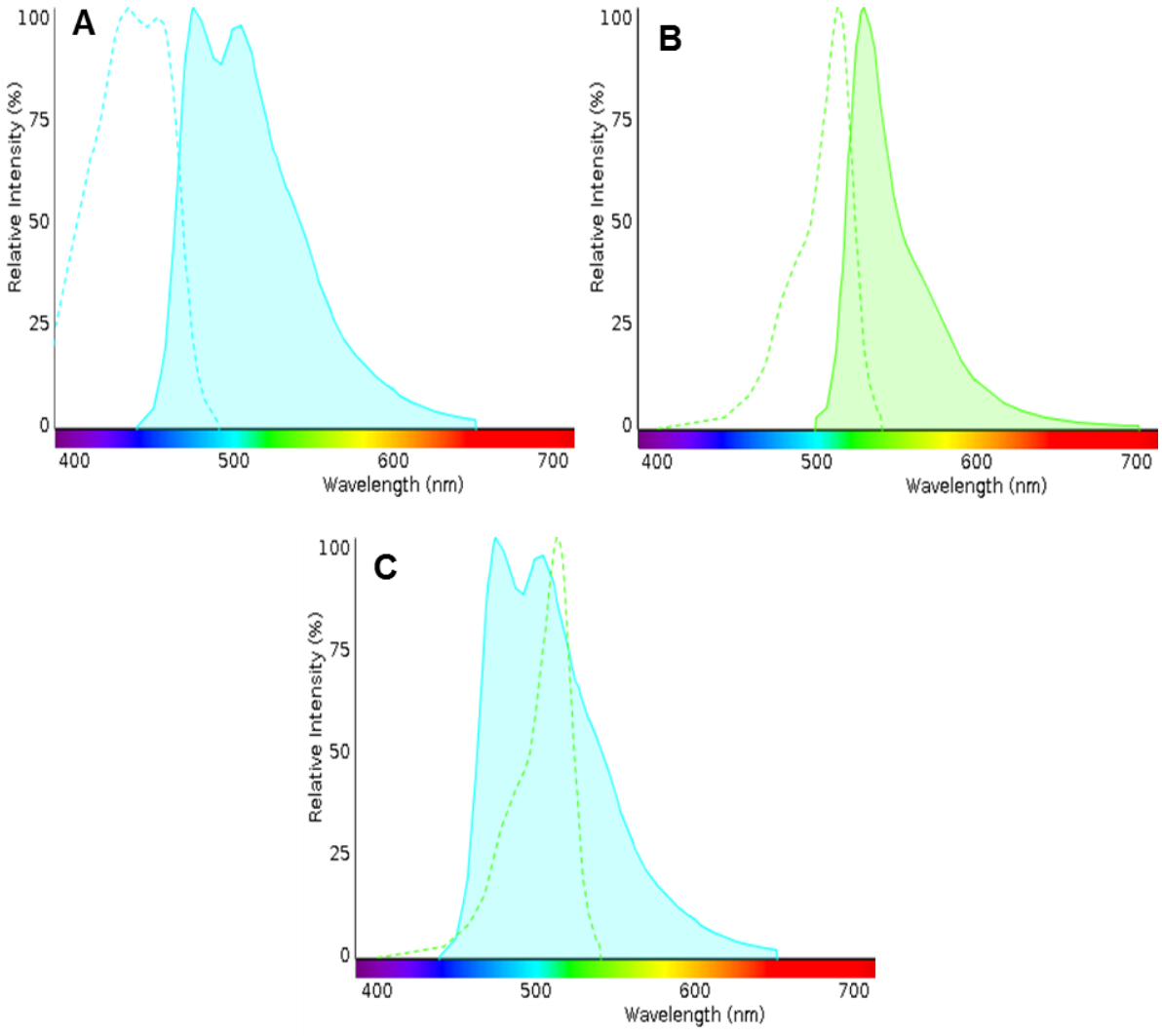

Figure 1-16 – Overlapping spectral characteristics of the two fluorophores enables FRET to occur. The excitation (dashed lines) and emission (solid lines) spectra of cyan fluorescent protein (CFP, blue) and yellow fluorescent protein (YFP, green) are shown individually in A and B, respectively. The CFP emission spectrum overlaps almost entirely with the excitation spectrum of YFP (C). This allows FRET to occur, as excitation of CFP can result in the excitation of nearby YFP, provided the two fluorophores are less than 10nm apart. Image adapted from Thermo Fischer Scientific, 2018.

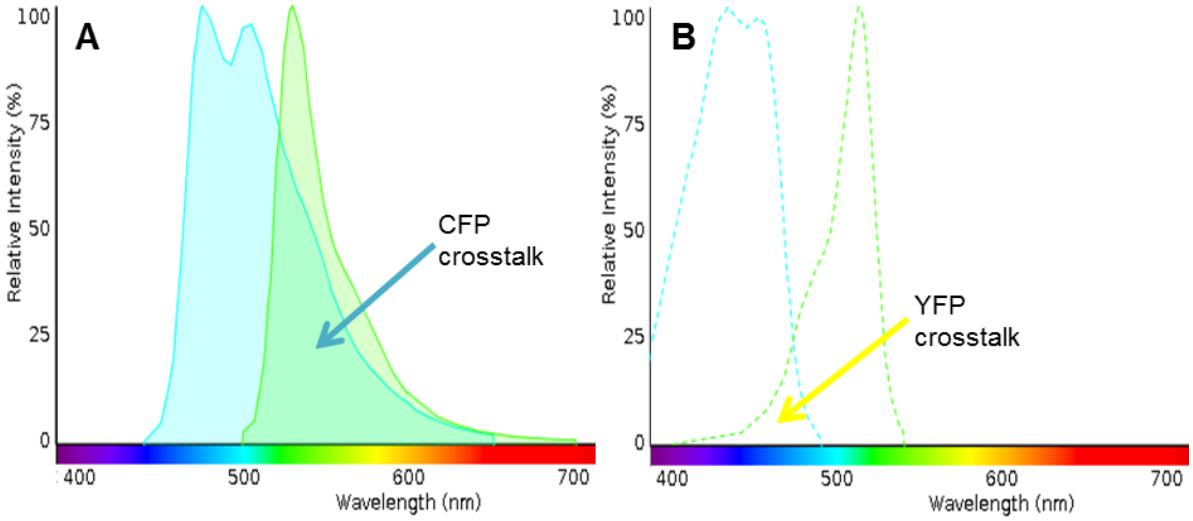

Figure 1-17 – Spectral overlap between fluorophores during FRET can also result in significant crosstalk which must be corrected for accurate analysis. The emission (solid lines) spectra of cyan fluorescent protein (CFP, blue) and yellow fluorescent protein (YFP, green) overlap substantially (A), therefore any emission filter which detects YFP emission will also detect a large amount of CFP emission, termed CFP crosstalk. Similarly, there is a small overlap between the excitation (dashed lines) spectra of CFP and YFP (B), therefore an excitation filter which excites CFP will also excite a small amount of YFP, termed YFP crosstalk. As this crosstalk interferes with the true FRET signal, it must be accounted for in order to obtain accurate FRET results. Image adapted from Thermo Fischer Scientific, 2018.

Second, as there is a myriad of methodologies which utilise FRET to study protein interactions, it is also important to select the most appropriate methodology for the investigations concerned. The method described here, whereby FRET is performed on cells co-transfected with two separate proteins each tagged with one fluorophore from the pair, is termed sensitised emission FRET (seFRET). Although this is the most technically simple method, extensive correction for the observed crosstalk is vital to obtain accurate results (Lamond, 2014, Piston and Kremers, 2007). An alternative methodology is acceptor photobleaching. This technique utilises the fact that when FRET occurs, some of the donor emission fluorescence is quenched as some of its energy is used to excite the acceptor. However, photobleaching the acceptor prevents this donor quenching occurring and therefore increases the donor emission fluorescence, which is indicative of protein interactions. Provided that the photobleaching reduces the acceptor emission down to at least 10% of its original values and that it does not affect the donor, this is a straightforward

technique which does not require such extensive data analysis. Consequently, it is often used after conducting other FRET methodologies as another control experiment. However, the major disadvantage of this technique is that it is single use only on a sample due to destruction of the acceptor. Furthermore, it takes time to photobleach the acceptor (at least 1 minute with laser excitation and longer with a lamp), so this can be quite a slow process (Piston and Kremers, 2007, Sun et al., 2011).

The concept of FRET causing donor quenching is also utilised by a separate methodology: fluorescence lifetime imaging microscopy (FLIM-FRET). This technique is based on the exponential decay of fluorescence of all fluorophores over a nanosecond timescale. In the presence of FRET, the rate of decay of the donor fluorophore is increased compared to when the donor fluorophore is expressed alone, thereby giving a robust indication of protein interaction. However, the major disadvantage of this technique is that the equipment required to carry out FLIM-FRET is very expensive due to the intricate nature of detecting changes in fluorescence in a nanosecond timescale, and consequently FLIM-FRET is not widely available (Piston and Kremers, 2007, Sun et al., 2011).

Other techniques can also be utilised which can obviate some of the disadvantages associated with FRET described above. One such technique is bioluminescence resonance energy transfer (BRET), which employs the same basic principle as FRET in which the non-radiative energy transfer from a donor to an acceptor is demonstrative of protein interaction, due to their close (<10nm) proximity. However, with BRET, the donor is not a fluorophore but a luciferase enzyme that emits photons directly upon addition of its substrate, which then go on to excite an acceptor fluorophore. Again, provided that the emission spectra for the luciferase and fluorophore overlap, any subsequent acceptor emission is indicative of protein interactions. As this does not require the use of fluorescent excitation, many of the problems

which occur with FRET due to the spectral overlap of the fluorophore pair are alleviated. However, there are limitations to the use of BRET. The most important one is that the fluorescence emitted during BRET is substantially weaker than that of FRET, meaning that most microscopes are not set up to be able to detect BRET emission (Xie et al., 2011).

Another alternative technique to FRET is bimolecular fluorescence complementation (BiFC), whereby two truncated halves of a fluorophore are conjugated separately to the protein(s) of interest. Fluorescence can only be observed if the two halves of the fluorophore are brought into close enough proximity to associate, thereby demonstrating a protein interaction. Consequently, the major advantage BiFC has over FRET is that the complications surrounding spectral overlap between the two required fluorophores is negated, as there is only one fluorophore involved which can only fluoresce if the proteins are in close enough proximity. However, BiFC can occur over larger distances compared to FRET, and so false-positive results may be generated whereby two proteins within the same complex but not directly binding may result in fluorescence. Consequently, a suitable negative control is required to confirm whether a direct interaction is occurring. An ideal negative control would be a protein containing a mutation at the binding interface which prevents the interaction from occurring (Miller et al., 2015); however, such a negative control is not possible if little is known about the interaction interface.

Methodologies which investigate protein dimerisation within the whole cell can provide information on the subcellular localisation of the interactions, which may shed light on the role of dimerisation for protein function, and can generally give a better indication of whether a direct interaction between two monomers is occurring. However, such techniques are often complex, requiring sophisticated microscope-based technologies and analysis. In

summary, investigations into protein dimerisation require both isolated protein and whole cell methodologies in order to validate any conclusions.

1.5 Hypothesis and aims

Although thyroid cancer incidence is increasing worldwide, the majority of patients have a good prognosis due to the extremely successful therapeutic administration of RAI, which harnesses the endogenous ability of the thyroid to accumulate I^- through expression of NIS at the plasma membrane. This has led to many investigations into NIS gene therapy, with the hope of using RAI to eventually treat other cancers with the same success as thyroid cancer.

Unfortunately, more advanced thyroid cancers become dedifferentiated and lose this functional expression of NIS, rendering the tumour RAI-refractory. This results in a significantly poorer prognosis for this subset of patients, as there is no successful alternative therapeutic option. Consequently, there is a great need to develop our understanding of how NIS is regulated in order to increase membranous NIS expression in such cases. One way in which protein function can be regulated is through dimerisation, and NIS has been previously suggested to form dimers. However, despite the potential clinical implications here, NIS dimerisation has neither been confirmed nor explored.

Given that dimerisation influences the function of a wide variety of proteins, we hypothesise that NIS dimerisation does occur and that it is important for NIS function. Therefore, the aims of this thesis were to firstly investigate conclusively whether NIS dimerisation occurs using multiple techniques, and secondly to generate novel mutants and examine their ability to dimerise in order to elucidate the residues involved and to establish the effect of dimerisation on NIS function.

CHAPTER 2 – MATERIALS AND METHODS

Unless otherwise stated, all reagents and kits described were obtained from Sigma-Aldrich (Poole, Dorset UK).

Additional materials and methods can be located within each chapter.

2.1 Cell Culture

2.1.1 Cell lines

SW1736 cells were kindly provided by Dr Rebecca Schweppe (University of Colarado). These cells are derived from a human anaplastic thyroid carcinoma of a female Caucasian, and are positive for the $BRAF^{V600E}$ mutation.

HeLa cells were obtained from the European Collection of Cell Cultures, UK. These cells, derived from a human epidermoid cervical carcinoma, were used because they are readily transfected and well-characterised.

2.1.2 Cell culture

All cell culture materials described in sections 2.1.2 and 2.1.3 were sourced from Gibco™ (Thermo Fisher Scientific, Waltham, MA, USA) unless otherwise stated.

SW1736 cells were cultured in Roswell Park Memorial Institute (RPMI) 1640 media supplemented with 10% (v/v) foetal bovine serum (FBS), penicillin (10^5U/L) and streptomycin (100mg/ml). HeLa cells were cultured in Dulbecco's Modified Eagle Medium (DMEM; Sigma-Aldrich) supplemented with 10% (v/v) FBS, 1% L-glutamine, penicillin (10^5U/L) and streptomycin (100mg/ml).

Both cell lines were cultured as a monolayer in 75cm^2 vented-cap flasks in at 37^{o}C and 5% CO_2 in humidified conditions and passaged twice weekly at 5-20%.

2.1.3 Cell seeding

Cells were washed with phosphate-buffered saline (PBS) prior to incubation with 0.125% trypsin-EDTA for 3 minutes at 37^{o}C. Trypsin was neutralised using appropriate complete media, with a portion of suspension transferred to a new flask to maintain the cell line.

Remaining cells were counted using a FastRead Counting Slide (Immune Systems Ltd, Paignton, Devon, UK), seeded as in Table 2-1 and cultured at 37^{o}C in 5% CO_2 for 24 hours prior to transfection.

	8-well chambered coverglass	24-well plates	6-well plates
Number of cells per well/flask	12,000	30,000	150,000
Volume of media per well/flask	400µl	0.5ml	2ml

Table 2-1 – Cell densities and volumes for seeding

2.2 Transfection

2.2.1 Vectors

Protein overexpression was achieved by transiently transfecting cells with mammalian expression vectors: pcDNA3.1(+) (Invitrogen^{TM}, Thermo Fisher Scientific) or C1 or N1 cloning vectors containing the full-length coding sequence for either Cerulean or Citrine (see section 9.4). The following plasmids were gifts from Michael Davidson & Dave Piston obtained from Addgene (Cambridge, MA, USA): Cerulean-C1 (#54604), Cerulean-N1 (#54742), Citrine-C1 (#54715) and Citrine-N1 (#54593). All plasmids contained full-length coding sequence for the gene of interest (see section 1.1), the human cytomegalovirus (CMV) immediate-early promoter and sites for antibiotic resistance (Figure 2-1).

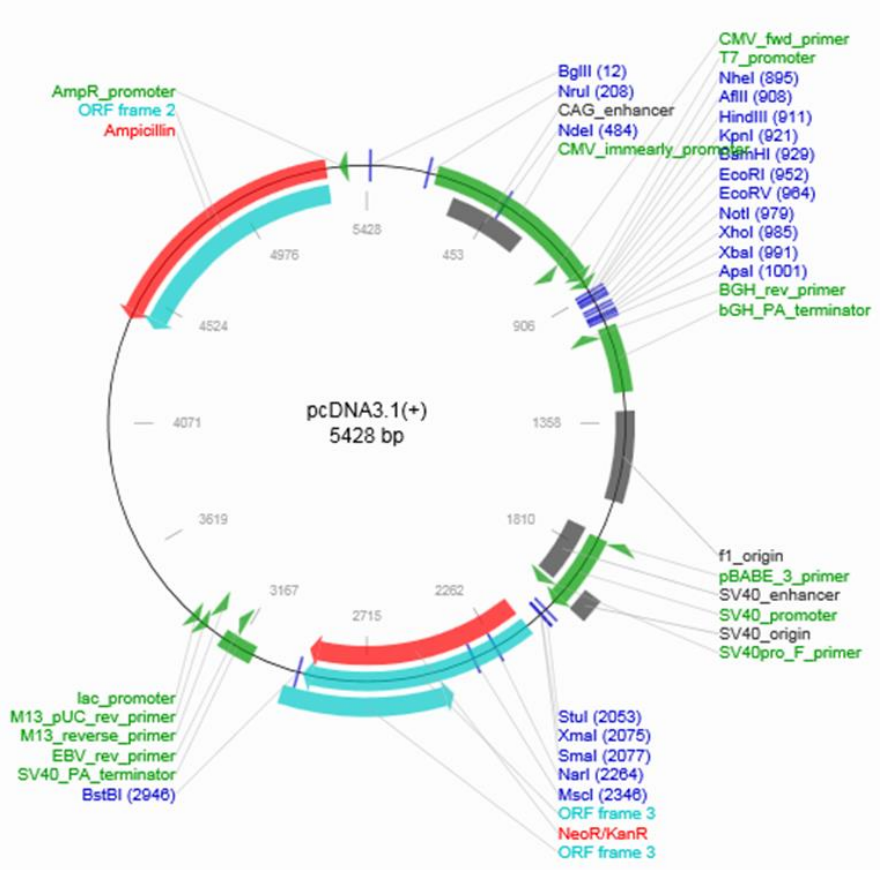

Figure 2-1 – Vector maps for pcDNA3.1(+) and the cloning vectors C1 and N1. All maps show the CMV promoter, bacterial resistance genes (ampicillin for pcDNA3.1(+); kanamycin for C1 and N1 cloning vectors) and the multiple cloning sites. The C1 and N1 vector maps (shown overleaf) depict the Cerulean coding region – as Citrine-C1 and -N1 vector backbones are identical to those for Cerulean, they are not shown. Images were taken from https://www.addgene.org/

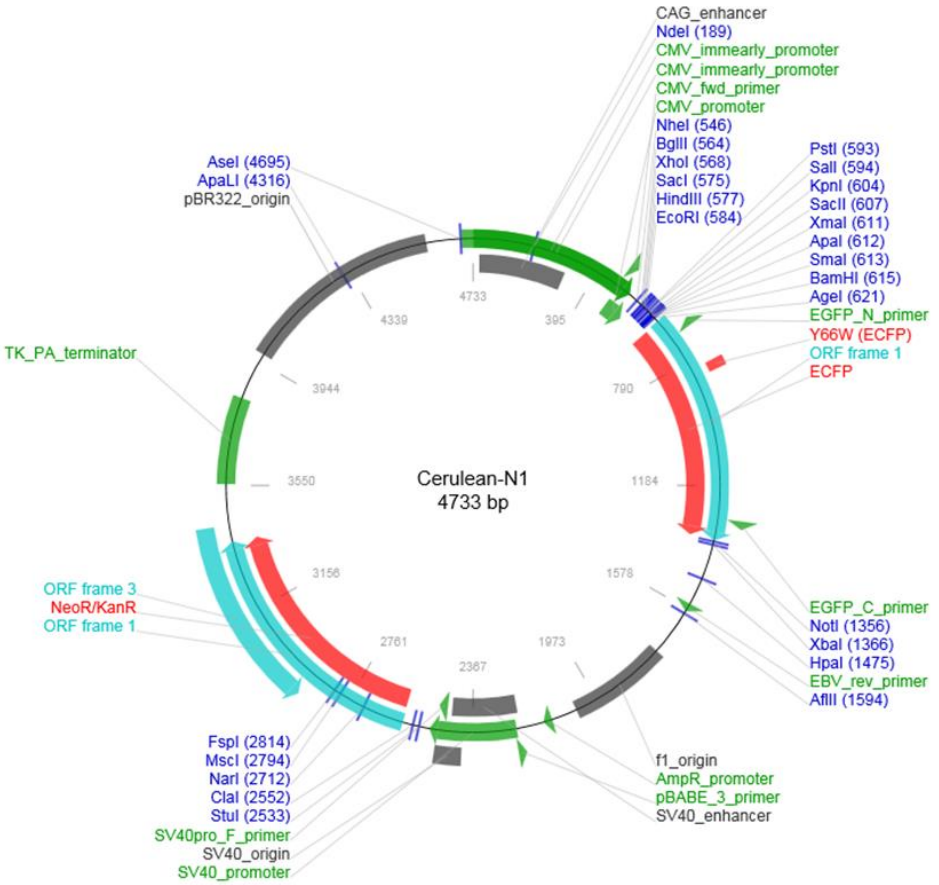
CAG_enhancer
NdeI (189)
CMV_immearly_promoter
CMV_immearly_promoter
CMV_fwd_primer
CMV_promoter
NheI (546)
BglII (564)
XhoI (568)
SacI (575)
HindIII (577)
EcoRI (584)
PstI (593)
SalI (594)
KpnI (604)
SacII (607)
XmaI (611)
ApaI (612)
SmaI (613)
BamHI (615)
AgeI (621)
EGFP_N_primer
Y66W (ECFP)
ORF frame 1
ECFP
AseI (4695)
ApaLI (4316)
pBR322_origin
TK_PA_terminator
Cerulean-N1
4733 bp
EGFP_C_primer
NotI (1356)
XbaI (1366)
HpaI (1475)
EBV_rev_primer
AflII (1594)
ORF frame 3
NeoR/KanR
ORF frame 1
FspI (2814)
MscI (2794)
NarI (2712)
ClaI (2552)
StuI (2533)
SV40pro_F_primer
SV40_origin
SV40_promoter
f1_origin
AmpR_promoter
pBABE_3_primer
SV40_enhancer

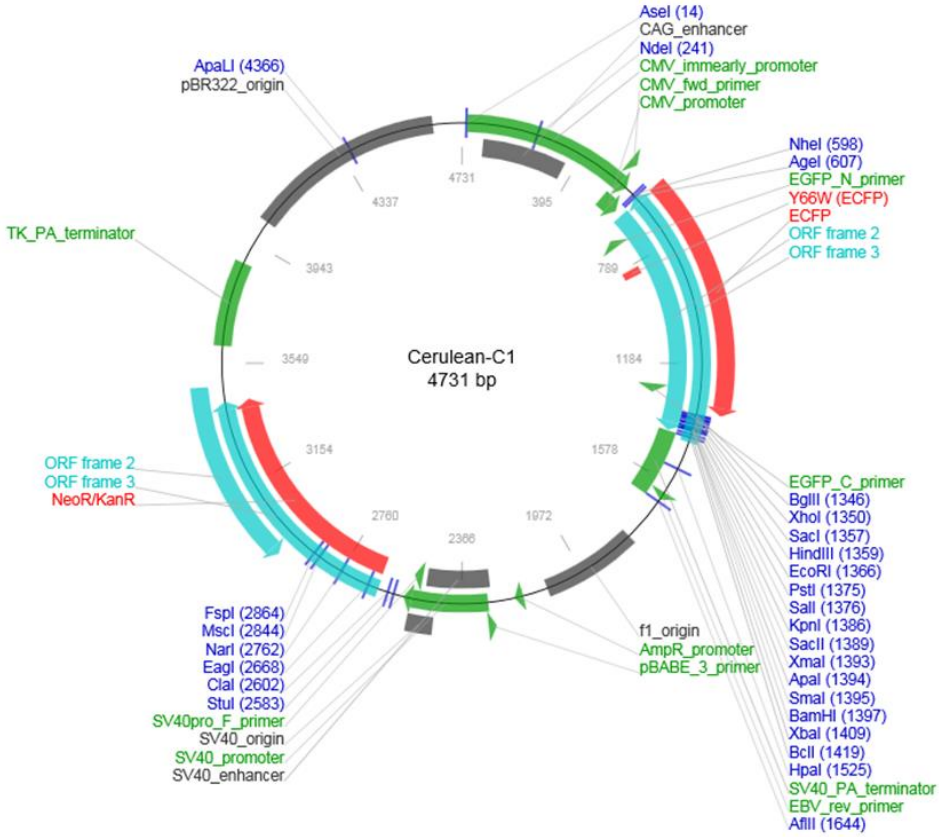
AseI (14)
CAG_enhancer
NdeI (241)
CMV_immearly_promoter
CMV_fwd_primer
CMV_promoter
NheI (598)
AgeI (607)
EGFP_N_primer
Y66W (ECFP)
ECFP
ORF frame 2
ORF frame 3
ApaLI (4366)
pBR322_origin
TK_PA_terminator
Cerulean-C1
4731 bp
EGFP_C_primer
BglII (1346)
XhoI (1350)
SacI (1357)
HindIII (1359)
EcoRI (1366)
PstI (1375)
SalI (1376)
KpnI (1386)
SacII (1389)
XmaI (1393)
ApaI (1394)
SmaI (1395)
BamHI (1397)
XbaI (1409)
BclI (1419)
HpaI (1525)
SV40_PA_terminator
EBV_rev_primer
AflII (1644)
ORF frame 2
ORF frame 3
NeoR/KanR
FspI (2864)
MscI (2844)
NarI (2762)
EagI (2668)
ClaI (2602)
StuI (2583)
SV40pro_F_primer
SV40_origin
SV40_promoter
SV40_enhancer
f1_origin
AmpR_promoter
pBABE_3_primer

2.2.1.1 PCR cloning

PCR cloning was used to create plasmids containing human NIS conjugated to the fluorophores Cerulean or Citrine at the N- or C-terminus for subsequent analysis using FRET (described in section 2.7). Forward and reverse primers were designed and produced (Alta Bioscience, Birmingham, UK) to clone wild-type (WT) NIS from the pcDNA3.1(+)_NIS-HA plasmid (kindly provided by Dr Vicki Smith, University of Birmingham) using Q5® High Fidelity DNA Polymerase (New England Biolabs, Ipswich, MA, USA) as per manufacturer's instructions. On ice, plasmid DNA (1µl) was combined with 30µM forward and reverse primers (Table 2-2), 4µl 10mM dNTP mix (Bioline, London, UK), 10µl 5x Q5 buffer, 0.5µl Q5 polymerase, 10µl 5x Q5 enhancer and made up to a total of 50µl with nuclease-free water (Gibco™). Following an initial denaturation step at 98°C for 30 seconds, 30 PCR cycles were performed (denaturation at 98°C for 10 seconds, primer annealing at 60°C for 30 seconds, and primer extension at 72°C for 90 seconds) before a final primer extension step at 72°C for 2 minutes.

Construct	Primer Sequence
NIS-Cerulean / NIS-Citrine	**F: 5' – GCGAAGCTTCCACCATGGAGGCCGTGG – 3'** **R: 5' – GGCGGATCCAGGTTTGTCTCCTGCTGGTC – 3'**
Cerulean-NIS / Citrine-NIS	**F: 5' – CTCAAGCTTTAGAGGCCGTGGAGACCGGG – 3'** **R: 5' – GTTGGATCCTCAAAGGTTTGTCTCCTGCTGGTC – 3'**

Table 2-2 – Sequences of forward (F) and reverse (R) primers used for PCR cloning. Underlined sequences indicate restriction enzyme sites (HindIII for forward primers; BamHI for reverse) and italicised sequences indicate stop codons

PCR product was combined with 6x Blue/Orange DNA loading buffer (Promega, Madison, WI, USA), loaded onto a 2% agarose gel (2% agarose (Bioline) w/v in 1x Bionic buffer + 1:10,000 SYBRSafe Gel Stain (Invitrogen™)) and ran at 100V for 1.5 hours. Bands (~2kbp) were excised from the gel and DNA extracted using QIAquick® Gel Extraction Kit (Qiagen, Manchester, UK) as per manufacturer's instructions. Excised bands were incubated with 3

gel volumes Buffer QG at 50°C for 10 minutes to dissolve the gel before adding 1 gel volume isopropanol. Samples were transferred to spin columns and centrifuged at 13,000rpm for 1 minute, discarding flow-through. Once loaded, columns were washed with 750µl Buffer PE, and a further centrifugation was performed to remove residual wash buffer. Columns were placed in fresh 1.5ml microcentrifuge tubes, loaded with 30µl nuclease-free water and centrifuged at 13,000rpm for 1 minute to elute DNA. PCR product DNA concentration was assessed using the NanoDrop™ ND-1000 Spectrophotometer (NanoDrop, Wilmington, DE, USA) and ND-1000 v3.3 software on the DNA-50 setting.

Restriction digests were then performed on PCR products and recipient plasmids (C1 or N1 cloning vectors, Figure 2-1) using BamHI and HindIII restriction enzymes (both Promega). PCR product (14µl) or recipient plasmid (1µg) was mixed with 1µl of each enzyme, 2µl Restriction Enzyme Buffer E (Promega) and made up to a total of 20µl with nuclease-free water before incubating at 37°C overnight.

Digested plasmid DNA was purified using gel extraction as described above, while digested PCR product was purified using QIAquick® PCR purification kit (Qiagen) as per manufacturer's instructions. Five volumes Buffer PB was added to digested PCR product, then transferred to spin columns and centrifuged at 13,000rpm for 1 minute, discarding flow-through. Once loaded, columns were washed with 750µl Buffer PE, and a further centrifugation was performed to remove residual wash buffer. Columns were placed in fresh 1.5ml microcentrifuge tubes, loaded with 30µl nuclease-free water and centrifuged at 13,000rpm for 1 minute to elute DNA. Digested plasmid and PCR product DNA concentration was assessed using the NanoDrop ND-1000 Spectrophotometer.

Digested PCR product and plasmid were ligated together using T4 ligase (New England Biolabs) as per manufacturer's instructions. To create constructs conjugating the fluorophore (Cerulean or Citrine) to NIS at the C-terminus, N1 plasmids were used, whereas C1 plasmids were used to conjugate the fluorophore to NIS at the N-terminus (Figure 2-1). Digested PCR product (14µl) and digested recipient plasmid (3µl) were combined with 1µl T4 ligase and 2µl ligase buffer (New England Biolabs) and incubated at room temperature for 3 hours.

2.2.1.1.1 Bacterial transformation

Subcloning Efficiency™ DH5α™ chemically competent E. coli cells (Invitrogen™) were transformed according to the manufacturer's instructions. Ligated plasmid (5µl) was added to 50µl DH5α cells and incubated on ice for 30 minutes. Cells were then heat-shocked at 42°C for 30 seconds to increase membrane permeability before incubating on ice for a further 2 minutes. Cells were incubated in 950µl Lysogeny broth (LB, 0.02% w/v in ultra-pure water) at 37°C for 1 hour at 225-250rpm prior to pelleting by centrifugation at 13,000rpm for 3 minutes. The supernatant was decanted and cells were resuspended in remaining ~50µl LB, plated onto pre-warmed LB-agar plates (3g agar + 4g LB in 200ml ultra-pure water) containing 50µg/ml kanamycin and incubated at 37°C overnight.

2.2.1.1.2 Site-directed mutagenesis

In order to investigate the importance of specific residues for NIS function and dimerisation, the WT NIS sequence in pcDNA3.1(+)_NIS-MYC and pcDNA3.1(+)_NIS-HA plasmids (kindly provided by Dr Vicki Smith, University of Birmingham) was mutated using the QuikChange II XL Site-Directed Mutagenesis kit (Agilent Technologies, Santa Clara, CA, USA). Forward and reverse primers were designed and produced (Sigma-Aldrich or Alta Bioscience) to introduce a series of point mutations to NIS (Table 2-3, section 1.1). Plasmid

DNA (10ng) was combined on ice with 125ng forward and reverse primers, 5µl 10x reaction buffer, 1µl dNTP mix, 3µl QuikSolution, 1µl PfuUltra High Fidelity DNA polymerase and made up to a total of 50µl with nuclease-free water. Following an initial denaturation step at 95°C for 1 minute, 18 PCR cycles were performed (denaturation at 95°C for 50 seconds, primer annealing at 60°C for 50 seconds, and primer extension at 68°C for 7.5 minutes) before a final primer extension step at 68°C for 7 minutes. After thermocycling, reactions were cooled to ≤37°C prior to the addition of 1µl DpnI restriction enzyme and incubation at 37°C for 1 hour to digest the parental DNA.

Mutant	Primer Sequence
GZM	**F: 5' – GCCTGCAACACACCG<u>GTC</u>GTCCTCGCG<u>GTA</u>CTAGGCGCGGGCTTG – 3'** **R: 5' – CAAGCCCGCGCCTAG<u>TAC</u>CGCGAGGAC<u>GAC</u>CGGTGTGTTGCAGGC – 3'**
LZM1	**F: 5' – CGTGGTGATG<u>GCA</u>AGTGGCTTCTGGGTTGTC<u>GCG</u>GCACGCGGTG – 3'** **R: 5' – CACCGCGTGC<u>CGC</u>GACAACCCAGAAGCCACT<u>TGC</u>CATCACCACG – 3**
LZM2	**F: 5' – CGGTGTCATG<u>GCT</u>GTGGGCGGGCCCCGCCAGGTG<u>GCC</u>ACGCTGGCCC – 3'** **R: 5' – GGGCCAGCGT<u>GGC</u>CAGCTGGCGGGGCCCGCCCAC<u>AGC</u>CATGACACCG – 3'**
D237A	**F: 5' – GACTTTAACCCTG<u>C</u>CCCGAGGAGCCGC – 3'** **R: 5' – GCGGCTCCTCGGG<u>G</u>CAGGGTTAAAGTC – 3'**
Y242A	**F: 5' – CCCGAGGAGCCGC<u>GC</u>TACATTCTGGACTTTTG – 3'** **R: 5' – CAAAAGTCCAGAATGTA<u>GC</u>GCGGCTCCTCGGG – 3'**
T243A	**F: 5' – CCGAGGAGCCGCTAT<u>G</u>CATTCTGGACTTTTG – 3'** **R: 5' – CAAAAGTCCAGAATG<u>C</u>ATAGCGGCTCCTCGG – 3'**
Q471A	**F: 5' – CCACCCAGCGAG<u>GC</u>GACCATGAGGGTCC – 3'** **R: 5' – GGACCCTCATGGTC<u>GC</u>CTCGCTGGGTGG – 3'**
A525F	**F: 5' – CCCGCCTTAGCTGACAGCTTCTAT<u>TT</u>CATCTCCTATCTC – 3'** **R: 5' – GAGATAGGAGATG<u>AA</u>ATAGAAGCTGTCAGCTAAGGCGGG – 3'**

Table 2-3 – Sequence of forward (F) and reverse (R) primers used for site-directed mutagenesis. Underlined sequences indicate mutated codons.

2.2.1.1.3 Bacterial transformation

XL10-Gold® ultracompetent cells (Agilent Technologies) were transformed according to the manufacturer's instructions. In pre-chilled round-bottom tubes, 45µl XL10-Gold cells were incubated with 2µl β-mercaptoethanol mix (Agilent Technologies) for 10 minutes on ice, swirling every 2 minutes, to increase transformation efficiency. Then, 2µl mutagenesis reaction mixture was added to the cells and incubated on ice for 30 minutes. Cells were then

heat-shocked at 42^{o}C for 30 seconds and returned to ice for 2 minutes. Cells were incubated with 0.5ml pre-warmed Super Optimal broth with Catabolite repression (S.O.C medium, Invitrogen^{TM}) at 37^{o}C for 1 hour at 225-250rpm before plating 250µl cells onto pre-warmed LB-agar plates containing 100µg/ml ampicillin and incubating at 37^{o}C overnight.

2.2.1.2 DNA purification

Four single colonies per construct/mutant were selected and streaked onto a fresh pre-warmed LB-agar plate containing appropriate antibiotic (see sections 2.2.1.1.1 and 2.2.1.1.3) and incubated at 37^{o}C overnight. A small amount of one reference-streaked colony per construct/mutant was cultured in 3ml LB broth containing appropriate antibiotic at 37^{o}C overnight at 225-250rpm. Reference-streaked LB-agar plates were wrapped and stored at 4^{o}C for future use (see section 2.2.1.3).

The Centrifugation Protocol of the Wizard® Plus SV Minipreps DNA Purification System (Promega) was used to isolate and purify the plasmids. The bacterial culture (3ml) was centrifuged at 13,000rpm for 5 minutes and the supernatant discarded. Bacterial pellets were resuspended in 250µl cell resuspension solution, before mixing with 250µl cell lysis solution and incubated for 5 minutes to partially clear the suspension. To inactivate endonucleases and other proteins released during lysis, solutions were incubated with 10µl alkaline protease for 5 minutes, before adding 350µl neutralisation solution to terminate lysis and centrifuging at 13,000rpm for 10 minutes. Cleared lysates were decanted into spin columns, centrifuged at 13,000rpm for 1 minute and flow-through discarded. Once loaded, columns were washed twice with column wash solution (750µl wash 1; 250µl wash 2), and centrifuged at 13,000rpm for 2 minutes to remove residual wash buffer. Columns were placed in fresh 1.5ml microcentrifuge tubes, loaded with 50µl nuclease-free water and centrifuged at

13,000rpm for 1 minute to elute DNA. Plasmid DNA concentration was assessed using the NanoDrop ND-1000 Spectrophotometer.

2.2.1.2.1 Sequencing

For sequencing, 500ng plasmid DNA was combined with 3.2pmol sequencing primer and made up to a total of 10µl with nuclease-free water. T7 forward and BGH reverse primers were used for sequencing pcDNA3.1(+) plasmids, CMV forward and EGFP_N reverse primers for N1 plasmids, EGFP_C forward and EBV reverse primers for C1 plasmids, and NIS forward and reverse primers for the middle portion of NIS (Table 2-4). Plasmid to profile sequencing was performed by Source Bioscience (Nottingham, UK) or the Functional Genomics Unit at the University of Birmingham.

Sequencing Primer	Primer Sequence
T7 (F)	**5' – TAATACGACTCACTATAGGG – 3'**
BGH (R)	**5' – TCCATGTATGGCGTGAACC – 3'**
CMV (F)	**5' – CGCAAATGGGCGGTAGGCGTG – 3'**
EGFP_N (R)	**5' – CGTCGCCGTCCAGCTCGACCAG – 3'**
EGFP_C (F)	**5' – CATGGTCCTGCTGGAGTTCGTG – 3'**
EBV (R)	**5' – GATGAGTTTGGACAAACCAC – 3'**
NIS_F	**5' – TCCATGTATGGCGTGAACC – 3'**
NIS_R	**5' – CATTGATGCTGGTGGATGC – 3'**

Table 2-4 – Sequences of forward (F) and reverse (R) primers used for sequencing

Sequencing data were viewed using Chromas Lite v2.01 software (Technelysium Pty Ltd, Brisbane, Australia) and analysed using National Centre for Biotechnology Information (NCBI) Basic Local Alignment Search Tool ((BLAST), Bethesda, MD, USA): Standard Nucleotide BLAST and Translated BLAST (blastx): (https://blast.ncbi.nlm.nih.gov/Blast.cgi?PROGRAM=blastn&PAGE_TYPE=BlastSearch&LINK_LOC=blasthome);

https://blast.ncbi.nlm.nih.gov/Blast.cgi?PROGRAM=blastx&PAGE_TYPE=BlastSearch&LINK_LOC=blasthome).

2.2.1.3 DNA amplification

Amplification of plasmid DNA with the correct sequence was performed using the GenElute™ High Performance (HP) Plasmid Maxiprep kit. Appropriate reference-streaked colony (see section 2.2.1.2) was cultured in 5ml LB broth containing appropriate antibiotic at 37°C for 8 hours at 225-250rpm before being transferred to 150ml LB broth containing appropriate antibiotic (see sections 2.2.1.1.1 and 2.2.1.1.2) and incubated at 37°C overnight at 225-250rpm.

After incubation, 1.53ml bacterial suspension was mixed with 270µl glycerol to create a glycerol stock, which was stored at -80°C, and used to re-amplify plasmid DNA if necessary.

Remaining suspension was centrifuged at 5,000rpm for 10 minutes, supernatant discarded and bacterial pellet resuspended in 12ml resuspension solution. Following addition of 12ml lysis solution, mixtures were inverted 8 times and incubated for 5 minutes to lyse bacterial cells. To terminate lysis, 12ml neutralisation solution was added and inverted 6 times before adding 9ml binding solution. Mixtures were inverted twice, immediately transferred to the barrel of a filter syringe and incubated for 5 minutes. During this incubation, binding columns were prepared by adding 12ml column preparation solution, centrifuging at 3,000rpm for 2 minutes and discarding the flow-through. Cleared bacterial lysate was filtered through the syringe into the binding column and centrifuged at 3,000rpm for 2 minutes. Columns were washed with 12ml column wash solution 1 and centrifuged at 3,000rpm for 2 minutes, and then with 12ml column wash solution 2 and centrifuged at 3,000rpm for 5 minutes to ensure removal of residual wash buffer. Columns were transferred

to fresh collection tubes, loaded with 3ml nuclease-free water and centrifuged at 3,000rpm for 5 minutes to elute DNA. Plasmid DNA concentration was assessed using the NanoDrop ND-1000 Spectrophotometer.

2.2.2 Transfection of bacterial plasmids

Cells were transiently transfected 24 hours post-seeding using TransIT®-LT-1 transfection reagent (Geneflow, Lichfield, UK) at a 3:1 ratio with plasmid DNA as in Table 2-5. Plasmid DNA was diluted in Opti-MEM™ reduced-serum media (Gibco™) and incubated for 5 minutes. After addition of transfection reagent, transfection mixtures were incubated for 30 minutes before adding to cell cultures. Transfected cells were cultured at 37°C in 5% CO_2 for 48 hours prior to further experimentation.

	8-well chambered coverglass	24-well plates	6-well plates
Total DNA per well/flask	0.25µg	0.5µg	2µg
Volume of LT-1 per well/flask	0.75µl	1.5µl	6µl
Total volume of transfection mix per well/flask	25µl	50µl	200µl

Table 2-5 – Conditions for transfection of bacterial plasmids

2.3 Western blot

2.3.1 Protein extraction and quantification

2.3.1.1 Cell lysis

Cells were seeded in 6-well plates (Table 2-1) and 48 hours post-transfection with NIS variants (Table 2-5), media were aspirated and cells washed with PBS. Cells were lysed in 150µl radioimmunoprecipitation assay (RIPA) lysis buffer (150mM sodium chloride, 50mM Tris pH7.4, 6mM sodium deoxycholate, 1% v/v Igepal CA-630 and 1mM ethylenediaminetetraacetic acid (EDTA)) containing 60µl/ml protease inhibitor cocktail, which inhibits aminopeptidases and serine, cysteine and aspartic proteases. To aid lysis, a

single freeze-thaw cycle was performed at -20^{o}C overnight before cells were scraped and lysates transferred to clean microcentrifuge tubes after a centrifugation step at 13,200rpm for 20 minutes at 4^{o}C to pellet cell debris.

2.3.1.2 Determining protein concentration

Protein concentration was determined by Pierce^{TM} bicinchoninic acid (BCA) colorimetric assay (Thermo Fisher Scientific). Bovine serum albumin (BSA; Stratech Scientific Ltd, Newmarket, UK) protein standards in RIPA buffer were prepared at concentrations ranging between 0-5mg/ml. Protein standards and cell lysates were measured in duplicate by combining 4µl standard or lysate with 80µl BCA reagent mix (78.4µl Reagent A and 1.6µl Reagent B) in a 96-well plate. After a 30 minute incubation at 37^{o}C, absorbance was measured at 560nm using a Victor^{3} 1420 Multilabel Counter (Perkin Elmer, Waltham, MA, USA). A standard curve was generated from the BSA protein standards, which was then used to determine protein concentration of lysates.

2.3.2 Western blotting

To examine protein expression, Western blotting was performed. First, protein lysates (20µg) were combined with 20% v/v 5x protein loading buffer (250mM Tris pH6.8, 10% w/v sodium dodecyl sulphate (SDS), 0.02% v/v bromophenol blue, 50% v/v glycerol and 12.5% v/v β-mercaptoethanol) and denatured at 37^{o}C for 30 minutes. Resolving gels (375mM Tris pH8.8, 12% v/v acrylamide (from 30% (w/v) acrylamide:0.8% (w/v) bis-acrylamide stock; Geneflow), 3.5mM SDS, 0.1% (v/v) tetramethylethylenediamine (TEMED) and 4.4mM ammonium persulphate (APS)) were prepared and denatured protein lysates were loaded onto the gel alongside 4µl protein ladder (BLUeye pre-stained protein ladder (10-245kDa) molecular weight marker; Geneflow). Proteins were then separated by

SDS-polyacrylamide gel electrophoresis (SDS-PAGE) in running buffer (24.8mM Tris, 192mM glycine and 3.5mM SDS) at 70 volts for 15-30 minutes before increasing to 140 volts.

Separated proteins were then transferred onto activated polyvinylidene difluoride (PVDF) membranes (Thermo Fisher Scientific) in transfer buffer (25mM Tris, 192mM glycine and 20% v/v methanol) at 360mA for 1 hour 20 minutes. Membranes were blocked with 5% w/v non-fat milk (Marvel dried milk powder; Premier Foods Group Ltd, London, UK) in Tris-buffered saline containing Tween (TBST; 20mM Tris pH7.6, 137mM sodium chloride and 0.025% v/v Tween-80®) for 2 hours at room temperature with rocking. Membranes were then incubated in 5ml 5% non-fat milk in TBST containing primary antibody (see section 2.8) overnight at 4°C with rocking. Three washes with TBST were performed to remove excess primary antibody before membranes were incubated in 5ml 5% non-fat milk in TBST containing the appropriate secondary antibody (see section 2.8) for 1 hour at room temperature with rocking. Three further washes with TBST were performed to remove excess secondary antibody, then membranes were incubated with Pierce™ ECL chemiluminescent substrate (Thermo Fisher Scientific) as per manufacturer's instructions in order to visualise antigen-antibody complexes on Kodak X-ray film for 30-60 minutes.

As a control for protein loading, membranes were stripped before probing for β-actin. Membranes were washed with TBST before incubation in Restore™ PLUS Western Blot Stripping Buffer (Thermo Fisher Scientific) for 5 minutes at room temperature. Membranes were washed three times with TBST before blocking with 10ml 5% milk in TBST for 1 hour. Membranes were incubated with 5ml 5% milk in TBS-T containing anti-β-actin primary antibody (see section 2.8) at room temperature for 30 minutes, and washed three times with TBST before incubation with 5ml 5% milk in TBST containing appropriate

secondary antibody at room temperature for 1 hour. Membranes were washed as above before developing with SuperSignal West Pico Chemiluminescent Substrate (Thermo Fisher Scientific) as per manufacturer's instructions and X-ray film.

2.4 Immunofluorescence

Cells were seeded on top of glass coverslips in 6-well plates (Table 2-1) and 48 hours post-transfection with NIS variants (Table 2-5), immunofluorescence was performed to determine protein subcellular localisation. First, media were aspirated and cells washed with PBS. Cells were then fixed in 800µl fixing solution (0.1M phosphate buffer pH7.4 containing 2% paraformaldehyde, 2% glucose and 0.2% sodium azide), washed twice, then permeabilised with 800µl chilled methanol for 10 minutes, and washed twice again. Coverslips were blocked in 800µl 10% newborn calf serum (NCS; Life Technologies^{TM}, Thermo Fisher Scientific) in PBS for 30 minutes, before incubation with 80µl 1% bovine serum albumin (BSA) in PBS containing primary antibodies (see section 2.8) for 1 hour in the dark. Coverslips were washed three times before incubation with 80µl 1% BSA + 1% NCS in PBS containing secondary antibodies (see section 2.8) and Hoescht 33342 stain (Invitrogen^{TM}) at 1:1000 for 1 hour in the dark. Coverslips were washed three times before mounting onto microscope slides using Fluorescent Mounting Medium (Dako^{TM}, Agilent Technologies) and left to dry. Slides were stored at 4^{o}C in the dark before viewing on Leica DM6000 fluorescence microscope (Leica Microsystems, Wetzlar, Germany) using a 40x objective.

2.5 Radioiodide uptake assay

Cells were seeded in 24-well plates (Table 2-1) using six wells per transfection condition and 48 hours post-transfection with NIS variants (Table 2-5), radioiodide uptake assays were performed to assess protein function. First, cells from two wells per condition were

incubated with 100µM sodium perchlorate for 1 hour at 37°C to block NIS function as controls. Cells in all wells were then incubated with 1µM sodium iodide containing 0.05µCi ^{125}I (Hartmann Analytic, Brunswick, Germany) for 1 hour at 37°C. Media were aspirated and cells washed twice with Hanks' Balanced Salt solution (HBSS) to remove excess radioiodide before cells were lysed in 200µl 2% SDS. Radioactivity of lysates was counted for 1 minute using a gamma counter (1260 MultiGammaII, Wallac). Protein concentration of lysates was determined with a BCA assay as described in 2.3.1.2 using BSA protein standards prepared in 2% SDS. Counts were normalised to protein concentration and data was expressed as pmol I^-/µg protein.

2.6 Proximity ligation assay

Cells were seeded on coverslips in 6-well plates (Table 2-1) and co-transfected with NIS variants conjugated to either MYC or HA (Table 2-5). After 48 hours, proximity ligation assay (PLA) was performed using the Duolink In Situ Fluorescence Protocol with Detection Reagents Red Kit as per manufacturer's instructions in order to investigate the proximity between differentially-tagged variants of NIS. Briefly, cells were fixed, permeabilised, and blocked as for immunofluorescence (see section 2.4). Coverslips were then incubated in 80µl 1% BSA in PBS containing primary antibodies (see section 2.8) for 1 hour at room temperature in a humidity chamber. Following two 5 minute washes with PBS, coverslips were incubated in 80µl 1% BSA + 1% NCS in PBS containing mouse-MINUS and rabbit-PLUS PLA probes (20% each, v/v) for 1 hour at 37°C in a humidity chamber. Two 5 minute washes in wash buffer A were performed before incubating coverslips in 80µl 20% v/v ligation stock and 2.5% v/v ligase in ultra-pure water for 30 minutes at 37°C in a humidity chamber. Two 2 minute washes in wash buffer A were performed before coverslips were incubated in 80µl 20% amplification stock v/v and 1.25% v/v polymerase in ultra-pure water

for 100 minutes at 37^{o}C in a humidity chamber. Two 10 minute washes in wash buffer B and a 1 minute wash in 0.01x wash buffer B were performed before mounting coverslips using Duolink In Situ Mounting Medium with DAPI. Slides were stored at -20^{o}C in the dark before viewing on Zeiss LSM 510 Meta confocal microscope (Carl Zeiss AG, Oberkochen, Germany) using a 40x objective.

2.7 Förster resonance energy transfer

Cells were seeded in 8-well chambered coverglass (Lab-Tek Nunc, Thermo Fisher Scientific) (Table 2-1) and co-transfected with NIS variants conjugated to either Cerulean or Citrine (Table 2-5). Förster resonance energy transfer (FRET) imaging was performed 48 hours post-transfection using Crest X-Light spinning disk head coupled to a Nikon Ti-E automated base and 60 x/1.40 NA objective to further investigate the proximity between differentially-tagged NIS variants.

Cells were washed and media replaced with HEPES-bicarbonate buffer (120mM sodium chloride, 4.8mM potassium chloride, 24mM sodium bicarbonate saturated with CO_2, 0.5mM sodium hydrogen phosphate, 5mM 4-(2-hydroxyethyl)-1-piperazineethanesulfonic acid (HEPES), 2.5mM calcium chloride, 1.2mM magnesium chloride). Live cell confocal microscopy was then performed and three concurrent versions of each image were captured: total Cerulean (CFP) image (Cerulean excitation/Cerulean emission (CFP/CFP)), total Citrine (YFP) image (Citrine excitation/Citrine emission (YFP/YFP)) and FRET image (Cerulean excitation/Citrine emission (CFP/YFP)). Excitation was delivered at λ=430-450nm for Cerulean and λ=500-520nm for Citrine using a Lumencor Spectra X Light Engine, and emitted signals detected at λ=460-500nm for Cerulean and λ=535-565nm for Citrine using a Photometrics Evolve Delta 512 EMCCD.

Data analysis was performed using MetaMorph® Version 7.8.13.0 software (Molecular Devices, Wokingham, UK). Background subtraction was performed on images prior to further analysis. Firstly, a series of controls were carried out to determine YFP and CFP crosstalk into the FRET channel. Cells expressing Citrine alone were imaged as above. A region of interest (ROI) was drawn around each cell and the ratio of the average grey level of the ROI in the FRET image to that in the YFP image was calculated as in Equation 1(a), and averaged to determine YFP crosstalk. To determine CFP crosstalk, cells expressing Cerulean alone were imaged as above, the ratio of the average grey level of the ROI in the FRET image to that in the CFP image was calculated as in Equation 1(b), and averaged.

(a) YFP crosstalk = FRET signal ÷ YFP signal	(b) CFP crosstalk = FRET signal ÷ CFP signal

Equation 1 – Calculations to determine crosstalk of YFP signal (a) and CFP signal (b) into FRET channel

To determine corrected FRET, cells expressing both fluorophores were imaged as above and the average grey level of the ROI in each of the three images was recorded. FRET was then corrected for crosstalk as in Equation 2, and averaged:

Corrected FRET = FRET signal – (YFP crosstalk x YFP signal) – (CFP crosstalk x CFP signal)

Equation 2 – Calculation to determine corrected FRET

2.8 List of antibodies

Antibody	Clone	Company	Western blot concentration	IF/PLA concentration
PRIMARY ANTIBODIES				
Anti-NIS	Rabbit polyclonal IgG	Protein Tech (24324-1-AP)	1:1000	1:600
Anti-MYC	Mouse monoclonal IgG2a (9B11)	Cell Signalling (2276S)	1:1000	1:750
Anti-HA	Mouse monoclonal IgG1 (16B12)	Covance (MMS-101P)	1:1000	1:100
Anti-HA	Rabbit polyclonal IgG (Y-11)	Santa Cruz (sc-805)	1:200	1:100
Anti-β-actin	Mouse monoclonal IgG1 (AC-15)	Sigma-Aldrich (A5441)	1:10,000	N/A
Anti-Na^+/K^+-ATPase	Rabbit monoclonal IgG (EP1845Y)	Abcam (ab76020)	N/A	1:250
Anti-Na^+/K^+-ATPase (Alexa Fluor® 488)	Rabbit monoclonal IgG (EP1845Y)	Abcam (ab197713)	N/A	1:50
SECONDARY ANTIBODIES				
Anti-rabbit (HRP-linked)	Goat polyclonal IgG	Cell Signalling (7074S)	1:2000	N/A
Anti-mouse (HRP-linked)	Rabbit polyclonal IgG	Cell Signalling (7076S)	1:2000	N/A
Anti-rabbit (Alexa Fluor® 594)	Goat polyclonal IgG	Invitrogen (A11037)	N/A	1:250
Anti-mouse (Alexa Fluor® 488)	Goat polyclonal IgG	Invitrogen (A11029)	N/A	1:250

Table 2-6 – Antibodies used in this study. HRP = horseradish peroxidase

2.9 Statistical analyses

Data were analysed using GraphPad Prism (Version 5.0). The Shapiro-Wilk test was performed to determine whether the data followed a normal distribution prior to further analysis. One-way analysis of variance (ANOVA) was used with Dunnett's multiple comparison test to compare to WT, or Tukey's multiple comparison test to compare all means. Two-way ANOVA with Sidak's multiple comparison test was also used. If data were non-parametric, one-way ANOVA with Kruskal-Wallis multiple comparison test were used instead. Significance was taken as $p<0.05$.

CHAPTER 3 – DETECTING WILD-TYPE NIS DIMERISATION

3.1 Introduction

Although it has been previously suggested that NIS forms dimers (Eskandari et al., 1997, Huc-Brandt et al., 2011), these studies do not show direct interaction between NIS monomers or where in the cell NIS dimerisation occurs. Similarly, they do not examine whether dimerisation is required for NIS function, despite having an important role for many membrane proteins. In order to challenge the hypothesis that dimerisation is important for NIS function, it was first imperative to demonstrate that NIS dimerisation occurs.

As a vast range of techniques exist to investigate protein dimerisation (as described in section 1.4.3), it was important to select which methods to use in these studies by considering which of the techniques that could be carried out here would be the most informative. Fortunately, the group already had plasmids encoding two differentially-tagged variants of NIS, tagged at the C-terminus with either MYC or HA. This enabled protein-protein interaction detection methods to be applied here using monoclonal antibodies against the tags. Given the group's previous expertise with both PLA and co-IP techniques, it was decided that these methods would be utilised in these studies. It was also advantageous that one technique detected protein-protein interactions in the whole cell (PLA) and the other in isolated proteins (co-IP), as this met the requirement of using varied methods to validate the conclusions drawn from these data on the occurrence of NIS dimerisation.

Unfortunately, neither technique could give a readily quantitative measure of NIS dimerisation which could be used to assess changes in the dimerisation of NIS mutants. However, around half-way through this PhD, a new microscope facility became available which enabled the possibility of using a FRET-based method to quantitatively evaluate NIS dimerisation. It was decided to transfect two variants of NIS, each conjugated to one of a

FRET-fluorophore pair, and that changes in the emission of the acceptor fluorophore would address NIS dimerisation. As previously described in section 1.4.3.2, one of the most commonly used FRET-fluorophore pairs is cyan fluorescent protein (CFP) and yellow fluorescent protein (YFP), and variants of both fluorophores exist which have improved properties (Day and Davidson, 2009). Consequently, the fluorophores used in these studies were Cerulean (as an improved variant of CFP (Rizzo et al., 2004)) and Citrine (as an improved YFP variant (Griesbeck et al., 2001)). However, as this would require co-transfection of two plasmids, there would not necessarily be a 1:1 fluorophore ratio within the cells due to variable levels of uptake of the two plasmids in individual cells and across the population. Consequently, the cross-talk that occurs due to the spectral overlap between the two fluorophores (discussed in section 1.4.3.2) must be corrected for. As this had not been necessary for previous use of the microscope facility, this required a novel method of analysis in order to accurately interpret the FRET data.

Similarly, it was important to select appropriate cell lines to conduct these studies in. It was crucial to use cell lines which readily transfect, as adequate co-transfection of two plasmids was a prerequisite in order to investigate NIS dimerisation. Furthermore, as many of the techniques used here to assess NIS dimerisation involved microscopy, it was also vital to use larger cells which are more suitable for microscopic analysis. While it was also important to use a thyroidal-based cell line which would have the appropriate cellular machinery to properly process NIS protein, many of these cell lines do not transfect reliably and/or are relatively small and therefore not the most practical choice for these studies. However, the human anaplastic thyroid carcinoma cell line SW1736 does transfect well and is of a suitable size for microscopy, hence was selected for these studies. As a secondary cell line to support

these studies, the human cervical carcinoma cell line HeLa was chosen, as these cells are renowned for their excellent transfection rates and are also suitable for microscopy.

The purpose of this chapter was to investigate whether NIS dimerisation could be observed by using the methodologies detailed above to detect close proximity and interactions between differentially-tagged variants of wild-type NIS in both cell lines.

3.2 Methods

3.2.1 Generation of NIS constructs conjugated to cerulean or citrine

PCR cloning methods as described in section 2.2.1.1 were followed to generate a plasmid containing a construct linking Cerulean to Citrine. Self-designed primers (Sigma-Aldrich, Table 3-1) were used to clone the Citrine coding sequence from Citrine-N1 plasmid (see section 9.4), which was then ligated into the Cerulean-C1 plasmid.

Construct	Primer Sequence
Cerulean-Citrine Linker	F: 5' – CTCAAGCTTTGGTGAGCAAGGGCGAGGAG – 3' R: 5' – GGTGGATCC*TTA*CTTGTACAGCTCGTCC – 3'

Table 3-1 – Sequences of forward (F) and reverse (R) primers used for PCR cloning of the Cerulean-Citrine Linker plasmid. Underlined sequences indicate restriction enzyme sites (HindIII for forward primers; BamHI for reverse) and italicised sequences indicate stop codons

3.2.2 Immunofluorescence

Immunofluorescence was performed as described in section 2.4 using rabbit anti-NIS primary antibody (see Table 2-6), with an additional step to identify the plasma membrane. After incubation with secondary antibody and Hoescht stain, coverslips were washed three times with PBS and incubated with 80µl 1% w/v BSA + 1% v/v NCS in PBS containing Alexa Fluor® 488-conjugated anti-Na^+K^+ATPase primary antibody (see Table 2-6) for 1 hour in the dark. Coverslips were washed three times and mounted as described in section 2.4.

3.2.3 PLA

PLA was performed as described in section 2.6 using mouse anti-MYC and rabbit anti-HA primary antibodies (see Table 2-5), with an additional step to label the plasma membrane. After the two 10 minute washes in wash buffer B, coverslips were incubated in 80µl 1% w/v BSA with 1% v/v NCS in PBS containing Alexa Fluor® 488-conjugated anti-Na^+K^+ATPase primary antibody (see Table 2-5) for 1 hour at room temperature in a humidity chamber. Two further 10 minute washes in wash buffer B and a 1 minute wash in 0.01x wash buffer B were performed before coverslips were mounted as described in section 2.6. As a positive control, PLA was also performed in cells co-transfected with pcDNA3.1(+) plasmids containing human MCT8 tagged with MYC or HA (kindly provided by Dr Vicki Smith, University of Birmingham).

3.2.4 Co-immunoprecipitation

SW1736 and HeLa cells were seeded in 75cm^2 flasks at 1x10^6 cells in 15ml media per flask. After 48 hours, cells were co-transfected with 10µg total DNA using TransIT®-LT-1 transfection reagent as a 3:1 ratio, as in section 2.2. Co-immunoprecipitation (co-IP) was performed 48 hours post-transfection to determine if there was a direct interaction between NIS variants conjugated to either MYC or HA. Media were aspirated and cells washed twice with PBS. Cells were then lysed in 1.5ml high-salt lysis buffer (50mM Tris pH7.4, 400mM NaCl and 1% v/v Igepal) containing 60µl/ml protease inhibitor cocktail. To aid lysis, flasks were rocked for 30 minutes at 4^{o}C before cells were scraped and transferred to a Dounce homogeniser. After homogenising on ice, lysates were transferred to 1.5ml microcentrifuge tubes, subjected to end-over-end rotation for 30 minutes at 4^{o}C and then centrifuged at 13,200rpm at 4^{o}C for 20 minutes to pellet cell debris. Supernatant was transferred to fresh microcentrifuge tubes and 100µl retained as whole-cell (WC) lysates before adding 5µl

primary antibody against the first tag (either mouse anti-MYC or rabbit anti-HA; see Table 2-6) to the remaining lysate and incubated at 4^{o}C overnight with end-over-end rotation in order to immunoprecipitate the first NIS variant and any proteins directly bound to it.

Protein G sepharose beads (GE Healthcare, Little Chalfont, Buckinghamshire, UK) were pulse-centrifuged at 4,000rpm for 1 minute at 4^{o}C to remove ethanol, washed three times and resuspended in high-salt lysis buffer. The bead slurry (100µl) was then added to each co-IP lysate and samples were incubated for 2 hours at 4^{o}C with end-over-end rotation. After samples were pulse-centrifuged to pellet the beads, the supernatant was discarded and beads were washed four times with high-salt lysis buffer to remove unbound protein. Bound protein was eluted by resuspending beads in 50µl loading buffer (2x Laemmli buffer (Bio-Rad Laboratories Ltd, Hercules, California, USA) containing 20% v/v β-mercaptoethanol) and denaturing for 30 minutes at 37^{o}C. Retained WC lysates were similarly denatured in the 2x loading buffer. All lysates were stored at -20^{o}C prior to subsequent Western blot analysis as described in section 2.3.2, probing with primary antibody against the second tag (either rabbit anti-HA or mouse anti-MYC) to determine whether the second NIS variant was immunoprecipitated with the first, thus showing direct interaction between the two variants.

3.2.5 FRET

FRET was performed as described in section 2.7, with cells transfected with either the Cerulean-Citrine Linker plasmid (see section 3.2.1) or the Epac2 plasmid containing a cAMP-sensing FRET probe (kindly provided by Professor David Hodson, University of Birmingham). The Linker and Epac2 proteins were used as positive controls as they both co-express Cerulean and Citrine within close enough proximity to undergo FRET.

In addition to performing data analysis on the whole cell, analysis was also carried out on a linear section across the cells in order to ascertain where in the cell NIS dimerisation occurs. This was achieved by using 'Linescan' to place a horizontal line across the cell on each of the three versions of every image, instead of drawing a region of interest around each cell. Corrected FRET analysis was then performed as detailed in section 2.7 and the FRET signal was plotted against its distance along the line.

3.3 Results

3.3.1 PLA demonstrates close proximity between differentially-tagged NIS variants, which is suggestive of dimerisation

In order to assess whether differentially-tagged variants of NIS were in close proximity within the cell, PLA was performed on fixed SW1736 and HeLa cells co-transfected with NIS-MYC and NIS-HA using mouse anti-MYC and rabbit anti-HA antibodies, and visualised with confocal microscopy. To help ascertain where interactions were occurring within the cell, incubation with Alexa Fluor® 488-conjugated antibodies against the Na^+K^+ATPase was also performed to identify the plasma membrane.

Appearance of red dots in SW1736 and HeLa cells co-transfected with NIS-MYC and NIS-HA (Figure 3-1A and Figure 3-2A, respectively) indicates that the two tags are in close proximity (less than 40nm apart) in both cell lines, which is suggestive of dimerisation. Similar results were seen in both SW1736 and HeLa cells co-transfected with differentially-tagged variants of MCT8 as a biological positive control (Figure 3-1D and Figure 3-2D, respectively), whereas no PLA signal was observed in cells only expressing one NIS variant as technical negative controls (Figure 3-1B & C and Figure 3-2B & C).

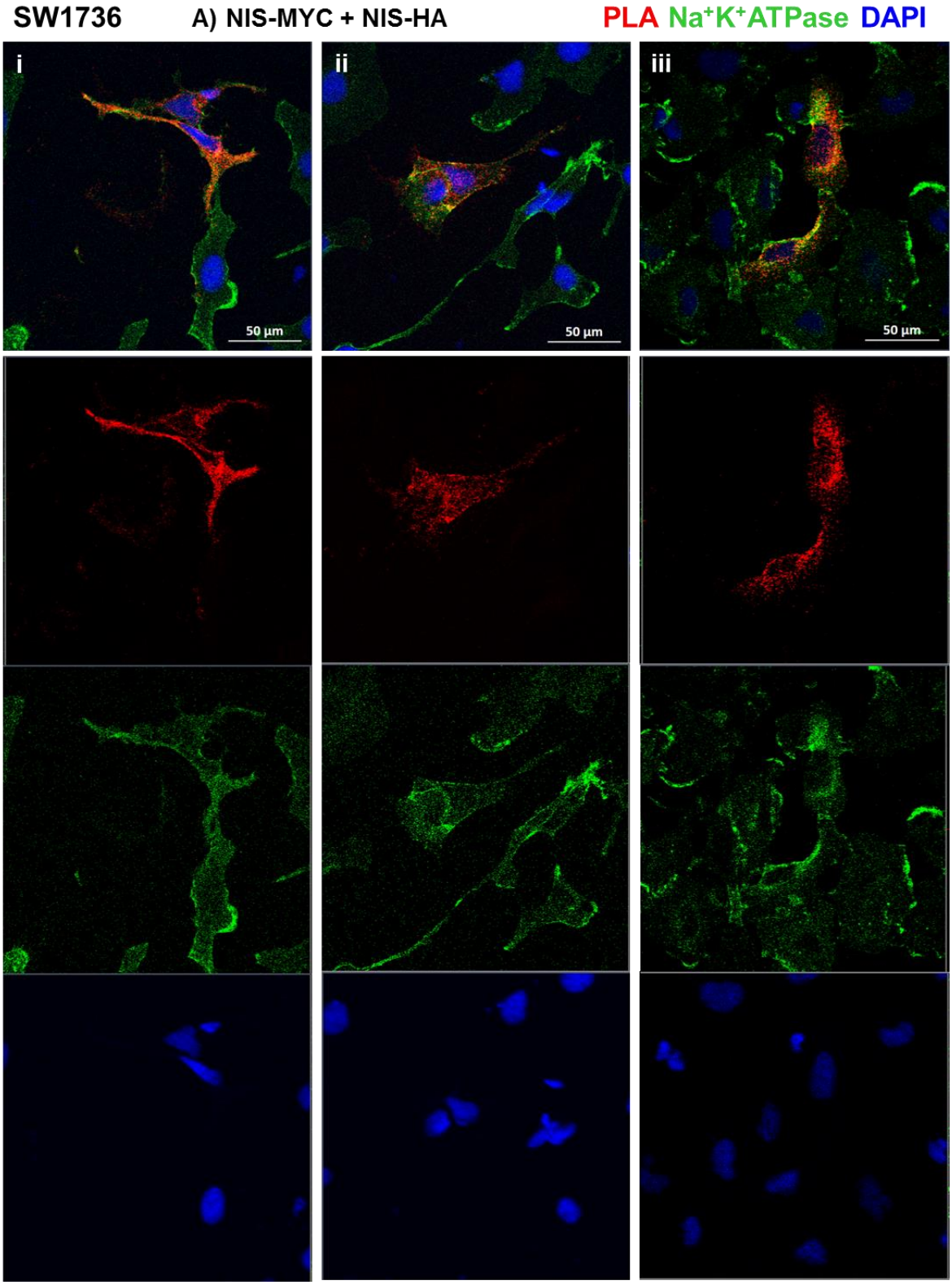

Figure 3-1 – PLA demonstrates close proximity between NIS-MYC and NIS-HA in SW1736 cells. PLA was performed on SW1736 cells co-transfected with NIS-MYC + NIS-HA (A i-iii), empty pcDNA3.1(+) vector (VO) + NIS-MYC (B, overleaf), VO + NIS-HA (C, overleaf) or MCT8-MYC + MCT8-HA (D, overleaf). PLA signal (in red) indicates close proximity (<40nm) between MYC and HA, which is suggestive of dimerisation and observed for both NIS and the known dimeric protein MCT8. Plasma

membrane is visualised using a fluorescent primary antibody to Na^+K^+ATPase (green). Nuclei are visualised in blue using DAPI. 40x magnification. (n=2).

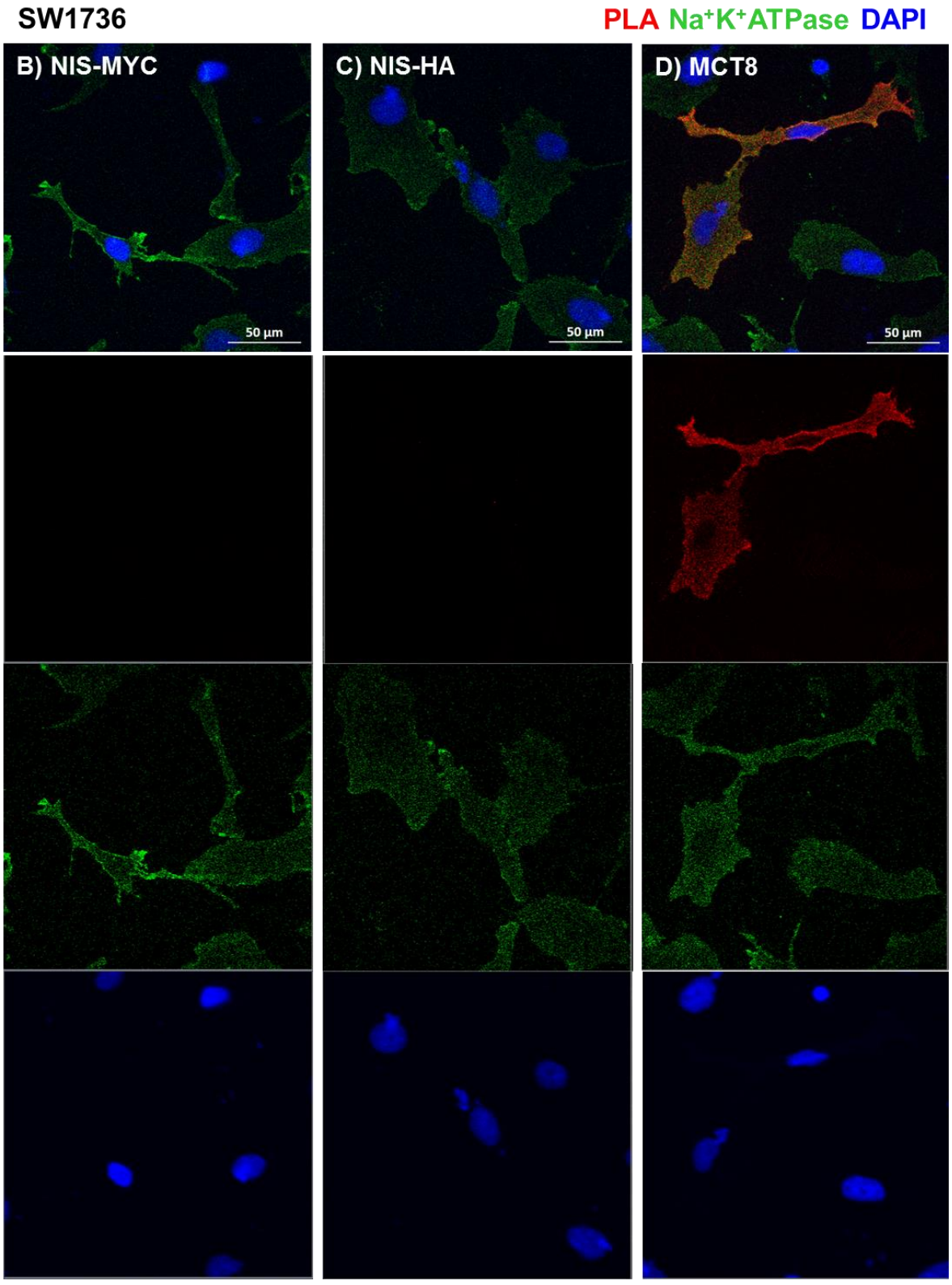

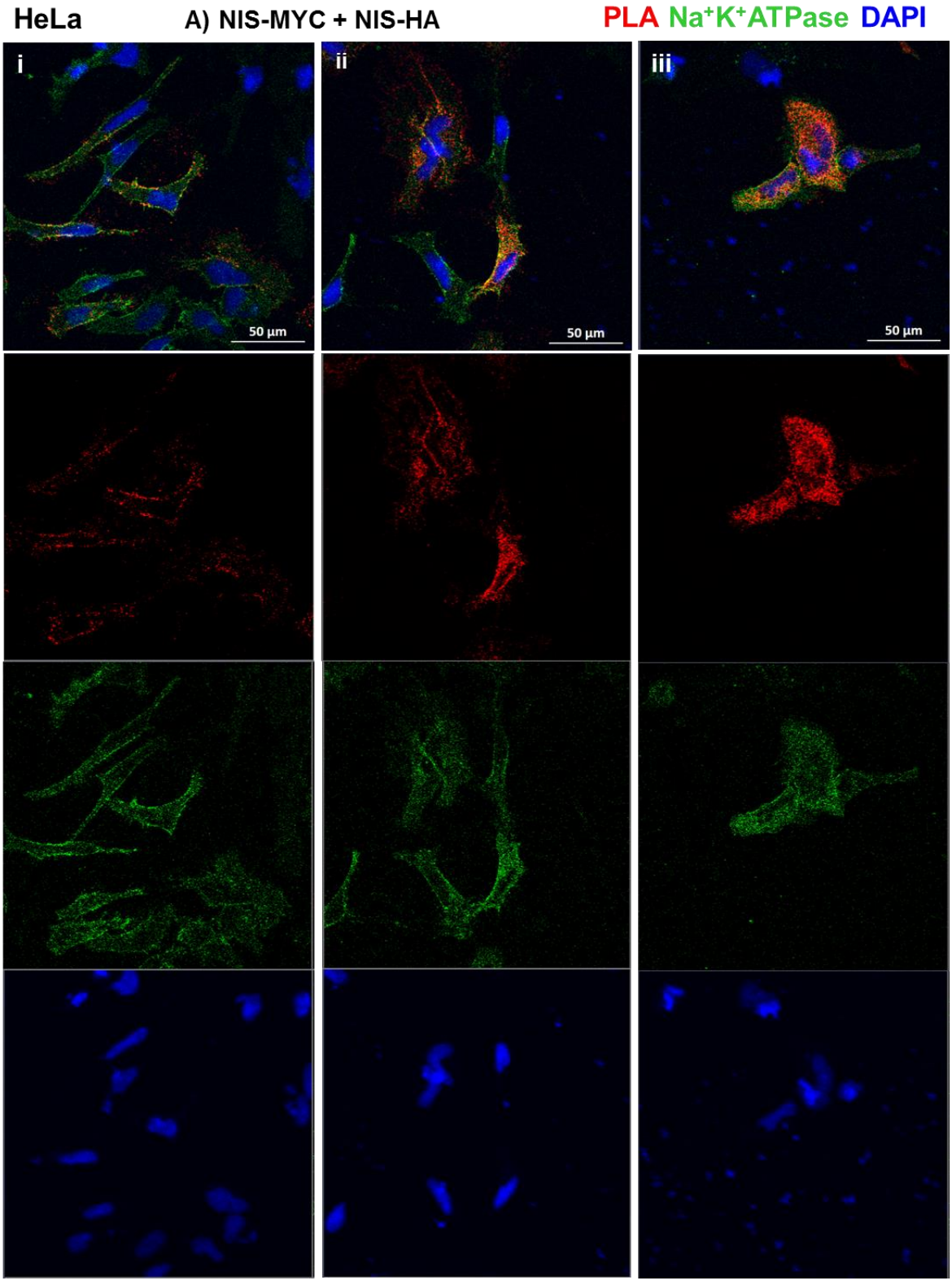

Figure 3-2 – PLA demonstrates close proximity between NIS-MYC and NIS-HA in HeLa cells. PLA was performed on HeLa cells co-transfected with NIS-MYC + NIS-HA (A i-iii), empty pcDNA3.1(+) vector (VO) + NIS-MYC (B, overleaf), VO + NIS-HA (C, overleaf) or MCT8-MYC + MCT8-HA (D, overleaf). PLA signal (in red) indicates close proximity (<40nm) between MYC and HA, which is suggestive of dimerisation and was observed for both NIS and the known dimeric protein MCT8. Plasma membranes

are visualised using a fluorescent primary antibody to Na^+K^+ATPase (green). Nuclei are visualised in blue using DAPI. 40x magnification. (n=2).

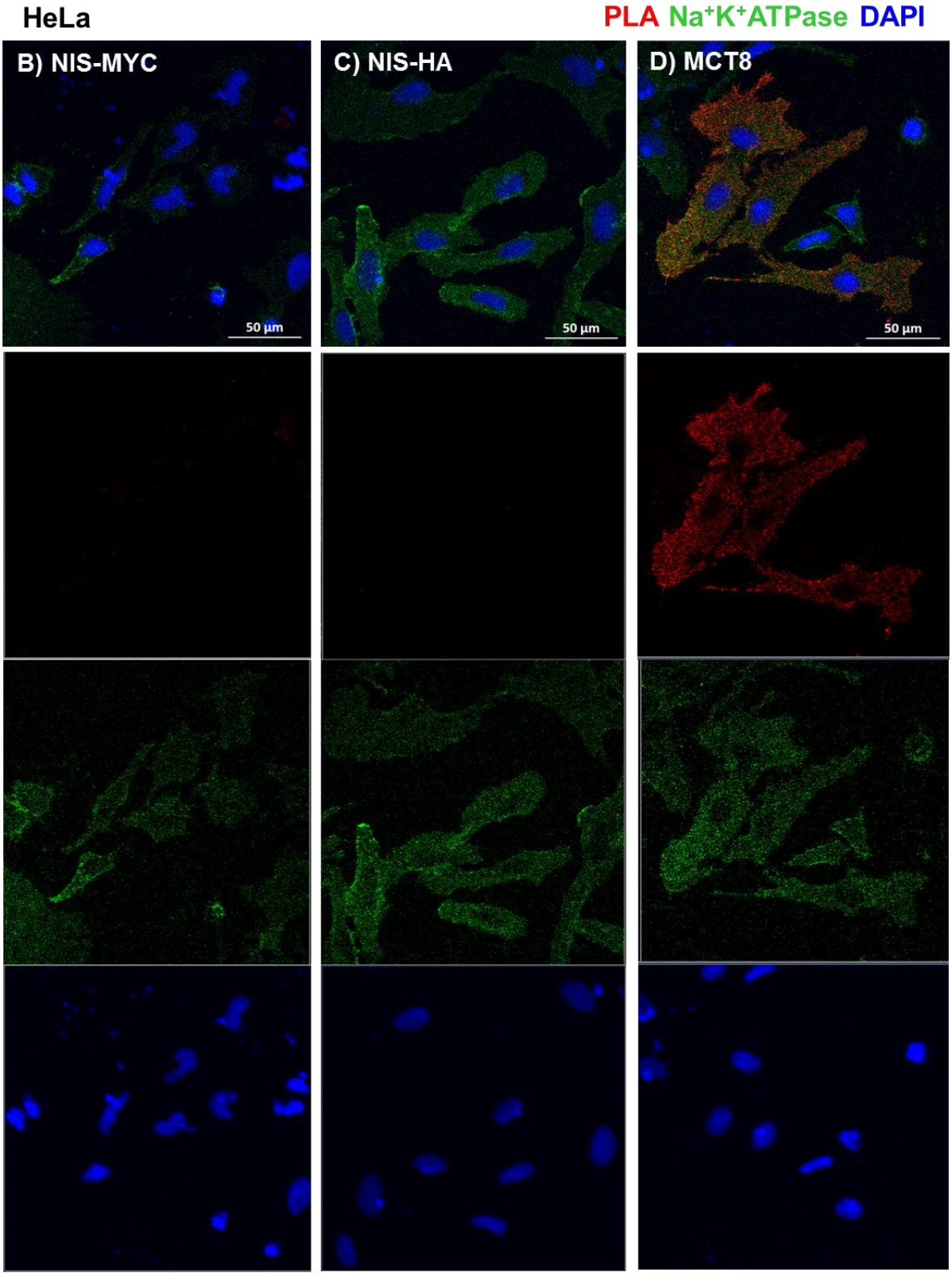

Enlargement of these PLA images highlights that while much of the PLA signal is intracellular, there is some colocalisation between the PLA signal and the plasma membrane marker (Figure 3-3), indicating that NIS-MYC and NIS-HA are in close proximity throughout the cell, including at the plasma membrane.

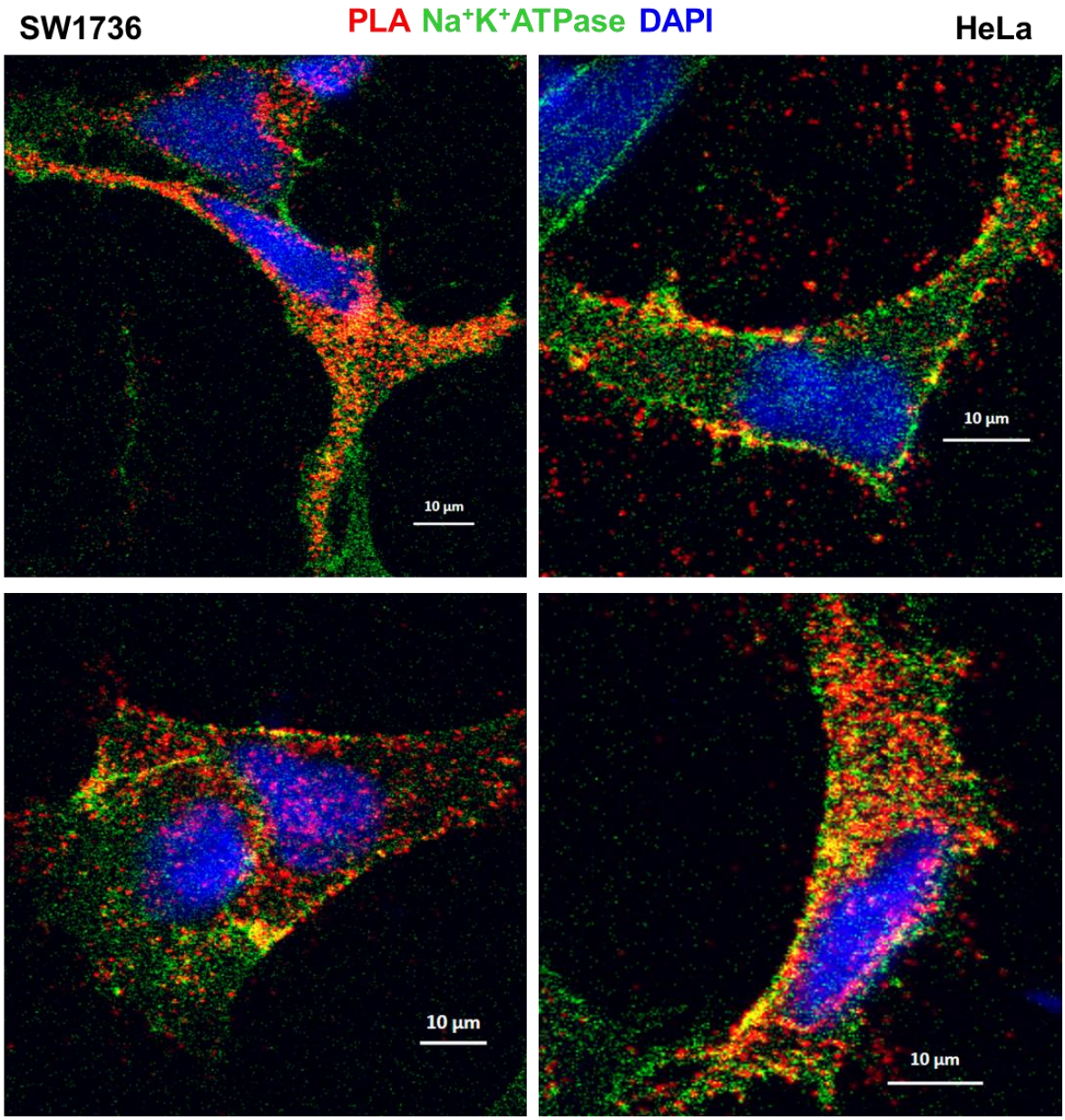

Figure 3-3 – Close proximity between NIS-MYC and NIS-HA occurs throughout the cell, including at the plasma membrane. Enlargement of PLA images reveals areas of colocalisation (yellow) between PLA signal generated by close proximity (<40nm) of NIS-MYC and NIS-HA (in red) with the plasma membrane marker, Na^+K^+ATPase (in green) in SW1736 (left) and HeLa (right) cells, although much of the PLA signal is intracellular.

3.3.2 Co-immunoprecipitation establishes a direct interaction between differentially-tagged NIS variants, which supports dimerisation

To investigate whether differentially tagged NIS variants interact directly, co-immunoprecipitation (co-IP) was performed. NIS protein was immunoprecipitated from lysates of SW1736 and HeLa cells co-transfected with NIS-MYC and NIS-HA using primary antibody to one tag (either mouse anti-MYC or rabbit anti-HA). Immunoprecipitated proteins were then separated via SDS-PAGE using primary antibody to the other tag to determine whether the second NIS variant had been immunoprecipitated with the first, indicating a direct interaction between the two variants.

A band of approximately 150kDa was observed in the co-IP blot of both cell lines when co-transfected with NIS-MYC and NIS-HA and in both orientations of antibody (i.e. immunoprecipitation with mouse anti-MYC and probing Western blot with rabbit anti-HA (Figure 3-4A, lane 5) and vice versa (Figure 3-4B, lane 5), demonstrating a direct interaction between NIS-MYC and NIS-HA which is suggestive of dimerisation. This was further confirmed by the negative controls, as this band was not observed in protein lysates from cells not expressing NIS (lane 1), cells only expressing one NIS variant (lanes 2 and 3) or cells co-expressing both NIS variants but which did not undergo immunoprecipitation (no antibody control, lane 4). Western blots performed on whole cell lysates (WCL) from each condition confirmed adequate transfection of NIS variants by probing for MYC and HA, and demonstrated even protein loading across all lanes by probing for β-actin.

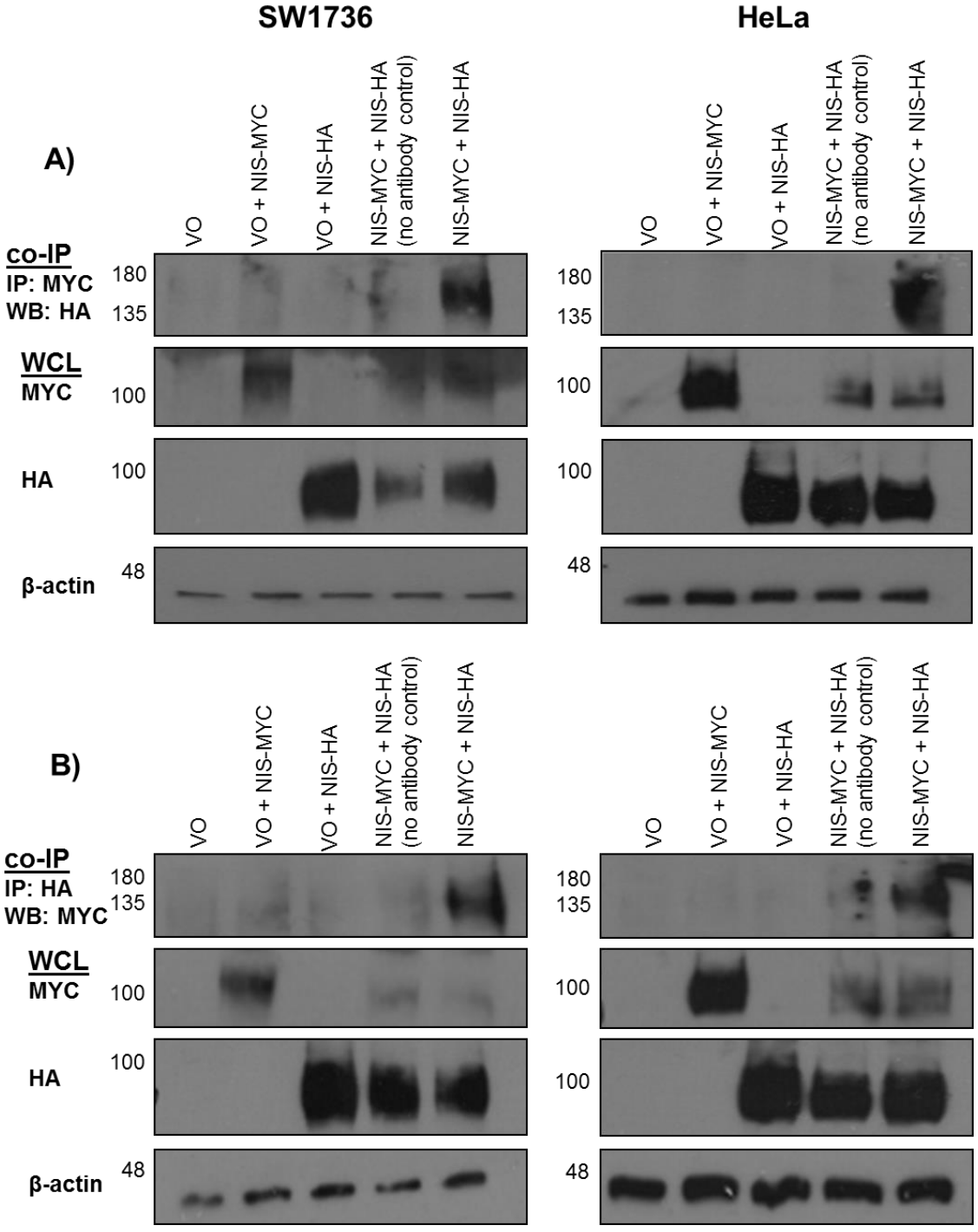

Figure 3-4 – Co-IP demonstrates direct interaction between NIS-MYC and NIS-HA in SW1736 and HeLa cells. SW1736 (left) and HeLa (right) cells were transfected with empty pcDNA3.1(+) vector (VO, lane 1), VO + NIS-MYC (lane 2), VO + NIS-HA (lane 3) or NIS-MYC + NIS-HA (lanes 4 and 5) and lysed. Co-IP was performed on all lysates (except no antibody control, lane 4) by immunoprecipitating (IP) with mouse anti-MYC (A) or rabbit anti-HA (B). Western blot (WB) after IP using antibody to the other tag was performed to detect the presence of the other NIS variant, which demonstrates a direct interaction between the two NIS variants (co-IP blots, top panel). WB of whole cell lysates (WCL) was used to confirm protein transfection by probing with MYC (middle-top panel) and HA (middle-bottom panel), and even protein loading (β-actin, bottom panel). (n=2).

3.3.3 Novel NIS-fluorophore constructs were developed and characterised to enable investigation of NIS dimerisation using FRET

Novel NIS constructs conjugated to the fluorophore Cerulean or Citrine at either the N- or C-terminus were created using PCR cloning methods to establish if NIS dimerisation could be quantitatively investigating using FRET. The expression, localisation and function of these constructs was assessed to determine whether the presence of the fluorophore affected the NIS protein and therefore ascertain their suitability for FRET analysis.

3.3.3.1 NIS maturation is lost by fluorophore-tagging at the N-terminus

Western blot analysis was performed on lysates of SW1736 and HeLa cells expressing one of the six differentially-tagged NIS constructs using the anti-NIS primary antibody to determine if the presence of a fluorophore at either terminus affected NIS protein expression.

Figure 3-5 illustrates the effect of fluorophore tags on NIS protein expression. When tagged at the C-terminus with MYC (lane 2) or HA (lane 3), the band at ~60kDa represents the immature, non-glycosylated NIS protein while the large band between 75-100kDa represents the mature, fully glycosylated NIS protein. With NIS tagged at the C-terminus with either Cerulean (lane 3) or Citrine (lane 4), a similar banding pattern was observed, indicating that fluorophores at the C-terminus do not affect protein maturation. The distinct shift in the molecular weight of this banding pattern reflects the addition of the molecular weight of the fluorophores (26.7kDa (Davidson and Piston, *unpublished*)), with the non-glycosylated band shifted to ~75kDa and the fully-glycosylated band shifted to ~100-125kDa. However, with NIS tagged at the N-terminus to either Cerulean (lane 5) or Citrine (lane 6), only one band was seen at ~75kDa, representing the non-glycosylated form of NIS, indicating that expression of the fluorophores at the N-terminus causes a loss of protein maturation.

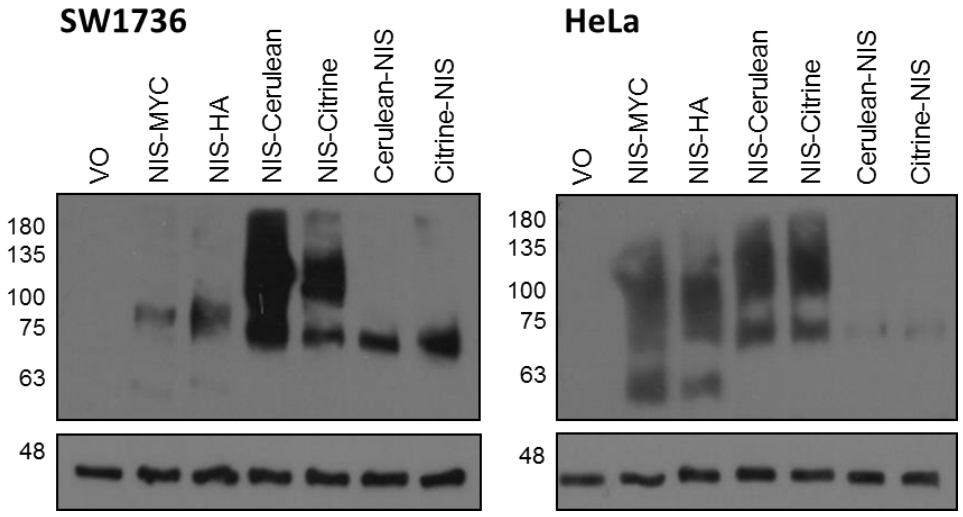

Figure 3-5 – Only NIS constructs tagged with fluorophore at the N-terminus do not undergo adequate glycosylation. SW1736 (left) and HeLa (right) cells were transfected with empty pcDNA3.1(+) vector (VO, lane 1) or one of six differentially-tagged NIS variants (lanes 2-7) and Western blot analysis was performed using the rabbit anti-NIS primary antibody. This revealed the presence of a non-glycosylated form of NIS (~60kDa with MYC and HA, ~75kDa with Cerulean and Citrine) in all NIS lanes, but the fully-glycosylated form of NIS (~75-100kDa with MYC and HA, ~100-125kDa with fluorophores) was not observed when fluorophores were expressed at the NIS N-terminus, indicating a lack of NIS maturation. β-actin primary antibody was used as a loading control. (n=2).

3.3.3.2 NIS expression at the plasma membrane is inhibited by fluorophore-tagging at the N-terminus

To assess whether tagging the fluorophore to the N- or C-terminus affects NIS subcellular localisation, immunofluorescence was performed on SW1736 and HeLa cells expressing one of the differentially-tagged NIS constructs using the anti-NIS primary antibody.

Colocalisation between both NIS-MYC and NIS-HA (red) with the plasma membrane marker Na^+K^+ATPase (green), demonstrates membranous expression of NIS in SW1736 and HeLa cells (Figure 3-6 and Figure 3-7, respectively). Similar colocalisation with the plasma membrane marker was observed with NIS-Cerulean and NIS-Citrine, indicating that the presence of the fluorophore at the C-terminus does not affect NIS expression at the plasma membrane. However, neither Cerulean-NIS nor Citrine-NIS could be detected at the plasma membrane, signifying that tagging NIS at the N-terminus with fluorophore resulted in complete lack of expression of these constructs at the plasma membrane.

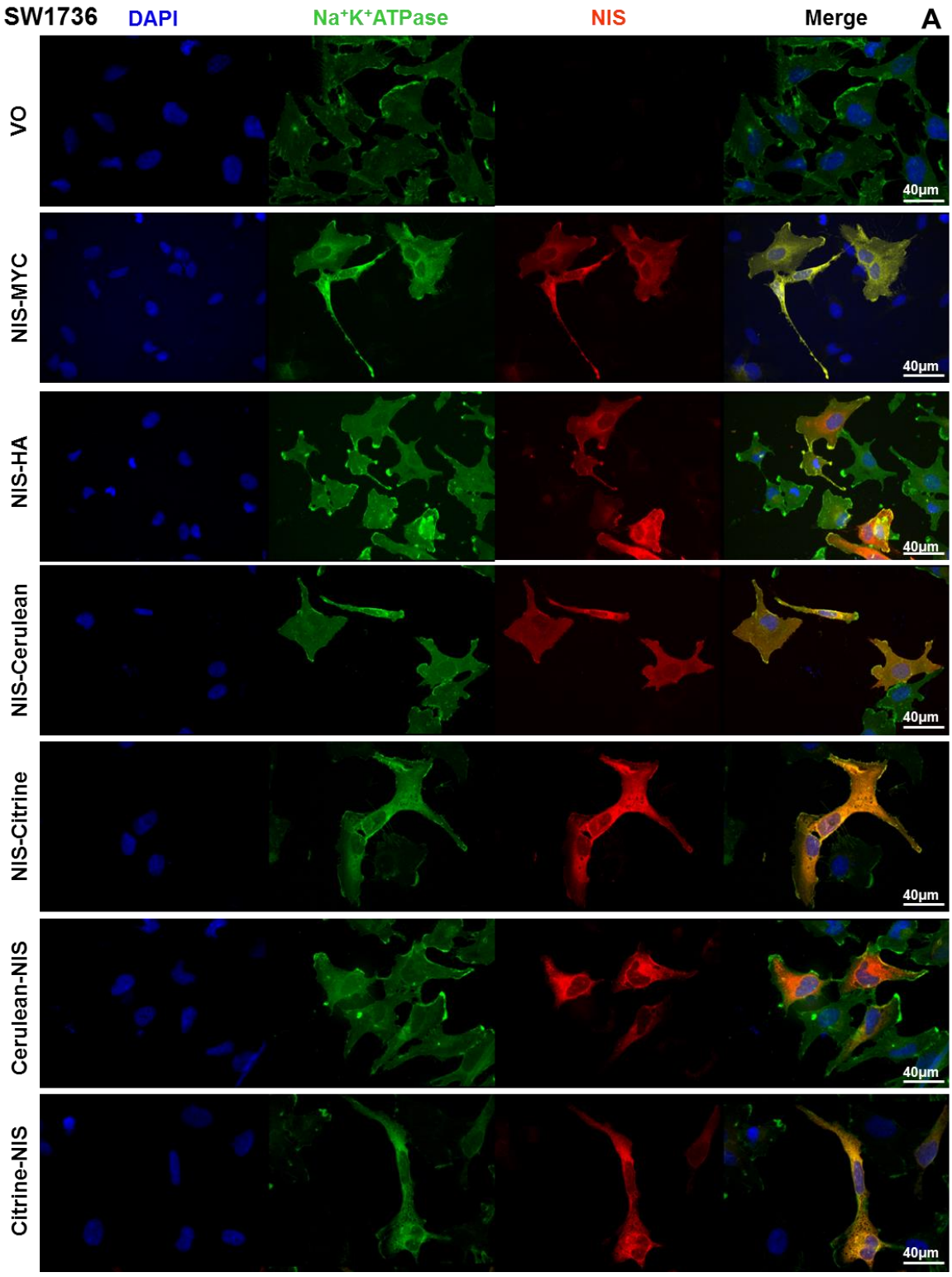

Figure 3-6 – NIS constructs tagged with fluorophore at the N-terminus only were intracellularly retained in SW1736 cells. Cells were transfected with empty pcDNA3.1(+) vector (VO) or one of six differentially-tagged NIS variants and immunofluorescence was performed. NIS protein is visualised using a rabbit anti-NIS primary antibody (in red) and plasma membranes are visualised using a fluorescent primary antibody to Na^+K^+ATPase (in green). Nuclei are visualised in blue using Hoescht stain. Single channels and merged images are shown in A, and enlarged merged images are shown in B (overleaf). 40x magnification. (n=2).

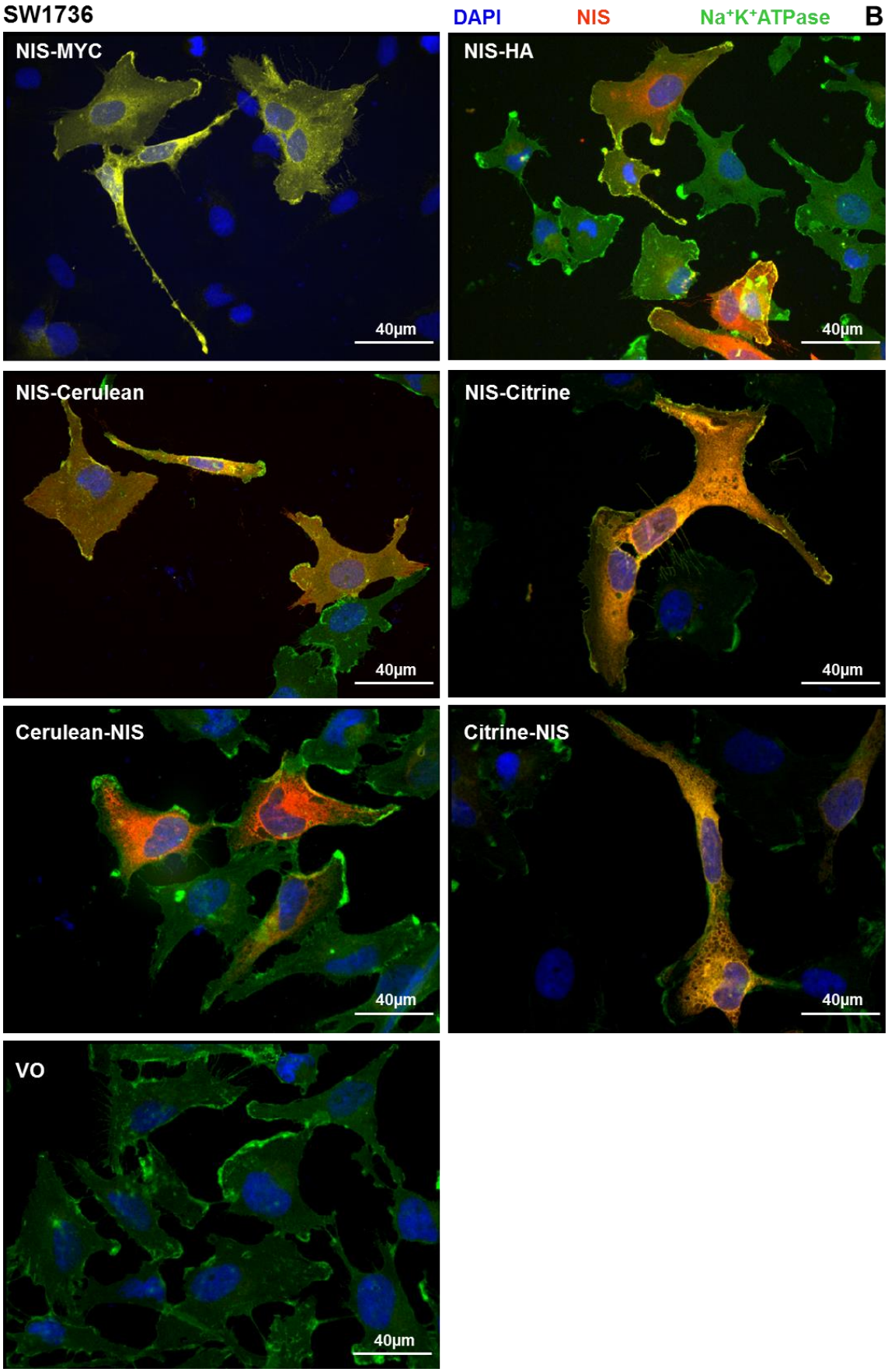
SW1736
DAPI
NIS
Na⁺K⁺ATPase
B
NIS-MYC
NIS-HA
NIS-Cerulean
NIS-Citrine
Cerulean-NIS
Citrine-NIS
VO
40µm

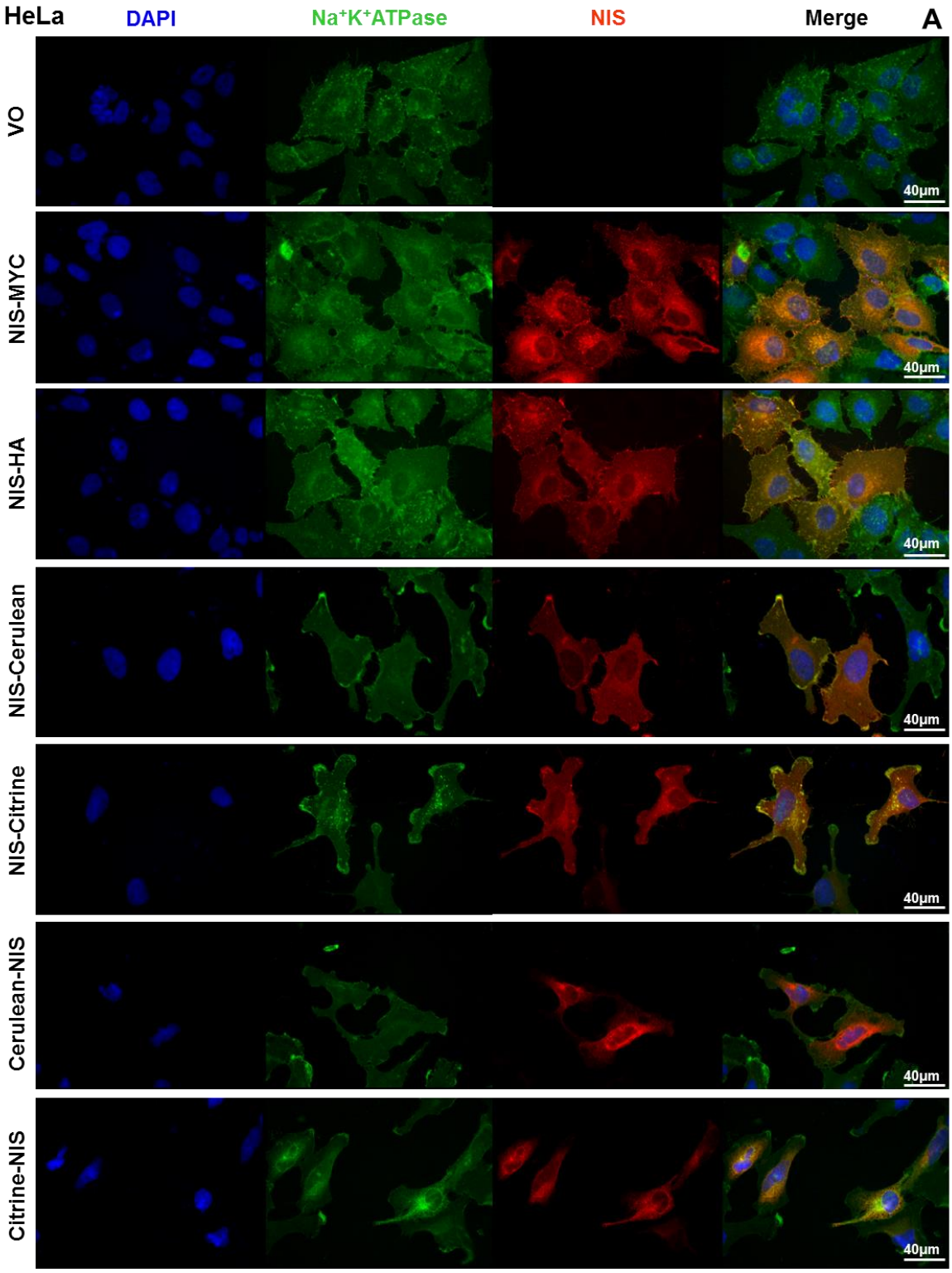

Figure 3-7 - NIS constructs tagged with fluorophore at the N-terminus only were intracellularly retained in HeLa cells. Cells were transfected with empty pcDNA3.1(+) vector (VO) or one of six differentially-tagged NIS variants and immunofluorescence was performed. NIS protein is visualised using a rabbit anti-NIS primary antibody (in red) and plasma membranes are visualised using a fluorescent primary antibody to Na^+K^+ATPase (in green). Nuclei are visualised in blue using Hoescht stain. Single channels and merged images are shown in A, and enlarged merged images are shown in B (overleaf). 40x magnification. (n=2).

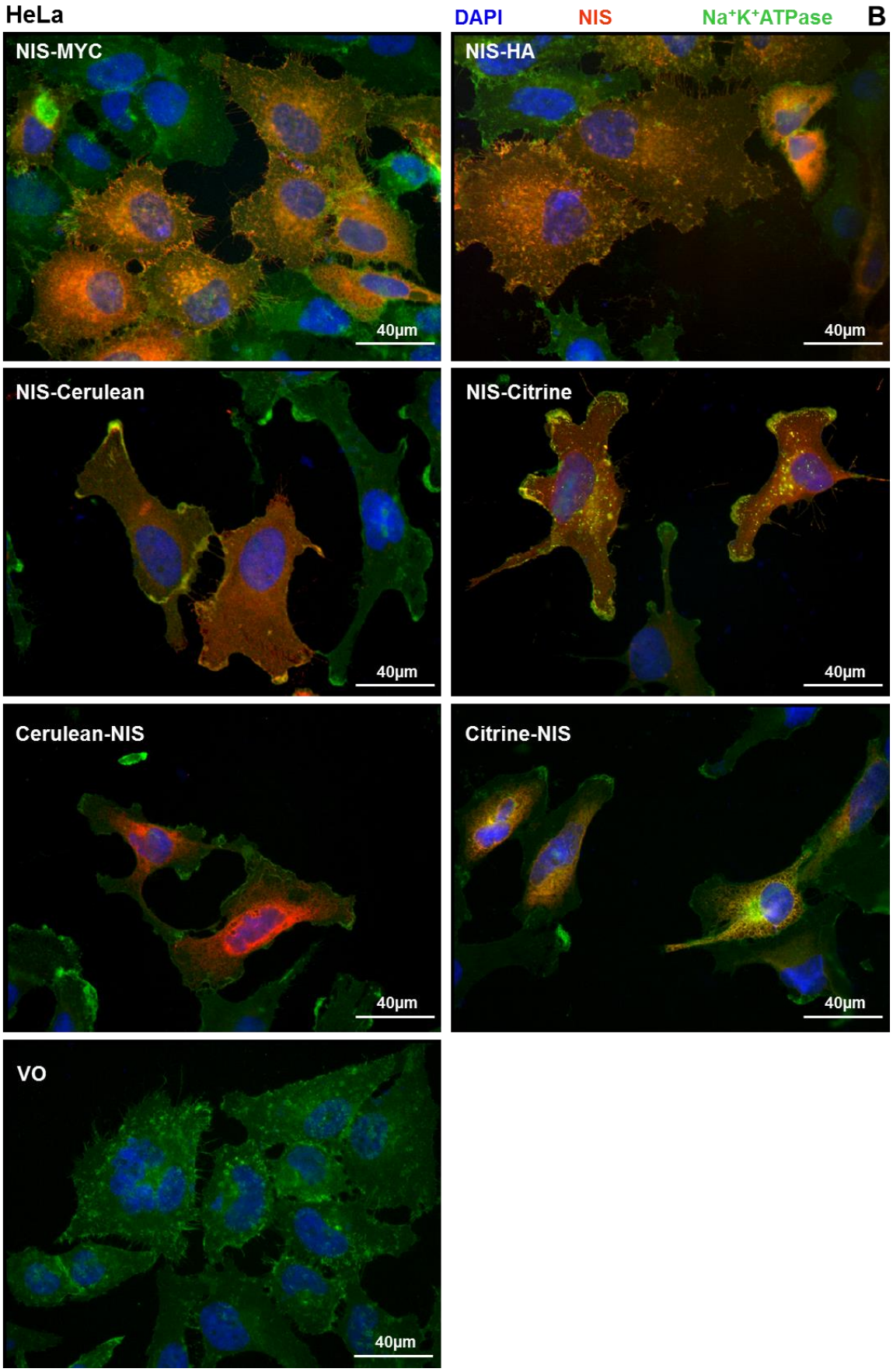
HeLa
DAPI
NIS
Na⁺K⁺ATPase
B
NIS-MYC
NIS-HA
NIS-Cerulean
NIS-Citrine
Cerulean-NIS
Citrine-NIS
VO
40µm

3.3.3.3 NIS function is abolished when tagged with fluorophore at the N-terminus

In order to determine whether tagging with a fluorophore at the N- or C-terminus alters NIS function, radioiodide uptake assays were performed on SW1736 and HeLa cells expressing one of the differentially-tagged NIS constructs. Two-way ANOVA with Sidak's multiple comparison tests were performed to identify any significant changes in uptake.

Figure 3-8 shows that expression of NIS-MYC and NIS-HA resulted in a significant increase in radioiodide uptake in both cell lines compared to VO (black bars, SW1736: 0.18±0.07pmol ^{125}I/µg protein (VO) vs. 1.13±0.26 (NIS-MYC) and 1.05±0.29 (NIS-HA); HeLa: 0.26±0.00 (VO) vs. 9.99±0.61 (NIS-MYC) and 12.89±0.51 (NIS-HA)). Similar results were observed with NIS-Cerulean and NIS-Citrine (black bars, SW1736: 2.27±0.43pmol ^{125}I/µg protein (NIS-Cerulean) and 1.78±0.36 (NIS-Citrine); HeLa: 14.90±0.48 (NIS-Cerulean) and 18.86±0.78 (NIS-Citrine)), demonstrating that tagging NIS at the C-terminus with fluorophore does not significantly affect its function. This radioiodide uptake was shown to be NIS-specific as it was inhibited by treatment with the NIS inhibitor, sodium perchlorate ($NaClO_4$, grey bars). However, radioiodide uptake was not observed in cells expressing Cerulean-NIS or Citrine-NIS (black bars, SW1736: 0.50±0.48 pmol ^{125}I/µg protein (Cerulean-NIS) and 0.50±0.36 (Citrine-NIS); HeLa: 0.61±0.57 (Cerulean-NIS) and 0.74±0.70 (Citrine-NIS)), indicating that tagging with fluorophore at the N-terminus renders NIS non-functional.

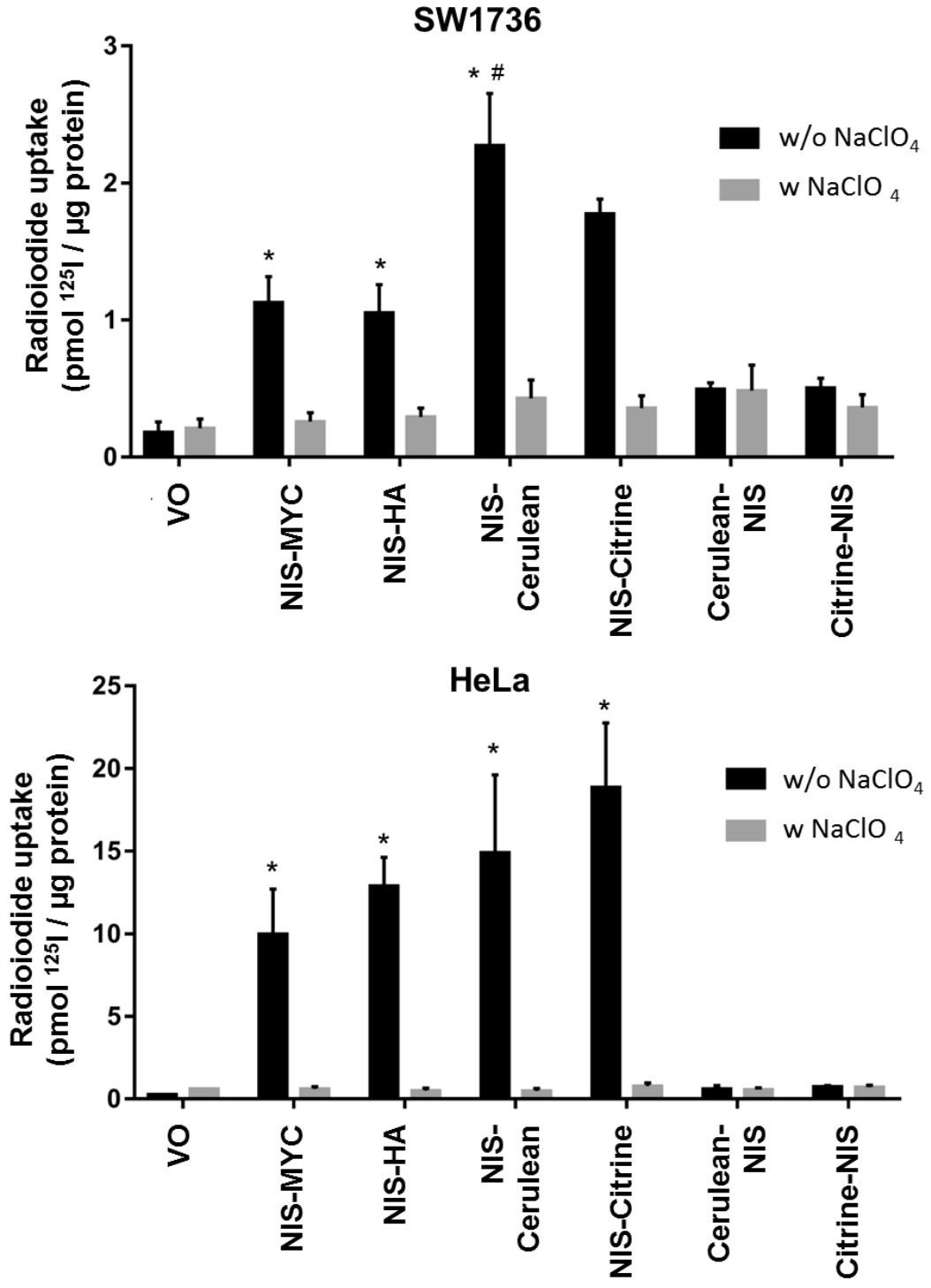

Figure 3-8 – NIS function was only lost when tagged with fluorophore at the N-terminus. SW1736 (top) and HeLa (bottom) cells were transfected with empty pcDNA3.1(+) vector (VO) or one of six differentially-tagged NIS variants and radioiodide uptake assays were performed. Significant radioiodide uptake compared to VO was observed with all NIS variants except those tagged at the N-terminus with fluorophore (black bars). Pre-treatment with sodium perchlorate ($NaClO_4$) to inhibit NIS (grey bars) demonstrates NIS-specific iodide uptake. Bars show mean radioiodide uptake in pmol ^{125}I/µg protein and error bars show SEM. Two-way ANOVA with Sidak's multiple comparison statistical tests were performed: * = p<0.05 compared to VO; # = p<0.05 compared to NIS-MYC and NIS-HA. (n=3 with 4 replicates in each n).

3.3.4 FRET-based methodology was developed to quantitatively evaluate interactions between differentially-tagged NIS-fluorophore variants

Since the fluorophore was demonstrated to have no negative impact on NIS function when tagged at the C-terminus, a novel methodology was developed to quantitatively measure the potential interaction between the two differentially-tagged NIS-fluorophore variants using FRET. This was to further challenge the occurrence of NIS dimerisation and to enable the evaluation of the potential impact of mutated residues on dimerisation in future experiments.

3.3.4.1 Calculations were devised to correct FRET data for the crosstalk of fluorophore signal into the FRET channel

In order to devise the method of data analysis for quantitatively assessing NIS dimerisation using FRET, it was first essential to determine the percentage of signal emitted by each fluorophore individually that was detected in the FRET image, termed crosstalk. As discussed in section 1.4.3.2, this arises due to the nature of the spectral overlap between the fluorophores which is required for FRET to occur, but must be corrected for during data analysis (Piston and Kremers, 2007). To do this, NIS-fluorophore constructs were singly expressed in both cell lines, and three concurrent versions of each image were captured and analysed to calculate crosstalk (see section 2.7). This was repeated in cells singly expressing the fluorophores not conjugated to NIS in order to confirm that the presence of NIS did not affect the amount of crosstalk.

Figure 3-9 confirms that only one fluorophore was expressed in the cell in these crosstalk calculation experiments, as shown by the total Cerulean (CFP) images (Cerulean excitation/Cerulean emission (CFP/CFP)) and the total Citrine (YFP) images (Citrine excitation/Citrine emission (YFP/YFP)). However, a large amount of this signal was

detected in the FRET image (Cerulean excitation/Citrine emission (CFP/YFP)). The crosstalk for NIS-Cerulean was calculated to be 42.8% in SW1736 cells and 41.0% in HeLa cells, while the crosstalk for Cerulean was 43.7% and in SW176 cell and 41.9% in HeLa cells. Similarly, NIS-Citrine crosstalk was calculated to be 30.0% in SW1736 cells and 24.3% in HeLa cells, while Citrine crosstalk was 23.1% in SW1736 cells and 23.3% in HeLa cells. This confirmed that the crosstalk was a property of the fluorophores themselves and was not influenced by NIS or cell type, and these crosstalk values were incorporated into the calculations to correct FRET for this crosstalk (see section 2.7).

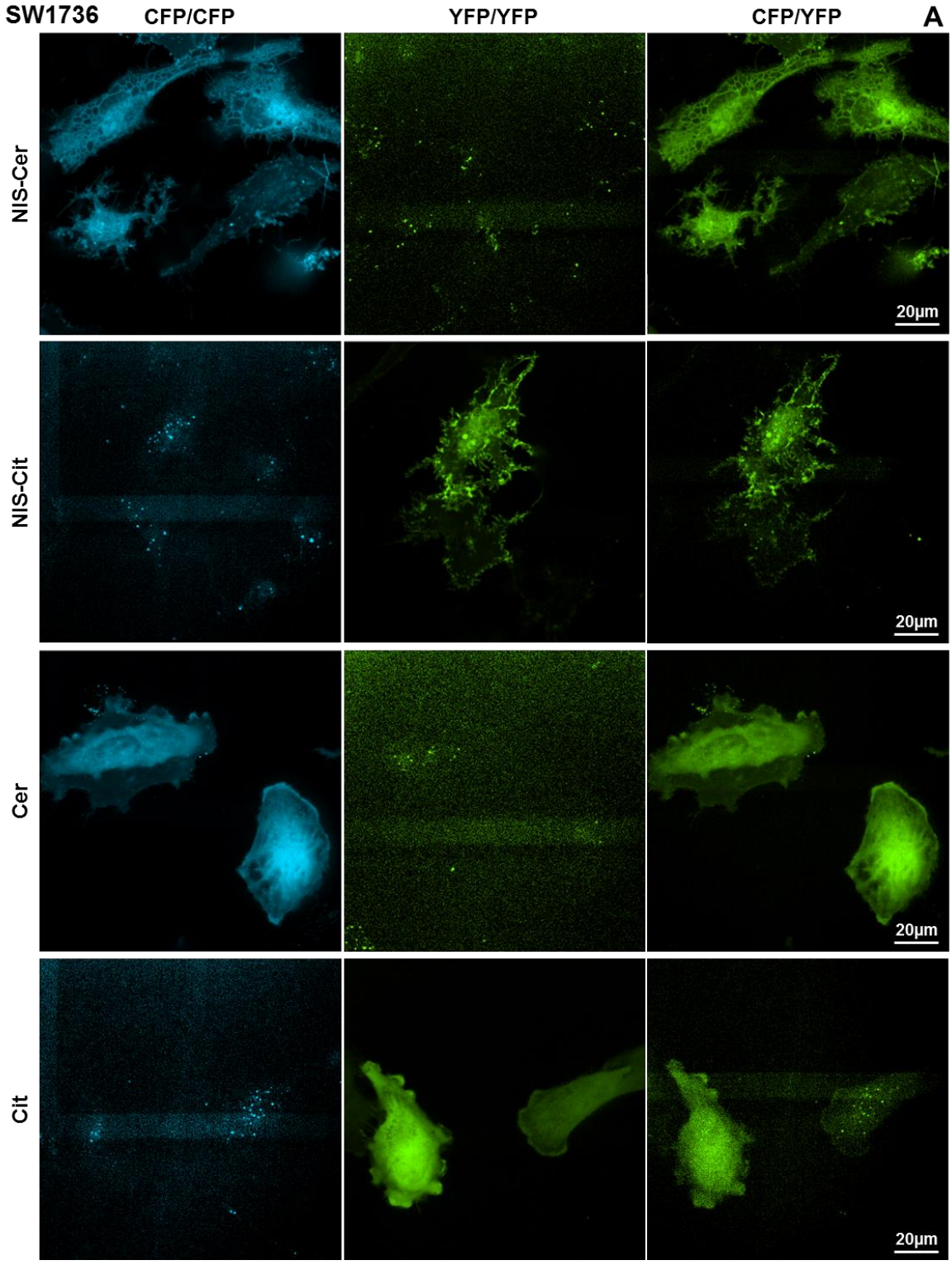

Figure 3-9 – The FRET image can detect emission from singly-expressed fluorophores, demonstrating crosstalk from both fluorophores which must be accounted for during FRET analysis. Each fluorophore construct was singly transfected into SW1736 (A) and HeLa (B, overleaf) cells and three concurrent versions of each image were taken: total Cerulean (CFP) image (Cerulean excitation/Cerulean emission (CFP/CFP)), total Citrine (YFP) image (Citrine excitation/Citrine emission (YFP/YFP)) and the FRET image (Cerulean excitation/YFP emission (CFP/YFP)). Single expression of each fluorophore was

confirmed by the total CFP and total YFP images, but a distinct percentage of this signal could be detected in the FRET image. (n=3, 10 cells in each n).

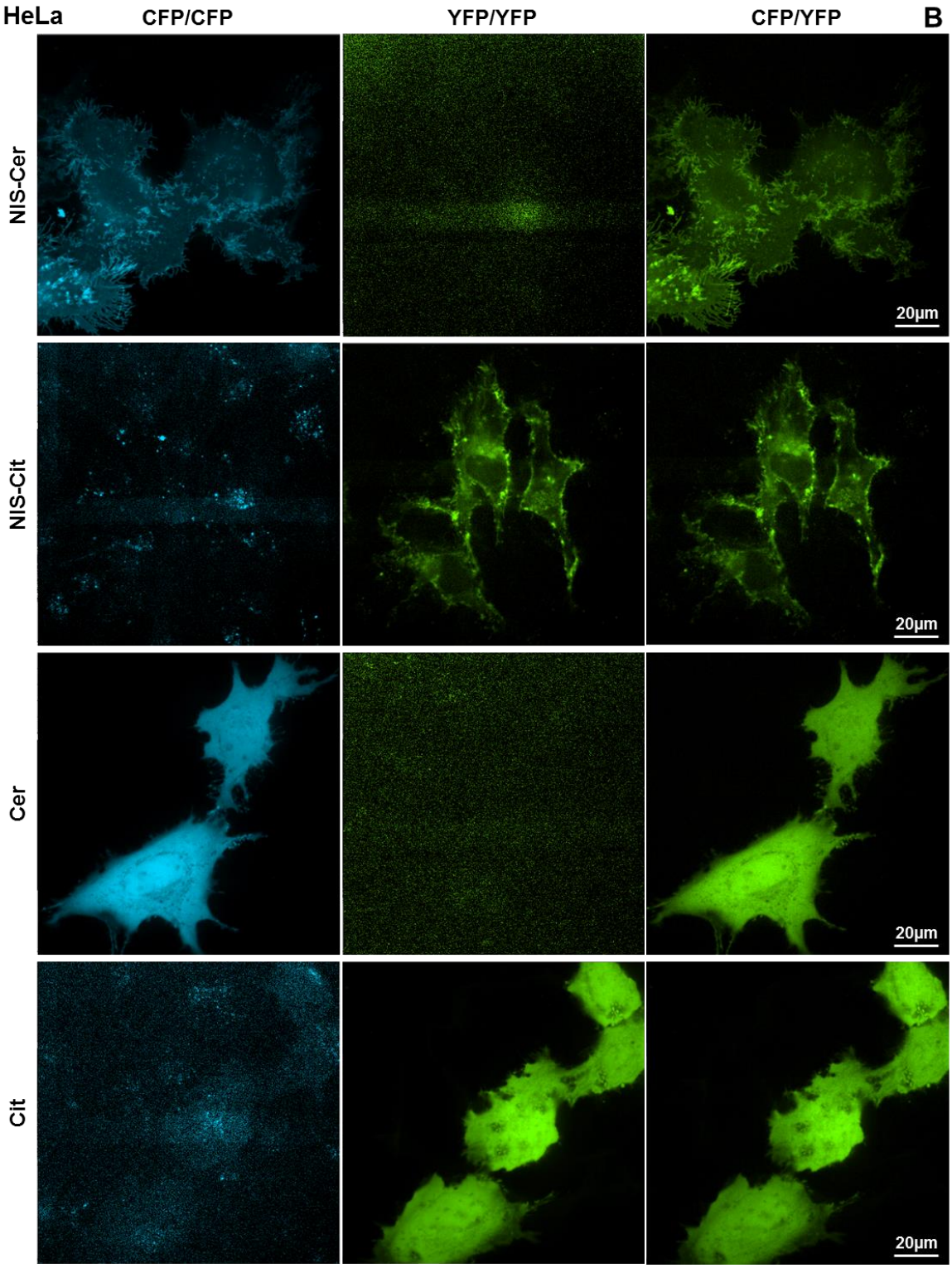

3.3.4.2 FRET analysis demonstrated very close proximity between differentially-tagged NIS-fluorophore variants, which further supports dimerisation

To quantitatively evaluate whether NIS dimerisation occurs, the two NIS-fluorophore constructs were co-expressed in both cell lines and FRET analysis was performed. For comparison, FRET analysis was also carried out on cells expressing both fluorophores alone as a negative control, and on cells expressing either the Linker or the cAMP-sensing FRET probe Epac2 as positive controls for FRET. One-way ANOVA with Tukey's multiple comparison tests were perform to identify any significant changes.

Figure 3-10 illustrates a representative set of images required to perform FRET analysis on each condition, while Figure 3-11 shows the results of this analysis. Due to the data analysis process, corrected FRET data is presented as arbitrary units. Extremely high signal observed with the Linker positive control in both cell lines (Figure 3-11A (9670.63±1060.41 (arbitrary units) in SW1736; 8773.50±2879.65 in HeLa)). As the Linker signal overpowered the other conditions, it was removed in Figure 3-11B to reveal the significant differences between the other conditions. In both cell lines, co-expression of the NIS-fluorophore constructs (NIS-CerCit) resulted in a significant increase in corrected FRET signal compared to the negative control cells (CerCit) expressing both free fluorophores (SW1736: 430.62±32.74 (NIS-CerCit) vs. -882.00±88.16 (CerCit); HeLa: 357.60±33.50 (NIS-CerCit) vs. -380.54±134.00 (CerCit)). This showed that the fluorophores were only able to undergo FRET when they were conjugated to NIS, signifying that the two NIS monomers were in close enough proximity to dimerise. The positive control Epac2 gave significantly greater corrected FRET signal compared to CerCit and NIS-CerCit (975.88±148.15 (SW1736) and 1502.30±170.76 (HeLa)), suggesting that FRET is more efficient with Epac2 than NIS-CerCit for reasons such as differences in the fluorophore ratios between the two conditions.

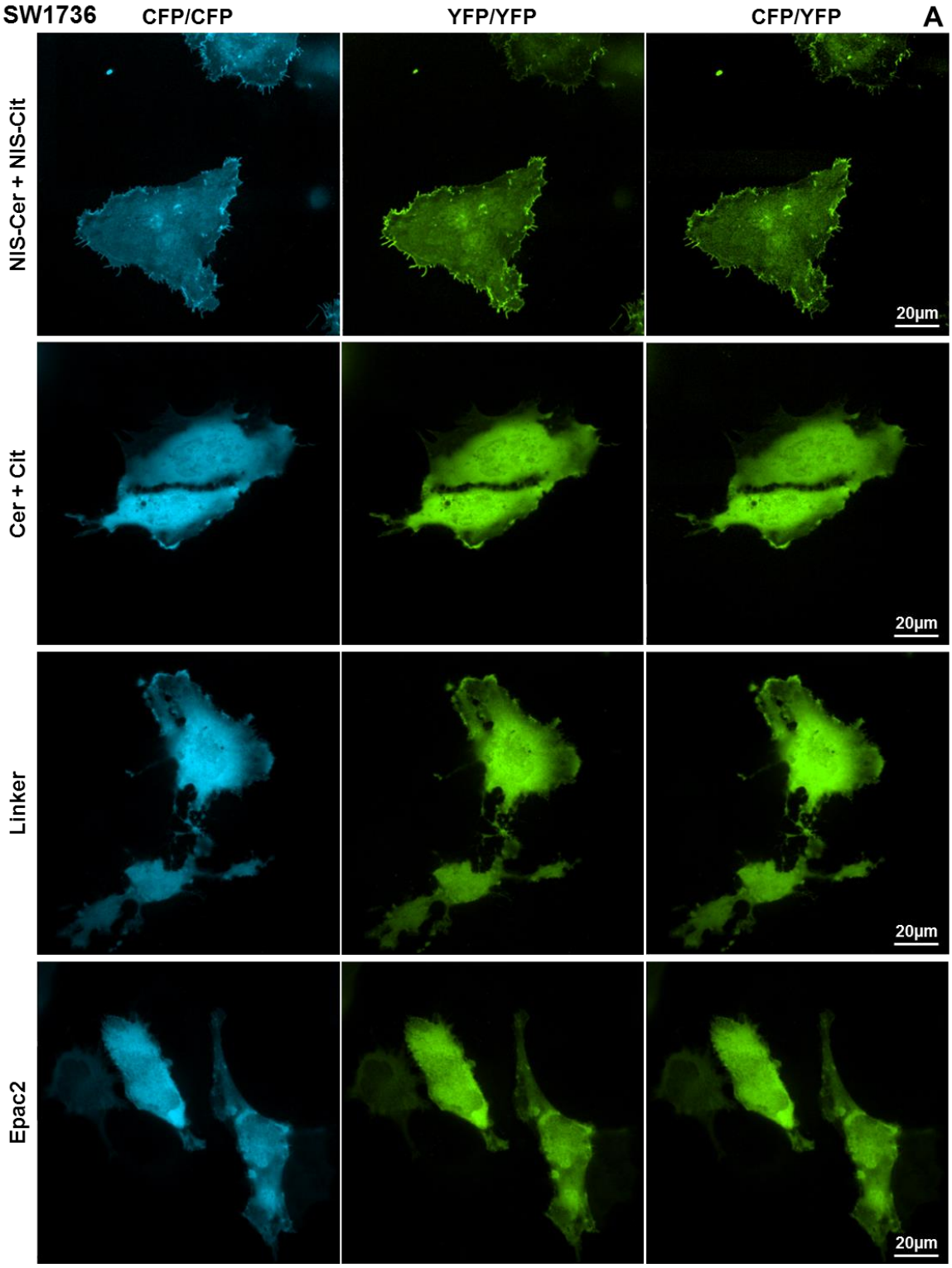

Figure 3-10 – A representation of the series of images captured during the investigation of NIS dimerisation using FRET. SW1736 (A) and HeLa (B, overleaf) cells were transfected with NIS-Cerulean + NIS-Citrine (top panel), Cerulean + Citrine (middle-top panel, negative control), Linker (middle-bottom panel, positive control) or Epac2 (bottom panel, positive control). Three concurrent versions of each image were taken: total Cerulean (CFP) image (Cerulean excitation/Cerulean emission (CFP/CFP)), total Citrine (YFP) image (Citrine excitation/Citrine emission (YFP/YFP)) and the FRET image (Cerulean excitation/YFP emission (CFP/YFP)).

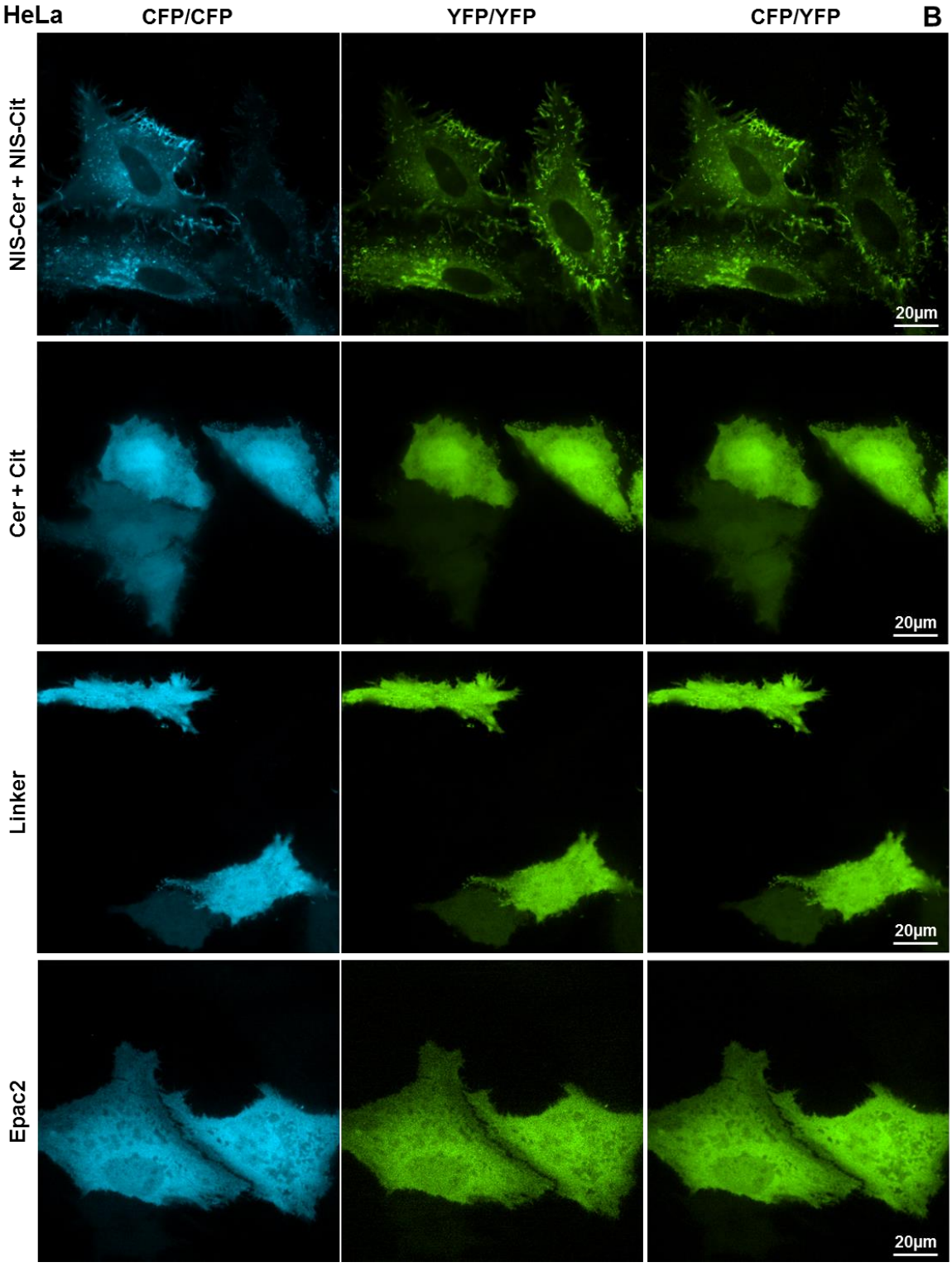
HeLa
CFP/CFP
YFP/YFP
CFP/YFP
B
NIS-Cer + NIS-Cit
Cer + Cit
Linker
Epac2
20µm
20µm
20µm
20µm

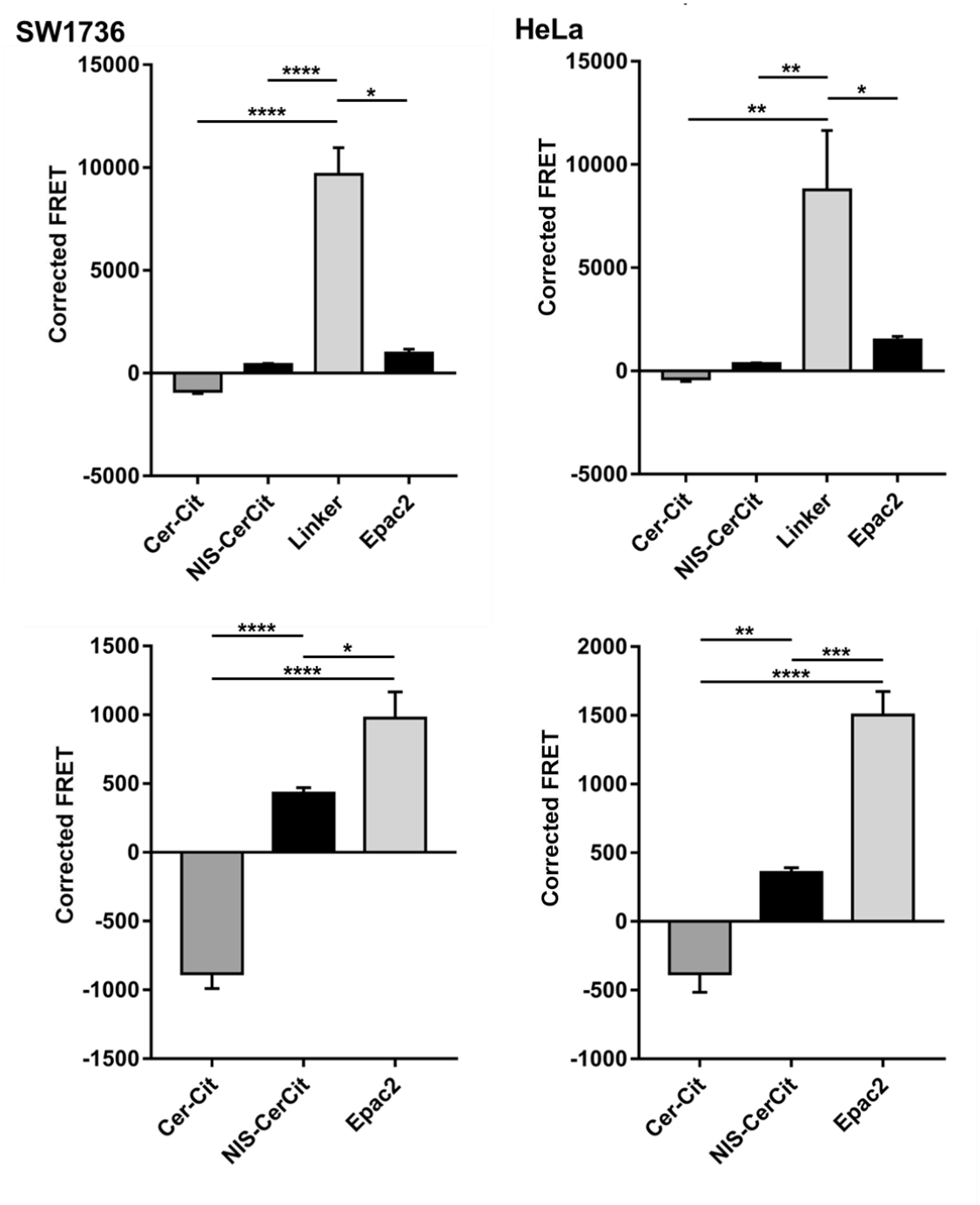

Figure 3-11 – Data analysis reveals a significant increase in FRET, which is indicative of NIS dimerisation. FRET analysis was performed on the corresponding images of SW1736 (left) and HeLa (right) cells transfected with Cerulean + Citrine (CerCit, negative control), NIS-Cerulean + NIS-Citrine (NIS-CerCit), Linker (positive control) or Epac2 (positive control). Linker gives a much larger corrected FRET signal compared to any other condition (top panels). Removing Linker data reveals the differences in the remaining conditions (bottom panels). Co-expression of both NIS-fluorophore constructs gave significantly greater corrected FRET signal compared to the negative control, demonstrating a very close proximity between the two fluorophores which is indicative of dimerisation. Epac2 also gives a significantly larger corrected FRET signal compared to both CerCit and NIS-CerCit. Bars show mean corrected FRET signal in arbitrary units and error bars show SEM. One-way ANOVA with Tukey's multiple comparison statistical tests were performed: * = p<0.05, ** = p<0.01, *** = p<0.005, **** = p<0.001. (n=5 with 10 cells in each n).

3.3.4.3 Linear analysis of FRET revealed that NIS dimerisation occurs throughout the cell

To elucidate the subcellular location of NIS dimerisation, corrected FRET analysis was performed on linear sections across SW1736 and HeLa cells co-transfected with NIS-Cerulean and NIS-Citrine and plotted against its distance along the line.

Figure 3-12 illustrates that FRET signal was distributed evenly across the width of the cells. Rapid spiking of peaks and troughs in the FRET signal may reflect vesicles of NIS being trafficking through the cell, possibly suggesting that NIS may be trafficking as a dimer.

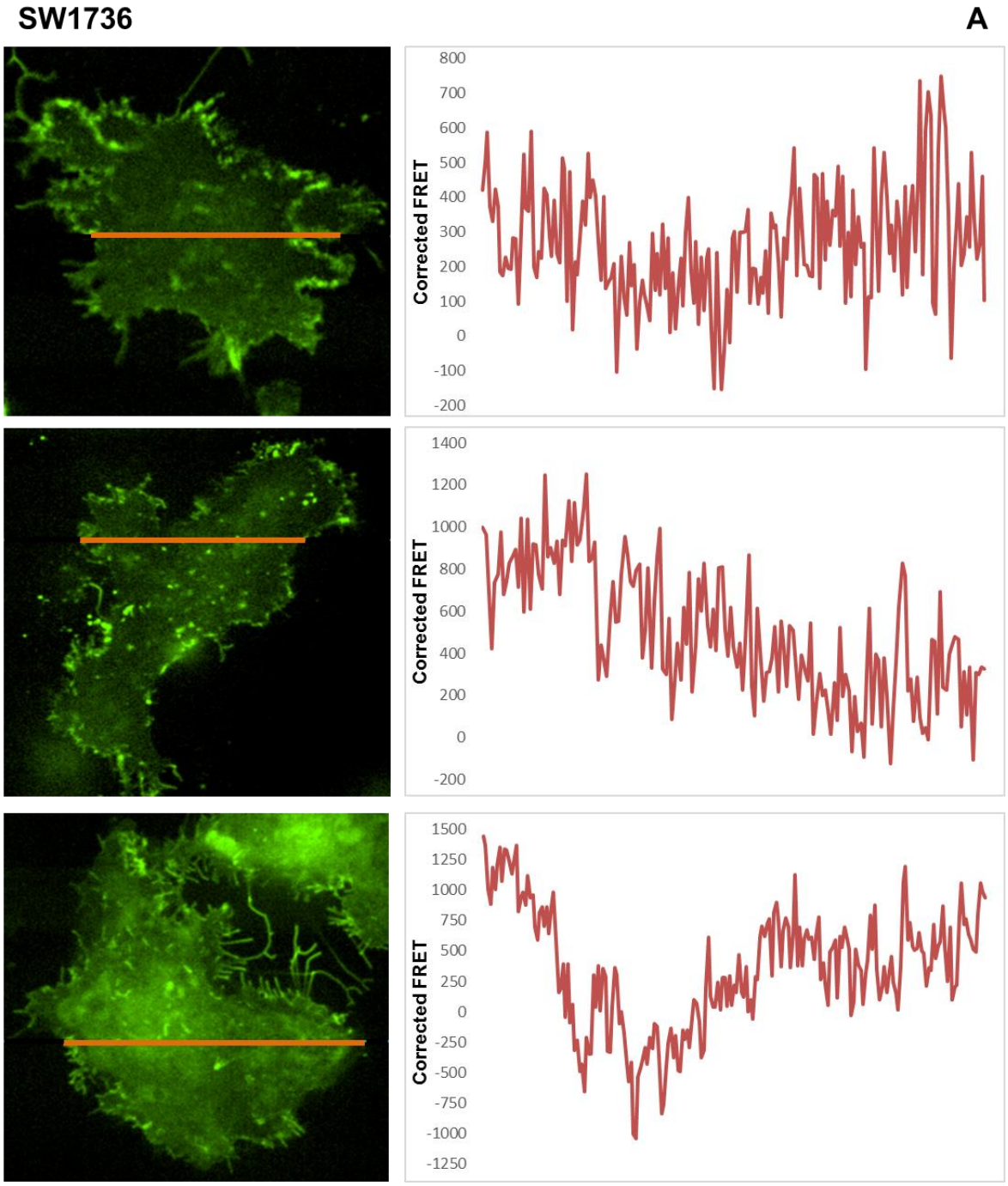

Figure 3-12 – NIS dimerisation occurs throughout the cell. SW1736 (A) and HeLa (B, overleaf) cells were transfected with NIS-Cerulean + NIS-Citrine and FRET analysis was performed on linear sections across the cell (image). Graphs depict the corrected FRET signal across the lines, suggesting that NIS dimerisation occurs throughout the cell. (n=5).

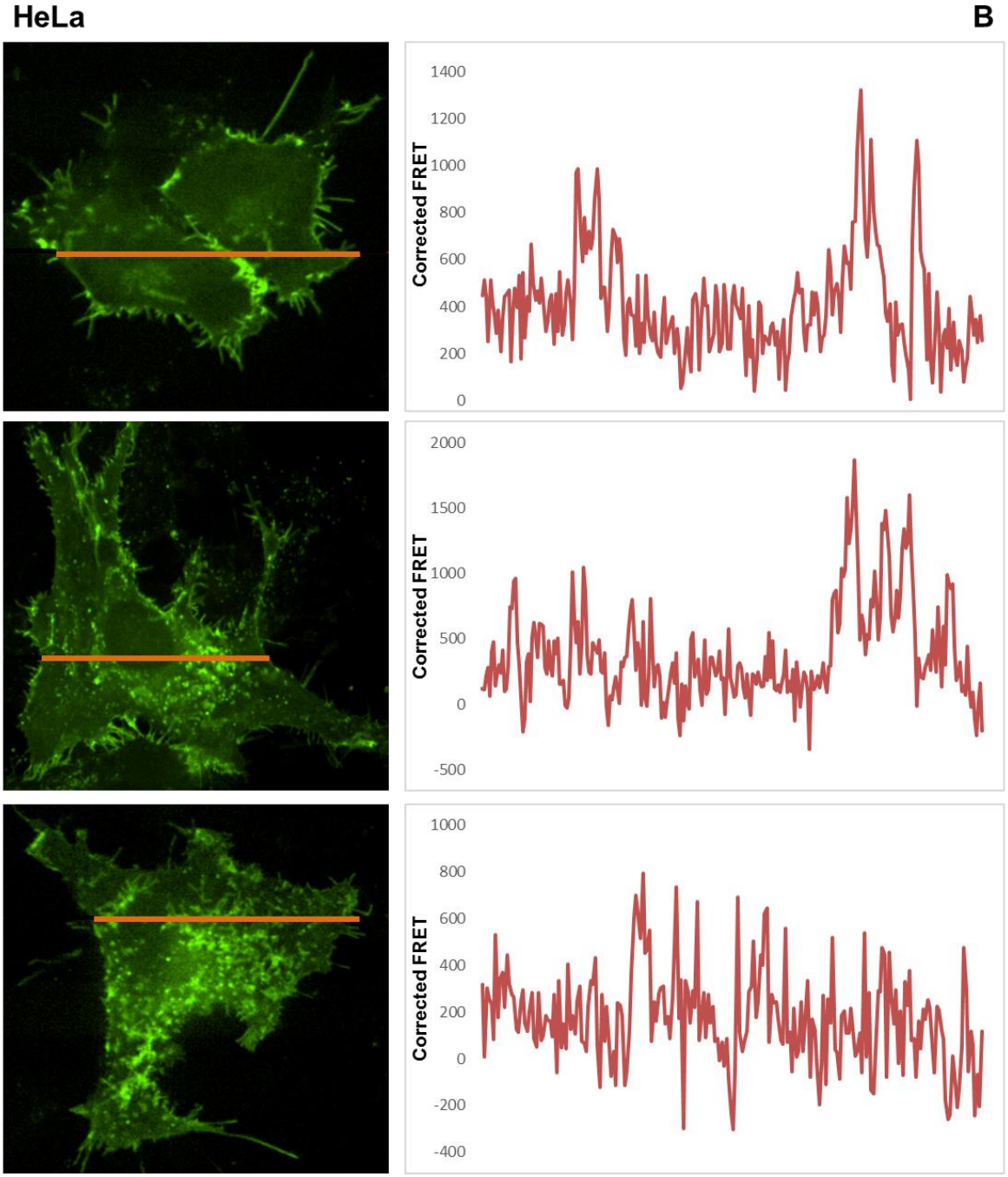
HeLa
B
Corrected FRET
1400
1200
1000
800
600
400
200
0
Corrected FRET
2000
1500
1000
500
0
-500
Corrected FRET
1000
800
600
400
200
0
-200
-400

3.4 Discussion

Prior to investigating whether dimerisation was important for NIS function, it was necessary to first show conclusively that NIS dimerisation could be detected. The aim of the current chapter was to determine whether NIS dimerisation could be observed with both qualitative and quantitative techniques using protein lysates and the whole cell. Together, the results presented in this chapter strongly support the hypothesis that NIS dimerisation occurs.

3.4.1 NIS dimerisation was strongly suggested to occur using qualitative techniques

PLA can be used to detect protein-protein interactions by identifying when two proteins are within 40nm of each other (Sigma-Aldrich, 2018b) and has previously been used to investigate protein dimerisation (Gajadhar and Guha, 2010, Gomes et al., 2016, Bart et al., 2015). In these studies, observation of PLA signal in SW1736 and HeLa cells co-transfected with NIS-MYC and NIS-HA demonstrates that the two NIS variants are in close enough proximity to dimerise. As this PLA signal was similar to that observed with the positive control, differentially-tagged MCT8 variants, this further supported the notion that PLA signal in these experiments was indicative of dimerisation. MCT8 was chosen as a positive control as it has been extensively shown to dimerise (Visser et al., 2009, Fischer et al., 2015). While many proteins are known to dimerise, MCT8 was selected because of its similarities to the NIS protein. MCT8 is also a membrane protein with 12 TMDs and a molecular weight of 61kDa (Visser et al., 2009), which is comparable to that of NIS. Furthermore, MCT8 is also expressed in thyroid follicular cells, where it is responsible for the release of THs from the follicle (Visser et al., 2011), so is likely to experience similar protein trafficking mechanisms to NIS.

Although PLA signal was observed throughout the cell, there were areas of colocalisation between PLA signal and the plasma membrane marker, indicating that NIS dimerisation occurs throughout the cell, including at the membrane, and suggesting dimerisation could be important for the trafficking of NIS. However, it remains unclear from these studies how this may occur. Further studies involving treatment with an endocytosis inhibitor prior to PLA analysis may help elucidate whether NIS dimerisation occurs during trafficking and if it is required for expression at the membrane, or whether NIS dimerisation occurs at the membrane and is internalised as dimers. In such studies, intracellular PLA signal would still be observed in the former, but not the latter situation due to the inhibition of endocytosis.

While PLA is widely used to detect protein interactions, this is solely based on their proximity and does not demonstrate a direct interaction, so PLA alone merely suggests that NIS dimerisation occurs. Consequently, a method to detect direct protein interactions was sought. As co-IP is frequently used to investigate protein dimerisation (Angers et al., 2000, Salim et al., 2002), it was utilised here to further investigate whether NIS dimerisation occurs by examining if differentially-tagged NIS variants directly interact. These data show the presence of a ~150kDa band only when co-IP was performed on cells co-expressing both NIS variants, and was not observed in any negative control. This is an appropriately sized band for a NIS dimer, given that the immature and mature NIS monomers are ~69kDa and ~87kDa, respectively (Smanik et al., 1996, Levy et al., 1998a). Furthermore, this band was observed in both cell lines and in both orientations of co-IP, thus providing additional evidence to support that this band was representative of NIS dimerisation.

Although co-IP demonstrated a direct interaction between NIS-MYC and NIS-HA which was indicative of dimerisation, co-IP does not provide any information on the subcellular localisation of NIS dimerisation as it is performed on protein lysates. However, in order to

potentially determine whether NIS dimerisation occurs at the membrane, an additional step to isolate the plasma membrane prior to conducting the co-IP could be used to investigate this further, although this is a complex experiment and is likely to be difficult to achieve.

3.4.2 NIS can tolerate conjugation to fluorophores at the C-terminus, but not the N-terminus

The results from PLA and co-IP studies suggest strongly that NIS dimerisation does occur. However, these techniques do not readily allow quantitative detection of NIS dimerisation, which would be required to assess the effect of mutations on NIS dimerisation (discussed in subsequent chapters). FRET is a frequently employed method for quantitatively evaluating protein interactions (Bart et al., 2015, Sarabipour et al., 2015, Boyer and Slesinger, 2010), but in order to use FRET in these studies, suitable NIS constructs were required. As the fluorophores Cerulean and Citrine are improved variants of CFP (Rizzo et al., 2004) and YFP (Griesbeck et al., 2001), respectively, which are commonly paired for FRET studies (Day and Davidson, 2009), novel constructs conjugating NIS to one of these fluorophores at the N- or C-terminus were created by using PCR cloning methods.

Prior to their use in FRET studies, the novel NIS-fluorophore constructs required extensive characterisation to ensure that the fluorophore did not affect NIS expression, localisation or function. To do this, results from these NIS-fluorophore constructs were compared to that of the existing NIS constructs conjugating NIS at the C terminus to the MYC or HA tag, which have been previously demonstrated not to impede NIS expression or function (Smith et al., 2009). The studies conducted here revealed that tagging NIS at the C-terminus with either fluorophore did not alter protein maturation or trafficking to the membrane, hence NIS function was retained. Conversely, these studies established that tagging NIS at the N-

terminus with either fluorophore resulted in the production of a protein which could not undergo the full maturation process nor be expressed at the plasma membrane, thus rendering NIS non-functional. It is likely that this was caused by the large fluorophore obstructing normal protein trafficking machinery, and so these constructs were abandoned.

3.4.3 A FRET-based method was developed which quantitatively established that NIS dimerisation occurs throughout the cell

Given that NIS constructs conjugated at the C-terminus to Cerulean or Citrine were validated as functional, FRET could be utilised to quantitatively assess NIS dimerisation. For FRET to occur, there must be spectral overlap between the fluorophore pair used (here, Cerulean (CFP) and Citrine (YFP)), but this results in crosstalk of each fluorophore into the FRET channel, as a percentage of Cerulean emission is detected by the YFP emission detection filter (termed CFP crosstalk, see Figure 1-17), while a percentage of Citrine is excited directly by the CFP excitation filter (YFP crosstalk, see Figure 1-17). This crosstalk must be corrected for during the data analysis to obtain a true measure of protein interaction (Piston and Kremers, 2007, Lamond, 2014, Stanley, 2003). The amount of crosstalk is based on the fluorophore itself and the excitation and emission filters used in the experimental setup and so the crosstalk values calculated here for Cerulean and Citrine were different to each other, but was similar between the cell lines and the presence/absence of NIS for each fluorophore.

With the crosstalk for each fluorophore determined, this could be corrected for during FRET data analysis, enabling NIS dimerisation to be quantitatively assessed. FRET signal was significantly higher in both cell lines expressing NIS-Cerulean + NIS-Citrine compared to those expressing Cerulean + Citrine, which was used as a negative control. This is because although these cells express both fluorophores, the two fluorophores must be within 10nm of

each other in order for FRET to occur (Piston and Kremers, 2007, Stanley, 2003). It is extremely unlikely that free fluorophores within the cell will be close enough to participate in FRET, hence this is a useful negative control as it highlights that FRET only occurs between these two fluorophores if they are conjugated to NIS to bring them together.

Positive controls were also used to compare the efficiency of NIS dimerisation to that of plasmids which express both fluorophores linked together (Linker and Epac2) and therefore in close enough proximity to undergo FRET. Both plasmids gave significantly greater FRET signal compared to NIS; however, this is not unexpected. The Linker encodes both fluorophores separated by a very short linker of just 10 amino acids; therefore, this will achieve a maximal FRET which is not biologically relevant. In Epac2, a cAMP-sensing FRET probe, the two fluorophores are conjugated to exchange protein directly activated by cAMP isoform 2 (Epac2), a cAMP binding protein involved in mediating the effects of cAMP signalling (Nikolaev et al., 2004). Epac2 is approximately 100kDa in size (Ster et al., 2007), which would separate the two fluorophores by a more biologically relevant distance than the Linker protein, hence the lower FRET signal of Epac2 compared to the Linker, despite also being a positive control. Although there was a significantly higher FRET signal with the Epac2 positive control compared to NIS despite the two proteins being of a similar size, this does not detract from the conclusion that this FRET signal is indicative of NIS dimerisation as there are several explanations for this. Firstly, with the NIS-fluorophore constructs, the fluorophores are expressed at the end of the long, intracellular C-terminus, which is intrinsically unstructured within the cytoplasm. Consequently, it is likely that while the two constructs are dimerised, the two fluorophores could be greater than 10nm apart and consequently unable to undergo FRET. Similarly, fluorophores must be parallel to each other for FRET to occur (Broussard et al., 2013), so it is also likely that the two fluorophores of

dimerised constructs may not be in the correct orientation to undergo FRET due to the unstructured nature of the NIS C-terminus. Furthermore, with Epac2, both fluorophores are expressed in a 1:1 stoichiometry within close enough distance to undergo FRET as a pair, but in these studies, the NIS-fluorophore constructs were in separate plasmids which had to be co-transfected into cells. Consequently, it is highly unlikely that both plasmids will transfect equally into every cell, resulting in deviation from the ideal 1:1 ratio between the two fluorophores, which will negatively affect the FRET signal (Stanley, 2003, Piston and Kremers, 2007). Additionally, FRET signal is only achieved when the NIS-fluorophore constructs heterodimerise, but there would also be homodimerisation of these constructs. This cannot be detected as FRET would not occur under these circumstances but may reduce the overall signal achieved here.

Since this FRET methodology was able to detect NIS dimerisation, additional analysis was performed to investigate where NIS dimerisation could be observed within the cell. Depiction of the corrected FRET signal across linear sections of the cell revealed that NIS dimerisation is present across the width of the cell, including at the plasma membrane, suggesting that NIS dimerisation occurs throughout the cell. Interestingly, the rapid spiking between peaks and troughs in the signal could be detecting NIS dimerisation within vesicles trafficking NIS to and from the plasma membrane. This suggests that NIS dimerisation may occur during the protein trafficking pathway and that NIS could be transported as dimers, indicating that dimerisation might be important for trafficking to the plasma membrane, in a similar way to GPCRs (Milligan, 2010). This would impact on NIS function, as it can only function at the plasma membrane, so events which alter NIS trafficking to the membrane would subsequently affect function. As the PLA data also depicted NIS dimerisation distributed throughout the cell, this adds further support to this hypothesis; however, further

work is required in order to confirm this. Similar to the PLA, FRET analysis on cells treated with endocytosis inhibitor may also be useful here. An alternative way to more conclusively investigate this would be to mutate residues important for NIS dimerisation and analyse the effect on NIS expression, localisation and function. However, it is not yet known which residues are involved in NIS dimerisation. Consequently, the subsequent chapters aimed to identify the residues involved in NIS dimerisation and evaluate how disrupting dimerisation through mutation of these residues impacted on NIS expression, localisation and function.

3.4.4 Concluding statements

The data presented in this chapter all demonstrate an interaction between differentially-tagged variants of NIS, which supports the hypothesis that NIS does dimerise. However, the implications of dimerisation for NIS function are yet to be determined. Consequently, it was of great interest to try to abrogate dimerisation through mutagenesis in order to potentially establish the effect dimerisation has on NIS function.

CHAPTER 4 – ASSESSING THE ABILITY OF PUTATIVE DIMERISATION MOTIFS TO DIMERISE

4.1 Introduction

The studies performed in Chapter 3 indicated that wild-type NIS dimerisation does occur. However, to investigate whether dimerisation is important for NIS function, it was imperative to be able to abrogate NIS dimerisation. Two putative dimerisation motifs have been proposed in the literature based on analysis of the NIS primary sequence: a glycine zipper motif (GZM) and a leucine zipper motif (LZM). Despite this, neither motif has been experimentally studied in NIS, so their function remains unknown.

4.1.1 Glycine zipper motif

The glycine zipper motif (GZM, alternatively known as GG_4 or GXXXG) is a well-known dimerisation motif consisting of two glycine residues separated by three non-specific residues. GZMs can often be extended to three glycine residues, or in the case of GZ-like motifs, one or more of the glycine residues can be substituted for another small residue, such as alanine. As the glycine (or similar) residues are spaced at every fourth position, they are located on the same surface of the helix, and the small size of the side chains exposes the amide and carbonyl atoms of the residue backbones. This strongly drives two or more helices to tightly pack together in a predominantly right-handed helical bundle, resulting in dimerisation (as illustrated in Figure 4-1). Interestingly, GZMs arise far more frequently in TM helices than would be expected by chance and are strongly conserved, which is highly indicative of a significant role for this motif in the structure of membrane proteins (Kim et al., 2005, Russ and Engelman, 2000).

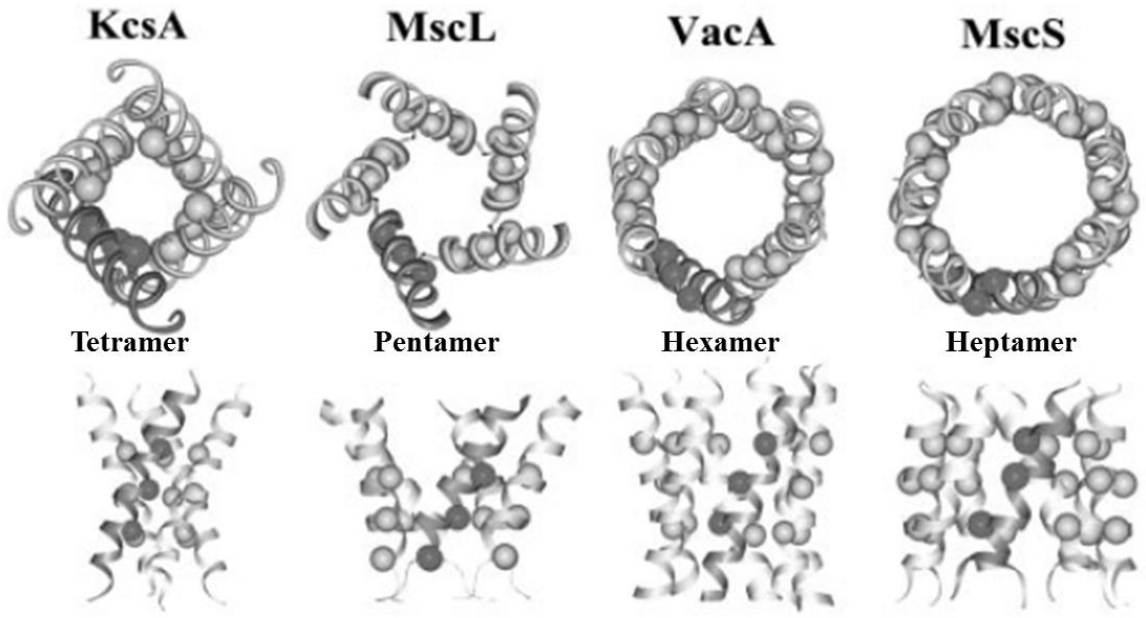

Figure 4-1 – The oligomerisation of channel proteins using glycine zipper motifs. The transmembrane domains of the potassium channel pore-lining helices (KcsA), mechanosensitive channel of large conductance (MscL), vacuolating toxin A anion selective channel (VacA) and mechanosensitive channel of small conductance (MscS) all oligomerise to form tetramers, pentamers, hexamers or heptamers, respectively. This is mediated by the packing together of glycine zipper motifs in the transmembrane helices (the three circles represent the glycine residues of the motif), which forms right-handed helical bundles, as highlighted by the orientation of the darker grey motif. Image adapted from Kim et al., 2005.

4.1.1.1 NIS and the glycine zipper motif

Another member of the SLC5A protein family, the high-affinity choline transporter (CHT1), has been demonstrated to dimerise. The authors proposed that this dimerisation may be mediated by a GZM within TMD 12 as this motif is highly conserved in members of the SLC5A family (Okuda et al., 2012), including NIS, where the putative GZM is comprised of glycine residues at positions 444 and 448 (see section 9.2). Consequently, this was identified as a key motif of interest for these studies into the effect of dimerisation on NIS function.

4.1.2 Leucine zipper motif

Another motif widely regarded as a dimerisation motif is the leucine zipper motif (LZM). Figure 4-2A illustrates that LZMs are comprised of a repeated leucine residue at every seventh position of an α helix (i.e. at position d, where the standard nomenclature for a seven

residue repeat sequence is *a*, *b*, *c*, *d*, *e*, *f* and *g*) for at least four leucine residues. In addition, residues at position *a* are also hydrophobic, while charged residues are often found at positions *e* and *g*. This forms a helix with hydrophobic face, comprised of residues at positions *a* and *d*. The hydrophobic faces of two α helices are able to pack together to form a hydrophobic core (as in Figure 4-2B) and then wind around each other in a predominantly left-handed parallel coiled-coil structure, thereby facilitating dimerisation (Krylov and Vinson, 2001, Hakoshima, 2005).

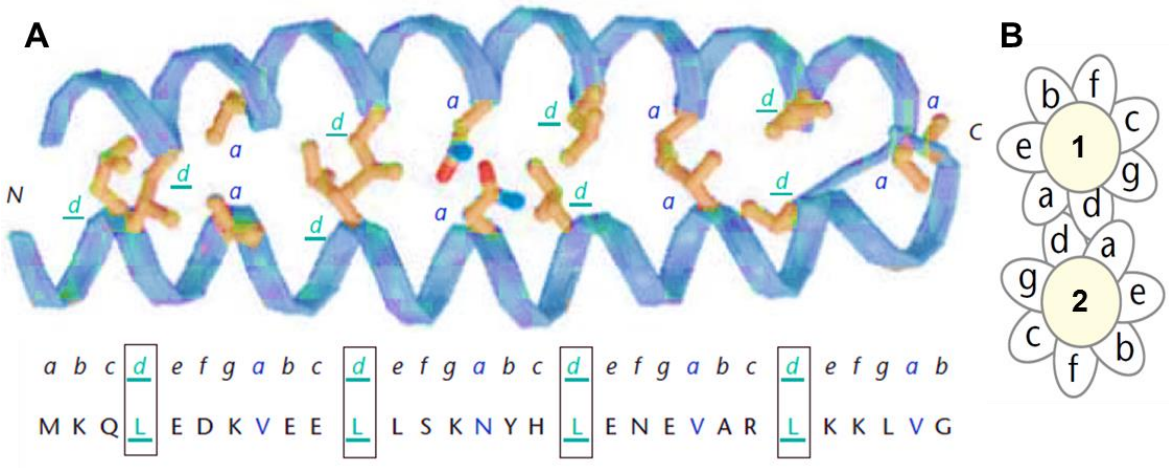

Figure 4-2 – Schematic of dimerisation via the leucine zipper motif. The side view of the motif in the yeast gene regulatory protein GCN4 is shown in A, with the backbone of the helices in blue and the residues identified below in the single-letter amino acid code and their positions within the seven-residue repeat are indicated (*a*-*g*). Side chains of residues involved in dimerisation (i.e. at positions *a* and *d*) shown as stick models, with carbon atoms in yellow, nitrogen atoms in blue and oxygen atoms in red. Leucine residues at position *d* are boxed, underlined and in green, while the residues at position *a* are shown in dark blue. These residues are generally hydrophobic; however the GCN4 leucine zipper motif has one polar asparagine residue at position *a*, which is uncommon. An end view of the motif is shown in B, demonstrating how the residues at positions *a* and *d* pack together to form a hydrophobic core. Images taken from Hakoshima, 2005 (A) and Krylov and Vinson, 2001 (B).

4.1.2.1 NIS and the leucine zipper motif

During the cloning of rat NIS in 1996, a putative LZM was observed, which led the authors to propose a role for this motif in NIS dimerisation (Dai et al., 1996). Cloning of human NIS revealed that this putative LZM was conserved in the human protein within TMD 6 (Smanik et al., 1996), comprised of leucine residues at positions 199, 206, 212 and 220 (see section 9.2). Consequently, this was also identified as a key motif of interest for these studies.

As NIS dimerisation was demonstrated to occur in Chapter 3 and putative dimerisation motifs have been proposed in the literature, the purpose of the current chapter was to determine if mutating either of these putative dimerisation motifs impairs NIS dimerisation, with the ultimate aim of investigating whether dimerisation is important for NIS function.

4.2 Methods

All methods used in this chapter are detailed in Chapter 2.

4.3 Results

To investigate whether putative dimerisation motifs are important for NIS dimerisation to occur, site-directed mutagenesis was performed to generate mutants of the motifs. To disrupt the GZM, both glycine residues were mutated to valine to add a branched side chain in place of the gaps created by glycine. Due to the large size of the LZM, two mutants were made. In the partial LZM mutant, LZM1, the first two leucine residues were mutated to alanine to remove the interactions mediated by the leucine side chains, while in the full LZM mutant, LZM2, all four of the leucines residues were mutated to alanine (see section 9.2).

4.3.1 Characterisation of putative dimerisation motif NIS mutants demonstrates the importance of both motifs for NIS function

Prior to investigating the effect of these mutations on NIS dimerisation, the mutants were characterised biochemically to determine whether the mutation altered NIS expression, localisation and function.

4.3.1.1 Mutating putative dimerisation motifs inhibits NIS maturation

To investigate if mutating a putative dimerisation motif affects NIS protein expression, Western blot analysis was performed on lysates of SW1736 and HeLa cells expressing wild-

type (WT) or mutant NIS constructs tagged at the C-terminus with HA using the mouse anti-HA primary antibody.

Figure 4-3 demonstrates the effect of mutating putative dimerisation motifs on NIS protein expression in SW1736 (left) and HeLa (right) cells. WT NIS (lane 2) was expressed in two forms, predominantly as a fully-glycosylated, mature form between 75-100kDa with a minor band at ~60kDa representing an immature, non-glycosylated form. While a similar banding pattern was observed with partial mutation of the LZM (LZM1, lane 4), expression of the mature form of NIS was lost when the LZM was fully mutated (LZM2, lane 5). Alongside a similar loss of expression of the mature form, mutating the GZM (lane 3) seemed to also affect total NIS expression levels, as a much weaker band was observed here. This suggests that both putative dimerisation motifs are important for adequate NIS protein expression.

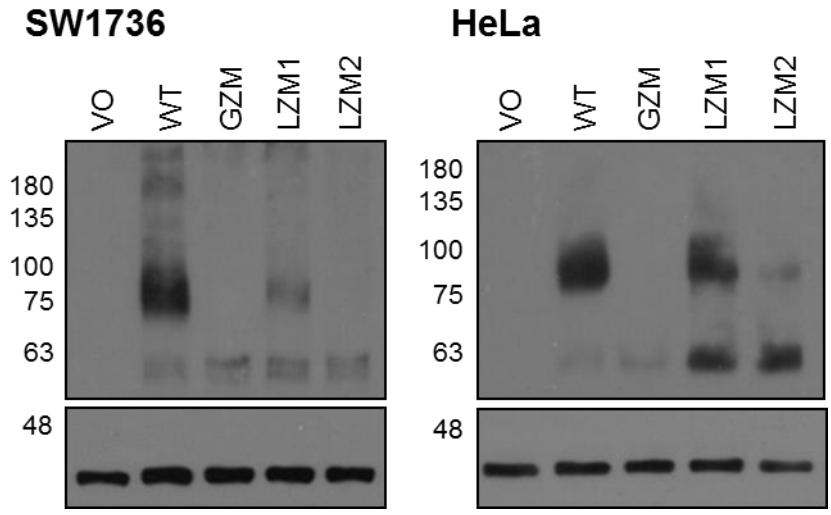

Figure 4-3 – Mutating putative dimerisation motifs prevents glycosylation of NIS. SW1736 (left) and HeLa (right) cells were transfected with empty pcDNA3.1(+) vector (VO (lane 1)), wild-type NIS-HA (WT (lane 2)) or HA-tagged NIS with either a mutated glycine zipper motif (GZM (lane 3)) or a partially or fully mutated leucine zipper motif (LZM1 (lane 4) or LZM2 (lane 5), respectively). Western blot analysis was performed using mouse anti-HA primary antibody. A band at 75-100kDa represents the fully glycosylated, mature form of NIS, while a band at ~60kDa represents the non-glycosylated, immature form of NIS. β-actin primary antibody was used as a loading control. (n=2).

4.3.1.2 NIS localisation at the plasma membrane is prevented by mutating putative dimerisation motifs

Immunofluorescence analysis was performed on SW1736 and HeLa cells expressing WT or mutant NIS constructs tagged at the C-terminus with HA using the mouse anti-HA primary antibody and the rabbit anti-Na^+/K^+-ATPase primary antibody as a plasma membrane marker to determine if mutating a putative dimerisation motif alters NIS subcellular localisation.

The colocalisation (yellow) observed between NIS (green) and the plasma membrane marker (red) represents expression of WT NIS at the membrane in both SW1736 and HeLa cells (Figure 4-4 and Figure 4-5, respectively). NIS with a partial mutation of the LZM (LZM1) could still be expressed at the membrane, but to a lesser extent than WT. However, NIS constructs with a fully mutated LZM (LZM2) or GZM were intracellularly retained. This indicates the importance of both putative dimerisation motifs for appropriate localisation of NIS at the plasma membrane.

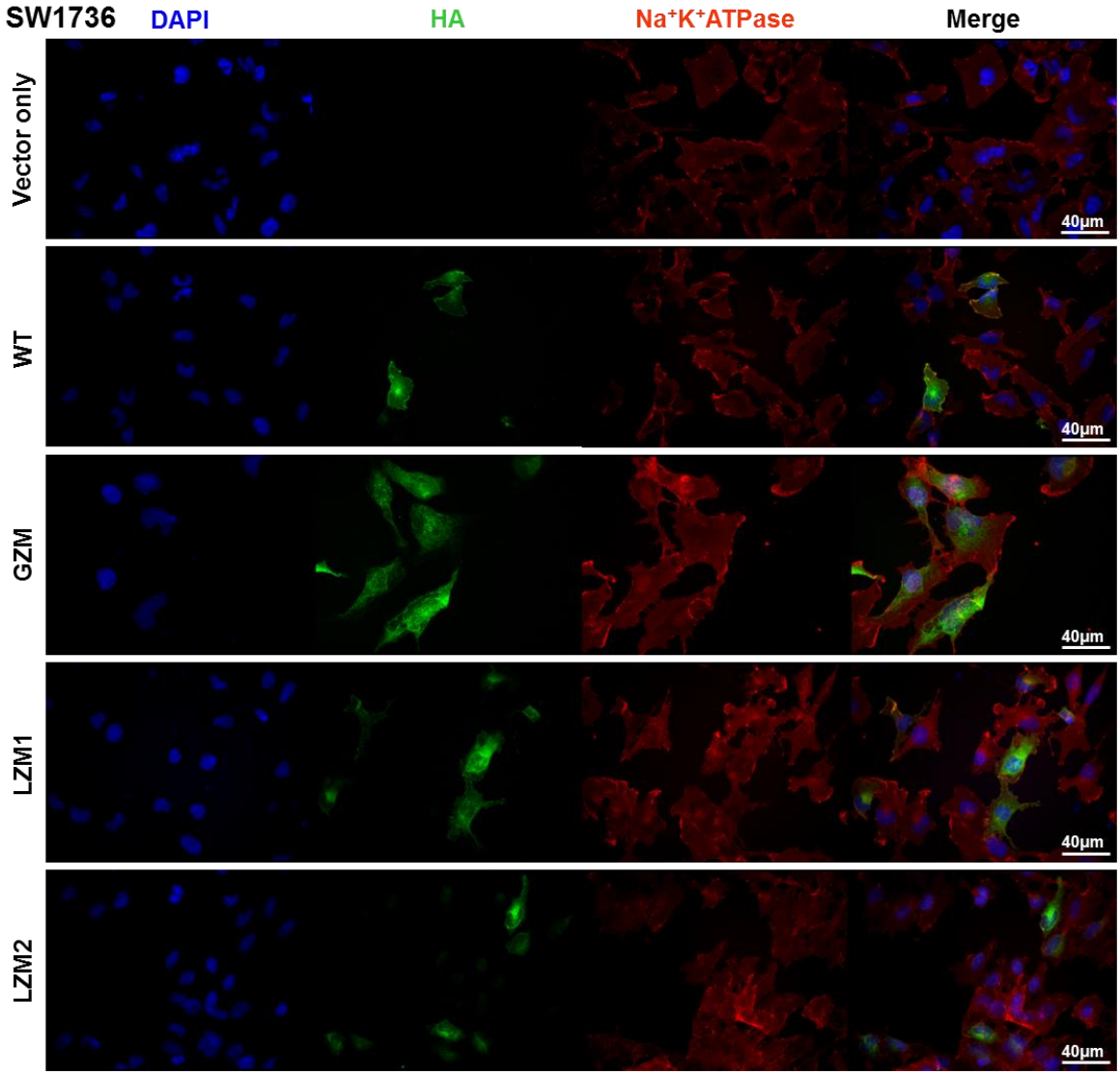

Figure 4-4 – NIS constructs with fully mutated putative dimerisation motifs are intracellularly retained in SW1736 cells. Cells were transfected with empty pcDNA3.1(+) vector (VO), wild-type NIS-HA (WT) or HA-tagged NIS with either a mutated glycine zipper motif (GZM) or a partially or fully mutated leucine zipper motif (LZM1 or LZM2, respectively). Immunofluorescence was performed using mouse anti-HA primary antibody to visualise NIS (in green), while rabbit anti-Na^+/K^+-ATPase primary antibody was used as a plasma membrane marker (in red). Nuclei are visualised in blue using Hoescht stain. Single channels and merged images are shown in A, and enlarged merged images are shown in B (overleaf). 40x magnification. (n=2).

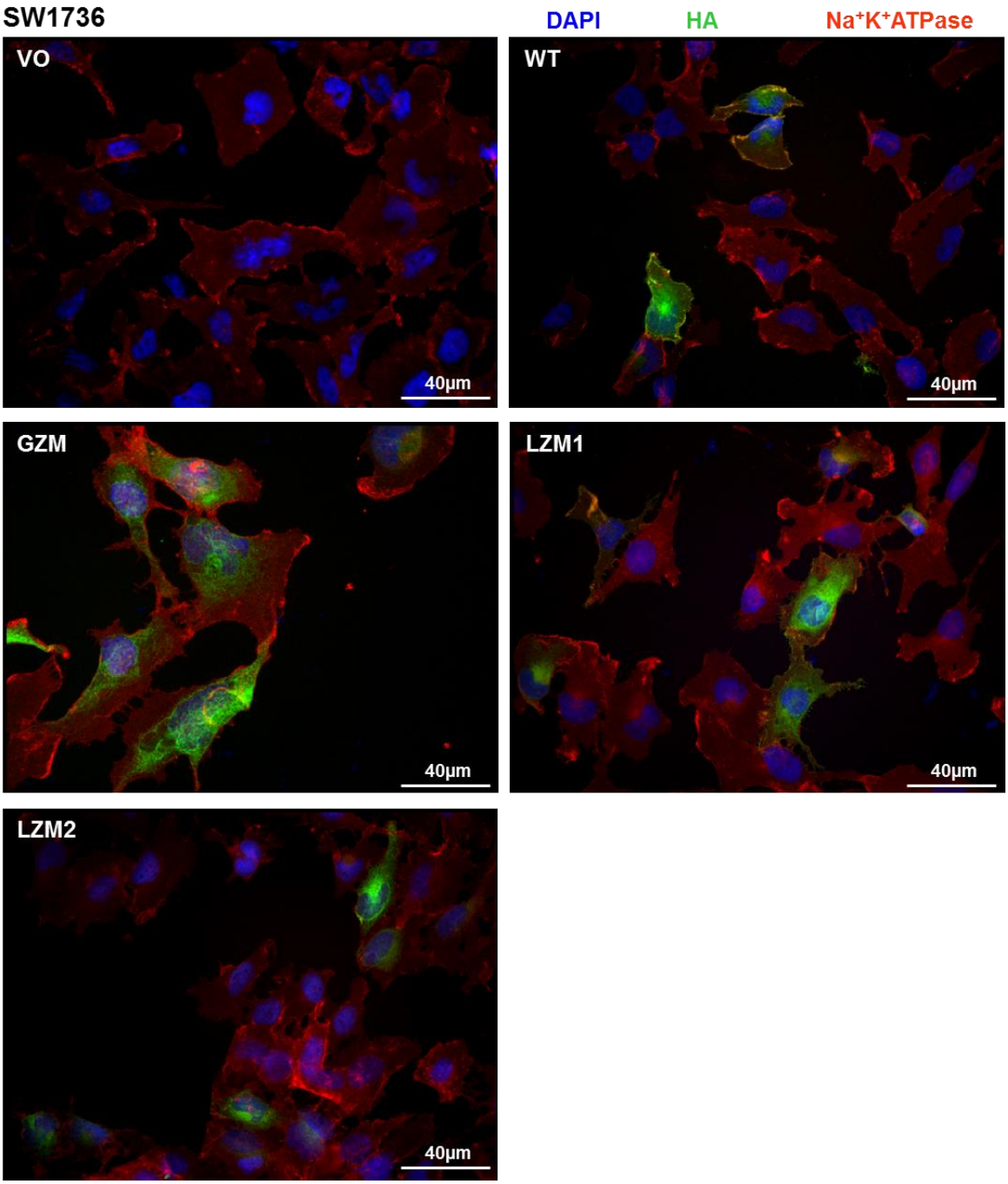
SW1736
DAPI
HA
Na+K+ATPase
VO
WT
GZM
LZM1
LZM2
40µm
40µm
40µm
40µm
40µm

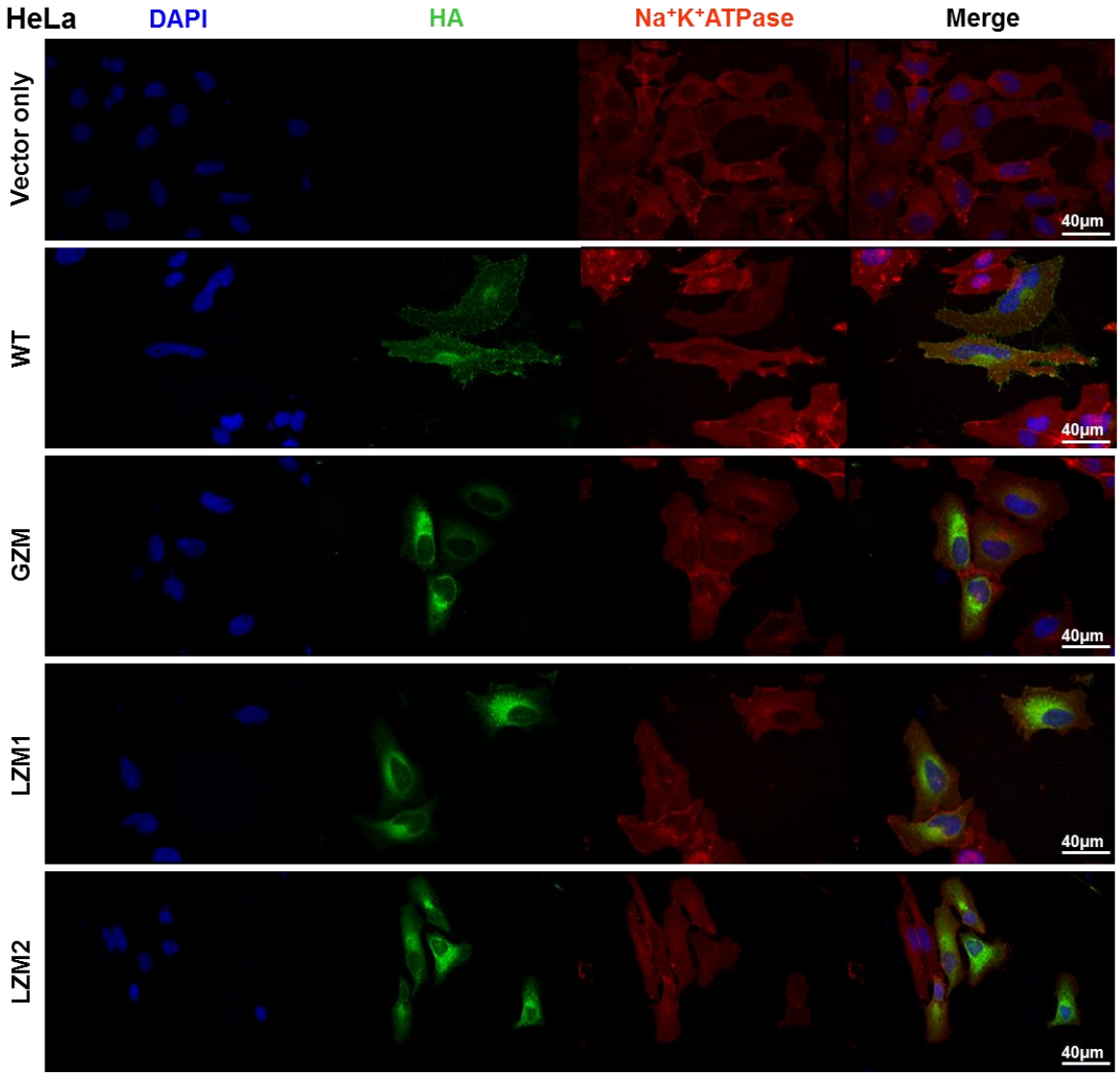

Figure 4-5 – NIS constructs with fully mutated putative dimerisation motifs are intracellularly retained in HeLa cells. Cells were transfected with empty pcDNA3.1(+) vector (VO), wild-type NIS-HA (WT) or HA-tagged NIS with either a mutated glycine zipper motif (GZM) or a partially or fully mutated leucine zipper motif (LZM1 or LZM2, respectively). Immunofluorescence was performed using mouse anti-HA primary antibody to visualise NIS (in green), while rabbit anti-Na^+/K^+-ATPase primary antibody was used as a plasma membrane marker (in red). Nuclei are visualised in blue using Hoescht stain. Single channels and merged images are shown in A, and enlarged merged images are shown in B (overleaf). 40x magnification. (n=2).

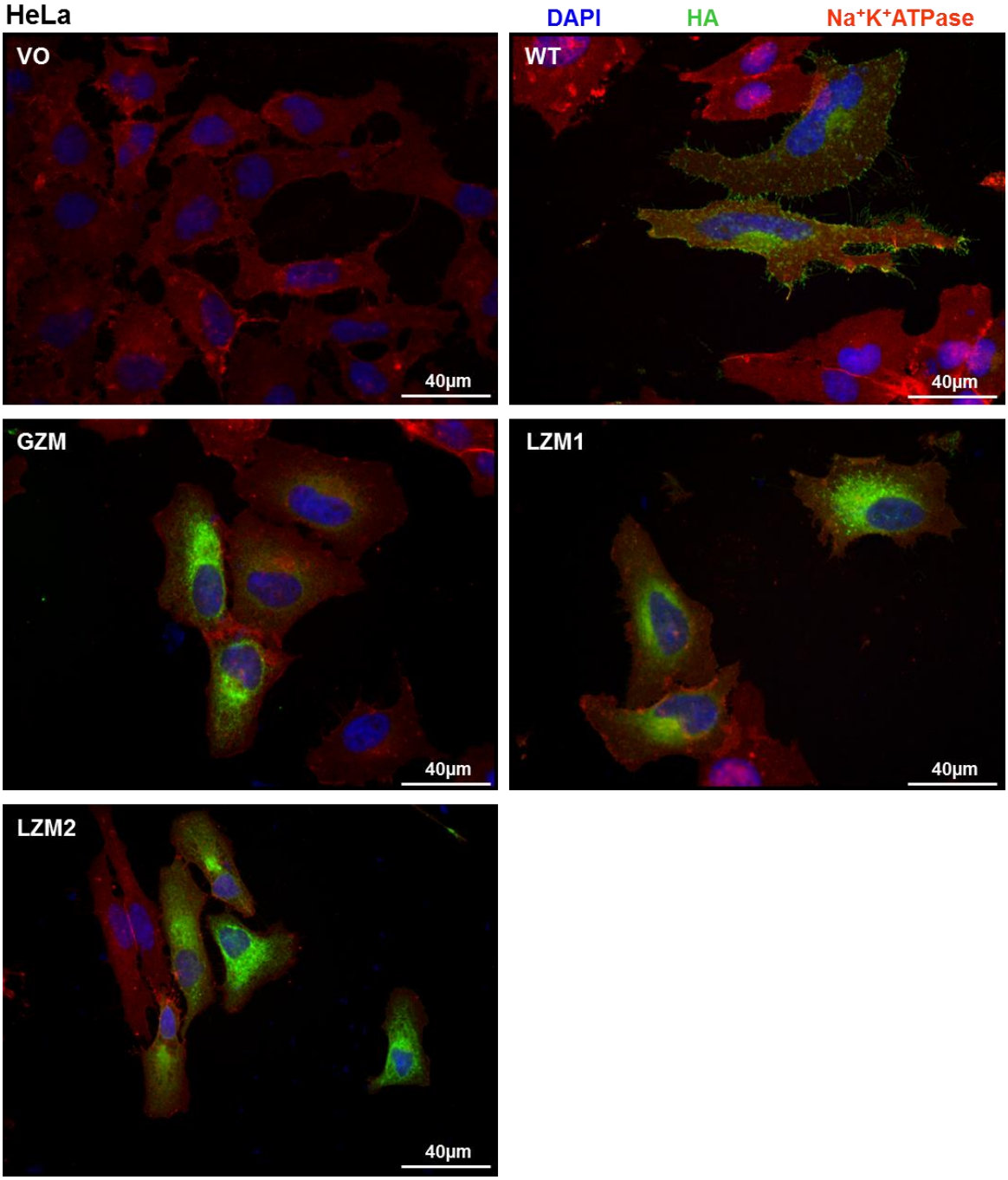
HeLa
DAPI
HA
Na+K+ATPase
VO
WT
GZM
LZM1
LZM2
40µm
40µm
40µm
40µm
40µm

4.3.1.3 Mutation of putative dimerisation motifs abolishes NIS function

To assess if NIS function was affected by mutating a putative dimerisation motif, radioiodide uptake assays were performed on SW1736 and HeLa cells expressing WT or mutant NIS constructs tagged with HA at the C-terminus. One-way ANOVA with Dunnett's multiple comparison tests were performed to identify significant changes in uptake compared to WT.

Figure 4-6 depicts the impact of mutating putative dimerisation motifs on NIS function in SW1736 and HeLa cells. Since expression of WT NIS resulted in significant radioiodide uptake, uptake for VO and mutants are presented as mean±SEM fold change relative to WT, which is given as 1. Radioiodide uptake was completely lost for all three putative dimerisation motif mutants, with uptake levels comparable to VO in both cell lines (SW1736: VO 0.32±0.05, GZM 0.40±0.09, LZM1 0.46±0.07 and LZM2 0.33±0.09; HeLa: VO 0.03±0.005, GZM 0.05±0.02, LZM1 0.19±0.03 and LZM2 0.04±0.003). This demonstrates that both putative dimerisation motifs are required for NIS function.

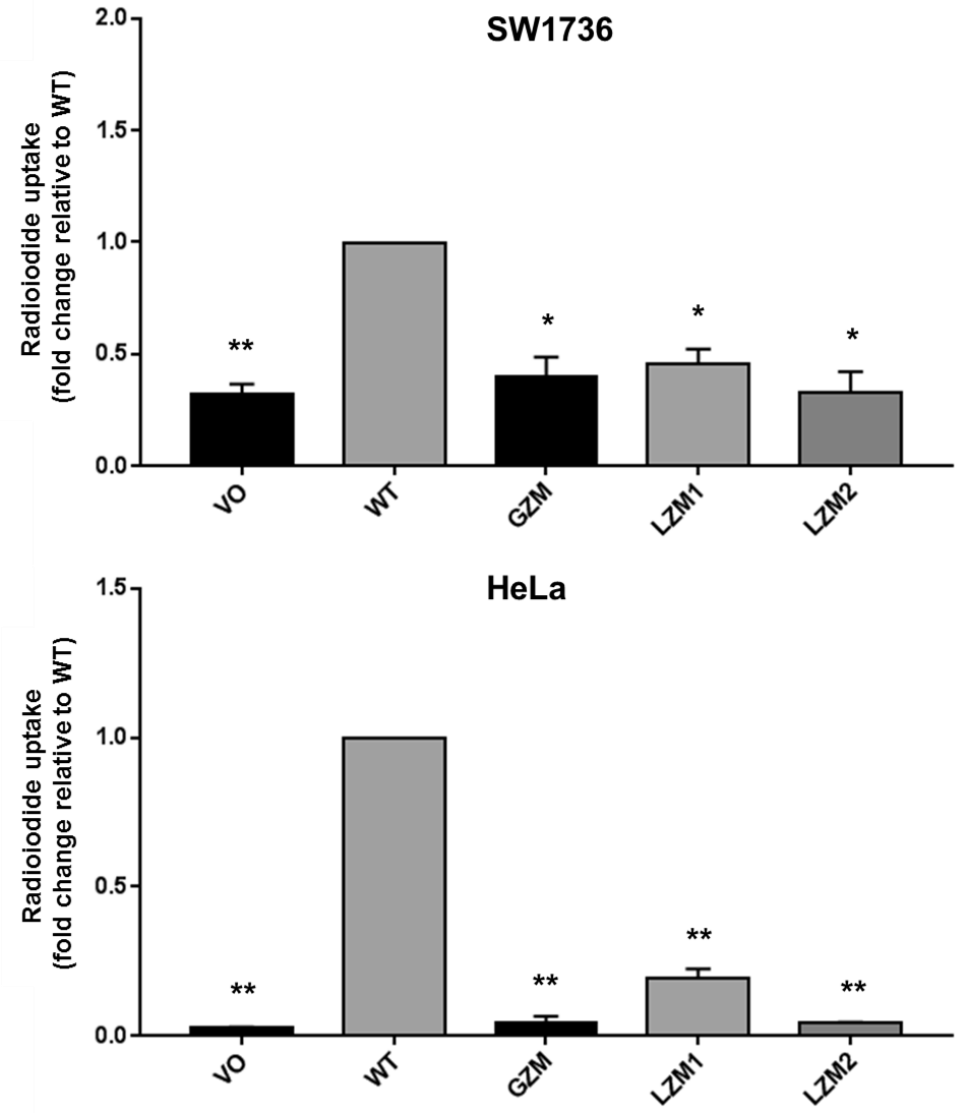

Figure 4-6 – Radioiodide uptake is lost when the putative dimerisation motifs of NIS are mutated. SW1736 (top) and HeLa (bottom) cells were transfected with empty pcDNA3.1(+) vector (VO), wild-type NIS-HA (WT) or HA-tagged NIS with a mutated glycine zipper motif (GZM) or a partially or fully mutated leucine zipper motif (LZM1 or LZM2, respectively) and radioiodide uptake assays were performed. Bars represent mean radioiodide uptake relative to that of WT and error bars show SEM relative to WT. One-way ANOVA with Dunnett's multiple comparison statistical tests were performed: * = p<0.001 and ** = p<0.0001 compared to WT. (n=3 with 4 replicates in each n).

4.3.2 Putative dimerisation motif NIS mutants retain the ability to dimerise

To examine whether putative dimerisation motifs are important for dimerisation, two of the three dimerisation methodologies described in Chapter 3 were implemented: PLA and FRET. To be able to use FRET to quantitatively assess any effect of these mutations on NIS dimerisation, PCR-cloning was used to conjugate the mutated NIS protein to either Cerulean or Citrine at the C-terminus.

4.3.2.1 NIS constructs with mutated putative dimerisation motifs were able to generate PLA signal

To investigate qualitatively whether disruption of the putative dimerisation motifs impacts on NIS dimerisation, PLA was performed on HeLa cells co-expressing differentially-tagged variants of WT or mutant NIS, tagged at the C-terminus with either MYC or HA.

The appearance of red dots in HeLa cells co-transfected with WT NIS-MYC and NIS-HA (Figure 4-7) signifies that the two tags are less than 40nm apart, which is suggestive of dimerisation. Similar PLA signal was observed for all three putative dimerisation motif mutants, demonstrating it is likely that these mutants are still capable of dimerisation. The subcellular distribution of PLA signal is different for the mutants compared to WT, reflecting the largely intracellular retention of these mutants (as shown in 4.3.1.2). No PLA signal was detected in the technical negative control (VO + WT NIS-HA).

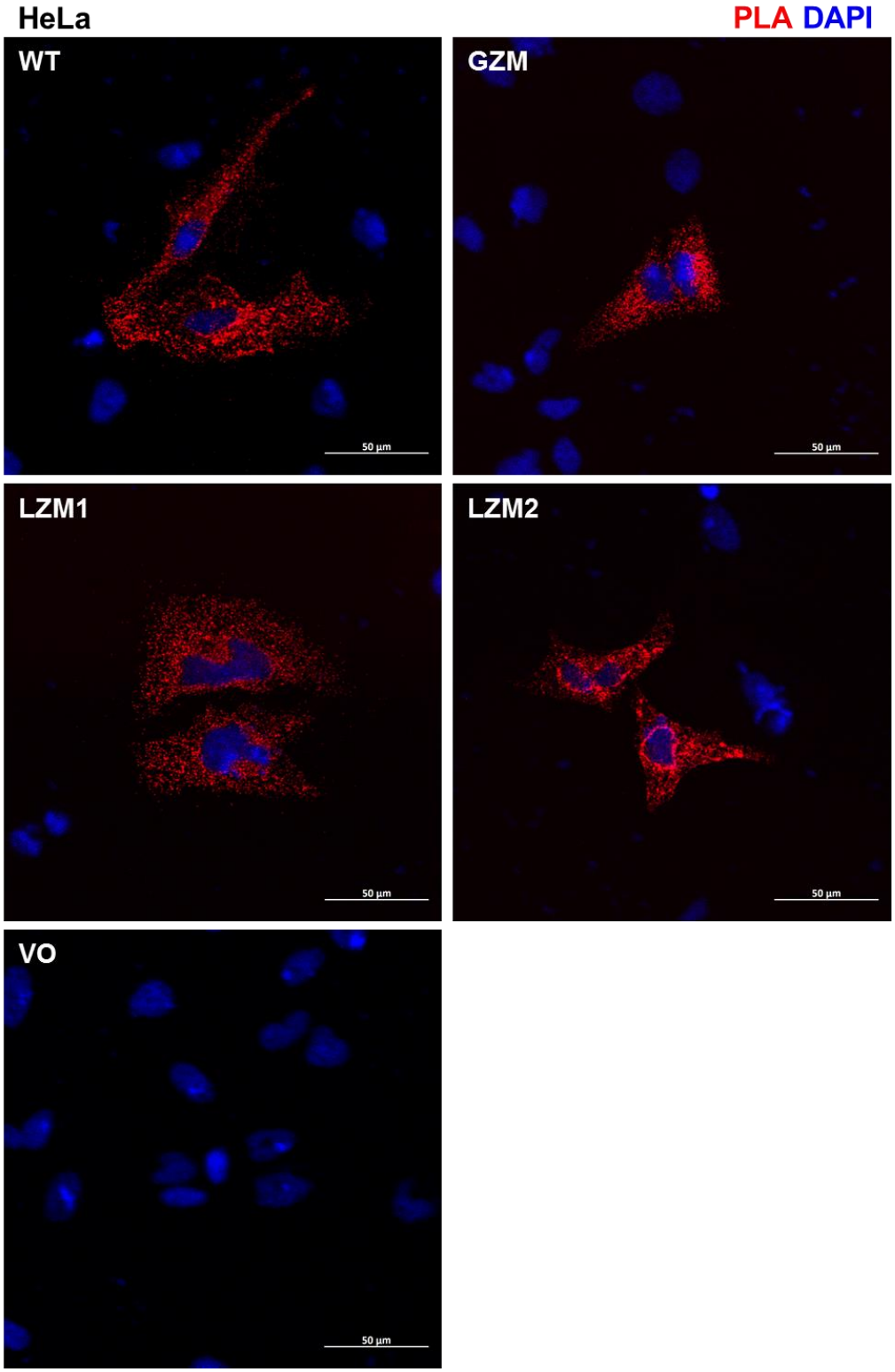

Figure 4-7 – PLA signal is still observed when the putative dimerisation motifs of NIS are mutated. PLA was performed on HeLa cells co-transfected with differentially-tagged variants of wild-type (WT) or NIS constructs with a mutated glycine zipper motif (GZM) or a partially or fully mutated leucine zipper motif (LZM1 or LZM2, respectively). PLA signal (in red) indicates close proximity (<40nm) between the MYC and HA tags, which suggests that dimerisation is occurring. Nuclei are visualised in blue using DAPI. 40x magnification.

4.3.2.2 Lack of significant change in FRET was observed with putative dimerisation motif-mutant NIS constructs compared to wild-type

In order to ascertain quantitatively whether mutating putative dimerisation motifs affects NIS dimerisation, FRET analysis was performed in SW1736 and HeLa cells co-expressing differentially-tagged variants of WT or mutant NIS, conjugated at the C-terminus to either Cerulean or Citrine. One-way ANOVA with Dunnett's multiple comparison tests were performed to identify significant changes in corrected FRET compared to WT.

Figure 4-8 depicts a representative set of images required to perform FRET analysis on each condition, while Figure 4-9 shows the results of this analysis. Corrected FRET data are presented as arbitrary units due to the data analysis process. The corrected FRET values in SW1736 cells expressing WT NIS ranged from -1070.34 to 805.43, with a mean of -72.83, while the mean WT corrected FRET value in HeLa cells was 56.20, with a range from -465.51 to 783.63. There was a statistically significant difference in corrected FRET compared to WT for LZM1 in HeLa cells, with a mean value of -83.37 and range of -668.95 to 469.30 ($p<0.05$), but similar results were not seen in SW1736 cells (mean -163.09, range -767.27 to 373.92). There was no significant difference in corrected FRET for the other putative dimerisation motif mutants in either cell line (GZM (SW1736: mean -189.91, range -576.55 to 133.06; HeLa: mean 62.62, range -538.03 to 791.79) or LZM2 (SW1736: mean -175.93, range -903.46 to 407.87; HeLa: mean -28.33, range -601.19 to 703.12)). As only one mutant in one cell line resulted in any significant change in FRET compared to WT, these data suggest that NIS dimerisation is unlikely to involve either of these putative dimerisation motifs as FRET remains largely unchanged.

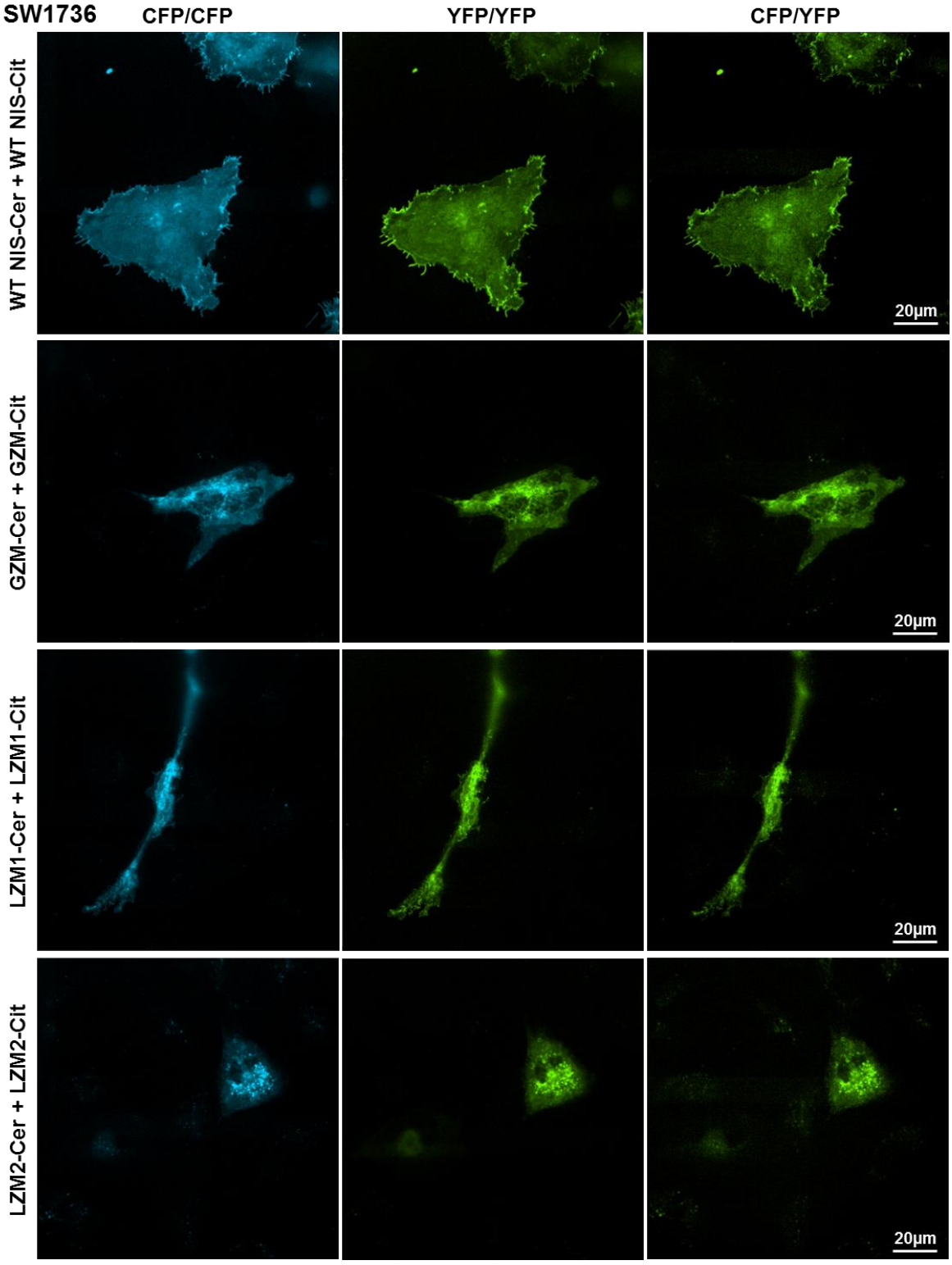

Figure 4-8 – Representative images captured during FRET analysis of the dimerisation capacity of putative dimerisation motif NIS mutants. SW1736 (A) and HeLa (B, overleaf) cells were co-transfected with differentially-tagged constructs of wild-type NIS (WT) or NIS with a mutated putative dimerisation motif (glycine zipper motif (GZM) or partially- or fully-mutated leucine zipper motif (LZM1 or LZM2, respectively)), conjugated at the C-terminus to Cerulean or Citrine. Three concurrent versions of each image were captured: total Cerulean (CFP) image (Cerulean excitation/Cerulean emission (CFP/CFP)),

total Citrine (YFP) image (YFP excitation/YFP emission (YFP/YFP)) and the FRET image (Cerulean excitation/Citrine emission (CFP/YFP)).

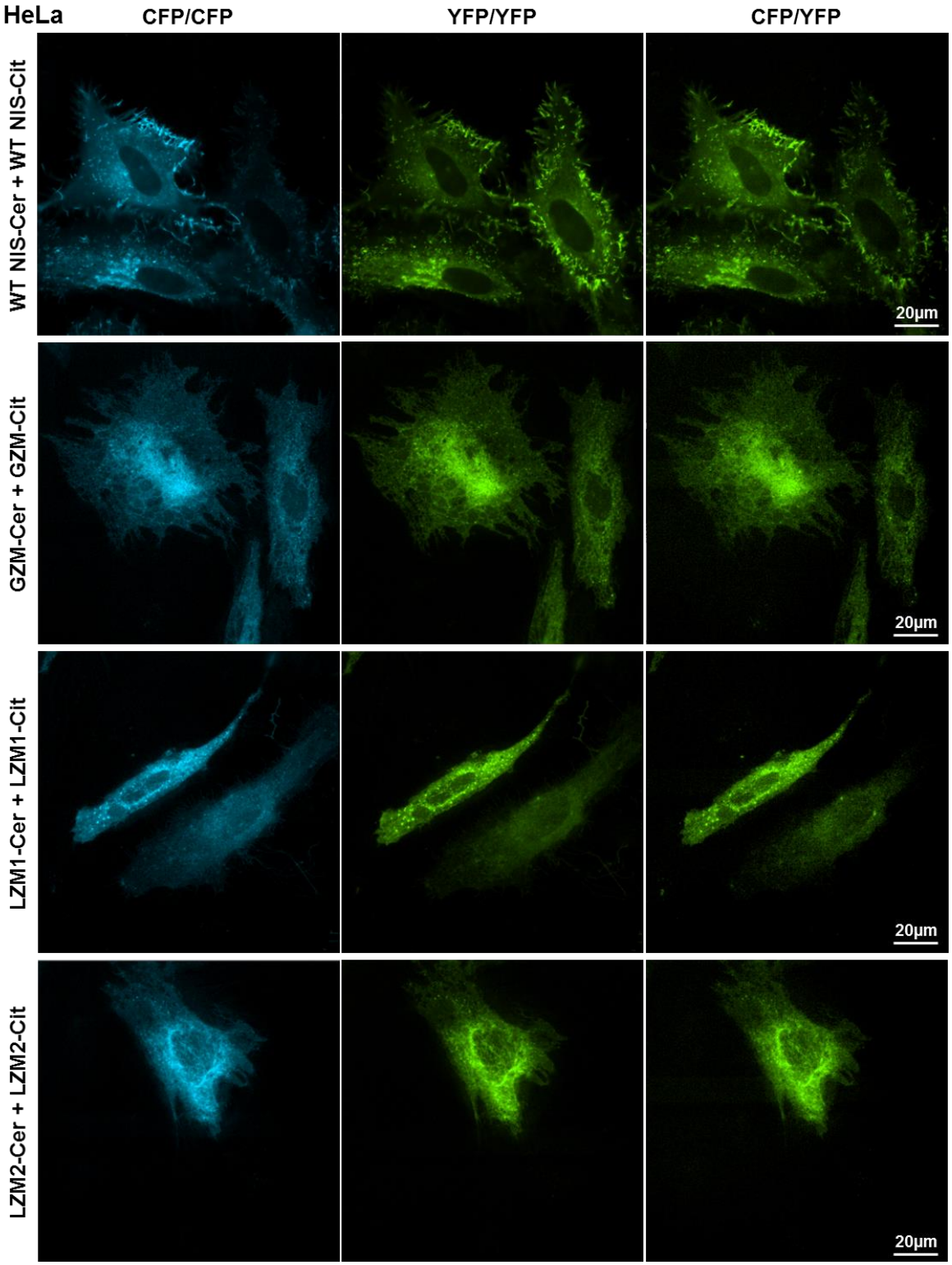

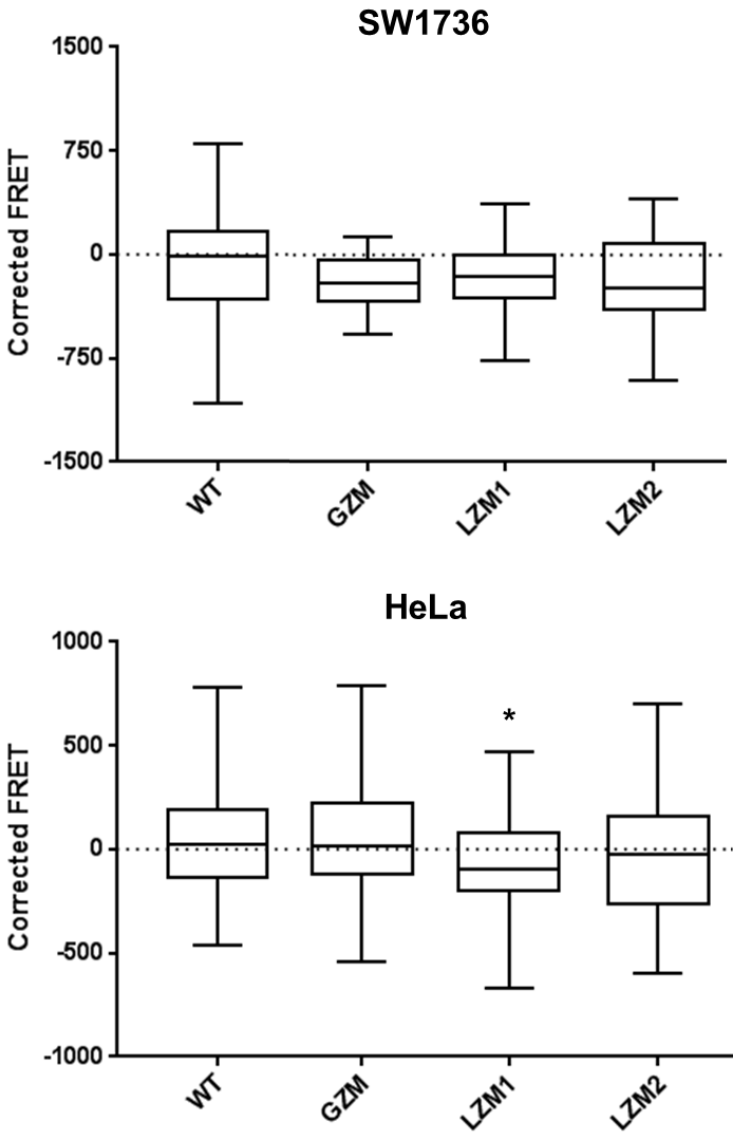

SW1736		HeLa	
Plasmid	**Corrected FRET (arbitrary units)**	**Plasmid**	**Corrected FRET (arbitrary units)**
WT	-72.83 (-1070.34 to 805.43)	**WT**	56.20 (-465.51 to 783.63)
GZM	-189.91 (-576.55 to 133.06)	**GZM**	62.62 (-538.03 to 791.79)
LZM1	-163.09 (-767.27 to 373.92)	**LZM1**	-83.37 (-668.95 to 469.30)
LZM2	-175.93 (-903.46 to 407.87)	**LZM2**	-28.33 (-601.19 to 703.12)

Figure 4-9 – Data analysis revealed that there was little significant change in corrected FRET when putative dimerisation motifs were mutated. FRET analysis was performed on SW1736 (top) and HeLa (bottom) cells transfected with differentially-tagged variants of wild-type (WT) NIS or NIS with a mutation in a putative dimerisation motif (glycine zipper motif (GZM) or a partial or full mutation of the leucine zipper motif (LZM1 or LZM2, respectively)), conjugated to Cerulean or Citrine at the C-terminus. Data are presented as a box and whisker plot, with the centre line representing the mean corrected FRET value (in arbitrary units), the box indicating the 25th and 75th percentiles and the whiskers denoting the minimum and maximum values. Data in the table are the mean corrected FRET, with the range of values given in parentheses. One-way ANOVA with Dunnett's multiple comparison statistical tests were performed: * = $p<0.05$. (n=2, with a minimum of 20 cells analysed in each n).

4.4 Discussion

Abrogation of dimerisation was required to investigate whether dimerisation is important for NIS function. In the current chapter, two putative dimerisation motifs proposed from the NIS primary sequence were disrupted by site-directed mutagenesis: GZM and LZM. These mutants were thoroughly characterised and their ability to dimerise was explored. Taken together, the data presented here demonstrate an important role for both motifs in NIS function, but it is highly unlikely that either motif is involved in NIS dimerisation.

4.4.1 Putative dimerisation motifs are important for NIS function

To investigate the effect of mutating the putative dimerisation motifs, a full characterisation of these mutants was conducted. While site-directed mutagenesis was carried out on pcDNA3.1(+)_NIS-MYC and pcDNA3.1(+)_NIS-HA plasmids to generate differentially-tagged variants of the mutants in order to perform dimerisation studies, characterisation was only performed on the HA-tagged mutants as the presence of the MYC or HA tag does not affect NIS expression, subcellular localisation or function (see section 3.3.3).

As well as performing radioiodide uptake assays to determine the effect of mutating the putative dimerisation motifs on NIS function, additional studies were applied to understand the effect of the mutations. The data presented in this chapter revealed that both GZM and LZM2 mutants are non-functional because they do not undergo glycosylation, signifying that these mutations prevent the protein from being processed in the ER and Golgi network as it should do in order to be trafficked to the plasma membrane where NIS is functional (see Figure 1-11 (Peer, 2011)). LZM1 is more complicated, as a small proportion of the partially mutated LZM mutant protein was able to become fully glycosylated and trafficked to the membrane, although function was still significantly impaired relative to WT. Overall, these

data show that the putative dimerisation motifs are important for NIS function as they appear to be implicated in ensuring NIS can undergo the trafficking process properly.

4.4.2 NIS dimerisation is unlikely to involve the putative dimerisation motifs

As GZM and LZM were demonstrated to be important for NIS function, PLA was carried out to investigate whether this could be due to altered NIS dimerisation. However, there was little difference in the PLA signal between WT NIS and NIS with a mutated putative dimerisation motif, suggesting that disrupting these motifs does not affect NIS dimerisation. Only HeLa cells were used in this PLA study because once no change in PLA signal was observed for these mutants in this cell line, FRET studies were conducted in order to quantitatively assess the dimerisation of the GZM and LZM mutants. This would establish whether this lack of alteration in PLA signal was due to the mutants retaining the ability to dimerise, or whether the PLA was detecting non-direct interactions between the two monomers due to the relatively large maximum distance of 40nm (Sigma-Aldrich, 2018b).

To enable the use of FRET to investigate the dimerisation of these mutants, PCR cloning was employed to create mutant NIS constructs conjugated at the C-terminus to either Cerulean or Citrine. As the presence of fluorophore at the C-terminus does not affect NIS expression, subcellular localisation or function (see section 3.3.3), characterisation of these mutant-fluorophore constructs was not carried out. Although the corrected FRET data are presented in box and whisker plots due to the wide range of values, this range alone is not indicative of a change in dimerisation, particularly because a negative corrected FRET value does not necessarily mean that no FRET is occurring. This is largely because the raw data must undergo several stages of processing in order to provide an accurate representation of FRET, which involves subtracting the background signal and then performing the necessary calculations in order to correct for the CFP and YFP crosstalk (see section 2.7 (Piston and

Kremers, 2007, Lamond, 2014)). As a result, corrected FRET is given in arbitrary units. Furthermore, an unequal transfection level of the two plasmids contributes to the wide data range and the negative values observed. It is highly unlikely that a cell will be transfected with exactly the same amount of both plasmids. For instance, a cell may take up twice as much Cerulean plasmid compared to Citrine plasmid, which would affect both the single fluorophore images (as the total Cerulean image would be brighter than that of Citrine) and the FRET image, as there is half as much Citrine available to undergo FRET compared to Cerulean. Similarly, this transfection level will vary greatly between different individual cells, as one cell may only transfect with half as much total plasmid as another cell. This would also subsequently affect the background signal, as a cell which has only transfected a small amount of plasmid would be less bright, thus increasing the signal:noise ratio, meaning that background subtraction has a greater impact on the corrected FRET values (Hoppe et al., 2002). Altogether, this gives rise to a very heterogeneous expression of the two fluorophores across the cell population, which contributes to the wide variation in corrected FRET values and explains why a negative corrected FRET value may not be due to a lack of dimerisation.

Consequently, to determine whether the putative dimerisation motif mutants were able to dimerise, the corrected FRET values for the mutants were compared statistically to that of WT using a one-way ANOVA. This revealed that the corrected FRET values for the mutants were not significantly different to that of WT, with the sole exception of LZM1 in HeLa cells. However, as this observation was not replicated for this mutant in SW1736 cells, nor was a similar result seen for the full mutation of the LZM (LZM2), it is most likely an anomalous result, possibly caused by the transfection issues described above. Hence, it was deemed very unlikely that the putative dimerisation motifs are involved in NIS dimerisation.

4.4.3 A novel role in NIS protein folding is suggested for the putative dimerisation motifs

The mutant characterisation data presented here clearly demonstrate that both putative dimerisation motifs have an important role for NIS function, as mutation of the key residues within the motifs leads to impairment of protein glycosylation and subsequent trafficking to the membrane. However, the PLA and FRET studies revealed it is highly unlikely that these motifs play a role in NIS dimerisation. Despite the high propensity for GZM motifs to mediate the dimerisation of single-pass membrane proteins by forming intermolecular helical interactions, it has been observed that GZMs are less likely to facilitate the dimerisation of multi-pass membrane proteins. Instead, they are more often involved in intramolecular helical interactions in multi-pass membrane proteins and thus play a more important role in the correct folding of such proteins (Teese and Langosch, 2015). As NIS is a large multi-pass membrane protein with 13 TMDs, it is interesting that mutating the GZM resulted in a lack of protein maturation which led to a non-functional protein, but did not result in altered dimerisation. This supports a role for the GZM in NIS protein folding, because it is likely that the GZM-mutant NIS did not undergo adequate maturation because it was misfolded. Similarly, the LZM mutants had aberrant glycosylation which resulted in non-functional proteins. Like GZMs, LZMs are important for helical interactions and packing, so it is probable that mutation of the LZM also caused the protein to be misfolded, thus also suggesting an important role for the LZM in NIS protein folding.

4.4.4 Concluding statements

The data shown in this chapter demonstrate an important role for both putative dimerisation motifs, GZM and LZM, in NIS protein maturation, subcellular localisation and, subsequently, function. However, disruption of these motifs did not abrogate NIS

dimerisation. As these motifs are well known to be involved in helical packing in multi-pass membrane proteins, these data offered a novel role for GZM and LZM in NIS, whereby these motifs are important for the correct folding of the NIS protein, rather than dimerisation. Consequently, a different approach was required to identify residues involved in NIS dimerisation in order to investigate the importance of dimerisation for NIS function.

CHAPTER 5 - HOMOLOGY MODELLING OF NIS DIMERISATION

5.1 Introduction

Much of our understanding of NIS structure and function has arisen from mutational studies, particularly focussing on mutations found in patients with ITD (see section 1.3.1.1; (Ravera et al., 2017)). However, a more detailed understanding of NIS function would be gained if its crystal structure could be determined, but unfortunately this still remains elusive.

However, crystal structures of several bacterial sodium-cotransporters from different protein families have been identified: LeuT of the neurotransmitter-sodium symporter (NSS) family (Yamashita et al., 2005); vSGLT of the sodium-solute symporter (SSS) family (Faham et al., 2008, Watanabe et al., 2010); Mhp1 of the nucleobase-cation symport-1 (NCS1) family (Weyand et al., 2008); BetP and CaiT of the betaine/choline/carnitine transporter (BCCT) family (Ressl et al., 2009, Schulze et al., 2010); and AdiC of the amino acid/polyamine/organocation (APC) family (Fang et al., 2009, Gao et al., 2009). These proteins (and members of their respective families) have a wide range of functions, but they all utilise the sodium gradient to actively co-transport their substrate into the cell. Despite little sequence homology between these proteins, their crystal structures revealed distinct structural homology, as they all share a common core domain (an inverted repeat of two bundles of five transmembrane domains) and highly conserved binding sites for sodium and their respective substrates. Consequently, it is widely believed that this common structural fold across different sodium-cotransporters is indicative of an evolutionary relationship between these proteins, and strongly suggests that their transport mechanism is also conserved (Abramson and Wright, 2009, Krishnamurthy et al., 2009, Portulano et al., 2014).

Given this structural homology between different families of sodium-cotransporters with limited sequence homology, it is highly likely that the other members of these protein

families also share this common structure, since members of the same protein family share a good degree of sequence homology. Hence, it is pertinent that NIS belongs to the same protein family (SSS) as the *Vibrio parahaemolyticus* sodium-galactose transporter (vSGLT). vSGLT is a homolog of the eukaryotic sodium-glucose transporter 1 (SGLT1), sharing 32% sequence identity and 60% sequence similarity with human SGLT1 (Faham et al., 2008), while sharing 27% identity and 57% similarity with human NIS (Portulano et al., 2014). Consequently, one can create a theoretical model of NIS 3D structure by 'threading' the primary sequence of NIS (i.e. the target protein) onto the crystal structure of vSGLT (i.e. the template). This is termed a 'homology model', as it is based on the finding that sequence homology between proteins from the same family usually extends to their 3D structures, with the structures of protein family members often being more highly conserved than their primary sequences (Al-Karadaghi, 2017). Despite the improved homology between NIS and human SGLT1, the vSGLT crystal structure is used because the crystal structure for human SGLT1 has not yet been determined. Clearly a homology model should not be taken as an exact representation of the actual structure, but as an approximation to provide valuable and novel insight into protein structure, which can then be taken forward into experimental studies for consolidation.

Previous homology models of NIS structure have revealed novel residues involved in ion binding and demonstrated how ITD-causing mutations impair NIS transporter function (Portulano et al., 2014, Darrouzet et al., 2014, Vergara-Jaque et al., 2017, Ravera et al., 2017). However, these models have only focussed on the NIS monomer, even though vSGLT was crystallised as a dimer (Faham et al., 2008). As NIS dimerisation was confirmed in Chapter 3, but putative dimerisation motifs within the primary structure were shown to not be involved in Chapter 4, a novel homology model of dimerised NIS was created based on

the dimeric crystal structure of vSGLT. This chapter details the generation, refinement and validation of our model of NIS dimerisation, and how novel residues potentially important for NIS dimerisation were proposed.

5.2 Methods

5.2.1 Creating a NIS homology model

5.2.1.1 Generation of predicted 3D structures for NIS

Predicted 3D protein structures of NIS monomers were generated as RCSB Protein Data Bank (PDB; (Berman et al., 2000)) files using the online protein structure prediction site Phyre2 (Protein Homology/analogy Recognition Engine V2.0), where NIS primary sequence (UniProtKB - Q92911; see section 9.1) was modelled using 'Intensive Mode' to model the entire protein sequence with maximised confidence (Kelley and Sternberg, 2009).

5.2.1.2 Viewing 3D protein structures

PDB files for the vSGLT crystal structure (PBD ID: 2XQ2 (Watanabe et al., 2010); UniProtKB - P96169) and predicted NIS structures (see section 5.2.1.1) were viewed using the modelling software YASARA View Version 15.3.8 (Krieger and Vriend, 2014) in the 'Cartoon' or 'Ribbon' style, with key residues shown in the 'Stick' style. Monomers or residues were coloured using the 'ColorObj', 'ColorMol' or 'ColorRes' commands.

5.2.1.2.1 Aligning predicted NIS protein structure onto vSGLT crystal structure to obtain a homology model of dimeric NIS

To create a model of NIS dimeric structure based on the crystal structure of dimerised vSGLT in YASARA, the monomers of vSGLT were first separated using the 'SplitObj' command. Then, an individual predicted NIS PBD 'Object' was aligned onto each vSGLT

monomer using the 'AlignMol' command. To create a NIS dimer PDB, the aligned NIS monomers were joined using the 'JoinObj' function.

5.2.1.2.2 Mapping the dimerisation interface

Residues potentially involved in NIS dimerisation were identified from the final refined NIS predicted dimeric structure using the 'ShowRes' and 'ListRes' commands in YASARA to reveal residues on monomer A which were less than 3Å from monomer B.

5.2.2 Methods for refining the NIS homology model

5.2.2.1 Topology predictions

To predict the locations of the transmembrane domains, the primary sequences of NIS and vSGLT were run through several online topology prediction sites: HMMTOP (Tusnády and Simon, 2001), TopPred II (Claros and von Heijne, 1994), TMHMM (Krogh et al., 2001), PredictProtein (Rost et al., 2004), TMpred (Hoffman and Stoffel, 1993) and UniProt (TheUniProtConsortium, 2017).

5.2.2.2 Sequence alignments

Primary sequences of NIS and vSGLT were aligned using two online global pairwise sequence alignment methods: EMBOSS Needle (Rice et al., 2000) and EMBOSS Stretcher (Rice et al., 2000).

5.3 Results

5.3.1 Initial homology model of NIS

The crystal structure of dimeric vSGLT (PBD ID: 2XQ2 (Watanabe et al., 2010)) is shown in Figure 5-1, and the homology model of NIS dimerisation (predicted by Phyre2 and aligned to the vSGLT dimer by YASARA) is shown in Figure 5-2. Three template proteins

were used to model NIS structure: the two vSGLT structures (PBD ID: 3DH4 (Faham et al., 2008) and 2XQ2 (Watanabe et al., 2010), both used with 100% confidence of homology between NIS and template sequence) and the ammonium transporter *Nitrosomonas europaea* Rh protein (PBD ID: 3B9Y (Li et al., 2007), used with 81.7% confidence). Using these three templates, 74% of NIS residues were modelled at >90% confidence, with 95 residues modelled *ab initio*, meaning they were modelled without reference to a template structure due to a lack of homology. Alignment of the two structures in YASARA had a root-mean-square deviation (RMSD) of atomic positions of 1.178Å, meaning that on average the distance between the backbone atoms of the two protein structures when aligned onto each other is 1.178Å (1Å is the equivalent of 0.1nm). The alignment also revealed large portions of NIS that could not be modelled against the vSGLT structure, which is detrimental to the model (Figure 5-3).

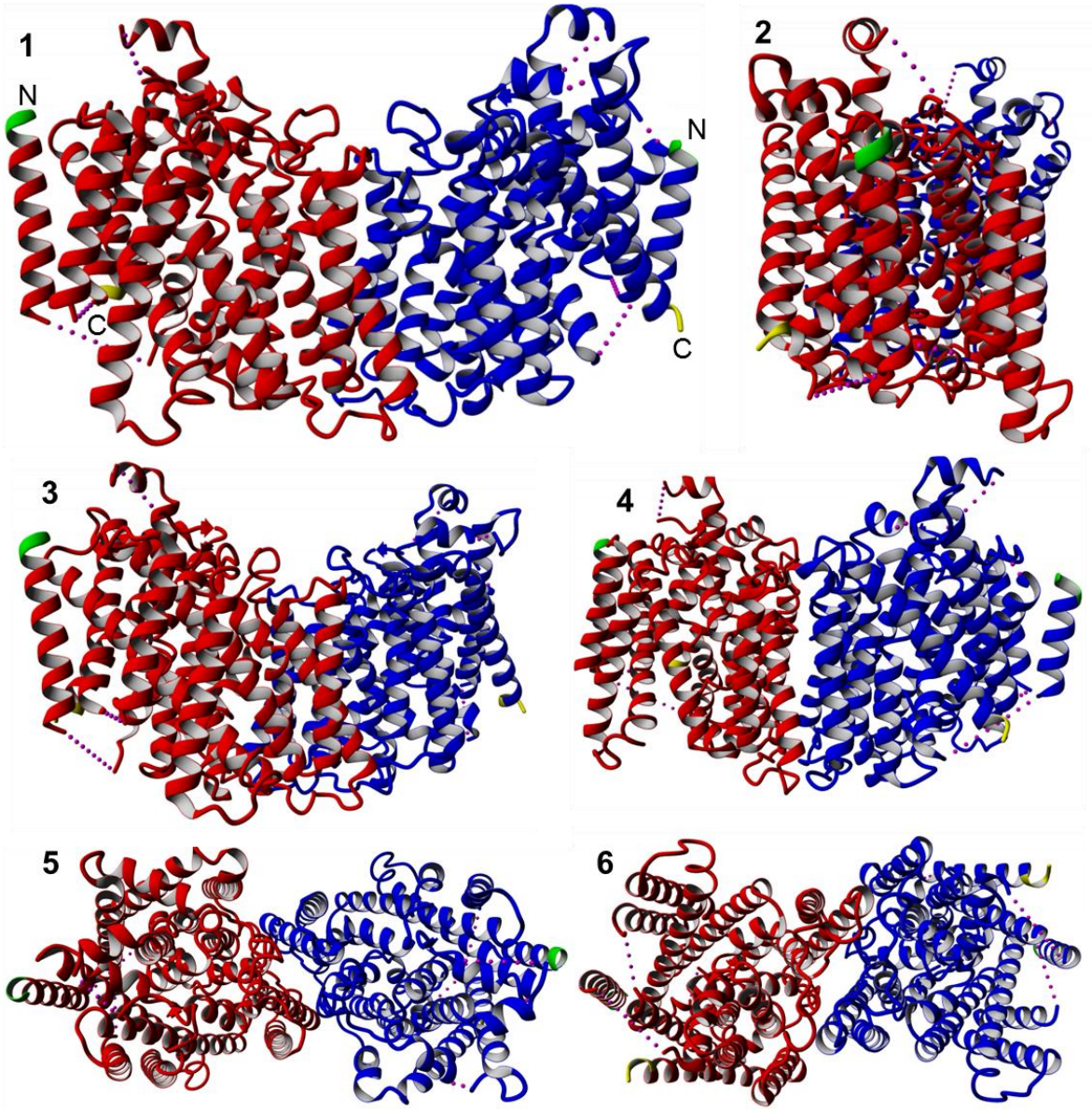

Figure 5-1 – Crystal structure of the vSGLT dimer. Monomers of the vSGLT crystal structure (Protein Data Bank (PBD) ID: 2XQ2 (Watanabe et al., 2010)) are coloured in red and blue. Both termini are labelled in panel 1 with N-termini coloured in green and C-termini coloured yellow throughout. Structures are viewed in the membrane plane so that the extracellular milieu is above the structure (panels 1-4), viewed from the extracellular side (panel 5) and viewed from the intracellular side (panel 6).

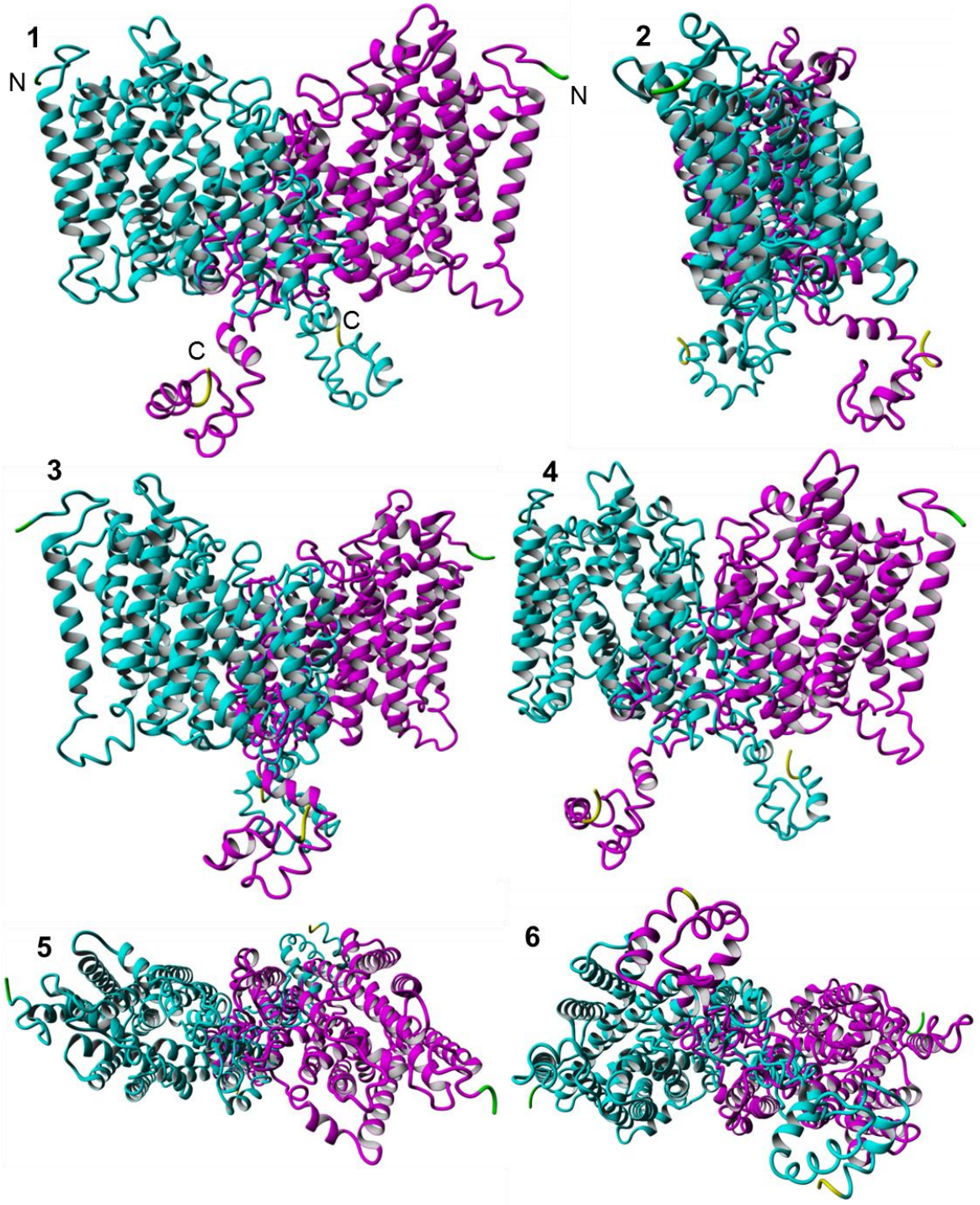

Figure 5-2 – Predicted 3D model of the NIS dimer. The entire length of NIS was modelled into a 3D structure using Phyre2, which was then aligned on to the crystal structure of the vSGLT dimer using YASARA to create a 3D model of dimerised NIS. NIS monomers are coloured in cyan and magenta. Both termini are labelled in panel 1, with N-termini coloured in green and C-termini coloured in yellow throughout. Structures are viewed in the membrane plane so that the extracellular milieu is above the structure (panels 1-4), viewed from the extracellular side (panel 5) and viewed from the intracellular side (panel 6).

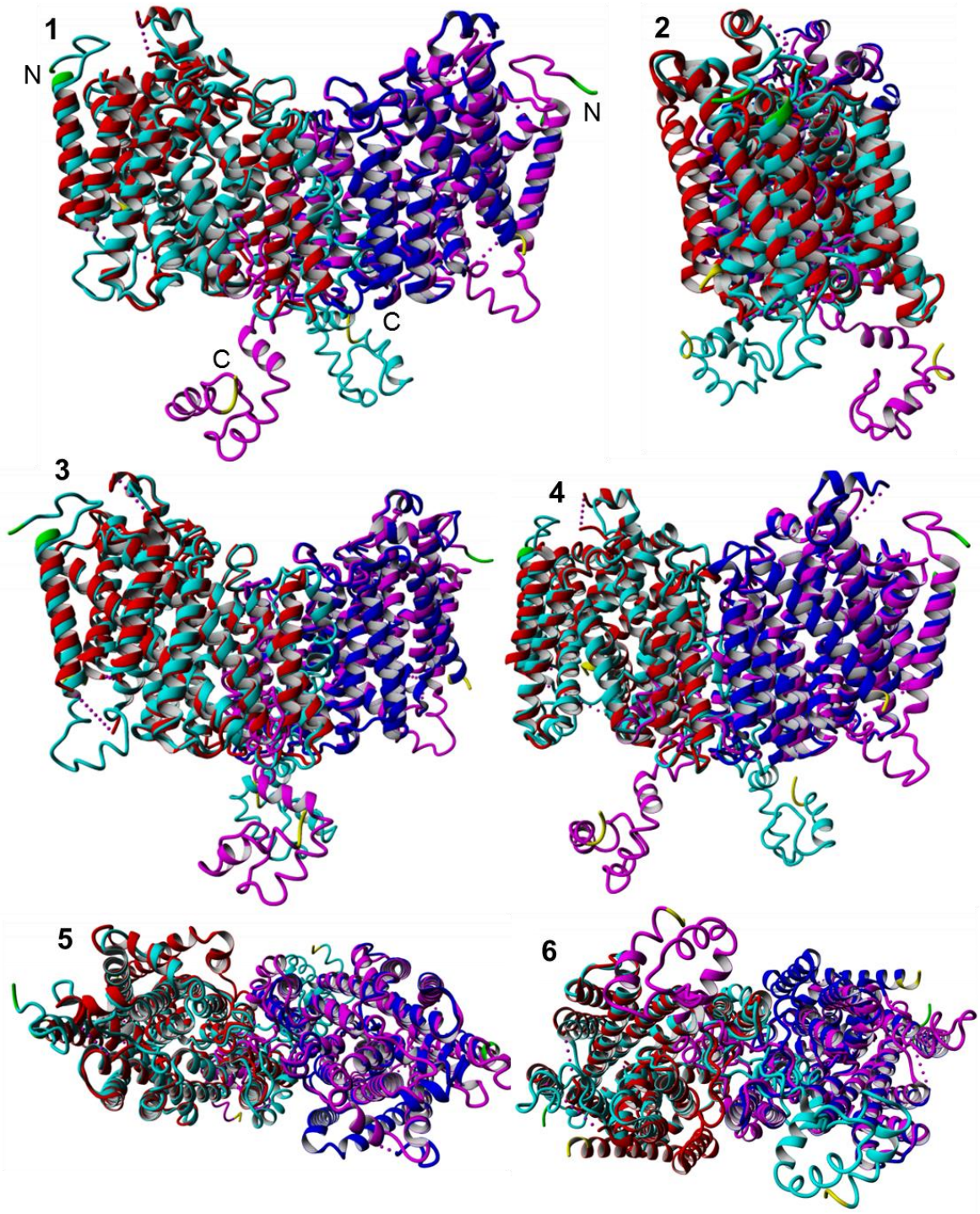

Figure 5-3 – Alignment of dimeric vSGLT crystal structure and predicted 3D NIS structure revealed large sections of NIS which could not be modelled against the vSGLT structure. Monomers of the vSGLT dimer crystal structure (Protein Data Bank (PDB) ID: 2XQ2 (Watanabe et al., 2010)) are coloured in red and blue, while monomers of the model of NIS structure (predicted using Phyre2) are coloured in cyan and magenta. Both termini are labelled in panel 1, with N-termini coloured in green and C-termini coloured in yellow throughout. Structures are viewed in the membrane plane oriented so extracellular milieu is above the structure (panels 1-4), from the extracellular side (panel 5) and the intracellular side (panel 6).

5.3.2 Refinement of homology model

5.3.2.1 Topology predictions and sequence alignments identified regions of poor homology

In order to improve the homology model of NIS dimerisation, the regions of NIS sequence which could not be aligned onto the vSGLT crystal structure needed to be identified and removed. To achieve this, six different topology predictions were performed on the NIS primary sequence to identify which regions of NIS are likely to form transmembrane domains (TMDs), as TMDs are well-structured and therefore more accurate to model.

The results from these six topology predictions on the NIS primary sequence are illustrated in Figure 5-4, with a different coloured line corresponding to a different topology prediction. Although there was noticeable variation at the TMD extremities between the different predictions, there was often clear overlap between most of the different predictions. The same predictions were also performed on the vSGLT primary sequence, with the actual TMDs identified from the vSGLT crystal structure shown alongside in green to demonstrate the accuracy of the different topology predictions (Figure 5-5). This demonstrated that the overlap between the different predictions largely corresponded with the actual TMDs identified from the crystal structure, indicating that these large areas of overlap can correctly identify TMDs. However, variability at the extremities of the predictions makes determining the precise start and end point of the TMD impossible without the crystal structure.

Figure 5-4 – Overlap between the topology predictions on the NIS sequence identified regions of NIS likely to form transmembrane domains. Results from the six different topology predictions are depicted in different colours: HMMTOP in purple, TopPred in pink, TMHMM in light blue, PredictProtein in red, TMPred in yellow, and UniProt in dark blue.

Figure 5-5 – Comparison of topology predictions on the vSGLT sequence with the actual transmembrane domains identified from the crystal structure demonstrated that the overlap between the predictions is largely accurate. Results from the six different topology predictions are depicted in different colours: HMMTOP in purple, TopPred in pink, TMHMM in light blue, PredictProtein in red, TMPred in yellow, and UniProt in dark blue, while the actual TMDs are in green.

Using the consensus overlap between the different topology predictions shown in Figure 5-4 above, the regions of NIS structure believed to form TMDs were identified. Table 5-1 sets out these residues alongside the confirmed TMD residues from the vSGLT crystal structure.

TMD	NIS	vSGLT		TMD	NIS	vSGLT
1	Y17-L36	I13-L28		**8**	V287-Y307	V280-T312
2	L57-L74	W53-S79*		**9**	G340-A363	V350-Y385
3	C91-Y110	A83-E108		**10**	L392-G410	K394-L417
4	Y137-I155	K124-T156		**11**	F417-L437	F424-F447
5	I164-M184	L162-Y179		**12**	G444-L437	S453-K471
6	V195-A207	Y186-G212		**13**	Y528-T550	L484-T501
7	W245-V261	A250-L275**		**14**	N/A	I526-F542

Table 5-1 – Transmembrane domains of NIS and vSGLT. Residues involved in NIS transmembrane domains (TMDs) were proposed using the consensus from the six topology predictions, while residues involved in vSGLT TMDs were identified from its crystal structure. * vSGLT TMD 2 has a break between N64-S66. ** vSGLT TMD 7 has a break between G265-Q268.

To use this information to ascertain areas of poor homology between NIS and vSGLT, two different sequence alignments were performed: EMBOSS Needle (Figure 5-6) and EMBOSS Stretcher (Figure 5-7). Needle gave a higher alignment score than Stretcher (425.5 vs. 181), largely because Needle aligned a greater number of residues with sequence identity (160 vs. 140) and sequence similarity (278 vs. 261), with fewer gaps in the alignment (206 residues vs. 261). The TMD regions of the proteins (as summarised in Table 5-1) were then depicted on both alignments (Figure 5-6 and Figure 5-7, respectively) to investigate the homology between the TMDs of the two proteins (NIS TMDs in red, vSGLT TMDs in blue). Both sequence alignments revealed distinct homology between TMDs 1-12 of NIS and vSGLT; however, there was much less homology towards the C-termini. Therefore, to create a more accurate model, improved homology between the proteins at the C-terminus is required.

```
NIS    1 MEAVETGERPTFGAWDYGVFALMLLVSTGIGLWVGL-ARGGQRSAEDFFTGGRRLAALPVGLSLSASFMSAVQVLGVPSEAYRYGL--KFLWMCLGQLL  96
         |..:|.|      ....|..|||:.:.:..|:|||||.. .:|.|:|.|..|:.|.....||.|.||.|:.:||.|.:|:....|..||    .:.||   ..:
vSGLT  1 MSNIEHG----LSFIDIMVFAIYVAIIIGVGLWVSRDKKGTQKSTEDYFLAGKSLPWWAVGASLIAANISAEQFIGMSGSGYSIGLAIASYEWM--SAI  93

        97 NSVLTALLFMPVFYRLGLTSTYEYLEMRFSRAVRLCGTLQYIVATMLYTGI----VIYAPALILNQVTGLDIWASLLSTGIICTFYTAVGGMKAVVWTDV 192
           ..:|.....|:|:|....|:.:..|.::|.||::.::    |:|...|.|..|:.:..|:.:...|:|...:....|:...|:.|||||||
        94 TLLIVGKYFLPIFIEKGIYTIPEFVEKRFNKKLK--TILAVFWISLYIFVNLTSVLYLGGLALETILGIPIMYSILGLALFALVYSIYGGLSAVVWTDV 190

       193 FQVVVMLSGFWVVLARGVMLVGGP-------RQVLTLAQNHSRINLMDFNPDPRSRYTFWTFVVGGTLVW---LSMYGVNQAQVQRYVACRTEKQAK--- 279
           .||...::.|.::.....|...:|||.      .:::..|..|....:.|....||....:.... ..:::|| :|   |...:|.||..:|:|.::...:|:
       191 IQVFFLVIGGFMTTYMAVSFIGGTDGWFAGVSKMVDAAPGHFEMILDQSNPQYMNLPGI-AVLIGG--LWVANLYYWGFNQYIIQRTLAAKSVSEAQKGI 287

       280 -----LALLINQVGLFLIVSSAACGGIVMFVFYTDCDPLL---LGRISA--------PDQYMPLLVLDIFEDLP-GVPGLFLACAYSGTLSTASTSINAM 362
              ||||::.    ||:|..   ||...:|...:   ||.|    ||.|:|        .|:...|.|.    :.||  ||.|:..|...:...:|:.::.:||:.
       288 VFAAFLALIVP----FLVVLP----GIAAYVITS--DPQLMASLGDIAATNLPSAANADKAYPWLT----QFLPVGVKGVVFAALAAAIVSSLASMLNST 373

       363 AAVTVEDLIKPRLRSLAP---RKLVIISKGLSLIYGSACLTVAALSSLLGGGVLQ----GSFTVMGVISGPLLGAFILGMFLPACNTPGVLAGLGAGL 453
           |.:....|:.|   ..::|   .|||.:.:..:::    .|.:|||.:.:.:||:.|     ...:|  |:::|...:|...|:|||:|......:.|.:|.:|.:
       374 ATIFTMDIYK---EYISPDSGDHKLVNVGRTAAVV----ALIIAALIAPMLGGIGQCFQYIQEYT--GLVSPGILAVFLLGLFWKKTTSKGAIIGVVASI 464

       454 ALSLWVALGATLYPPSEQ-------TMRVLPSSAARCVALSVNASGLLDP-------ALLPANDSSRAPSSGMDASRPALADSFYA-----ISYLYYGAL 534
           ..:|:|:.....|..:|   ||.|:  |...::.|:||..   ||          ::....:.|.....|:.....|...|:.     |:.:.::|.:
       465 PFALFLKFMPLSMPFFMDQMLYTLLFTMVVI---AFTSLSTSINDD---DPKGISWTSSMFVTDRSFNIAAYGTMIVLAVLYTLFWVNADAEITLIIFGVM 558

       535 -GTLTTVLCGALIS----CLTGPTKRSTLAPGLLWMDLARQTASVAPKEEVAILDDNLVKGPEELPTGNKKPPGFLPTNEDRLFFLGQKELEGAGSWTP 628
            |.:.|:|  |||    .:.....|
       559 AGVIGTIL---LISYGIKKLIKASYK----------------------------------------------------------------------- 581

       629 CVGHDGGRDQQETNL   643
                                                  EMBOSS Needle alignment                Length:      715
                                                  # Identity:  160/715 (22.4%)           # Similarity:  278/715 (38.9%)
           ---------------   581                  # Gaps:      206/715 (28.8%)           # Score:     425.5
```

Figure 5-6 – EMBOSS Needle sequence alignment of NIS and vSGLT. Depiction of the transmembrane domain regions for NIS (in red) and vSGLT (in blue) on the Needle alignment highlighted that the region of poor homology between the two proteins was at the C-terminus.

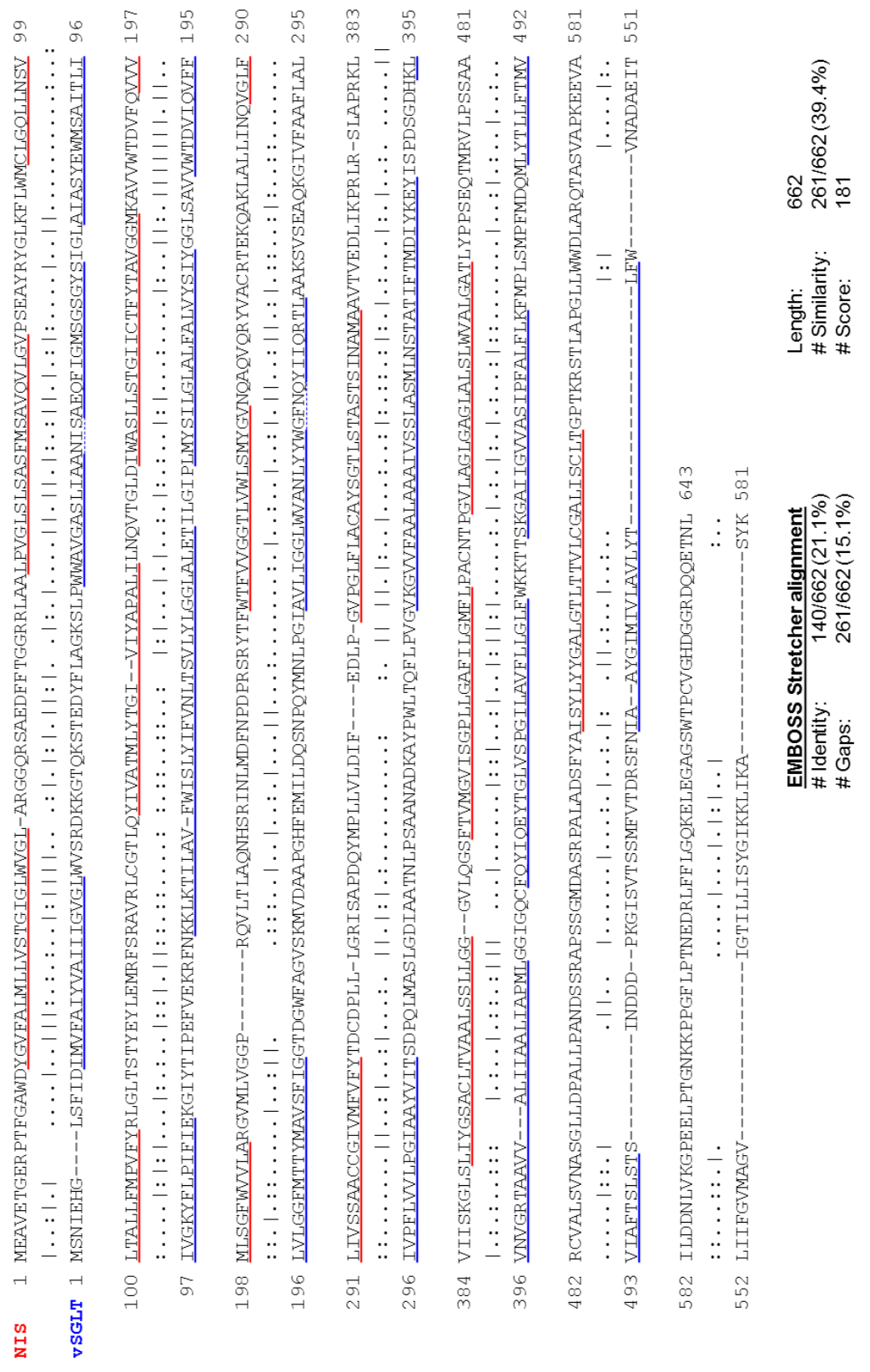

Figure 5-7 - EMBOSS Stretcher sequence alignment of NIS and vSGLT. Depicting the transmembrane domain regions for NIS (in red) and vSGLT (in blue) on the Stretcher alignment revealed that the region of poor homology between the two proteins was at the C-terminus.

5.3.2.2 Removing regions of poor homology improved the sequence alignment

To improve homology between the two proteins, the large intracellular C-terminal tail of NIS (from S556 onwards) was removed. To further improve homology, the large extracellular domain between TMDs 12-13 (from T472 to Y524) was also removed from the NIS sequence. Sequence alignment was then performed between this modified NIS sequence and vSGLT (Figure 5-8). Only EMBOSS Needle was used for this second alignment as it gave a higher alignment score than EMBOSS Stretcher (419.0 vs 181). The TMD regions were also depicted on the alignment (NIS predicted TMDs in red, vSGLT confirmed TMDs in blue, see Table 5-1). This alignment demonstrated improved homology between the modified NIS sequence and vSGLT, as all 13 NIS TMDs were aligned to vSGLT TMDs 1-13 and the EMBOSS Needle alignment score increased from 419.0 to 425.5 as an increased percentage of residues were aligned with sequence identity (23% vs. 22.4%) and sequence similarity (40.4% vs. 38.9%), with fewer gaps in the alignment (25.6% vs. 28.8%).

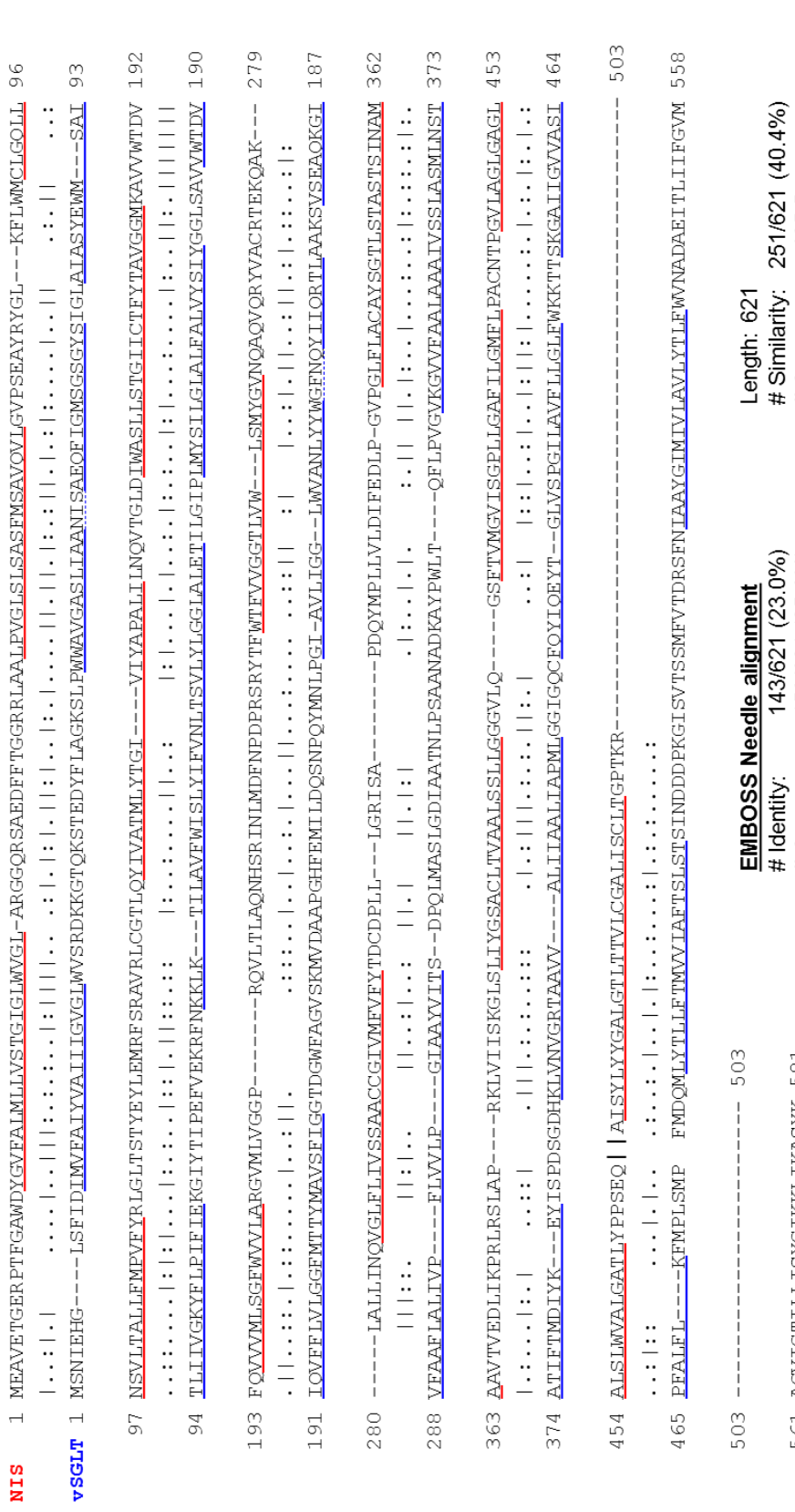

Figure 5-8 – EMBOSS Needle sequence alignment of vSGLT and the modified NIS sequence. Removing the large unstructured C-terminus and extracellular loop between transmembrane domains (TMDs) 12 and 13 improved the alignment of NIS to vSGLT, demonstrating improved homology between the two proteins. NIS predicted TMDs are underlined in red and vSGLT TMDs are underlined in blue.

5.3.3 Final homology model of NIS

5.3.3.1 Improved sequence alignment resulted in a more refined homology model of NIS 3D structure

Given the improved sequence alignment in Figure 5-8, the 3D structure of the modified NIS sequence was generated in Phyre2 (Figure 5-9). Here, NIS structure was modelled based on two protein templates: the two vSGLT structures (PDB ID: 2XQ2 (Watanabe et al., 2010) and 3DH4 (Faham et al., 2008)), both used with 100% confidence of sequence homology between NIS and template sequence. Using these templates, 93% NIS residues were modelled at >90% confidence (compared to 74% in the initial model), with just 33 residues modelled *ab initio* (vs. 95 in the initial model). Alignment of this NIS structure with the crystal structure of vSGLT (PBD ID: 2XQ2 (Watanabe et al., 2010)) in YASARA revealed a more refined homology model (Figure 5-10), with an RMSD of atomic positions of 0.993Å vs 1.178Å for the initial model (see section 5.3.1), indicating a smaller distance between the backbone atoms of the two aligned protein structures. Hence, the model shown in Figure 5-9 was taken as the final model of dimeric NIS.

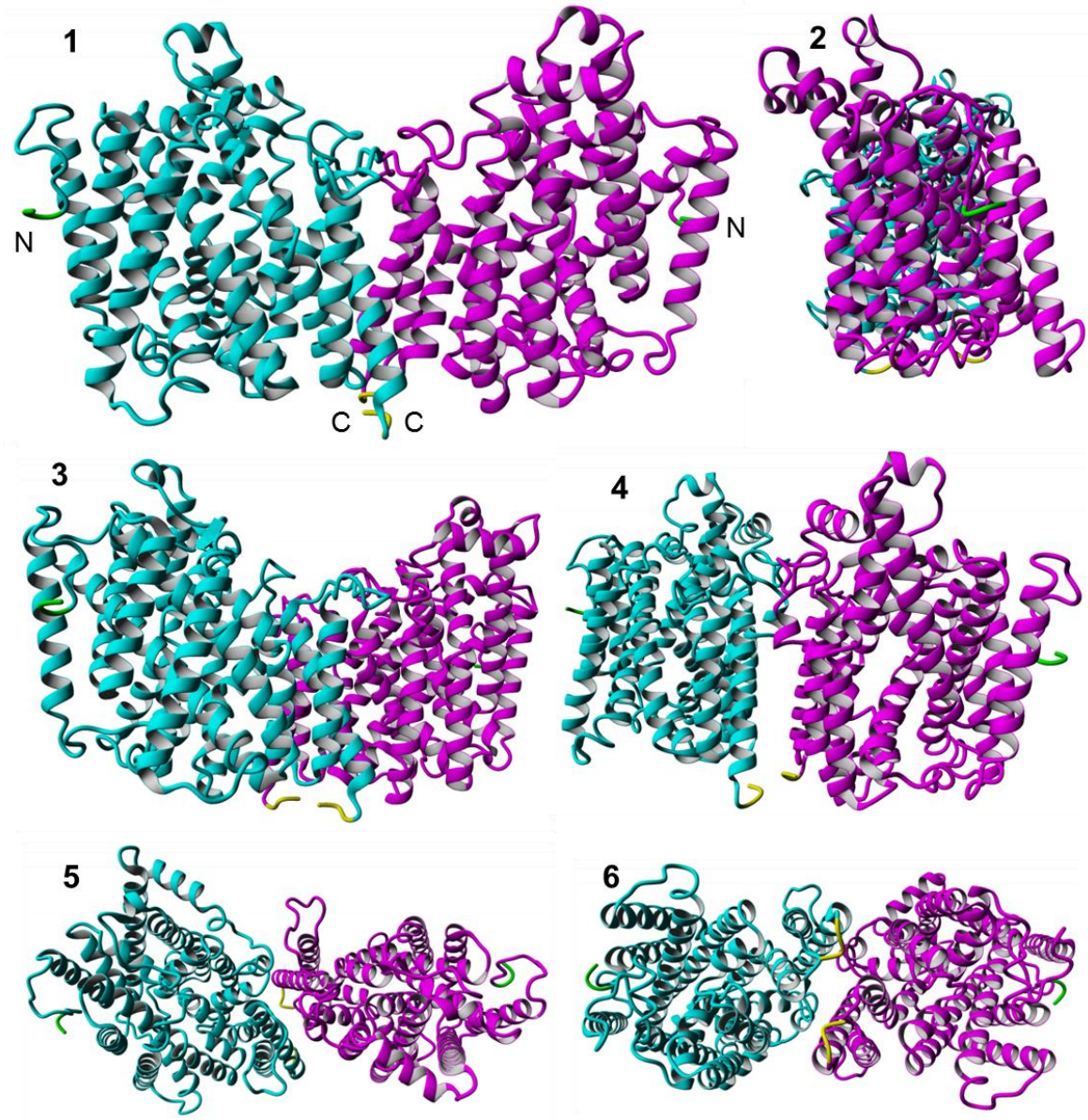

Figure 5-9 - Predicted 3D model of the refined NIS dimer. The modified NIS sequence was modelled into a 3D structure using Phyre2, which was then aligned on to the crystal structure of the vSGLT dimer using YASARA to create a 3D model of dimerised NIS. NIS monomers are coloured in cyan and magenta. Both termini are labelled in panel 1, with N-termini coloured in green and C-termini coloured in yellow throughout. Structures are viewed in the membrane plane so that the extracellular milieu is above the structure (panels 1-4), viewed from the extracellular side (panel 5) and viewed from the intracellular side (panel 6).

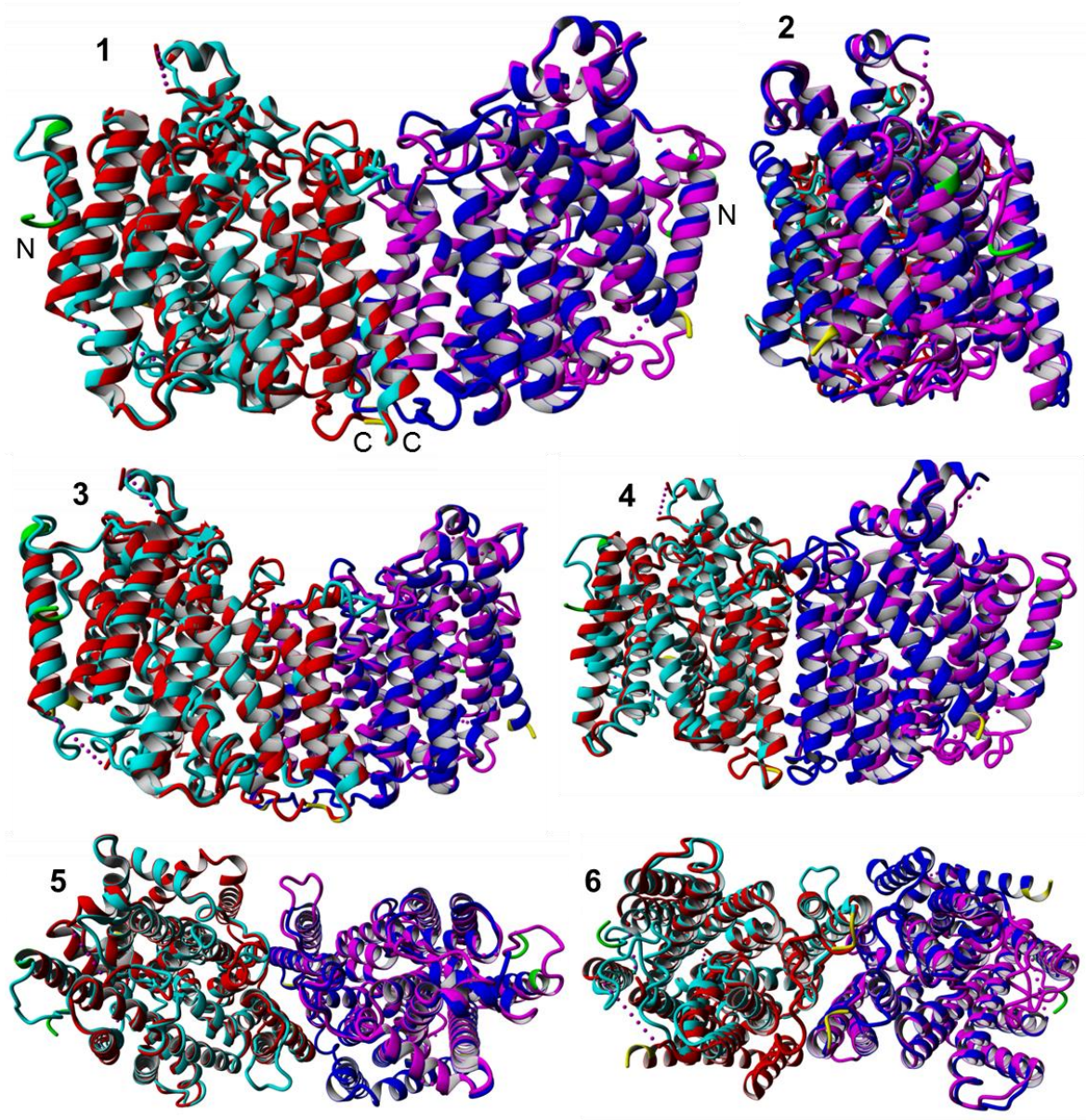

Figure 5-10 – Alignment of the dimeric vSGLT crystal structure and the modified predicted NIS 3D structure revealed a much closer alignment, demonstrating a more refined homology model of dimeric NIS. Monomers of the vSGLT dimer crystal structure (Protein Data Bank (PDB) ID: 2XQ2 (Watanabe et al., 2010)) are coloured in red and blue, while monomers of the modified model of NIS structure (predicted using Phyre2) are coloured in cyan and magenta. Both termini are labelled in panel 1, with N-termini coloured in green and C-termini coloured in yellow throughout. Structures are viewed in the membrane plane oriented so extracellular milieu is above the structure (panels 1-4), from the extracellular side (panel 5) and the intracellular side (panel 6).

The topology predictions of NIS (as summarised in Figure 5-4 and Table 5-1) were then used to depict the most likely regions to be TMDs on the modified NIS homology model, which were coloured as a rainbow, with the first TMD in red through to the last TMD in purple (Figure 5-11). The TMDs were similarly depicted on the vSGLT crystal structure for comparison (Figure 5-12). Interestingly, both dimeric structures are asymmetric, meaning that the right-hand monomer (as viewed in Panel 1 of Figure 5-11 and Figure 5-12) is not simply a mirror image of the left-hand monomer, but it has been rotated 180^{o} about the centre of the right-hand monomer. For example, TMD 1 (in red) is on the far left of the left-hand monomer for both proteins, angled so that the N-terminal end of the TMD is pointing in to the page, and obscured by the yellow-green TMD 5, indicating TMD 1 is behind TMD 5. In the right-hand monomer for both proteins, TMD 1 is on the far right, as would be expected for a mirror image. However, TMD 1 is now angled so the N-terminal end of the TMD is pointing out of the page, and no longer obscured by the yellow-green TMD 5, indicating TMD 1 is now in front of TMD 5, thus demonstrating the 180^{o} rotation of the right-hand monomer about its centre.

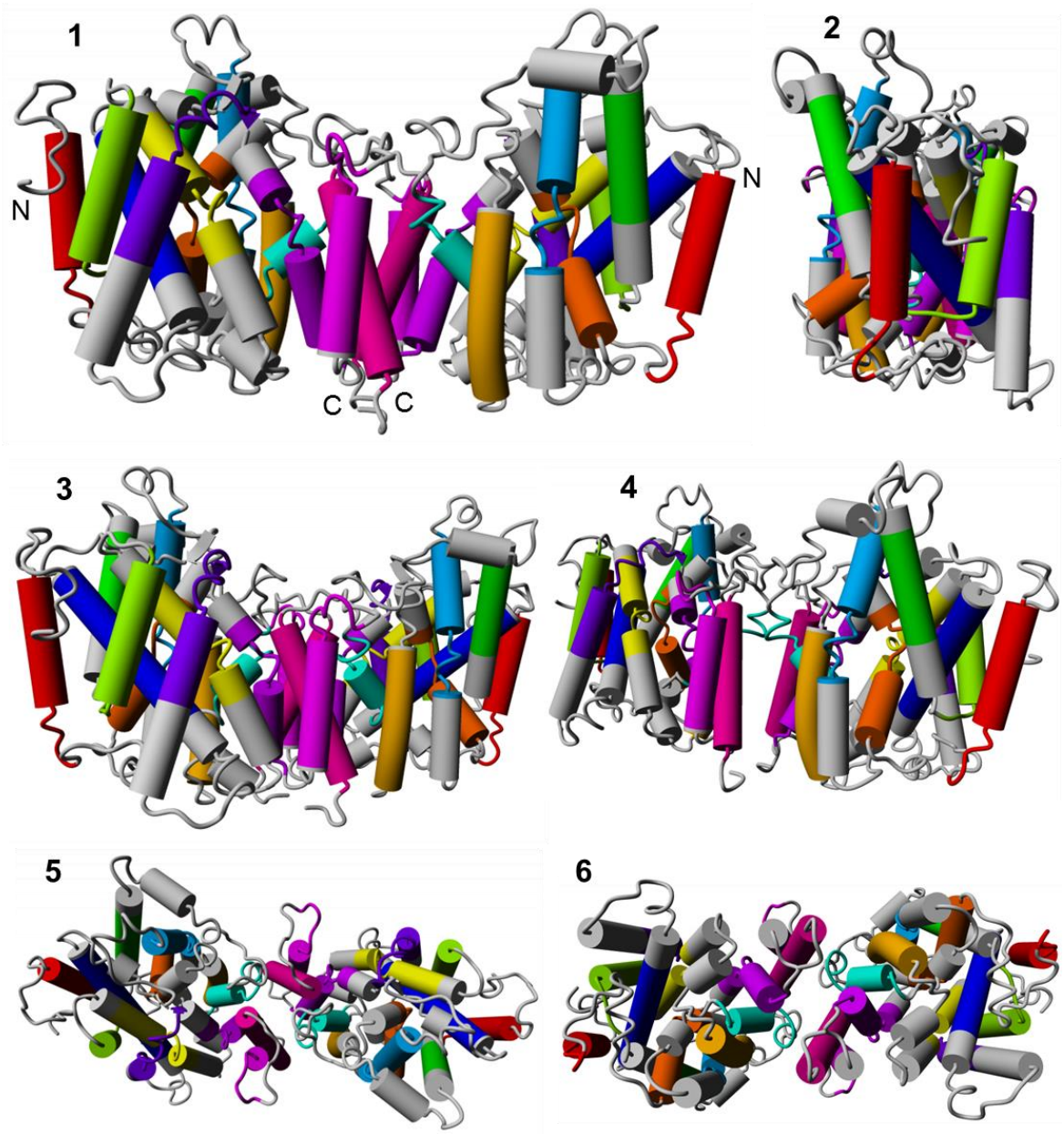

Figure 5-11 – Highlighting the transmembrane domains on the refined NIS homology model revealed an asymmetric dimeric structure. Transmembrane domains (TMDs) are coloured as a rainbow, with N-terminal TMD 1 coloured red through to the C-terminal TMD 13 coloured purple, and non-TMD regions coloured grey. All termini are labelled in panel 1. Structures are viewed in the membrane plane oriented so extracellular milieu is above the structure (panels 1-4), from the extracellular side (panel 5) and the intracellular side (panel 6).

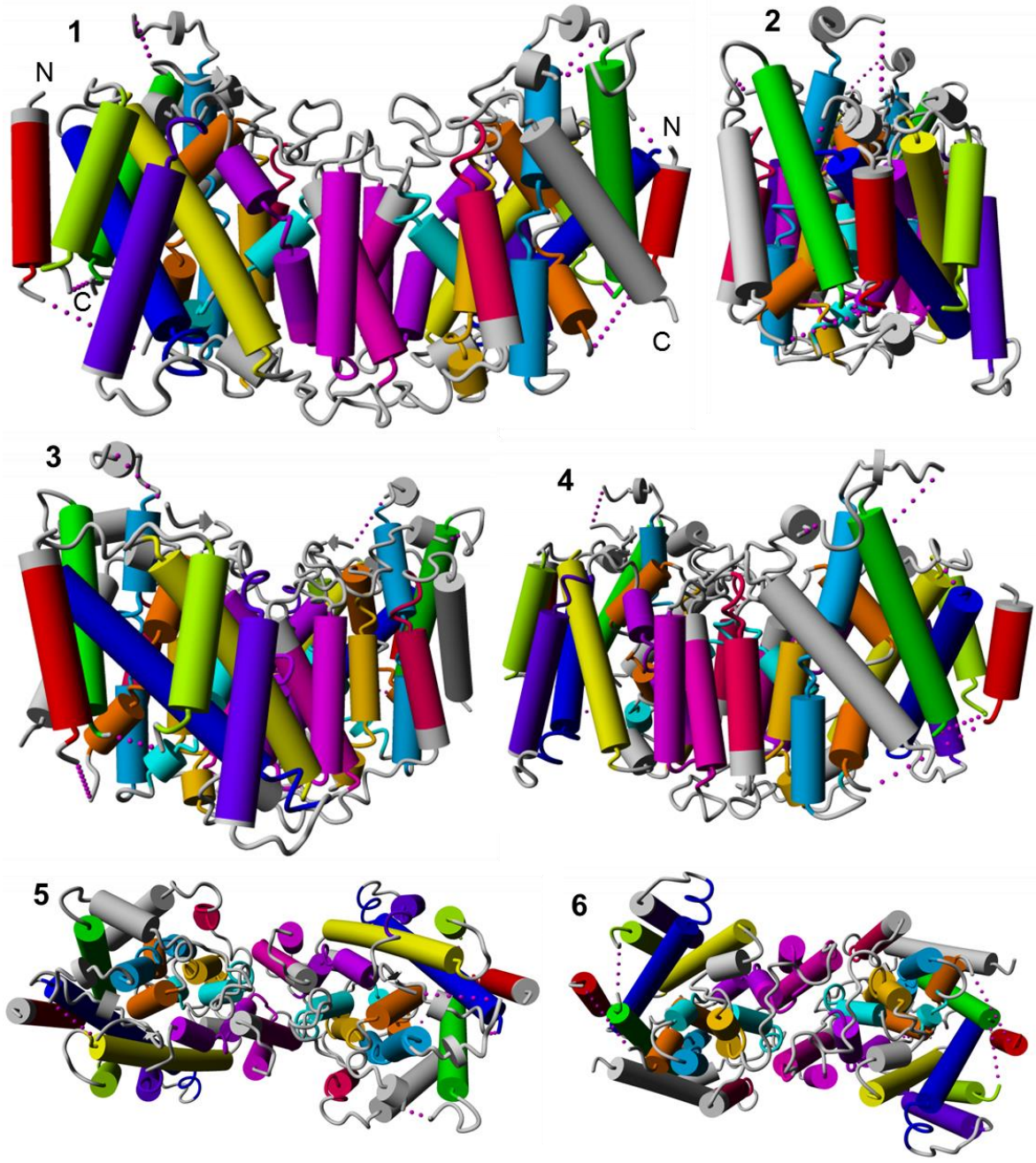

Figure 5-12 – Highlighting the transmembrane domains on the vSGLT crystal structure revealed an asymmetric dimeric structure. Transmembrane domains (TMDs) are coloured as a rainbow, with N-terminal TMD 1 coloured red through to the C-terminal TMD 14 coloured purple, and non-TMD regions coloured grey. All termini are labelled in panel 1. Structures are viewed in the membrane plane oriented so extracellular milieu is above the structure (panels 1-4), from the extracellular side (panel 5) and the intracellular side (panel 6).

5.3.3.2 The distribution of charged residues within the dimeric NIS model is as expected for membrane proteins, therefore demonstrating physiological relevance of the model

Given that the hydrophilicity of charged residues generally prevents their presence in TMDs due to the hydrophobic nature of the membrane, charged residues are predominantly located at the extra- and intracellular portions of membrane proteins in physiology. Therefore, to determine how physiologically relevant the NIS homology model is, the charged residues were identified on the model. As shown in Figure 5-13, the charged residues were located on the extracellular and intracellular surfaces of the NIS homology model but not the TMDs. This follows the expected distribution pattern of charged residues in membrane proteins, as illustrated on the vSGLT crystal structure in Figure 5-14, thereby demonstrating the physiological relevance of the NIS homology model and suggesting that the model is representative of the true NIS protein structure.

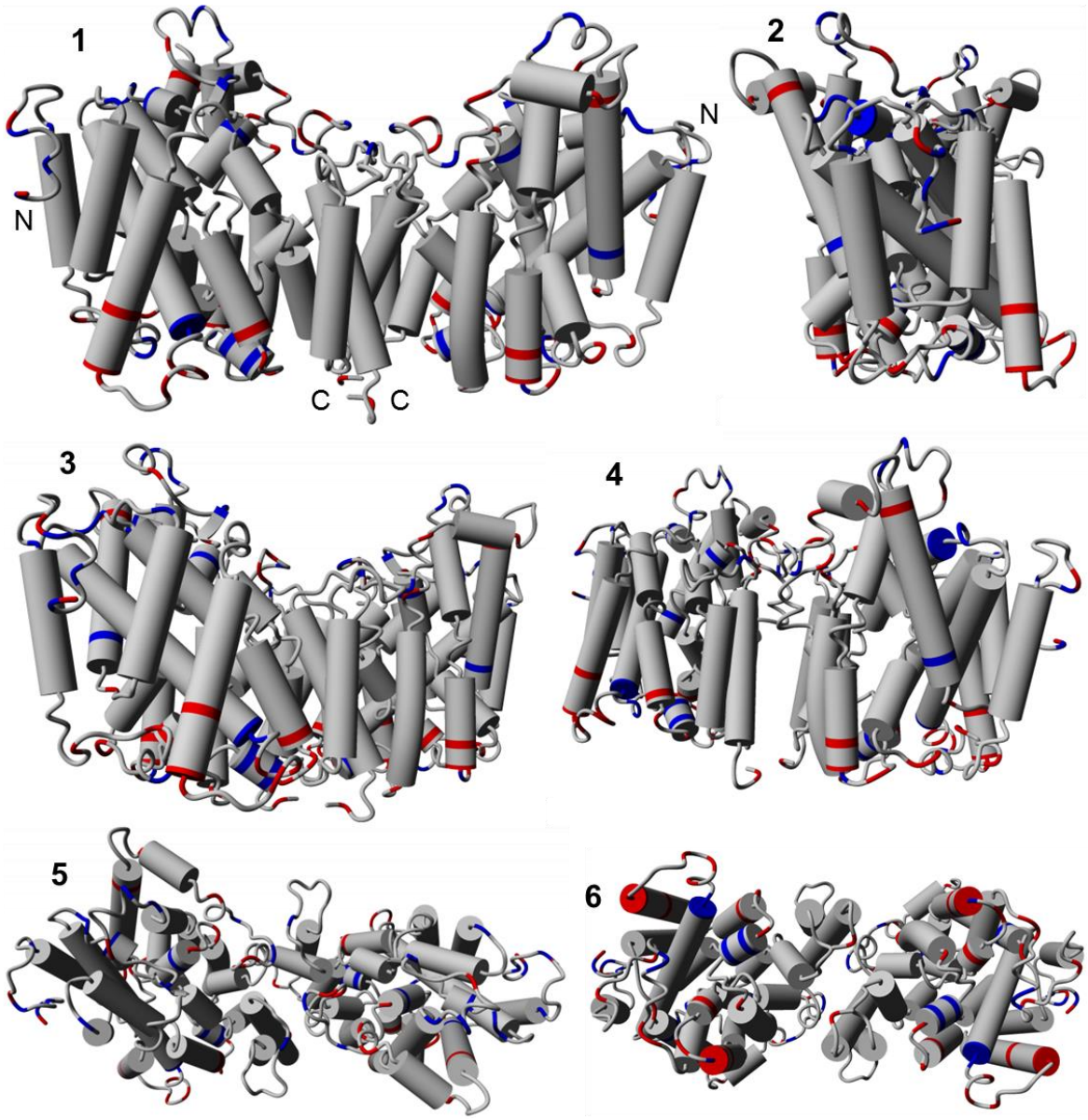

Figure 5-13 – Charged residues were located at the extra- and intracellular regions of the NIS homology model, thereby demonstrating that the model is physiologically relevant. Positively and negatively charged residues are shown in red and blue, respectively, while non-charged residues are in grey. Charged residues were located at the extra- and intracellular regions of the structure. All termini are labelled in panel 1. Structures are viewed in the membrane plane oriented so extracellular milieu is above the structure (panels 1-4), from the extracellular side (panel 5) and the intracellular side (panel 6).

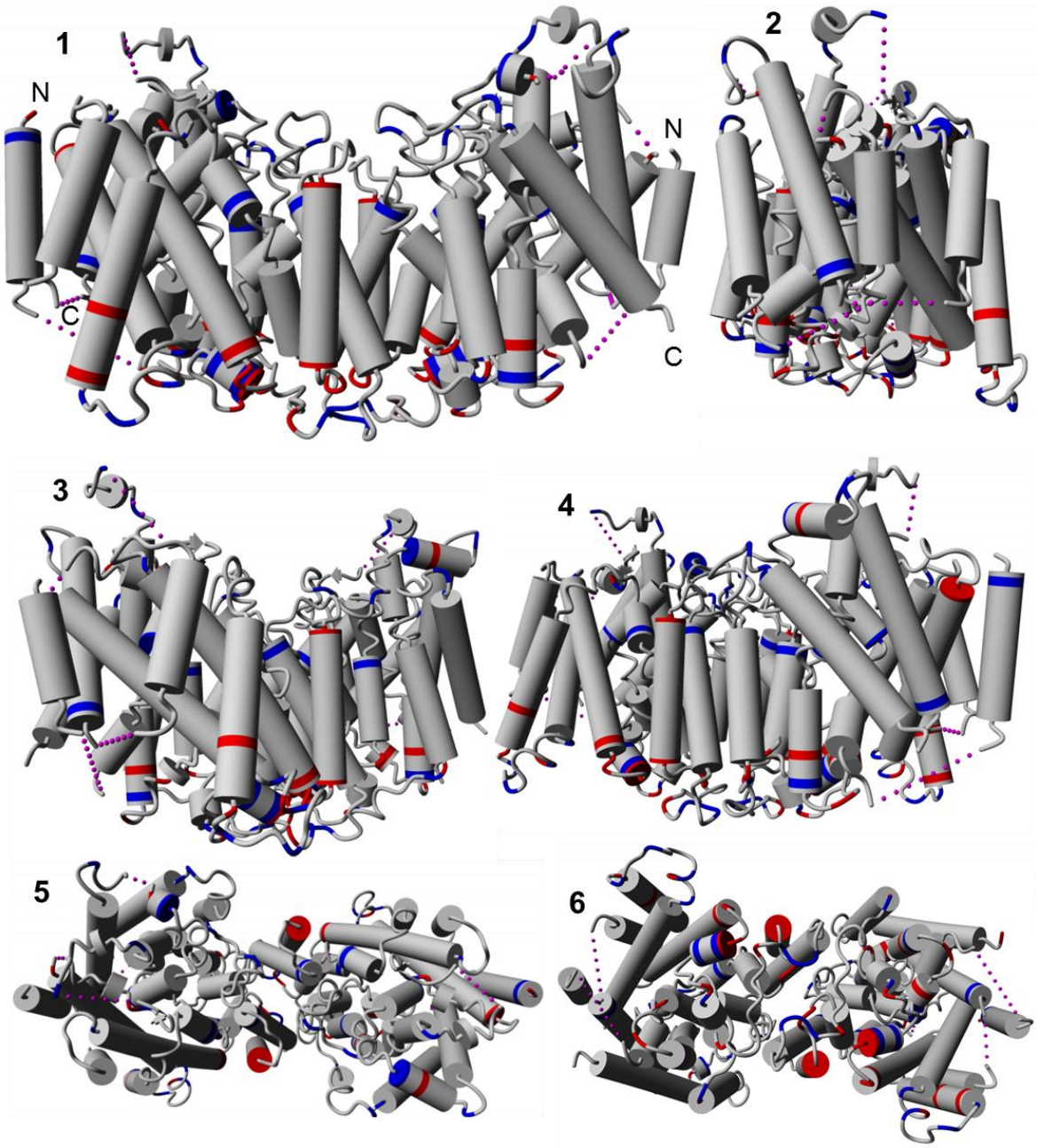

Figure 5-14 – The physiological distribution of charged residues within a membrane protein is illustrated on the vSGLT crystal structure. Positively and negatively charged residues are shown in red and blue, respectively, while non-charged residues are in grey. Charged residues were located at the extra- and intracellular regions of the structure. All termini are labelled in panel 1. Structures are viewed in the membrane plane oriented so extracellular milieu is above the structure (panels 1-4), from the extracellular side (panel 5) and the intracellular side (panel 6).

5.3.3.3 Locations of residues involved in sodium or substrate binding further validated the physiological relevance of the NIS model

Mutation analysis studies have elucidated many residues involved in the sodium or substrate binding of both NIS and vSGLT. Consequently, to further demonstrate the physiological relevance of the NIS homology model, the residues known to be involved in sodium or iodide binding were identified on the homology model. These residues were shown to cluster together, resulting in the formation of distinct sodium (magenta) and iodide (cyan) binding pockets in Figure 5-15. Similar binding pockets for sodium (magenta) and galactose (cyan) were observed on the vSGLT crystal structure in Figure 5-16. This further supports the physiological relevance of the NIS homology model and indicates that the model is likely to be an accurate representation of the actual NIS protein structure.

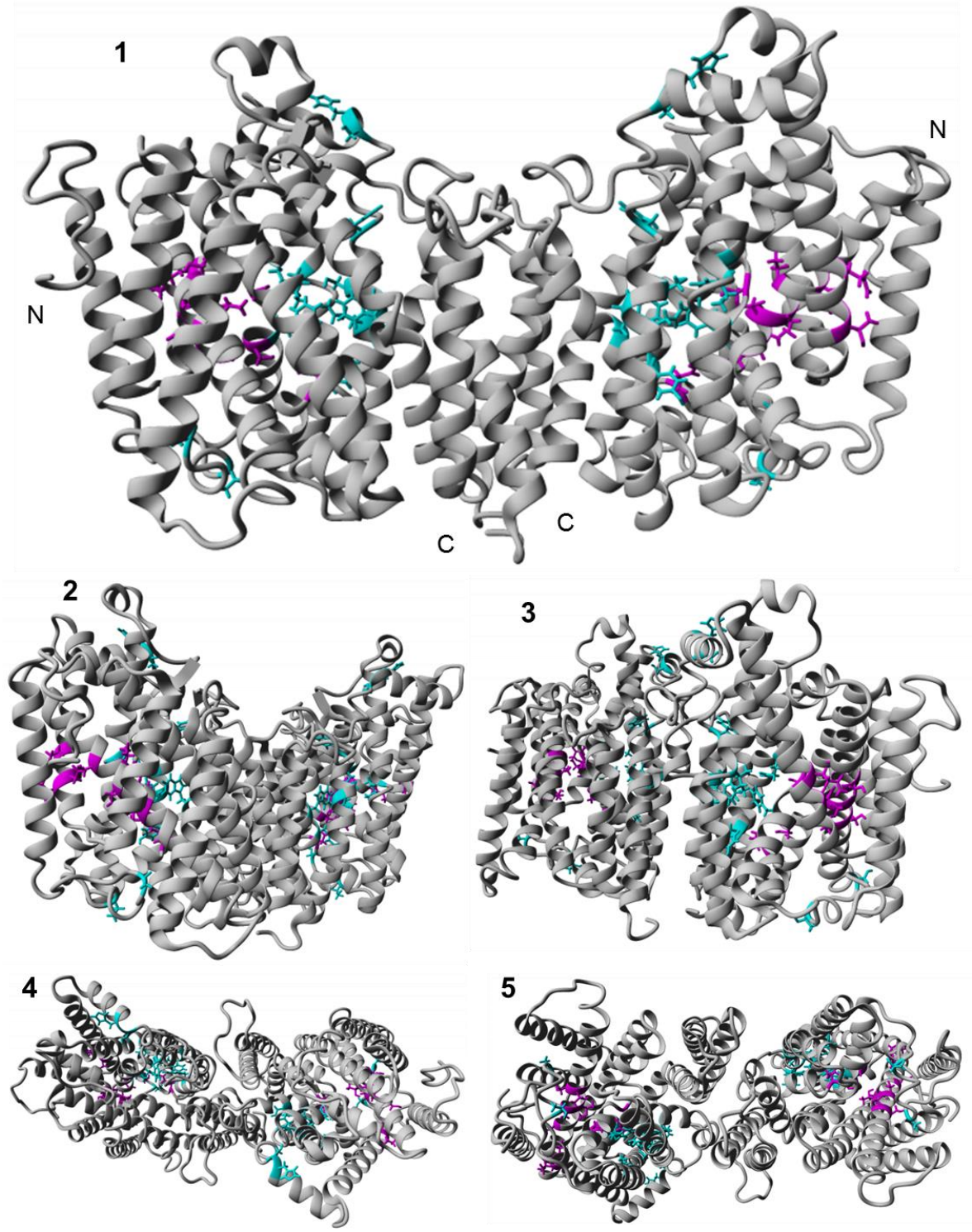

Figure 5-15 – Identifying residues known to be involved in sodium or iodide binding on the NIS homology model revealed distinct binding sites, further demonstrating the physiological relevance of the model. Residues known to be involved in sodium or iodide binding were shown in 'Stick' form and coloured in magenta and cyan, respectively, while remaining residues are coloured in grey. All termini are labelled in panel 1. Structures are viewed in the membrane plane oriented so extracellular milieu is above the structure (panels 1-3), from the extracellular side (panel 4) and the intracellular side (panel 5).

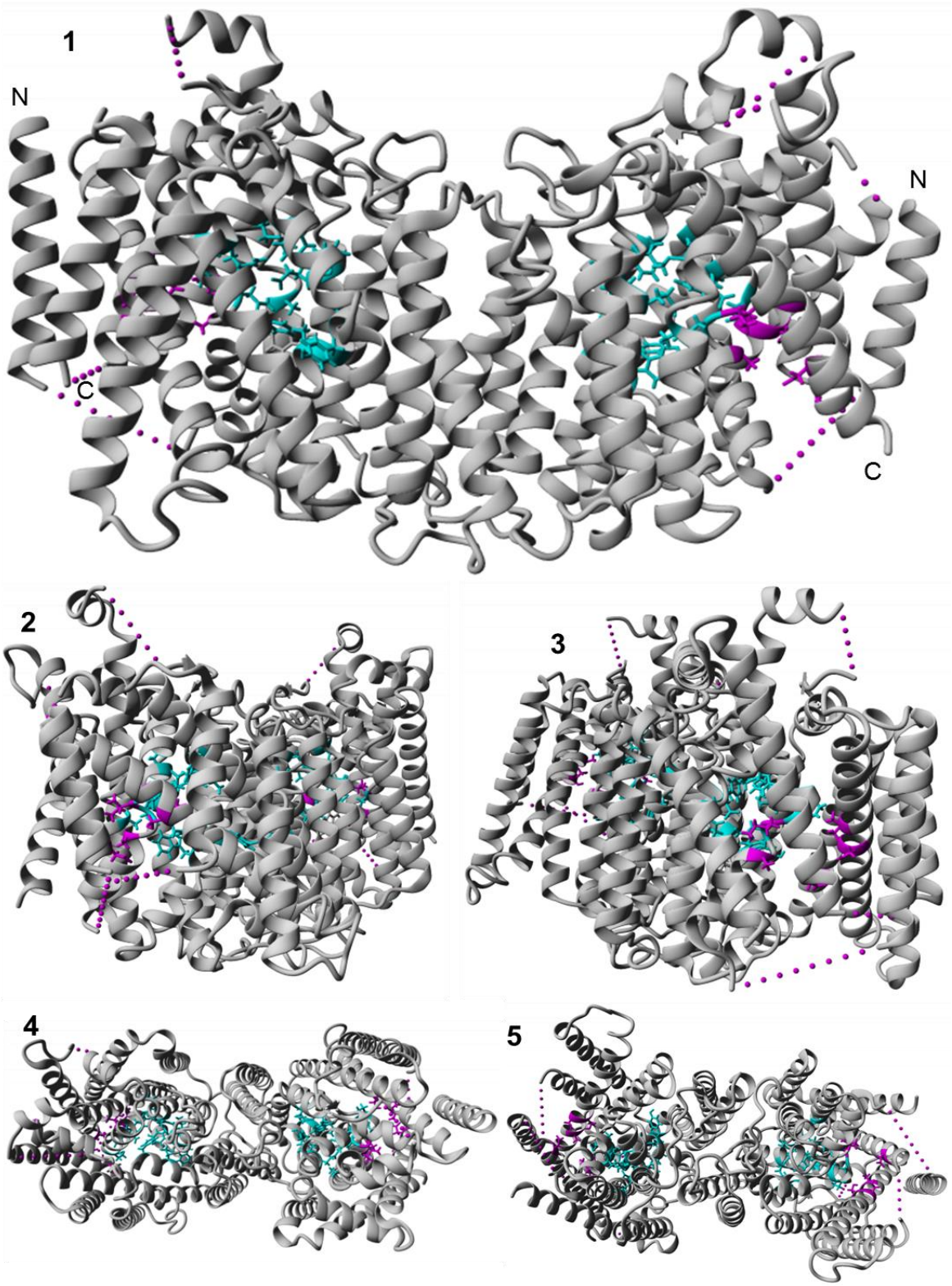

Figure 5-16 – Locations of the sodium and galactose binding sites on the vSGLT crystal structure. Residues known to be involved in sodium or galactose binding were shown in 'Stick' form and coloured in magenta and cyan, respectively, to highlight the binding sites. Remaining residues are coloured grey. All termini are labelled in panel 1. Structures are viewed in the membrane plane oriented so extracellular milieu is above the structure (panels 1-3), from the extracellular side (panel 4) and the intracellular side (panel 5).

5.3.4 Identification of residues potentially involved in NIS dimerisation

5.3.4.1 Dimerisation motifs identified in the literature are not located at the dimerisation interface of the NIS model

In order to provide an explanation as to why mutating the putative dimerisation motifs did not alter NIS dimerisation (as described in Chapter 4), the key residues in the glycine zipper motif (GZM) on TMD 12 and the leucine zipper motif (LZM) on TMD 6 were depicted on the NIS homology model in red and blue, respectively. Interestingly, Figure 5-17 revealed that neither motif was located close enough to the opposing monomer (shown in cyan or magenta) to be likely to be involved in NIS dimerisation.

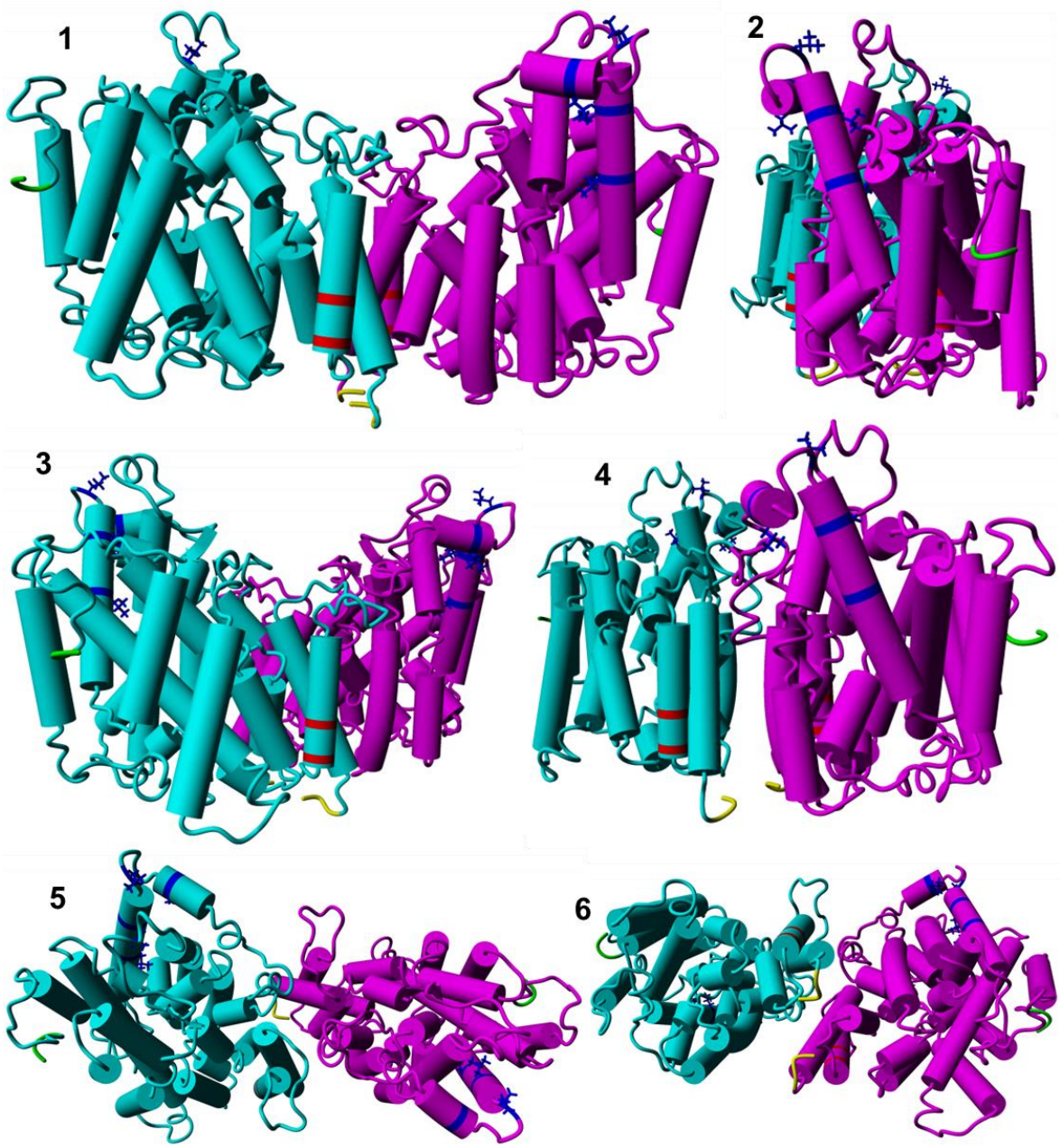

Figure 5-17 – The putative dimerisation motifs are not in close enough proximity to the opposing monomer to be involved in NIS dimerisation. Side chains of the key residues in the glycine zipper motif and leucine zipper motif are shown in 'Stick' form and coloured in red and blue, respectively. Remaining residues of each monomer are coloured cyan and magenta, respectively. All termini are labelled in panel 1, with N termini coloured green and C termini yellow throughout. Structures are viewed in the membrane plane oriented so extracellular milieu is above the structure (panels 1-4), from the extracellular side (panel 5) and the intracellular side (panel 6).

5.3.4.2 Eight novel residues potentially involved in NIS dimerisation were identified from the homology model

To identify resides in close enough proximity to the opposing monomer to be potentially involved in NIS dimerisation, a search was performed in YASARA to reveal residues less than 3Å from the opposing monomer. This identified the following eight residues: D237, Y242, T243, F244, Q471, A525, K554 and R555. The side chains of these residues are shown in Figure 5-18 to illustrate the location of these residues. Remarkably, this revealed two distinct putative dimerisation interfaces within the NIS homology model structure. The majority of the identified residues cluster together at the extracellular surface of the model and seem to form a large primary putative dimerisation interface, (circled in red), while two of the residues (K554 and R555) are located at the intracellular C-terminus and appear to form a smaller secondary putative dimerisation interface (circled in blue).

Figure 5-18 – Eight novel residues were identified as potentially involved in NIS dimerisation using the refined NIS homology model and appear to form two distinct putative dimerisation interfaces. Side-chains of residues found to be <3Å from the opposing monomer are shown in 'Stick' form, and monomers are coloured cyan or magenta, respectively. The residues comprising the larger interface (circled in red) are labelled, while the residues invovled in the smaller interface (circled in blue) are also identified. All termini are labelled in panel 1. Structures are viewed in the membrane plane oriented so extracellular milieu is above the structure (panels 1-3), from the extracellular side (panel 4) and the intracellular side (panel 5).

5.4 Discussion

In this chapter, a refined homology model of NIS dimerisation was proposed which addressed the lack of effect of mutated putative dimerisation motifs on NIS dimerisation described in Chapter 4, and identified novel residues which may be involved in dimerisation.

5.4.1 A novel homology model of NIS dimerisation was developed

Although the initial structure of dimeric NIS predicted by Phyre2 was modelled against the vSGLT crystal structure with a good degree of confidence (74% residues modelled at >90% confidence), there were still large portions of the NIS primary amino acid sequence that could not be modelled (as illustrated in Figure 5-3), with 95 residues being modelled *ab initio*. This is a highly unreliable method of modelling as it is performed without a template due to a lack of homology (Kelley and Sternberg, 2009). To ascertain residues involved in NIS dimerisation with improved accuracy and confidence, the model was improved by identifying, and subsequently removing, regions of poor homology.

Membrane proteins consist of two main components: transmembrane domains (TMDs) and connecting loops, which are either extracellular or intracellular depending on the orientation of the protein. This is termed protein secondary structure, or 'topology' (Krogh et al., 2001). TMDs have a rigid, α-helical structure, enabling them to be easily modelled but connecting loops have a much more disordered structure. Consequently, while predicting regions of disorder is straightforward, it is near-impossible to accurately model regions of disordered structure, owing to their much more fluid nature (Kelley and Sternberg, 2009, Krogh et al., 2001). Hence, in order to obtain a NIS model with greater homology to vSGLT, it was imperative to best predict the locations of the TMDs of NIS.

To do this, a wide variety of topology predictions were performed (see section 5.2.2.1) on the NIS primary sequence. Although TMDs of vSGLT had been identified from the crystal structure (Table 5-1; (Faham et al., 2008)), the same topology predictions were also performed on the vSGLT primary sequence to demonstrate the accuracy of the different predictions to correctly identify TMDs. As experimental evidence confirmed the topology of NIS as 13 TMDs with an extracellular N-terminus and intracellular C-terminus (Ravera et al., 2017) and vSGLT as 14 TMDs with extracellular N- and C-termini (Xie et al., 2000, Faham et al., 2008), any variations predicting a different topology were excluded. Compared to the actual vSGLT TMDs (Figure 5-5, green; Table 5-1), no single prediction site was able to correctly identify all vSGLT TMDs. Despite this, there was significant overlap between most of the sites, which correctly identified large portions of vSGLT TMDs. However, the least reliable topology prediction was TMPred (Figure 5-5, yellow), as this had the least overlap with the other sites and incorrectly identified several large regions of vSGLT as TMDs. Thus, it can be assumed with a good degree of confidence that areas predicted as TMDs by multiple prediction sites (with the exception of TMPred) have been correctly identified, but the extremities of the TMDs remain uncertain.

Given this information, the regions of NIS involved in TMDs could be predicted based on overlap between multiple topology prediction sites in Figure 5-4. However, Table 5-1 is by no means an exhaustive list and it is highly likely that other residues are involved in NIS TMDs but remain unidentified without a crystal structure of NIS. Furthermore, there is a break in the helical structure of vSGLT TMDs 2 and 7, which has been widely hypothesised as important for transport function of the protein due to structural homology here with other families of sodium-coupled transporters (Faham et al., 2008, Karpowich and Wang, 2008, Abramson and Wright, 2009, Krishnamurthy et al., 2009). Given then that NIS and vSGLT

are members of the same protein family and widely assumed to have similar structures, it is reasonable to expect NIS to have similar breaks in its equivalent TMDs, especially if these discontinuous helices are pertinent to function. However, where these breaks occur in NIS cannot be identified without a crystal structure, as topology prediction sites are not designed to pick up such unusual breaks in TMD sequence.

To ascertain how homologous the two proteins are, their primary sequences were aligned. Two global sequence alignments were performed to obtain a better alignment, because alignment tools often use different algorithms which can affect the results (Rice et al., 2000). To see how homologous the secondary structures of the two proteins are, the residues identified as TMDs in Table 5-1 were depicted on the two alignments. This demonstrated strong homology between the TMDs 1-12 of the two proteins, but there was much less homology between their C-termini. This is to be expected for several reasons. Firstly, they have different topologies: vSGLT has 14 TMDs with extracellular N- and C-termini (Xie et al., 2000, Faham et al., 2008), while NIS has 13 TMDs with an extracellular N- and intracellular C-terminus (Levy et al., 1998a). Secondly, NIS is a larger protein (643 residues vs. 580), with its C-terminus comprising approximately 100 residues (Darrouzet et al., 2014), thus has large portions of disordered structure which cannot be modelled. Finally, there is significant structural homology in TMDs 1-12 between vSGLT and other bacterial sodium-coupled transporters of known structure (LeuT (Yamashita et al., 2005), Mhp1 (Weyand et al., 2008), BetP (Ressl et al., 2009), CaiT (Schulze et al., 2010) and AdiC (Gao et al., 2009, Fang et al., 2009)), but these protein structures vary greatly towards their C-termini. This suggests that, while the first 12 TMDs of sodium-coupled transporters are important for general transporter function, the C-terminal region might play alternative, as yet unidentified, roles for protein function specific to individual transporters.

Nevertheless, to design a model of NIS structure with improved homology to vSGLT, the large regions of disorder from the NIS primary structure needed to be removed. To do this, the EMBOSS Needle alignment was used to identify large sections of disordered sequence, owing to its higher alignment score compared to EMBOSS Stretcher (419.0 vs 181.0). As a result, both the disordered intracellular C-terminus from S556 onwards and the large extracellular loop between TMDs 12 and 13 (from T472 to Y524) were removed from the NIS sequence. EMBOSS Needle alignment was then performed between this modified NIS primary sequence and vSGLT (Figure 5-8), and the resultant increase in alignment score from 419.0 to 425.5 confirmed that removal of disordered regions of NIS improved its primary sequence homology with vSGLT.

Phyre2 was then used to predict the 3D structure of this modified NIS primary sequence (Figure 5-9). Due to improved primary sequence homology, the resultant structure was predicted to a much greater degree of confidence, with 93% residues modelled with >90% confidence (compared to 74% for the original model) and a substantial reduction in the number of residues modelled *ab initio* (33 vs. 95). Furthermore, the RMSD of atomic positions value calculated during the alignment of NIS predicted structure onto vSGLT crystal structure in YASARA decreased from 1.178Å (Figure 5-3) to 0.993Å (Figure 5-10), indicating a better alignment with the modified NIS structure (Krieger and Vriend, 2014). Given this improvements, this was taken to be the final model of dimerised NIS.

5.4.2 The physiological relevance of the dimeric NIS homology model was demonstrated by the appropriate locations of residues which are charged or known to be involved in sodium or iodide binding

As the crystal structure for NIS remains elusive, the physiological relevance of this model was investigated to determine the likelihood that this model is reflective of the true NIS structure. First, the locations of charged residues were identified within the structure, as charged residues are rarely present in TMDs due to unfavourable energetics (Ulmschneider and Sansom, 2001). As Figure 5-13 revealed charged residues to be predominantly excluded from the TMDs of our NIS model in a similar pattern to that of the vSGLT crystal structure (Figure 5-14), this adds weight to this model having a physiologically relevant structure.

To then determine whether our NIS model is likely to be functional, residues known to be important for sodium and/or iodide binding were identified on the model. To achieve this, a literature search was performed for NIS mutagenesis studies identifying residues directly involved in binding of sodium and/or iodide, rather than transport (Levy et al., 1998b, De la Vieja et al., 2007, Paroder-Belenitsky et al., 2011, Ferrandino et al., 2016, Vergara-Jaque et al., 2017). Additional residues proposed to be involved in the iodide binding site using computational docking, molecular dynamics simulations and free energy calculations on a homology model of NIS were also included (Vergara-Jaque et al., 2017). When located on the model, these residues clustered together, forming specific binding pockets for sodium and iodide (Figure 5-15) which strongly resembled the sodium and galactose binding sites identified on the vSGLT crystal structure (Figure 5-16 (Faham et al., 2008, Xie et al., 2000)). As such binding sites are required for transporter function (Abramson and Wright, 2009), this further strengthens the functional relevance of this model.

5.4.3 Eight novel residues were identified from the model as potentially important for NIS dimerisation

While vSGLT was crystallised as a dimer, no investigation was carried out into elucidating the dimerisation interface (Faham et al., 2008). Furthermore, studies on previous homology models of NIS based on the vSGLT structure focused on understanding transporter function and did not explore dimerisation (Portulano et al., 2014, Darrouzet et al., 2014). As the data presented in Chapter 3 confirmed that NIS dimerisation occurs, but putative dimerisation motifs are unlikely to be involved (Chapter 4**)**, a novel homology model of NIS dimerisation was created (Figure 5-9) to identify residues important for NIS dimerisation, which could be experimentally manipulated to illuminate the role dimerisation plays in NIS function.

To help explain why mutating the putative dimerisation motifs did not alter NIS dimerisation, these motifs were located on the homology model of NIS dimerisation. Given the results in Chapter 4, it was unsurprising to observe that neither motif directly interacted with the opposite monomer (Figure 5-17). Given that these dimerisation motifs are known to be important for helical packing (Hakoshima, 2005, Krylov and Vinson, 2001, Senes et al., 2000, Senes et al., 2004, Russ and Engelman, 2000), and that our mutants of these motifs resulted in proteins that could no longer be processed and trafficked to the plasma membrane, it was proposed that these motifs are instead crucial for the proper folding of the TMDs of the NIS monomer.

To then identify residues that are potentially involved in NIS dimerisation, a search was conducted for residues <3Å (0.3nm) from the opposite monomer. This was selected as a cut-off because this is the closest atoms can be to each other given their Van der Waals radii

(1.2Å for hydrogen; 1.4Å for oxygen (Chemistry-LibreTexts, 2018a)) and the length of various atomic interactions that could occur (see Table 5-2).

Interaction	Distance (Å)
Van der Waals interaction	3-6
Hydrogen bond	3
Ionic bond (salt bridge)	2.5

Table 5-2 – Distances (in Å) of intermolecular interactions. Adapted from (Chemistry-LibreTexts, 2018b)

While it is possible that other residues are interacting at a greater distance than 3Å, searching for residues at greater distances increases the chance of false-positive results, i.e. identifying residues that are not directly interacting. This search revealed eight novel residues which appear to form a putative dimerisation interface: D237, Y242, T243, F244, Q471, A525, K554 and R555 (Figure 5-18), which were mutated in order to investigate their role in NIS dimerisation in Chapter 6.

5.4.4 Concluding statements

In the current chapter, a homology model of NIS dimerisation was presented which was intensively refined and validated to improve its accuracy. This model demonstrated that the putative dimerisation motifs were not in close enough proximity to be involved in NIS dimerisation, thus explaining the results in Chapter 4. Using the model, eight novel mutants were proposed to be important for dimerisation based on their proximity in the model, which were experimentally manipulated to investigate their role in NIS dimerisation in Chapter 6

CHAPTER 6 – INVESTIGATING THE PUTATIVE DIMERISATION INTERFACE

6.1 Introduction

The data described in Chapter 3 demonstrated that the wild-type NIS protein does dimerise. However, the studies performed in Chapter 4 indicated that mutating the proposed putative dimerisation motifs did not alter NIS dimerisation, suggesting that other residues might be involved. This prompted the generation of a homology model of dimerised NIS structure based on the dimeric crystal structure of the family member protein vSGLT, which was presented in Chapter 5. This revealed eight novel residues which are within close enough proximity (i.e. less than 3Å) to be potentially involved in NIS dimerisation. These residues are generally clustered together to form two distinct putative dimerisation interfaces, as illustrated in Figure 6-1. The larger primary putative dimerisation interface is positioned at the extracellular surface of the NIS dimer and is comprised of residues D237, Y242, T243 and F244, which are located in the region where the third extracellular loop meets the start of TMD 7, and residues Q471 and A525, which are towards the start and end of the sixth extracellular loop (between TMDs 12 and 13). However, these residues are located next to each other in the homology model, as the large extracellular loop between the two residues was removed from the model in order to improve the homology and alignment of NIS to vSGLT, thereby refining the model. There is also a smaller secondary putative dimerisation interface towards the intracellular NIS C-terminus, comprising residues K554 and R555. These are the last residues used in the homology model, as the long, intrinsically unstructured NIS C-terminus was removed to further refine the homology model.

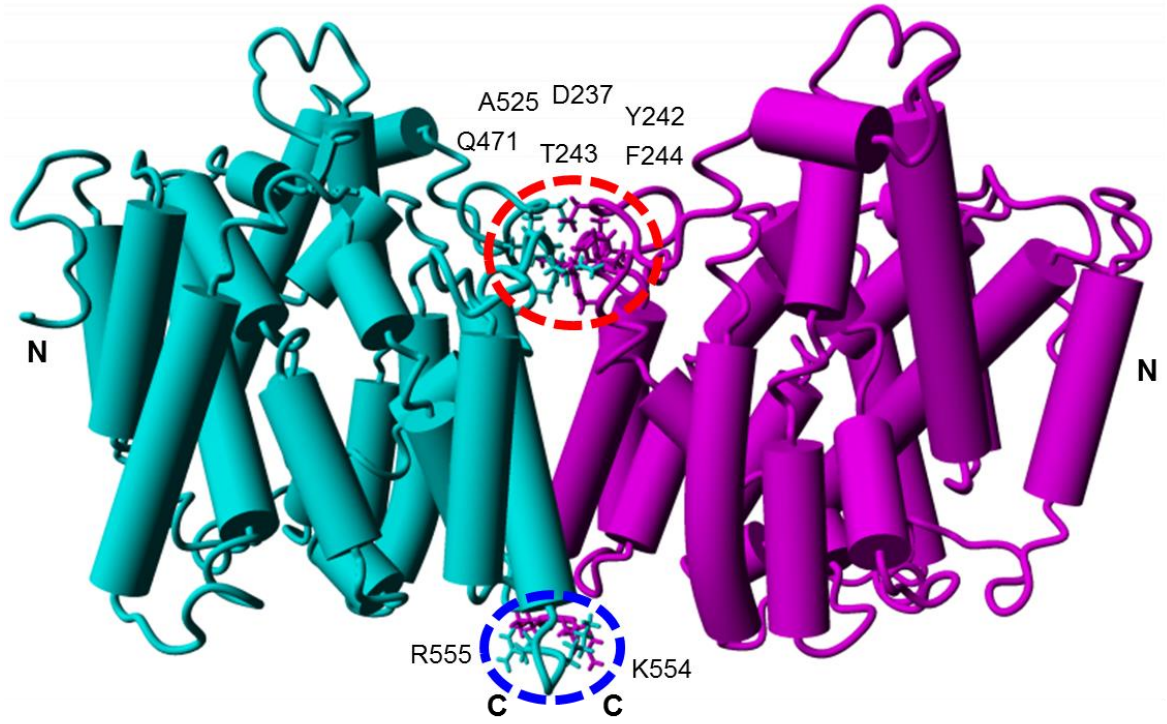

Figure 6-1 – The homology model of NIS dimerisation identified eight novel residues as close enough in proximity to potentially mediate dimerisation. The side chains of the residues found to be <3Å from the opposing monomer are shown in 'Stick' form. The majority of residues (D237, Y242, T243, F244, Q471 and A525) appear to cluster together in a primary putative interface at the extracellular surface of the dimer (circled in red), while there seems to be a secondary putative dimerisation interface at the intracellular surface comprised of residues K554 and R555 (circled in blue).

Given that the homology model of NIS dimerisation proposed a putative dimerisation interface, the purpose of this chapter was to investigate whether mutating these residues affects NIS dimerisation, with the overarching aim of exploring the importance of dimerisation for NIS function.

6.2 Methods

All methods used in this chapter are detailed in Chapter 2.

6.3 Results

To establish whether the residues within this putative dimerisation interface do mediate NIS dimerisation and subsequently investigate the importance of dimerisation for NIS function, potential interactions between these residues must first be disrupted. To achieve this, site-

directed mutagenesis was performed to generate NIS plasmids each with a different single point mutation to disrupt interactions mediated by the side chain of individual residues. While this successfully generated five mutants (D237A, Y242A, T243A, Q471A and A525F, see section 9.2), the primers designed to generate the F244A, K554A and R555A mutants failed. As the majority of the novel residues had been successfully mutated, particularly within the primary putative dimerisation interface, the three failed mutants were abandoned and subsequent experiments were carried out on the five successful mutants.

6.3.1 Characterisation of the putative dimerisation interface NIS mutants demonstrates the importance of the majority of these residues for NIS function

Before examining whether these mutations altered NIS dimerisation, the mutants were first extensively characterised to ascertain if NIS expression, localisation and function was affected by the mutation.

6.3.1.1 Mutation of residues in the putative dimerisation interface alters NIS protein expression

Western blot analysis was conducted on lysates of SW1736 and HeLa cells expressing WT or mutant NIS constructs tagged with HA at the C-terminus using the mouse anti-HA primary antibody in order to investigate whether mutating residues within the putative dimerisation interface affects NIS protein expression.

Figure 6-2 illustrates the impact of mutating putative dimerisation interface residues on NIS protein expression in SW1736 and HeLa cells. There are two forms of WT NIS (lane 2): a mature, fully-glycosylated form between 75-100kDa and an immature, non-glycosylated form at ~60kDa. The intensity of the bands reflects the relative proportion of the two forms,

with the mature form being the most abundant in WT NIS. With the exception of Q471A (lane 6), which had a similar banding pattern to WT, the proportion of glycosylated vs. non-glycosylated NIS was lower for the mutants compared to WT. This indicates that mutating the majority of the putative dimerisation interface residues impairs NIS protein maturation.

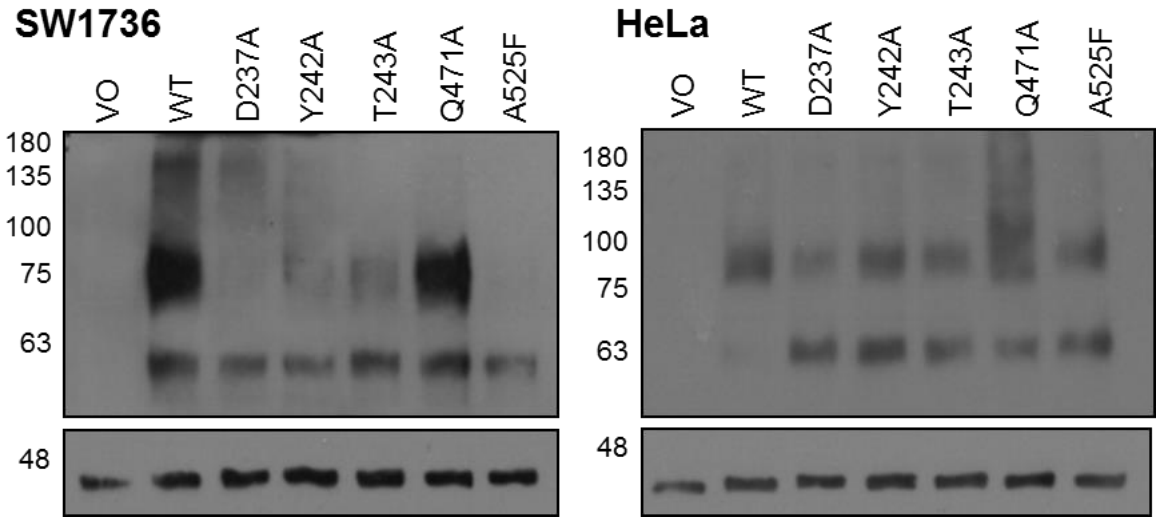

Figure 6-2 – Mutating residues within the putative dimerisation interface alters NIS glycosylation. SW1736 (left) and HeLa (right) cells were transfected with empty pcDNA3.1(+) vector (VO (lane 1)), wild-type NIS-HA (WT (lane 2)) or HA-tagged NIS with a mutation in one of the residues in the putative dimerisation interface (lanes 3-7). Western blot analysis was performed using the mouse anti-NIS antibody. A band at 75-100kDa represents the fully glycosylated, mature form of NIS, while a band at ~60kDa represents the non-glycosylated, immature form of NIS. β-actin primary antibody was used as a loading control. (n=2).

6.3.1.2 NIS localisation at the plasma membrane is affected by mutating residues in the putative dimerisation interface

To determine whether mutating residues within the putative dimerisation interface alters NIS subcellular localisation, immunofluorescence analysis was performed on SW1736 and HeLa cells expressing WT or mutant NIS constructs tagged at the C-terminus with HA using the mouse anti-HA primary antibody and the rabbit anti-Na^+/K^+-ATPase primary antibody as a plasma membrane marker.

The effect of mutating residues in the putative dimerisation interface is shown in Figure 6-3 (SW1736 cells) and Figure 6-4 (HeLa cells). Colocalisation (yellow) between NIS (green)

and the plasma membrane marker (red) represents membranous expression of WT NIS. A similar amount of colocalisation was observed with Q471A, indicating that this mutant is also expressed at the membrane. However, no membrane localisation was observed for the mutants D237A or A525F. Interestingly, while the majority of Y242A and T243A NIS protein was intracellularly retained, a small proportion of both mutants was expressed at the plasma membrane. This demonstrates that the trafficking to the plasma membrane of NIS with mutations in the putative dimerisation interface is usually impaired, but to different extents depending on the mutation, suggesting that some mutations may be more tolerated than others.

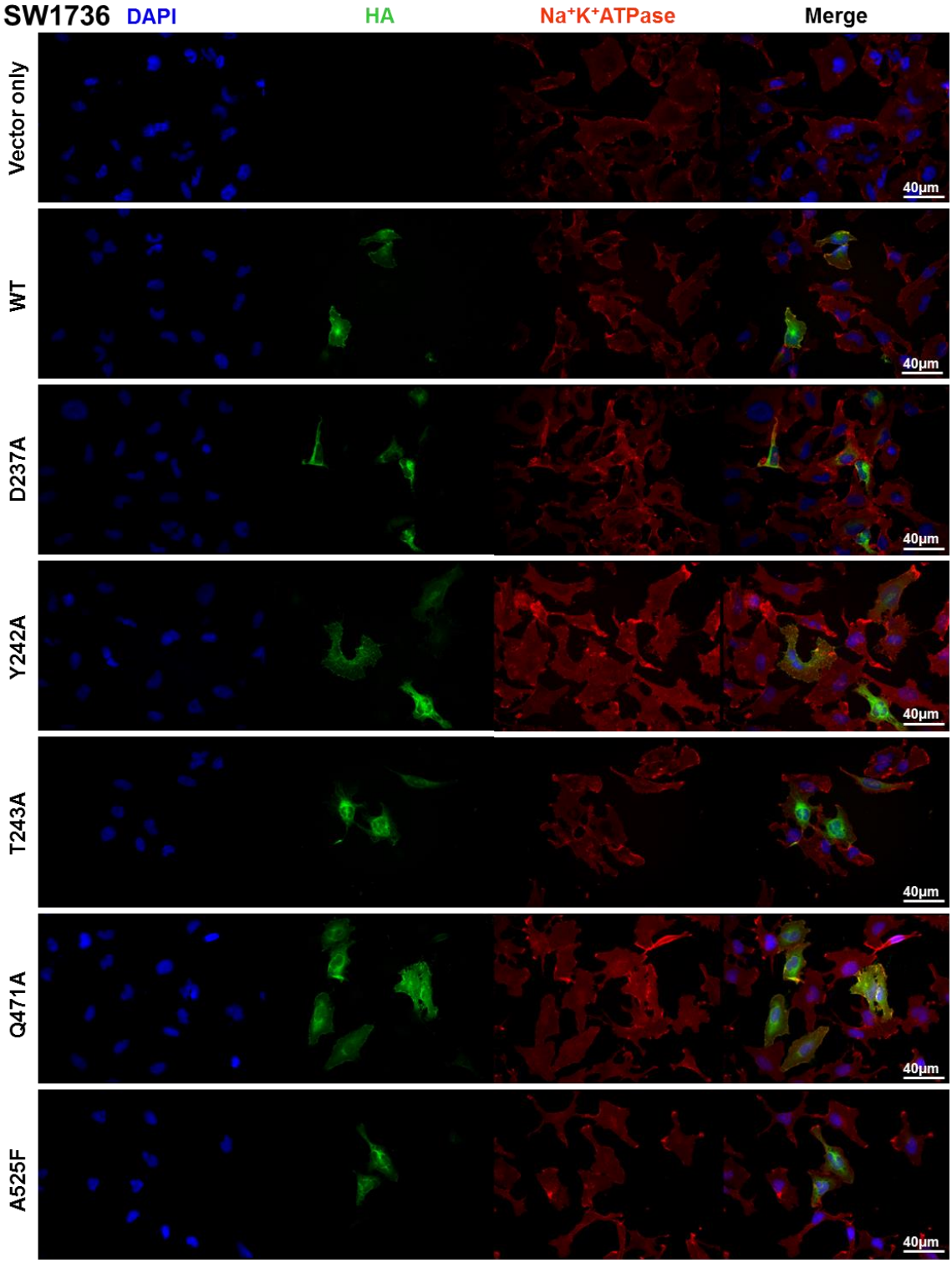

Figure 6-3 – Mutation of the putative dimerisation interface residues affects NIS localisation at the plasma membrane in SW1736 cells. Cells were transfected with empty pcDNA3.1(+) vector (VO), wild-type NIS-HA (WT) or HA-tagged NIS with a mutation in one of the residues of the putative dimerisation interface. Immunofluorescence analysis was performed using mouse anti-HA primary antibody to visualise NIS (in green), while rabbit anti-Na^+/K^+-ATPase primary antibody was used as a plasma membrane marker (in red). Nuclei are visualised in blue using Hoescht stain. Single channels and merged images are shown in A, and enlarged merged images are shown in B (overleaf). 40x magnification. (n=2).

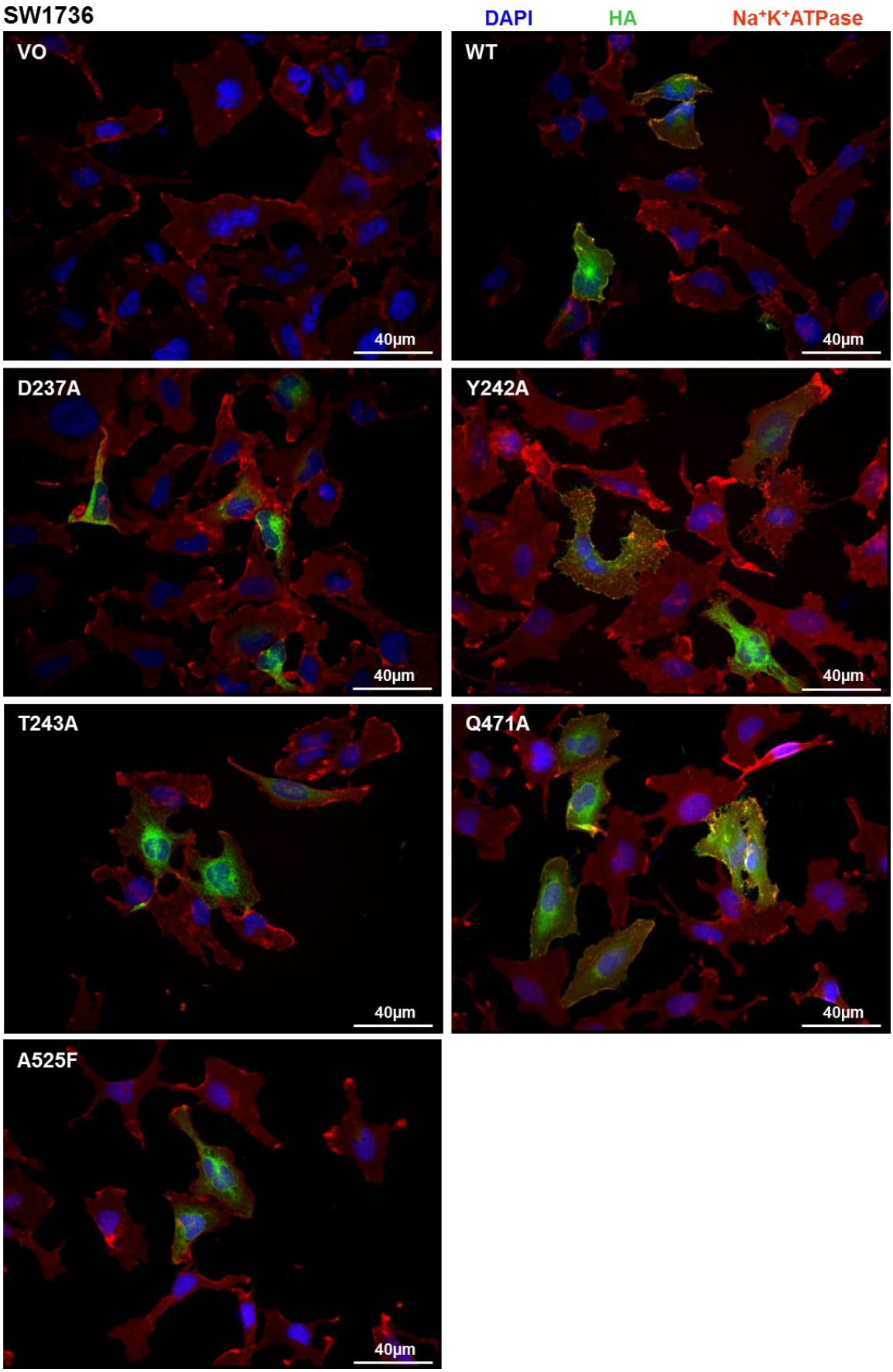
SW1736
DAPI
HA
Na+K+ATPase
VO
WT
D237A
Y242A
T243A
Q471A
A525F
40µm

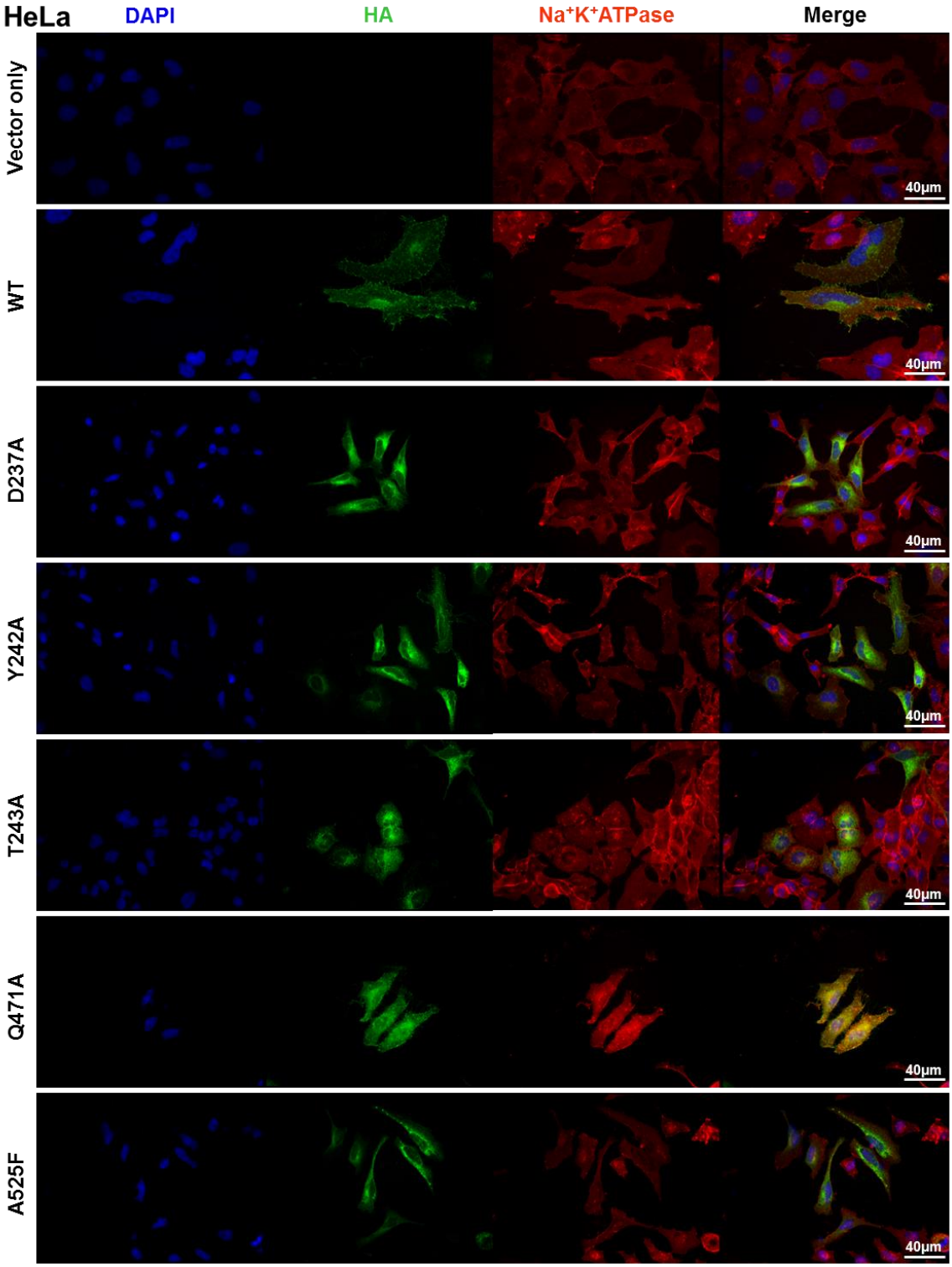

Figure 6-4 – Mutation of the putative dimerisation interface residues affects NIS localisation at the plasma membrane in HeLa cells. Cells were transfected with empty pcDNA3.1(+) vector (VO), wild-type NIS-HA (WT) or HA-tagged NIS with a mutation in one of the residues of the putative dimerisation interface. Immunofluorescence analysis was performed using mouse anti-HA primary antibody to visualise NIS (in green), while rabbit anti-Na^+/K^+-ATPase primary antibody was used as a plasma membrane marker (in red). Nuclei are visualised in blue using Hoescht stain. Single channels and merged images are shown in A, and enlarged merged images are shown in B (overleaf). 40x magnification. (n=2).

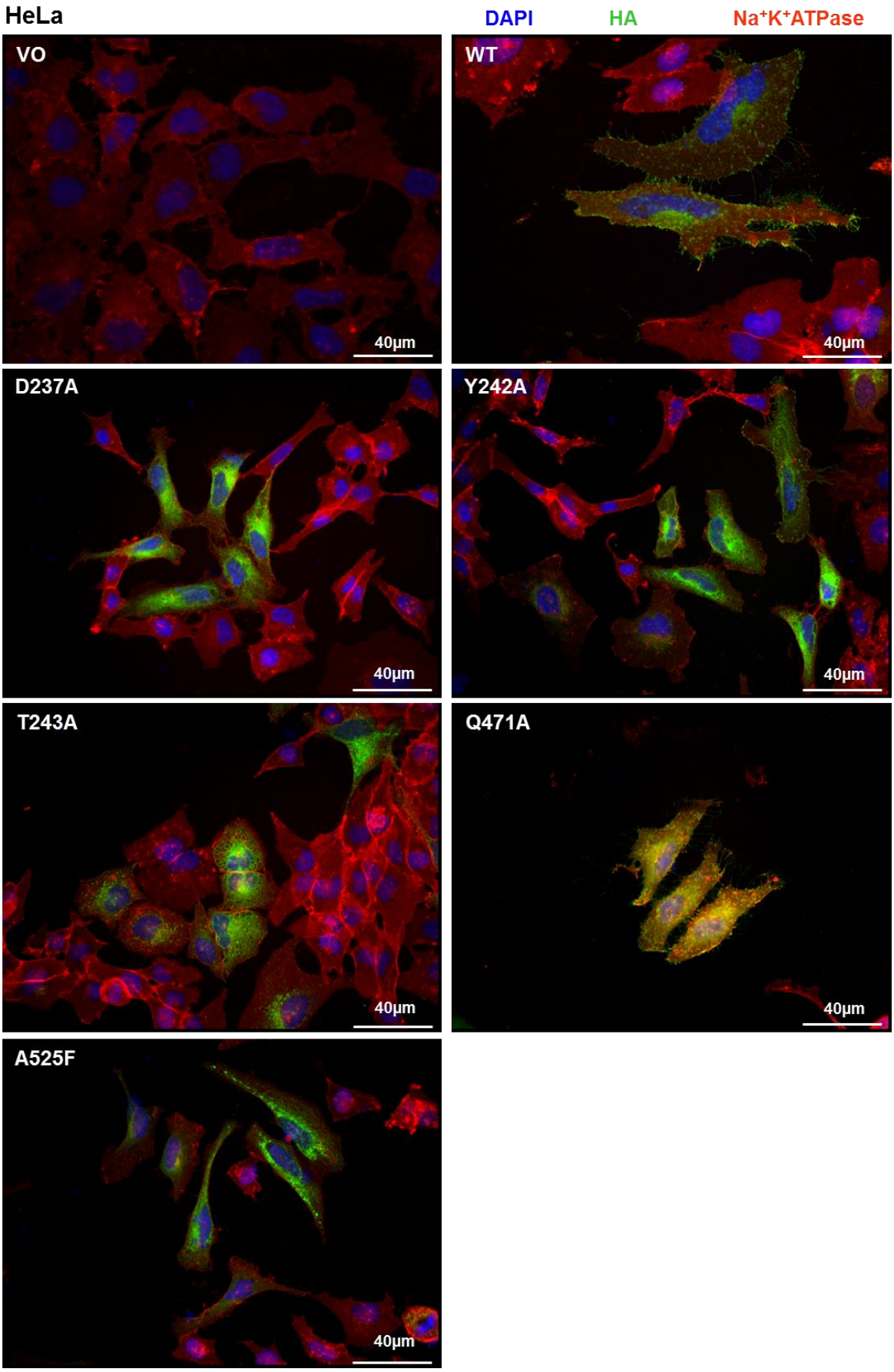
HeLa
DAPI
HA
Na+K+ATPase
VO
WT
D237A
Y242A
T243A
Q471A
A525F
40µm

6.3.1.3 Mutating residues in the putative dimerisation interface impairs NIS function, with the exception of Q471

Radioiodide uptake assays were performed on SW1736 and HeLa cells expressing WT or mutant NIS constructs tagged at the C-terminus with HA to assess whether mutating residues within the putative dimerisation interface impacts on NIS function. One-way ANOVA with Dunnett's multiple comparison tests were performed to identify significant changes in uptake compared to WT.

Figure 6-5 shows the effect of mutating residues within the putative dimerisation interface on NIS function in SW1736 and HeLa cells. Since expression of WT NIS resulted in significant radioiodide uptake, the uptake levels for VO and mutants are given as mean±SEM fold change relative to WT (shown as 1). While the radioiodide uptake of mutant Q471A was similar to WT in SW1736 cells (1.07±0.16 relative to WT) and even significantly greater than WT in HeLa cells (1.56±0.15 relative to WT), the radioiodide uptake of the remaining mutants was significantly lower relative to WT and was comparable to VO in both cell lines (SW1736: VO 0.32±0.05, D237A 0.30±0.005, Y242A 0.46±0.07, T243A 0.43±0.08 and A525F 0.46±0.08; HeLa: VO 0.03±0.005, D237A 0.27±0.09, Y242A 0.27±0.02, T243A 0.36±0.08 and A525F 0.31±0.04). This indicates that the majority of residues within the putative dimerisation interface are important for NIS function, with the possible exception of Q471 as mutating this residue did not impair NIS function.

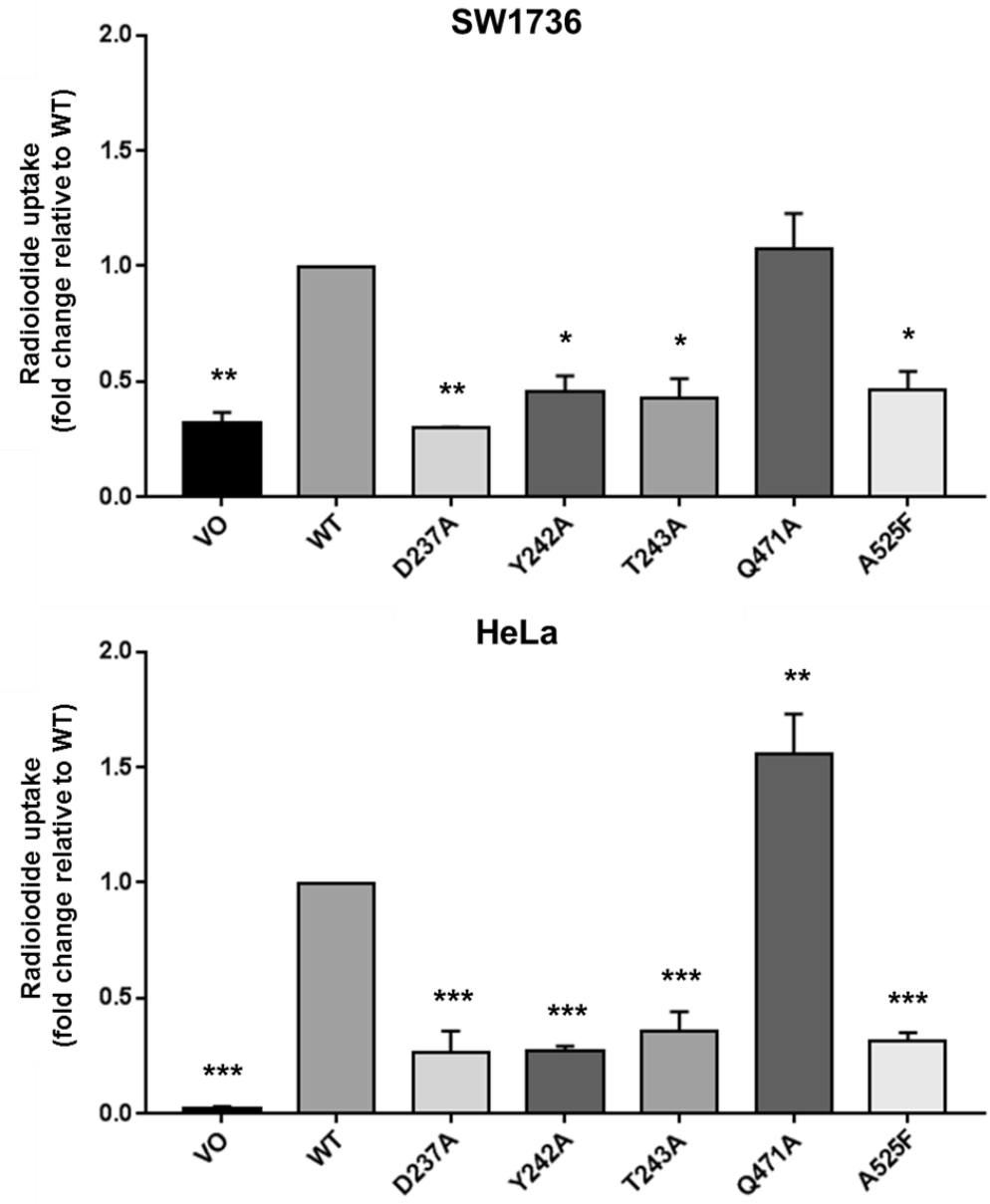

Figure 6-5 – Radioiodide uptake is abolished when residues within the putative dimerisation interface are mutated, with the exception of Q471A. SW1736 (top) and HeLa (bottom) cells were transfected with empty pcDNA3.1(+) vector (VO), wild-type NIS-HA (WT) or HA-tagged NIS with a mutation in one of the residues in the putative dimerisation interface and radioiodide uptake assays were performed. Bars represent mean radioiodide uptake relative to WT and error bars show SEM relative to WT. One-way ANOVA with Dunnett's multiple comparison statistical tests were performed: * = $p<0.005$, ** = $p<0.0005$ and *** = $p<0.0001$ compared to WT. (n=3 with 4 replicates in each n).

6.3.2 Mutation of residues within the putative dimerisation interface failed to disrupt NIS dimerisation

To explore whether this region is involved in NIS dimerisation, PLA and FRET were performed to assess the ability of mutants of the putative dimerisation interface to dimerise. In order to utilise FRET to quantitatively measure any change in dimerisation with these mutations, PCR cloning was used to conjugate the mutated NIS protein to either Cerulean or Citrine at the C-terminus.

6.3.2.1 PLA signal was observed for NIS constructs with mutations in the putative dimerisation interface

To examine qualitatively if mutating residues within the putative dimerisation interface affects NIS dimerisation, PLA was performed on HeLa cells co-expressing differentially-tagged variants of WT or mutant NIS, tagged with MYC or HA at the C-terminus.

The red dots observed in HeLa cells co-transfected with WT NIS-MYC and NIS-HA indicate that the two tags are less than 40nm apart and therefore suggests that dimerisation is occurring. Comparable PLA signal was observed for all five putative dimerisation interface mutants, therefore implying that these mutants retain the ability to dimerise. As the majority of these mutants are intracellularly retained (except Q471A), PLA signal was not observed at the plasma membrane for these mutants. No PLA signal was observed in the technical negative control (VO + WT NIS-HA).

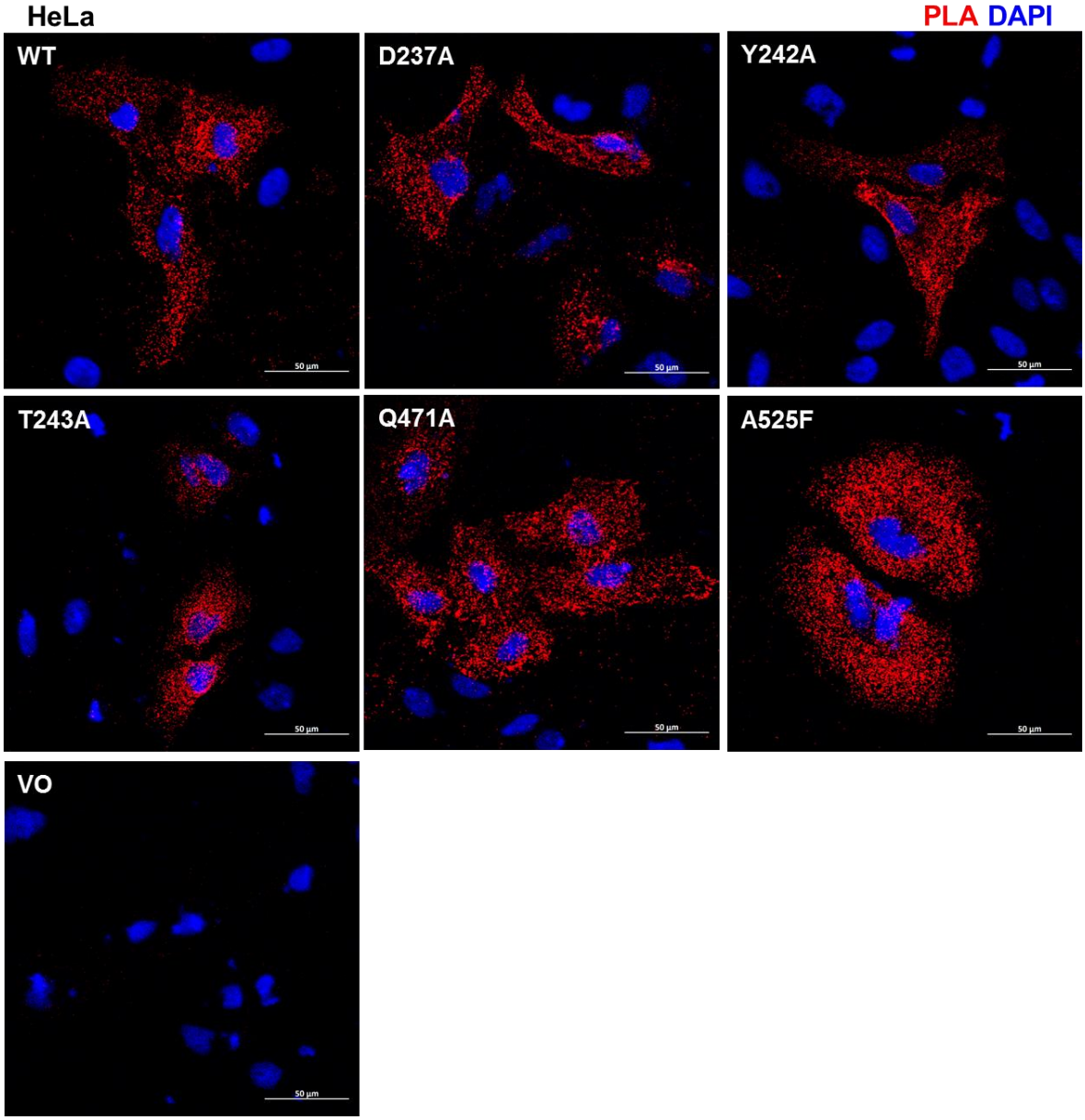

Figure 6-6 – PLA signal is still observed when single residues in the putative dimerisation interface are mutated. PLA was performed on HeLa cells co-transfected with differentially-tagged variants of wild-type (WT) or mutant NIS constructs. PLA signal (in red) indicates close proximity (<40nm) between the MYC and HA tags, which is suggestive of dimerisation. Nuclei are visualised in blue using DAPI. 40x magnification.

6.3.2.2 Mutants of the putative dimerisation interface had little significant difference in corrected FRET compared to wild-type NIS

To investigate quantitatively if mutants of the putative dimerisation interface have an altered capacity to dimerise, SW1736 and HeLa cells were co-transfected with differentially-tagged variants of WT or mutant NIS, conjugated to either Cerulean or Citrine at the C-terminus, and FRET analysis was performed. One-way ANOVA with Dunnett's multiple comparison tests were performed to identify significant changes in corrected FRET compared to WT.

Figure 6-7 and Figure 6-8 illustrate a representative set of images captured to perform FRET analysis and Figure 6-9 displays the results of this analysis. Corrected FRET data are presented as arbitrary units as a result of the data analysis process. In SW1736 cells expressing WT NIS, the mean corrected FRET value was -72.83 and ranged from -1070.34 to 805.43, whereas in HeLa cells expressing WT NIS, corrected FRET ranged from -465.51 to 783.63, with a mean value of 56.20. Although there was a statistically significant difference in corrected FRET compared to WT for Q471A in SW1736 cells, with a mean value of -227.89 and range of -899.20 to 645.66 ($p<0.05$), similar results were not observed in HeLa cells (mean -15.10, range -527.08 to 454.41). None of the other mutations gave a statistically significant difference in corrected FRET in either cell line (D237A (SW1736: mean -98.32, range -943.86 to 428.55; HeLa: mean 29.45, range -492.21 to 666.76), Y242A (SW1736: mean -75.45, range -713.60 to 450.30; HeLa: mean 3.42, range -551.75 to 608.86), T243A (SW1736: mean -194.85, range -896.29 to 717.27; HeLa: mean -14.24, range -634.98 to 548.52) and A525F (SW1736: mean 27.26, range -666.74 to 736.98; HeLa: mean 175.75, range -497.19 to 902.97)). As just one mutant in one cell line gave a significant change in corrected FRET, these data suggest that NIS dimerisation remains unchanged by single mutations within the putative dimerisation interface.

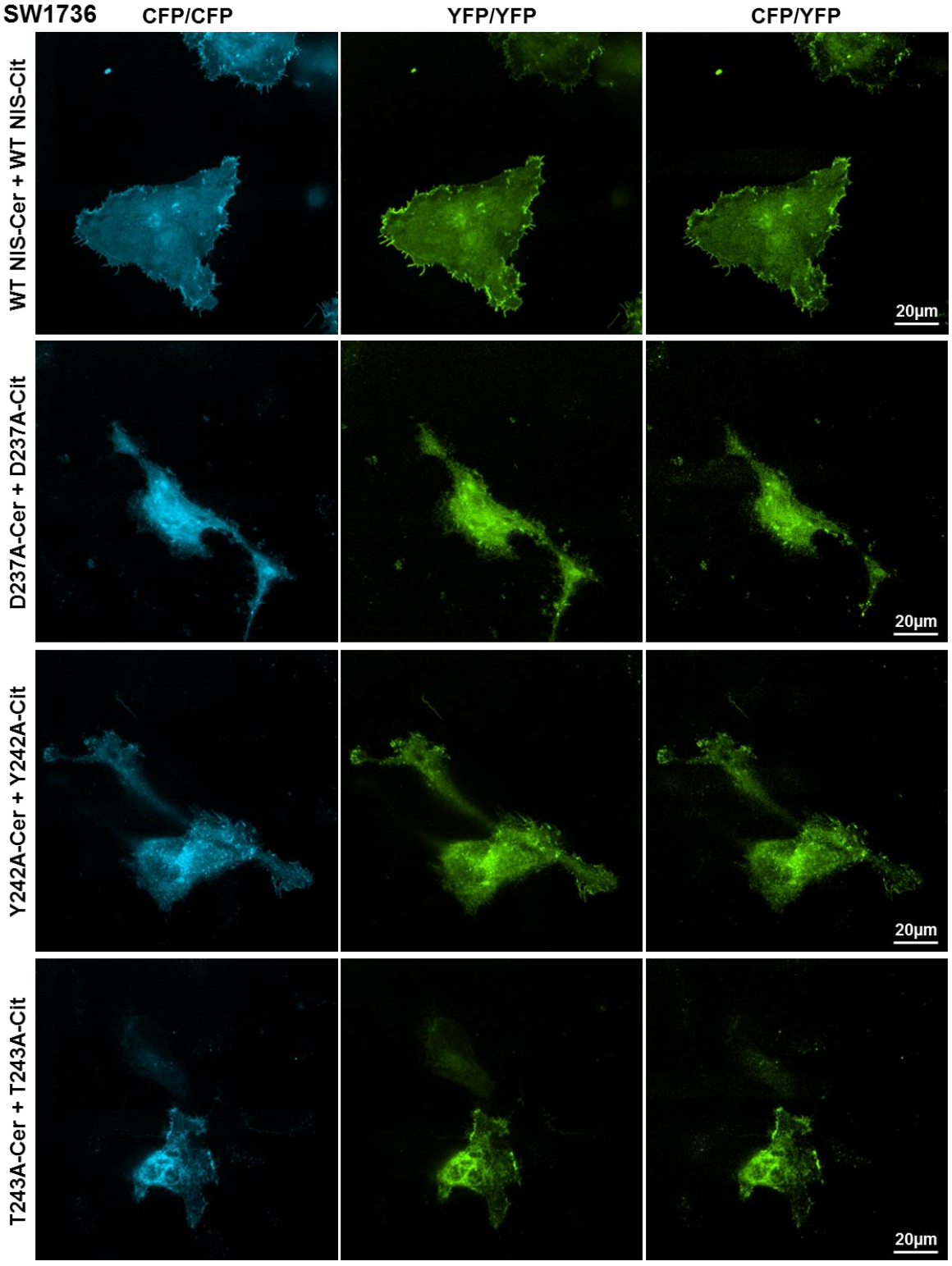

Figure 6-7 – Representative images captured during FRET analysis of the ability of putative dimerisation interface NIS mutants to dimerise in SW1736 cells. Cells were co-transfected with differentially-tagged constructs of wild-type NIS (WT) or NIS constructs with a mutation in the putative dimerisation interface, conjugated to Cerulean or Citrine at the C-terminus (continued overleaf). Three concurrent versions of each image were taken: total Cerulean (CFP) image (Cerulean

excitation/Cerulean emission (CFP/CFP)), total Citrine (YFP) image (Citrine excitation/Citrine emission (YFP/YFP) and the FRET image (Cerulean excitation/Citrine emission (CFP/YFP)).

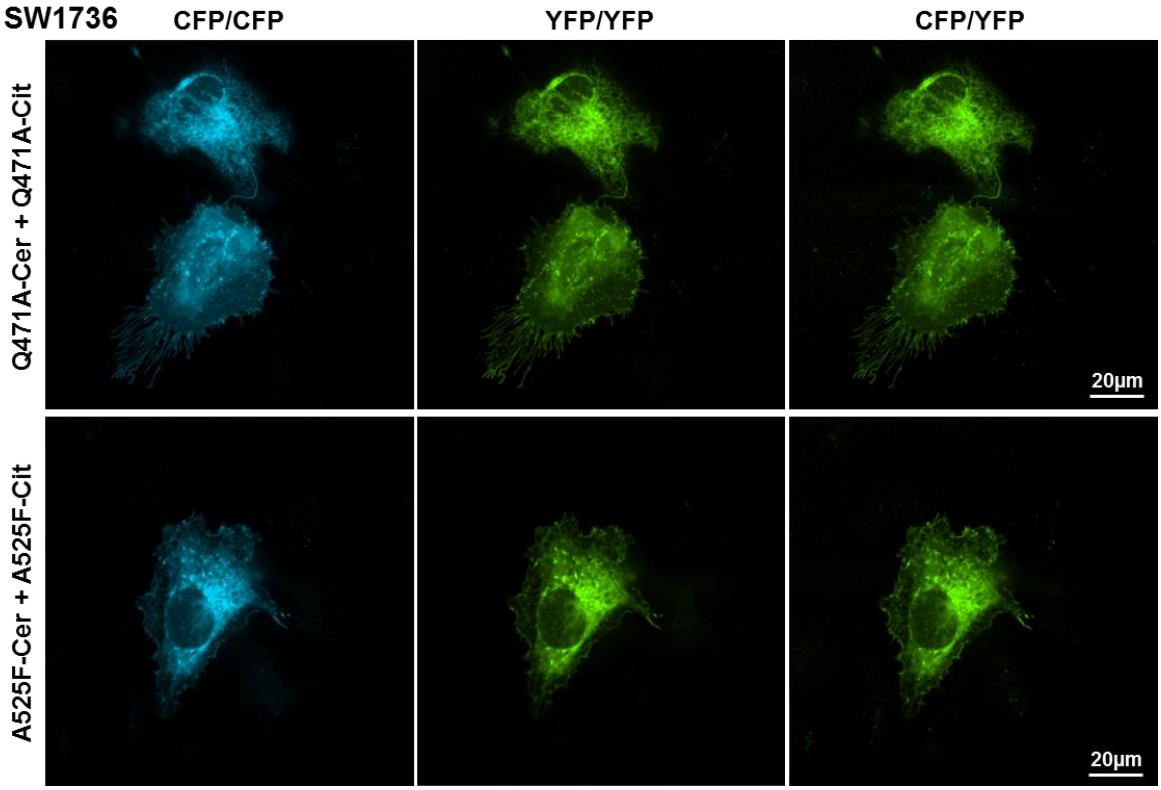

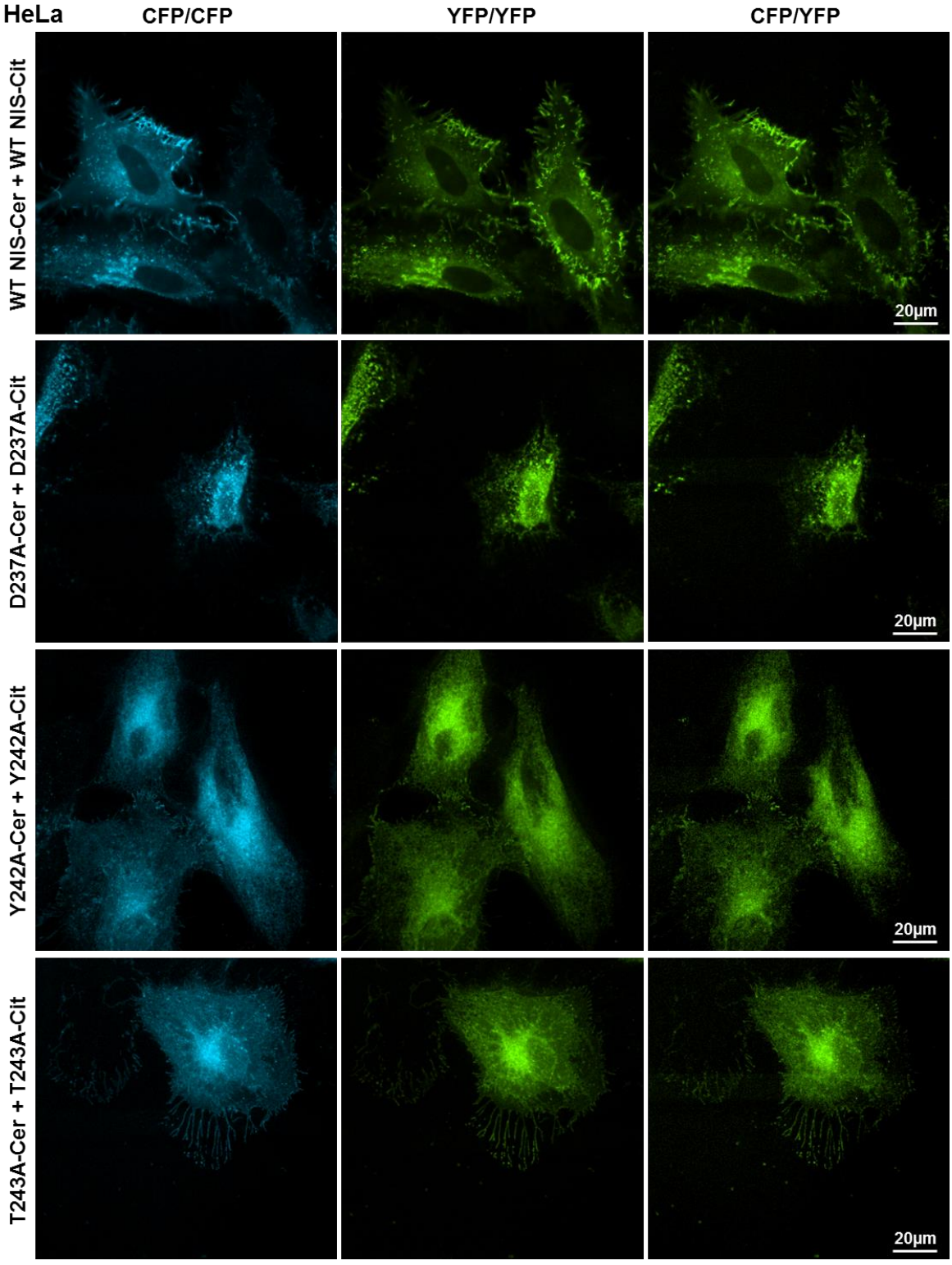

Figure 6-8 – Representative images captured during FRET analysis of the ability of putative dimerisation interface NIS mutants to dimerise in HeLa cells. Cells were co-transfected with differentially-tagged constructs of wild-type NIS (WT) or NIS constructs with a mutation in the putative dimerisation interface, conjugated to Cerulean or Citrine at the C-terminus (continued overleaf). Three concurrent versions of each image were taken: total Cerulean (CFP) image (Cerulean

excitation/Cerulean emission (CFP/CFP)), total Citrine (YFP) image (Citrine excitation/Citrine emission (YFP/YFP) and the FRET image (Cerulean excitation/Citrine emission (CFP/YFP)).

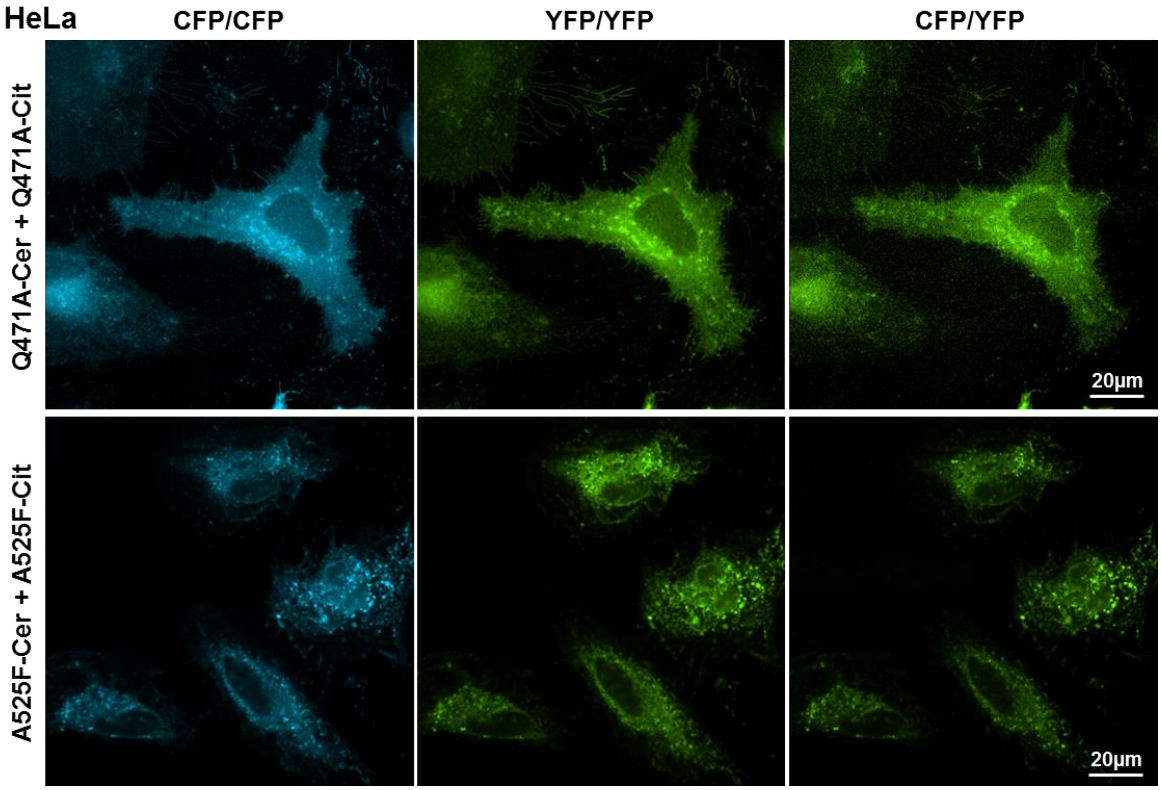

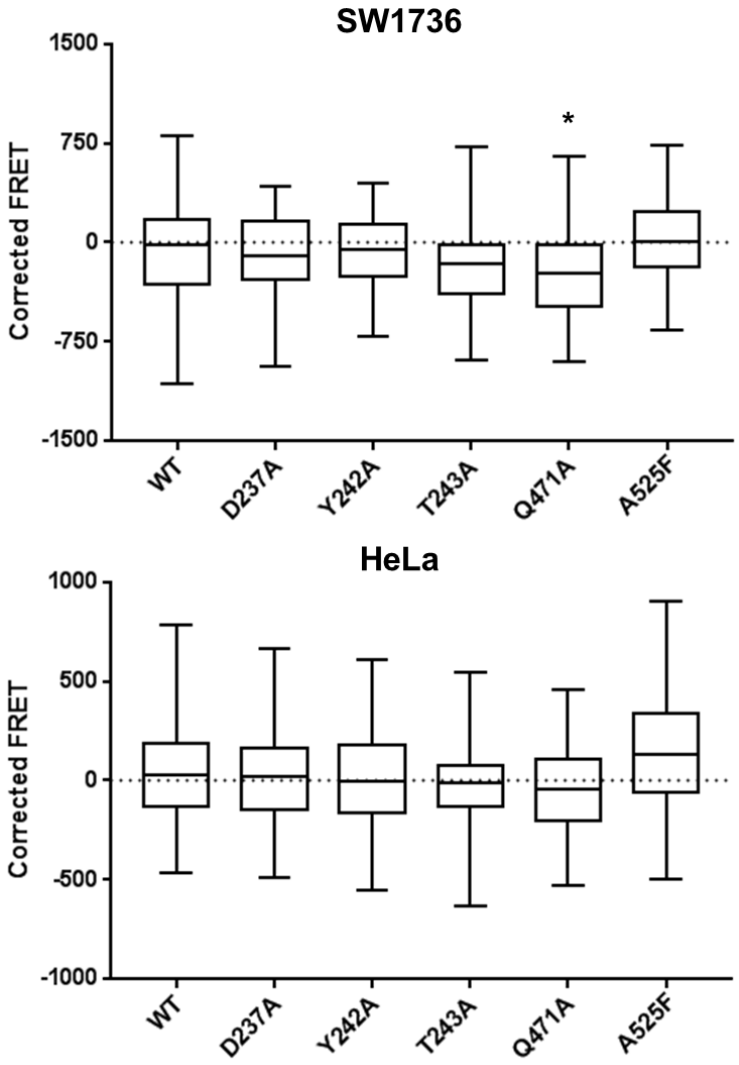

SW1736		HeLa	
Plasmid	**Corrected FRET (arbitrary units)**	**Plasmid**	**Corrected FRET (arbitrary units)**
WT	-72.83 (-1070.34 to 805.43)	**WT**	56.20 (-465.51 to 783.63)
D237A	-98.32 (-943.86 to 428.55)	**D237A**	29.45 (-492.21 to 666.76)
Y242A	-75.47 (-713.60 to 450.30)	**Y242A**	3.42 (-551.75 to 608.86)
T243A	-194.85 (-896.29 to 717.27)	**T243A**	-14.24 (-634.98 to 548.52)
Q471A	-227.89 (-899.20 to 645.66)	**Q471A**	-15.10 (-257.08 to 454.41)
A525F	27.26 (-666.74 to 736.98)	**A525F**	175.75 (-497.19 to 902.97)

Figure 6-9 – Data analysis showed little significant difference in corrected FRET when residues of the putative dimerisation interface were mutated. FRET analysis was performed on SW1736 (top) and HeLa (bottom) cells co-transfected with differentially-tagged variants of wild-type (WT) NIS or NIS with a mutation in the putative dimerisation interface, tagged at the C-terminus to Cerulean or Citrine. Data are presented as a box and whisker plot, with the centre line indicating the mean corrected FRET value (in arbitrary units), the box representing the 25th and 75th percentiles and the whiskers denoting the minimum and maximum values. Data in the table comprise the mean corrected FRET, with the range of values given in parentheses. One-way ANOVA with Dunnett's multiple comparison statistical tests were performed: * = p<0.05. (n=2, with a minimum of 20 cells analysed in each n).

6.3.3 Closer investigation of the putative dimerisation interface revealed potential interactions between certain residues within the interface

Although these data demonstrate that mutating single residues within the putative dimerisation interface is unlikely to affect NIS dimerisation, it is plausible that single mutations within the interface may be tolerated. As such, the interface was more closely investigated on the homology model in order to identify potential interactions between the residues which could be targeted via multiple mutations.

Upon closer inspection of the primary putative dimerisation interface, several potential interactions between different residues were observed (as illustrated in Figure 6-10, with residue side chains shown in 'stick' form). The primary putative dimerisation interface comprises residues on two separate extracellular loops: the third (D237, Y242 and T243) and the sixth (Q471 and A525) loops. Interestingly, Figure 6-10 revealed that the residues on the third extracellular loop on one monomer (in cyan) interact with those of the sixth extracellular loop on the opposite monomer (in magenta). Of these residues, Q471 (red), Y242 (yellow) and T243 (orange) seem to cluster together (circled in brown), while A525 (green) and D237 (blue) appear to form a separate cluster (circled in grey), with Y242A also possibly involved in this cluster. In order to investigate whether the residues of the putative dimerisation interface are involved in mediating NIS dimerisation, certain single-residue NIS mutants were combined, with the aim of disrupting potential interactions between these clustered residues within the putative dimerisation interface, namely Q471A + Y242A, Q471A + T243A, A525F + D237A, and A525F + Y242A.

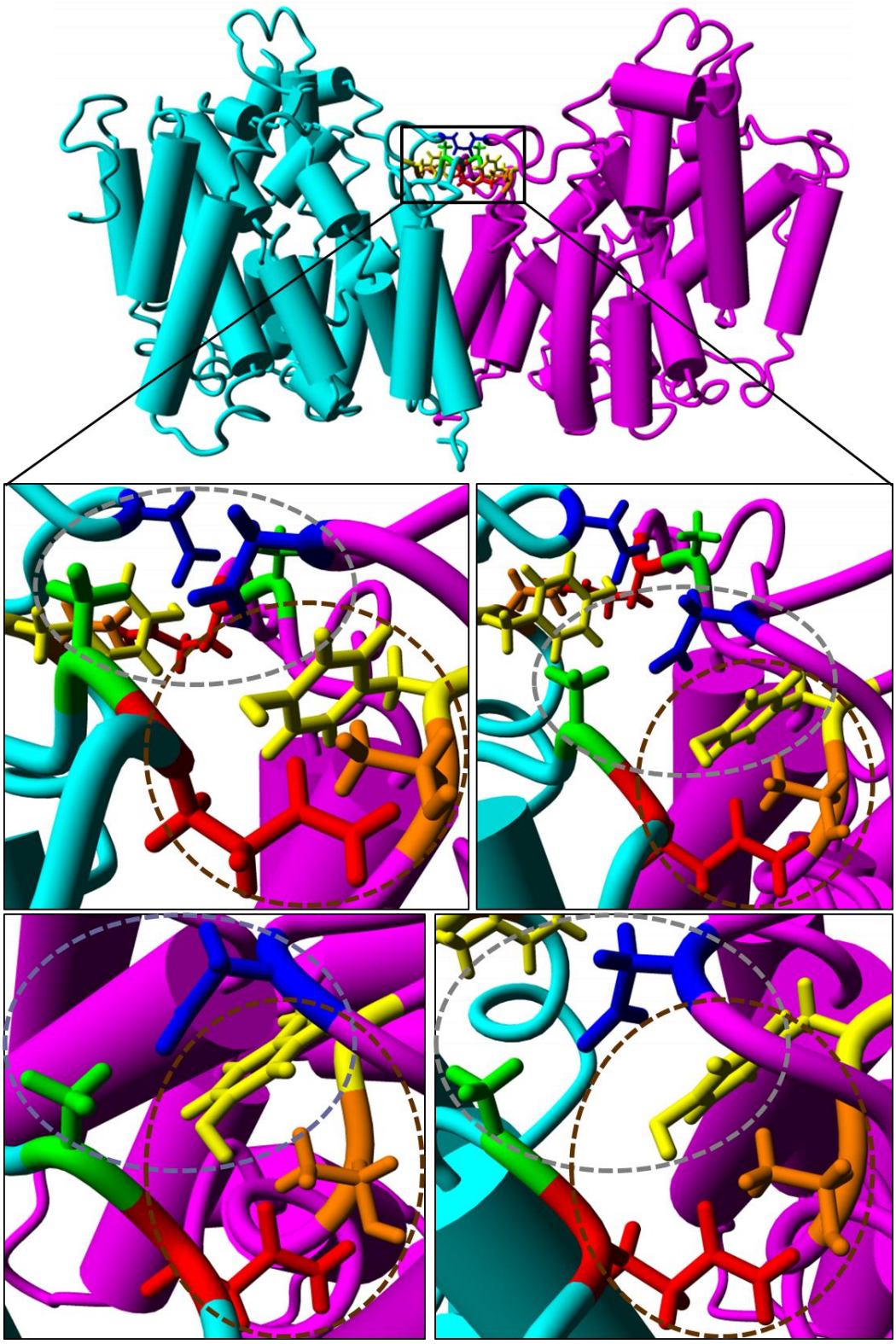

Figure 6-10 – Closer examination of the primary putative dimerisation interface revealed two distinct clusters of residues which may form interactions which mediate NIS dimerisation. One cluster (circled in brown) clearly appears to form between Q471 (in red) of one monomer (cyan) and Y242 (in yellow) and T243 (in orange) of the opposite monomer (magenta). A secondary cluster (circled in grey) seems to form between A525 (in green) of one monomer and D237 (in blue) and potentially Y242 of the opposite monomer.

6.3.4 Disrupting multiple interactions within the putative dimerisation interface caused a significant reduction in NIS dimerisation

To quantitatively evaluate if mutating multiple residues within the putative dimerisation interface disrupts NIS dimerisation, FRET analysis was performed on SW1736 and HeLa cells co-expressing one of the following combinations of differentially-tagged NIS mutants: Q471A-Cerulean + Y242A-Citrine, Q471A-Cerulean + T243A-Citrine, A525F-Cerulean + D237A-Citrine, or A525F-Cerulean + Y242A-Citrine. One-way ANOVA with Dunnett's multiple comparison tests were performed to identify significant changes in corrected FRET.

A representative set of images required for FRET analysis is shown in Figure 6-11, with the results of this analysis depicted in Figure 6-12. Due to the data analysis method, corrected FRET data are presented as arbitrary units. In SW1736 cells, the mean corrected FRET value was -72.83, ranging from -1070.34 to 805.43, while the corrected FRET values in HeLa cells ranged from -465.51 to 783.63, with a mean value of 56.20. A statistically significant reduction in corrected FRET compared to WT was observed for two of the combinations in both cell lines: Q471A + Y242A (SW1736: mean -241.68, range -997.58 to 411.97; HeLa: mean -82.14, range -516.51 to 354.33) and Q471A + T242A (SW1736: mean -349.69, range -986.66 to 168.42; HeLa: mean -104.45, range -424.75 to 158.84). However, there was no significant change in corrected FRET compared to WT for the remaining two combinations in either cell line: A525F + D237A (SW1736: mean -193.97, range -709.43 to 335.35; HeLa: mean 60.05, range -384.21 to 484.29) or A525F + Y242A (SW1736: mean -62.84, range -501.87 to 592.71; HeLa: mean 119.42, range -257.78 to 713.90). Consequently, these data demonstrate that, although interactions between residues A525, D237 and Y242 are less likely to be involved, the interactions between residues Q471A, Y242A and T243A within the primary putative dimerisation interface are essential for NIS dimerisation to occur.

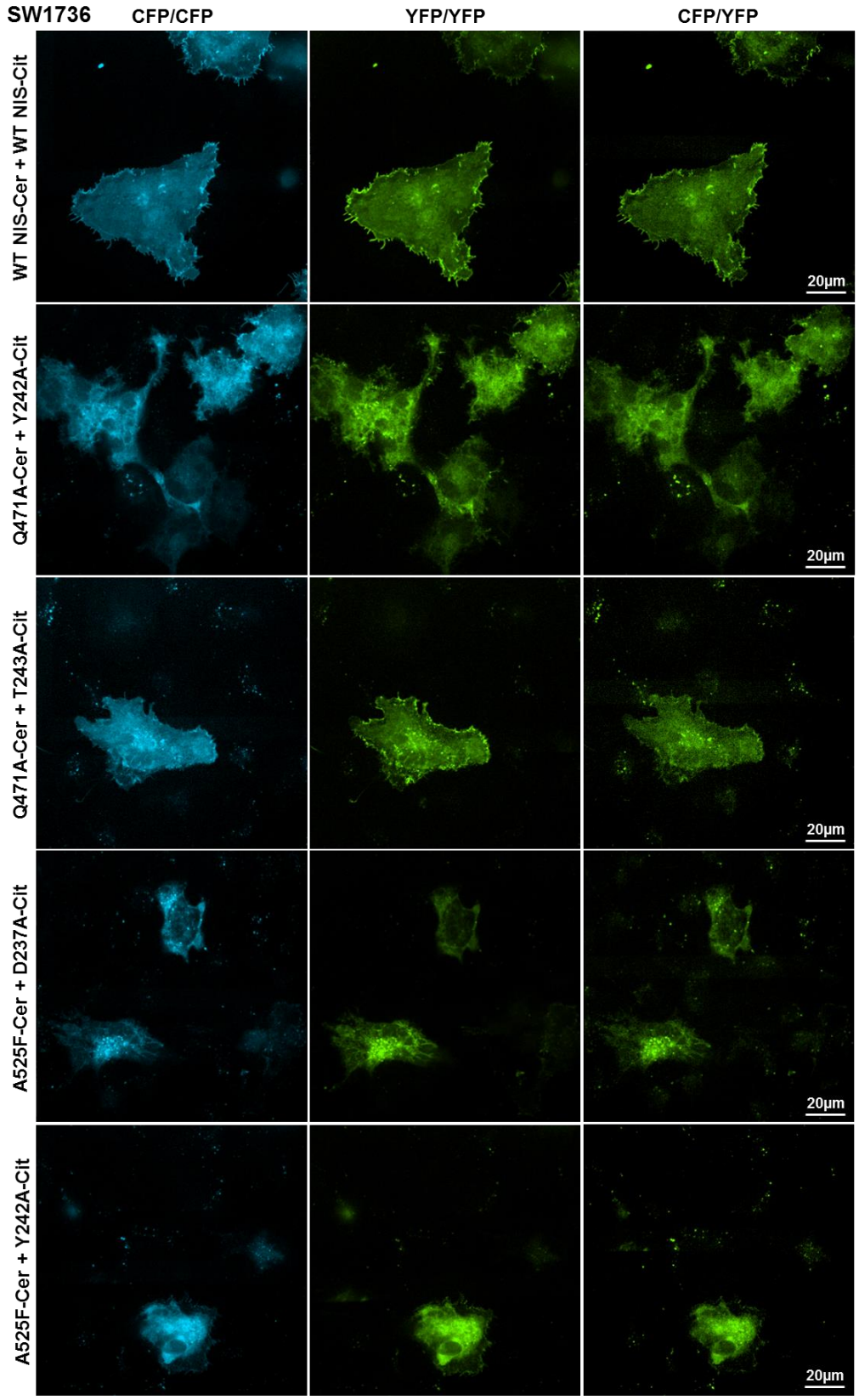

Figure 6-11 – Representative images captured during FRET analysis of the effect of combining mutants of residues within the putative dimerisation interface on NIS dimerisation. SW1736 and HeLa (overleaf) cells were co-transfected with differentially-tagged NIS constructs, either wild-type NIS (WT) or

combinations of NIS mutants, each with a different mutation within the putative dimerisation interface. Three concurrent versions of each image were taken: total Cerulean (CFP) image (Cerulean excitation/Cerulean emission (CFP/CFP)), total Citrine (YFP) image (YFP excitation/YFP emission (YFP/YFP)) and the FRET image (Cerulean excitation/Citrine emission (CFP/YFP)).

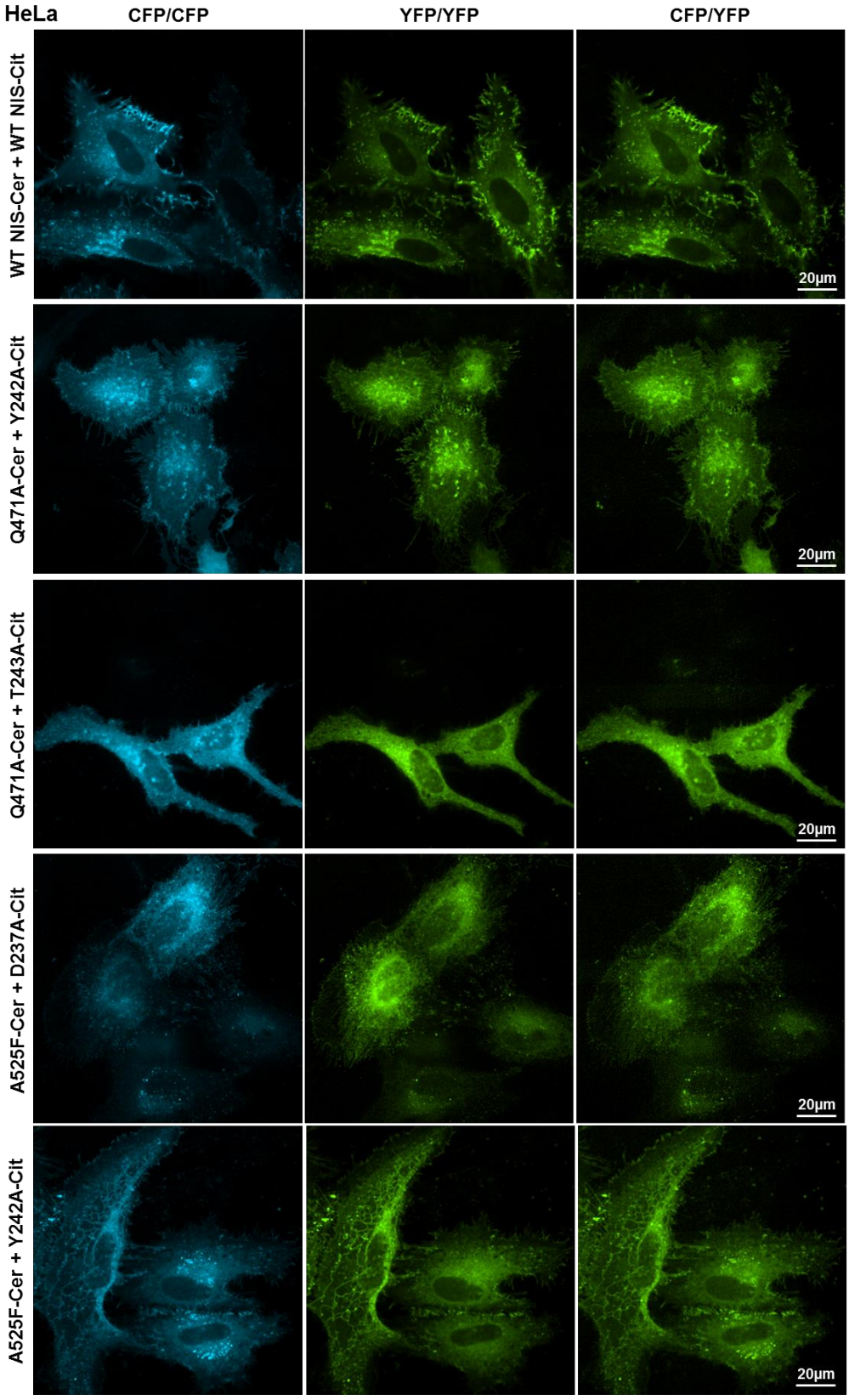

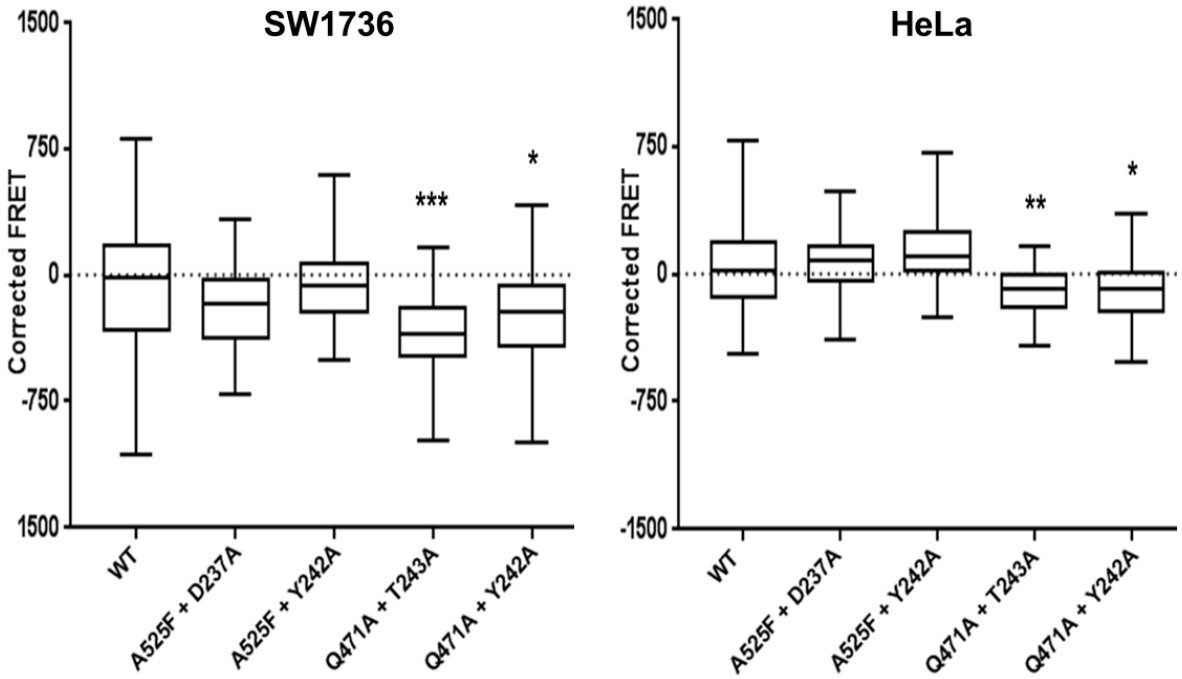

SW1736		HeLa	
Combination	**Corrected FRET (arbitrary units)**	**Combination**	**Corrected FRET (arbitrary units)**
WT	-72.83 (-1070.34 to 805.43)	**WT**	56.20 (-465.51 to 783.63)
A525F + D237A	-193.97 (-709.43 to 335.35)	**A525F + D237A**	60.05 (-384.21 to 484.29)
A525F + Y242A	-62.84 (-501.87 to 592.71)	**A525F + Y242A**	119.42 (-257.78 to 713.90)
Q471A + T243A	-349.69 (-986.66 to 168.42)	**Q471A + T243A**	-104.45 (-424.75 to 158.84)
Q471A + Y242A	-241.68 (-997.58 to 411.97)	**Q471A + Y242A**	-82.14 (-516.51 to 354.33)

Figure 6-12 – Data analysis showed a significant difference in corrected FRET when putative dimerisation interface mutants were combined. FRET analysis was conducted on SW1736 (top) and HeLa (bottom) cells co-transfected with differentially-tagged variants of wild-type (WT) NIS or a combination of two NIS mutants, each with a different mutation in the putative dimerisation interface and a different fluorophore (either Cerulean or Citrine) at the C-terminus. Data are presented as a box and whisker plot, with the centre line denoting the mean corrected FRET value (in arbitrary units), the box representing the 25th and 75th percentiles and the whiskers denoting the minimum and maximum values. Data in the table are the mean corrected FRET values, with the range of values given in parentheses. One-way ANOVA with Dunnett's multiple comparison statistical tests were performed: * = $p<0.05$, ** = $p<0.005$, *** = $p<0.0001$. (n=2, with a minimum of 20 cells analysed in each n).

6.3.5 The putative dimerisation interface can tolerate the loss of one, but not two, of the three residues clustered residues

Given that the dimerisation studies demonstrated that NIS dimerisation was only disrupted when two residues were lost through mutation, the three key residues of the primary putative dimerisation interface were closely investigated on the homology model to provide an explanation for these observations.

As shown in Figure 6-13A, residues Q471 (red), Y242 (yellow) and T243 (orange) appear to form close interactions which are likely to be important for NIS dimerisation. When one of these three residues is removed by mutation to alanine, the remaining two residues still seem able to interact to preserve NIS dimerisation (Figure 6-13B-D), whereas removing two residues has a much greater impact, as the sole remaining residue is no longer able to form these interactions (Figure 6-13E and F), and consequently NIS dimerisation is impaired. It is surprising that the Q471A individual mutant retains the ability to dimerise, given that this seems to result in a lack of contact between the two monomers in Figure 6-13C. This suggests that there may be other, as yet unidentified, residues interacting in this putative dimerisation interface which preserves dimerisation in the absence of the Q471 side chain.

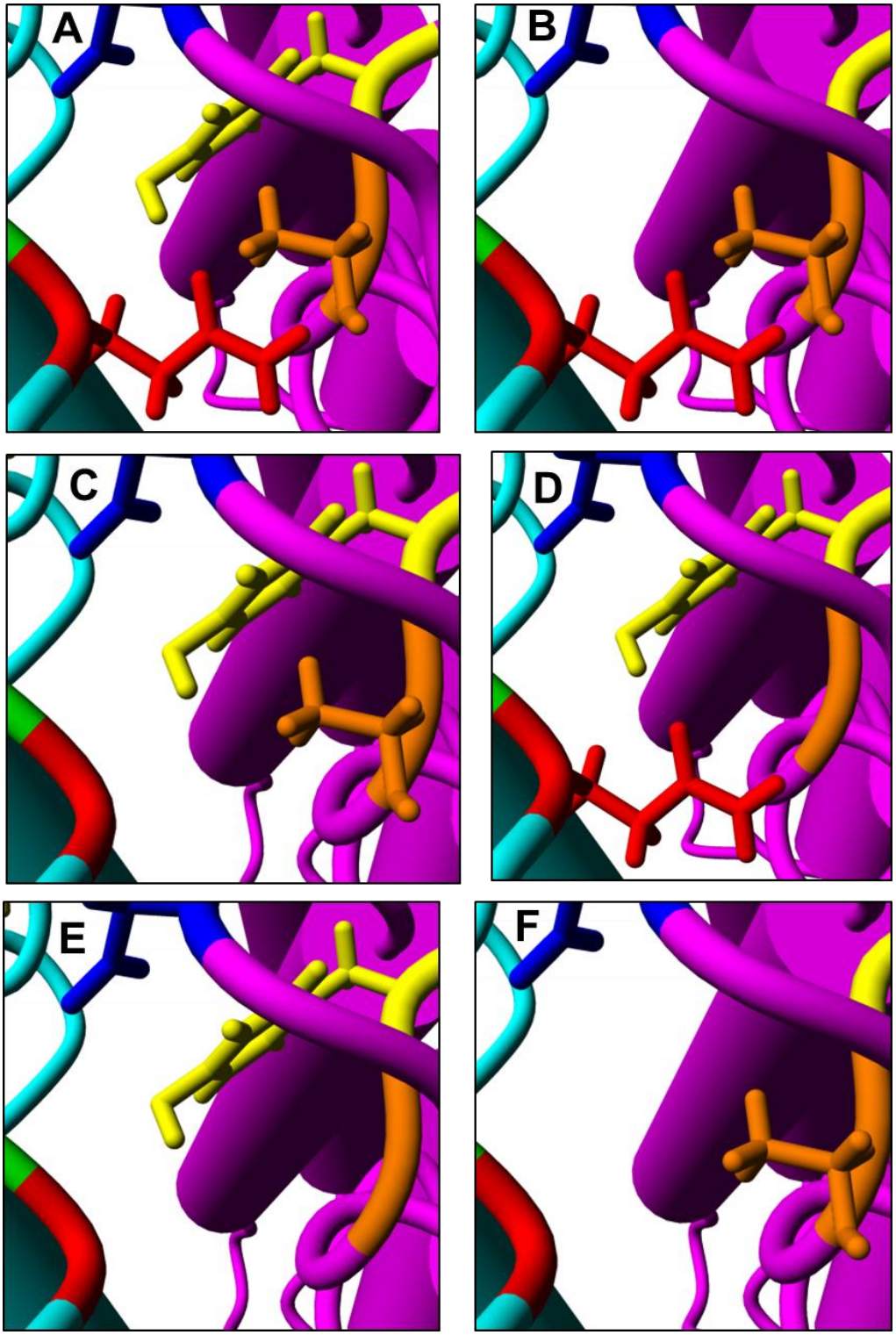

Figure 6-13 – Closer inspection of the three significant residues within the primary putative dimerisation interface reveals how key interactions between the residues are likely to facilitate NIS dimerisation. In the primary putative dimerisation interface (panel A), Q471 (in red) from one monomer (cyan) clusters with Y242 (in yellow) and T243 (in orange) on the opposite monomer (magenta) and form interactions which are likely to mediate NIS dimerisation. When one of these residues is removed, the remaining two residues can still form interactions which preserve dimerisation (panels B-D). However, these interactions are lost when two of the residues are lost (panels E and F).

6.3.6 Complex radioiodide uptake assays were performed to help understand the effects of disrupting NIS dimerisation on function

Radioiodide uptake assays were performed on SW1736 and HeLa cells expressing the mutant combinations with disrupted dimerisation (either Q471A-HA + Y242A-HA or Q471A-HA + T243A-HA) in order to explore the impact of disrupting dimerisation on NIS function. To aid data interpretation, single mutations were combined with WT NIS-HA as controls and data were normalised to WT.

Figure 6-14 showed that expressing WT NIS-HA (WT) results in a substantial increase in radioiodide uptake compared to VO (SW1736: VO 0.12±0.03 pmol ^{125}I/µg protein, WT 1.25±0.00; HeLa: VO 0.05±0.06, WT 1.71±0.00). Unsurprisingly, the WT + Q471A combination had similar uptake to WT (WT + QA: 1.36±0.07 (SW1736), 1.94±0.13 (HeLa)). However, a different pattern in radioiodide uptake for the WT + non-functional mutant combinations was observed for the two cell lines, although statistical tests could not be performed as time constraints prevented further replication, so it is unclear whether these trends are signficant. In SW1736 cells, both combinations had lower uptake compared to WT (1.13±0.05 (WT + YA), 0.89±0.01 (WT + TA)), whereas an increase in uptake was seen in HeLa cells (2.09±0.11 (WT + YA), 2.14±0.55 (WT + TA)). Similarly, different trends in uptake were observed between the two cell lines expressing the mutant combinations which had disrupted dimerisation, but this may not be significant. In SW1736 cells, the disrupted dimerisation mutant combinations resulted in a lower radioiodide uptake compared to WT (0.92±0.05 (QA + YA), 1.10±0.18 (QA + TA)), but gave an increase in uptake when expressed in HeLa cells (2.08±0.29 (QA + YA), 2.46±0.53 (QA + TA)). Altogether, these data revealed a complex relationship between dimerisation and NIS function but further repeats are required to determine the significance of this.

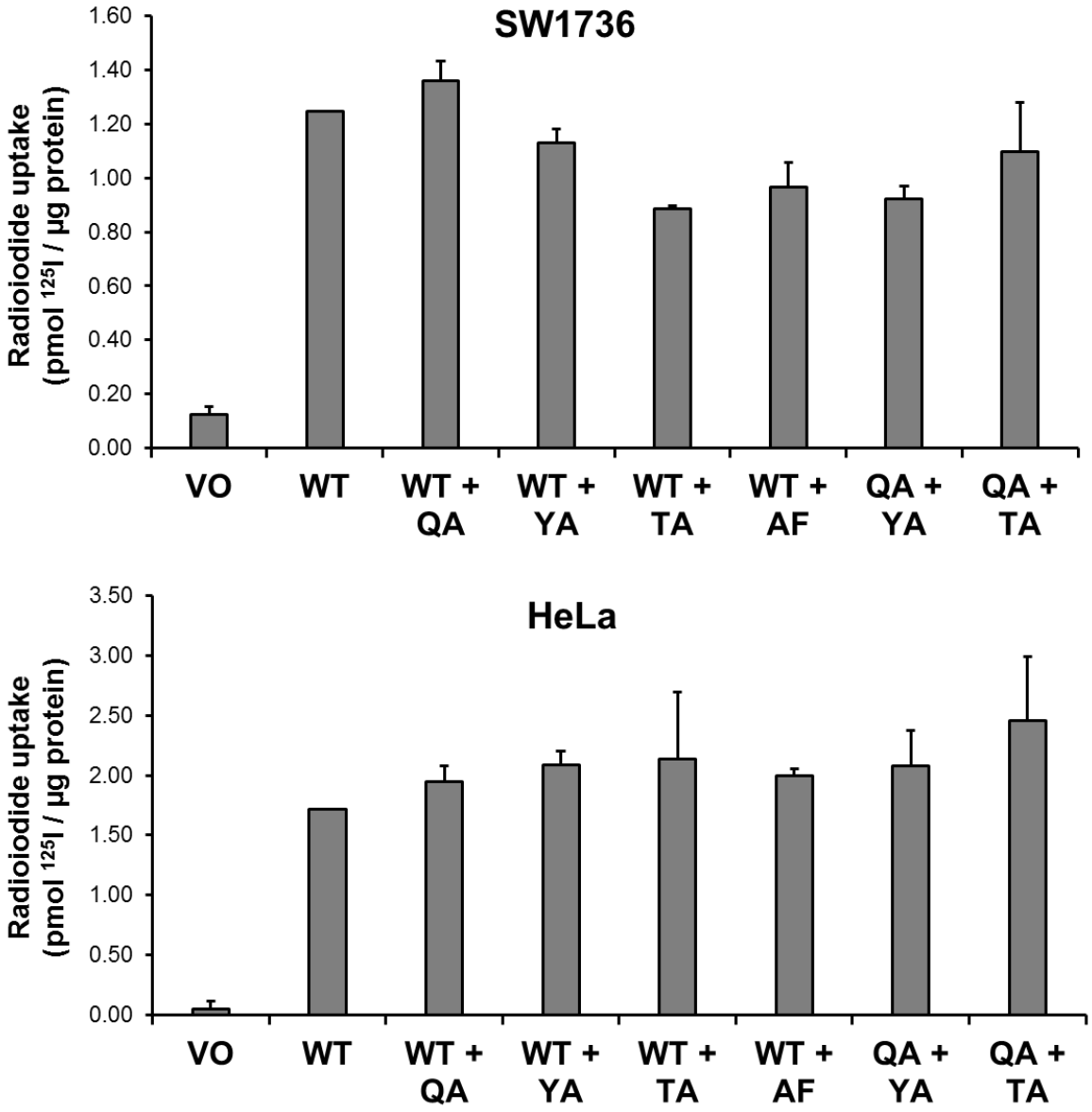

Figure 6-14 – Radioiodide uptake assays highlighted the complexity with which dimerisation affects NIS function. SW1736 (top) and HeLa (bottom) cells were co-transfected with empty pcDNA3.1(+) vector (VO), wild-type NIS-HA (WT) or combinations of HA-tagged WT or mutant NIS with a mutation in one of the three key residues of the primary putative dimerisation interface: Q471A (QA), Y242A (YA) or T243A (TA). Radioiodide uptake assays were performed and data were normalised to WT. Bars represent mean radioiodide uptake in pmol ^{125}I/µg protein and error bars show SEM. (n=2 with 4 replicates in each n).

6.4 Discussion

Since the homology model of NIS dimerisation presented in Chapter 5 revealed a putative dimerisation interface, the aim of the current chapter was to investigate this interface further and confirm whether these residues are involved in NIS dimerisation, with the ultimate aim of determining the importance of dimerisation for NIS function. The data described in this chapter support the hypothesis that the residues in the putative dimerisation interface mediate NIS dimerisation, but the exact role dimerisation plays in NIS function remains unclear.

6.4.1 Mutating residues in the putative dimerisation interface significantly impairs NIS function

To examine the impact of mutating residues within the putative dimerisation interface, an extensive characterisation of these mutants was carried out. Site-directed mutagenesis was conducted on pcDNA3.1(+)_NIS-MYC and pcDNA3.1(+)_NIS-HA plasmids to generate differentially-tagged variants of the mutants for future dimerisation studies, but only the HA-tagged mutants required characterisation as the presence of MYC or HA tag does not alter NIS expression, subcellular localisation or function.

In addition to conducting radioiodide uptake assays to investigate the impact of mutating residues in the putative dimerisation interface on NIS function, studies were also carried out in order to understand how these mutations affected NIS function. The data presented here demonstrate that, while mutating Q471 does not affect NIS function, the remaining mutants of the putative dimerisation interface are non-functional, presumably due to impaired glycosylation. This suggests that these mutations are not processed properly by the ER and Golgi network, potentially as a result of protein misfolding. This impedes the membrane protein trafficking pathway (see Figure 1-11) and results in reduced or absent expression at

the plasma membrane (Peer, 2011). Overall, these data show that the residues in the putative dimerisation interface are important for the correct processing and trafficking of NIS and ultimately demonstrate a crucial role for these residues for NIS function.

6.4.2 Multiple mutations within the putative dimerisation interface are required to affect NIS dimerisation

As mutating these putative dimerisation interface residues caused abrogation of NIS function (with the exception of Q471A), PLA was performed to examine if this was due to impaired NIS dimerisation. However, there was no noticeable change in PLA signal between WT and mutant NIS, implying that individually mutating residues within the putative dimerisation interface does not impact on NIS dimerisation. PLA was only conducted in HeLa cells as FRET studies were then carried out as a quantitative measure of mutant NIS dimerisation to elucidate if these mutants can dimerise or if non-direct interactions were being observed in the PLA (Sigma-Aldrich, 2018b).

In order to use FRET to quantitatively determine any change in mutant NIS dimerisation, PCR cloning was performed to generate mutant NIS constructs conjugated to either Cerulean or Citrine at the C-terminus. Characterisation of these constructs was not required as the presence of fluorophore at the C-terminus does not impair NIS expression, subcellular localisation or function. A large range in corrected FRET values were observed, but negative corrected FRET values are not always reflective of a lack of FRET occurring, partly due to the correction processes required during data analysis (Lamond, 2014, Piston and Kremers, 2007) and also due to heterogeneity with the transfection levels of each plasmid both in single cells and across the cell population (Hoppe et al., 2002). As a result, corrected FRET values for each of the mutants were compared to that of WT using a one-way ANOVA to

identify any significant differences in the ability of putative dimerisation interface mutants to dimerise. However, only one significant difference was achieved: Q471A in SW1736 cells. As this difference was only observed in one cell line, it was decided that this was likely to be an anomalous result, possibly due to heterogeneous transfection levels. Consequently, it would appear that the residues within the primary putative dimerisation interface do not mediate NIS dimerisation.

However, it is highly plausible that the putative dimerisation interface is robust and can tolerate the loss of a single residue through mutation, as the remaining residues may still form interactions which prevent the loss of dimerisation. Therefore, more extensive mutation within the interface was required to further investigate whether these residues mediate NIS dimerisation. To identify potential interactions between the residues of the putative dimerisation interface which would be best targeted in these studies, the interface was examined more closely on the homology model. Interestingly, this revealed a clear cluster of three residues: Y242 and T243 from one monomer and Q471 from the opposite monomer. Residues D237 and A525 (from separate monomers) appeared to form a separate cluster, with Y242 also potentially interacting in this cluster.

Consequently, the following single-residue NIS mutants were co-transfected together into SW1736 and HeLa cells: Q471A + Y242A, Q471A + T243A, A525F + D237A, or A525F + Y242A. FRET analysis was performed to explore if this increased perturbation of the putative dimerisation interface would affect NIS dimerisation. Interestingly, the two combinations which gave significantly reduced corrected FRET in both cell lines were those which disrupted the clear cluster of residues within the interface: Q471A + Y242A and Q471A + T243A. These dimerisation data also support the homology model, as they illustrate that when one residue of the three key residues is removed, interactions between

the remaining residues mediate dimerisation. However, when two of the key residues are removed, these interactions are lost and therefore prevent NIS dimerisation occurring. In summary, not only do these data demonstrate that interactions between residues Q471, Y242A and T243A of the primary putative dimerisation interface are essential for NIS dimerisation to occur, they also strengthen the accuracy of the homology model as it correctly identified several residues which are important for NIS dimerisation.

Conversely, no significant change in corrected FRET was observed for the combinations of mutations which targeted the secondary cluster of residues: A525F + Y242A or A525F + T243A. The most plausible reason for this is that these residues may not actually interact during NIS dimerisation, despite being in close enough proximity to each other on the model. However, this is unlikely to be a flaw with the model because, as detailed in Chapter 5, residues Q471 and A525 are separated by a large extracellular loop which was removed from the sequence to refine the homology model. This resulted in these residues being located next to each other in the model, which is not likely to be reflective of the actual NIS protein structure. It is plausible that residues D237 and Y242 may form interactions with other residues of the extracellular loop which were removed from the model (such as T472, M473, F523 or Y524), which may be also be important for NIS dimerisation. This may also explain the ability of the Q471A mutant to dimerise, as these residues which are missing from the model may form interactions with Y242 and T243 to mediate dimerisation in the absence of the Q471 side chain. Unfortunately, studies involving these nearby residues were not carried out due to time constraints, but they could provide further detailed understanding of the interactions within this dimerisation interface.

6.4.3 While a full understanding of how dimerisation affects NIS function remains elusive, a potential role for dimerisation in NIS membrane trafficking was proposed

As the dimerisation studies revealed that mutant combinations Q471A + Y242A and Q471A + T243A significantly impaired NIS dimerisation, radioiodide uptake assays were performed to explore the impact of this loss of dimerisation on NIS function. Unfortunately, time constraints prevented further repeats of this experiment from being performed so statistical analyses could not be carried out.

A set of control combinations was performed alongside to aid interpretation of the results, as neither Y242 nor T243 are functional mutants, so dimerisation between functional and non-functional NIS is liable to affect radioiodide uptake. Further complications arise from the mixed population of dimers occurring during these experiments. In previous dimerisation experiments, only heterodimerisation between two distinct proteins was investigated, either between differentially-tagged variants of the same mutant, or between two different mutants, such as Q471A and Y242A. However, in radioiodide uptake assays, there is no way to distinguish between heterodimers (i.e. WT + mutant) and homodimers (i.e. WT + WT, or mutant + mutant). So, in the case of dimerisation between WT and a non-functional NIS mutant, non-functional mutant homodimers would be intracellularly retained and therefore cannot mediate radioiodide uptake, but both WT homodimers and WT + non-functional mutant heterodimers could be expressed at the plasma membrane and therefore contribute to the radioiodide uptake. However, if the heterodimers are also intracellularly retained, only WT homodimers would be mediating radioiodide uptake. In isolation, it would be impossible to state the effect of heterodimerisation on radioiodide uptake.

Consequently, prior to understanding how disrupting dimerisation impacts on NIS function, it was important to first determine how heterodimerisation between functional NIS and a non-functional mutant affects radioiodide uptake. To achieve this, cells were co-transfected with individual mutants and WT NIS. It was anticipated that dimerisation between WT NIS and the non-functional mutants might cause a reduction in radioiodide uptake compared to WT alone or WT with the functional Q471A mutant, as mutants Y242A and T243A are largely intracellularly retained. This would imply that dimerisation occurs during the trafficking process and that dimerisation with a non-functional mutant prevents WT NIS from being trafficked to the membrane. While this trend was observed in SW1736 cells, therefore supporting this hypothesis, the opposite trend was seen in HeLa cells, as radioiodide uptake was higher in cells transfected with WT + non-functional mutant combinations than WT alone, although statistical analyses could not be performed here. This also suggests that these mutants dimerise with WT during the trafficking process, but that dimerisation with WT NIS may potentially overcome the intracellular retention of these mutants, enabling the mutant to be trafficked in conjunction with WT NIS to the plasma membrane where it can function. Although these are two conflicting hypotheses, it is possible that the two different cell types may process NIS differently. To determine the impact of dimerisation between functional NIS and intracellularly-retained mutants on NIS subcellular localisation and to elucidate if the two cell lines differ in this aspect, it would be prudent to conduct immunofluorescence studies on both cell types expressing WT and the non-functional mutants alone or in combination to determine whether there is any change in the subcellular localisation of the mutants.

By the same token, it was expected that cells expressing the mutant combinations which were shown to have disrupted dimerisation (Q471A + Y242A and Q471A + T243A) would

have similar radioiodide uptake to WT alone or WT + Q471A, as the functional Q471A mutant would not interact with the non-functional, intracellularly-retained mutants and so its trafficking to the membrane, and therefore function, would be unimpaired. Again, this was observed in HeLa cells, but in SW1736 cells there was little change in the radioiodide uptake of these mutant combinations with impaired dimerisation compared to the WT + non-functional mutant combinations. Again, this could be due to differences in NIS processing in the two cell lines, but statistical analyses could not be conducted here to investigate this.

6.4.4 Concluding statements

The data presented in this chapter established an important role for the residues of the primary putative dimerisation interface in NIS protein maturation, subcellular localisation and, ultimately, function. While mutating single residues in the interface was insufficient to affect NIS dimerisation, combining two mutations to disrupt interactions between key residues of the interface successfully inhibited NIS dimerisation. Although radioiodide experiments were conducted to determine the effect of this disruption of dimerisation on NIS function, the results remain inconclusive and require further study. However, these results suggest that NIS dimerisation occurs during the protein trafficking process, either in the ER or Golgi network, so there may be a role for dimerisation in the successful trafficking of NIS to the plasma membrane.

CHAPTER 7 – DISCUSSION, FINAL CONCLUSIONS AND FUTURE STUDIES

The research presented in this thesis explored NIS dimerisation, with particular focus on utilising multiple techniques to robustly challenge its occurrence and to elucidate regions of the protein involved in mediating dimerisation. These studies were founded on observations that NIS exists at molecular weights that are suggestive of dimerisation. Freeze-fracture electron microscopy showed that NIS intramembrane particles were approximately 9nm in diameter, which is comparable to that of other dimeric proteins with a similar molecular weight to NIS (Eskandari et al., 1997). Additionally, size exclusion chromatography and light scattering analysis of purified NIS protein demonstrated that NIS exists at higher molecular weights than expected (Huc-Brandt et al., 2011), with similar results seen in other Western blot studies (Levy et al., 1997, Castro et al., 1999, Dayem et al., 2008). However, none of these studies sought to investigate NIS dimerisation further, despite dimerisation playing a crucial role for the function of many membrane proteins.

7.1 Multiple methodologies demonstrated the dimerisation of NIS

Although previous studies suggested that NIS dimerisation might occur, it was crucial to convincingly investigate if NIS does dimerise. A vast array of methods can be utilised to study protein dimerisation, but there is no ‘gold-standard’ as each one has its own merits and drawbacks. Therefore, a range of methods are used when investigating dimerisation to support the conclusions and minimise the shortcomings of individual approaches.

Two methods were readily available at the start of this PhD to investigate NIS dimerisation. PLA can detect whether two proteins are within 40nm of each other in the whole cell (Sigma-Aldrich, 2018b). Interestingly, substantial PLA signal was observed in cells co-transfected with NIS-MYC and NIS-HA. This signal was comparable to the positive control, the known dimeric membrane protein MCT8 (Visser et al., 2009), which provided further

support that this PLA signal was indicative of protein dimerisation. It was also intriguing to observe that PLA signal of both proteins was distributed throughout the cell, not just at the plasma membrane where these proteins are functional, suggesting that NIS dimerisation occurs in the protein trafficking pathway. Additionally, co-IP, which detects interactions in isolated proteins, revealed a band of ~150kDa only when NIS-MYC and NIS-HA were co-expressed. As this band was an appropriate size for a dimer, given that the mature and immature NIS monomers are ~87kDa and ~69kDa, respectively (Levy et al., 1998a, Smanik et al., 1996), it was considered very likely that this band was indicative of dimerisation.

However, the main disadvantage of both methods is the possibility of false positive results. As protein trafficking vesicles can vary in size from 30-50nm to 200-1200nm, PLA may detect NIS monomers which are in the same trafficking vesicles but not directly interacting (Jena, 2008). Similarly, co-IP can detect monomers which indirectly interact via another protein or aggregation (Phizicky and Fields, 1995). To address these concerns, a FRET-based methodology was developed, as the maximum distance is just 10nm and therefore unlikely to give false positive results (Stanley, 2003, Piston and Kremers, 2007). Analysis revealed a significant increase in corrected FRET in cells co-expressing NIS-Cerulean and NIS-Citrine compared to the negative control, thereby demonstrating NIS dimerisation and also validating the PLA and co-IP results. To investigate the subcellular localisation of NIS dimerisation, corrected FRET analysis was performed on linear regions across the cell. Interestingly, this showed dimerisation occurs throughout the cell, with rapid peaks in the signal potentially corresponding to dimerisation within vesicles. This suggests that NIS dimerisation may occur during in the protein trafficking pathway, which was also hypothesised from the cell-wide distribution of PLA signal.

7.2 An alternative role for putative dimerisation motifs in NIS protein folding was proposed

To explore the role of dimerisation in NIS function, it was necessary to disrupt dimerisation. Fortuitously, two putative dimerisation motifs have been proposed in the NIS primary sequence: a GZM involving residues G444 and G448 in TMD 12 (Okuda et al., 2012), and a LZM comprising residues L199, L206, L212 and L220 in TMD 6 (Smanik et al., 1996). Interestingly, the putative dimerisation motif mutants were non-functional due to inadequate glycosylation, which prevented trafficking to the plasma membrane. To further elucidate the subcellular localisation of these mutants, immunofluorescence could be performed to probe for colocalisation between the mutant NIS and markers of the ER and Golgi network.

Since both motifs were shown to be critical for NIS function, the ability of these mutants to dimerise was explored. As two methods would provide sufficient information on mutant NIS dimerisation, FRET was used both as a quantitative method and as a more accurate indicator of proximity between the two monomers, while PLA was used as the qualitative methodology in the mutant studies because using another whole cell technique may help support any changes in subcellular localisation of dimerisation.

It was surprising to observe no significant change in corrected FRET or PLA signal with any putative dimerisation motif mutant compared to WT, as this suggests these motifs are unlikely to be involved in NIS dimerisation. However, these motifs were essential for NIS function, indicating that these motifs have an alternative role. It has been previously suggested that, in multi-pass membrane proteins, GZMs are more likely to mediate interactions between the TMD helices, and subsequently facilitate correct protein folding, than dimerisation (Teese and Langosch, 2015). This is a credible explanation for these

results, as NIS is a multi-pass membrane protein and mutating the GZM prevented adequate glycosylation of the protein, indicating that the mutant cannot undergo the normal protein trafficking pathway and is subsequently retained in the ER/Golgi network (Peer, 2011), which strongly suggests that the GZM mutant NIS protein is misfolded. Similar results were seen for the LZM mutants, and as LZMs also facilitate helical interactions, it is highly likely that the LZM mutant proteins were also misfolded. Together, these data indirectly supported a novel role for the GZM and LZM in NIS protein folding.

7.3 A novel homology model of NIS dimerisation was developed which revealed residues which form a putative dimerisation interface

Since the putative dimerisation motifs are unlikely to be involved in NIS dimerisation, a different approach was required to identify those residues involved. While a crystal structure for NIS would be the optimal way to achieve this, it has not yet been determined, given the complexity of membrane protein crystallography. However, the crystal structure has been resolved for dimerised vSGLT, a bacterial protein from the same family as NIS (Faham et al., 2008, Watanabe et al., 2010). Although the vSGLT structure has been used for NIS homology modelling previously, these studies only modelled the monomer (Portulano et al., 2014, Darrouzet et al., 2014, Vergara-Jaque et al., 2017, Ravera et al., 2017).

A novel homology model of NIS dimerisation was created here by ‘threading’ the NIS primary sequence on to the crystal structure of the vSGLT dimer (Al-Karadaghi, 2017) and subsequently refined by removing large unstructured regions of the NIS sequence to improve homology between NIS and vSGLT. Investigations were then conducted to determine the accuracy of the model. Reassuringly, no charged residues were located in the TMDs of the NIS model as, in physiology, unfavourable energetics prevent TMDs from containing

charged residues (Ulmschneider and Sansom, 2001). Furthermore, residues known from mutagenesis studies to be involved in sodium or iodide binding (Levy et al., 1998b, De la Vieja et al., 2007, Paroder-Belenitsky et al., 2011, Ferrandino et al., 2016, Vergara-Jaque et al., 2017) were identified on the model and appeared to cluster together, forming distinct binding pockets resembling those in the vSGLT crystal structure (Faham et al., 2008, Xie et al., 2000). Altogether, these results were encouraging and indicated that this homology model is likely to be an accurate representation of the true NIS structure.

This model was then used to identify residues potentially involved in NIS dimerisation for future experimental studies by searching for residues less than 3Å (0.3nm) from the opposite monomer. This revealed eight residues to be in close enough proximity to dimerise and it was promising to observe these residues clustering together to form two distinct putative dimerisation motifs. The larger primary interface at the extracellular surface consists of residues D237, Y242, T243 and F244 from the third extracellular loop (close to the start of TMD 7) and residues Q471 and A525 from the start and end of the sixth extracellular loop between TMDs 12 and 13, while the smaller secondary interface comprises residues K554 and R555 from the start of the intracellular C-terminus. These residues were novel targets for site-directed mutagenesis to explore NIS dimerisation.

7.4 Multiple interactions occur between residues Q471, Y242 and T243 to facilitate dimerisation, which require disrupting to affect dimerisation

Although site-directed mutagenesis failed for three of the putative dimerisation interface residues (F2444, K554 and R555), out of the five mutants successfully created (D237A, Y242A, T243A, Q471A and A525F), only Q471A retained function. The other mutants were non-functional and suggested to have impaired glycosylation, with reduced expression at the

plasma membrane. As these observations are consistent with a compromised protein trafficking pathway (Peer, 2011), a potential role for these residues in mediating the correct folding of NIS was proposed. Additional immunofluorescence studies could be performed with ER and Golgi network markers to clarify the subcellular localisation of these mutants.

Studies were then conducted to explore the importance of these putative dimerisation interface residues for NIS dimerisation. As little significant change in PLA signal or corrected FRET was observed for any mutant, the primary putative dimerisation interface of the homology model was examined in closer detail to identify potential interactions between these residues which could be targeted for disruption by co-expressing two different mutants. Interestingly, this revealed a distinct clustering of three residues: Q471 of one monomer with Y242 and T243 of the opposite monomer. Consequently, dimerisation studies were performed on cells expressing one of the following mutant combinations: Q471A + Y242A, or Q471A + T243A. These studies revealed a significant reduction in corrected FRET for both combinations in both cell lines compared to WT, demonstrating that interactions between these are crucial for NIS dimerisation.

7.5 A role for NIS dimerisation in membrane trafficking was postulated

To explore the effect of disrupting dimerisation on NIS function, extensive radioiodide uptake assays were performed on cells expressing these mutant combinations. Contrasting results were observed in the two cell lines, but as time constraints prevented a third repeat of the experiment, statistical analyses could not be performed and therefore the significance of these trends remains unknown. However, these preliminary data suggest that dimerisation may occur during the trafficking process and propose a potential role for dimerisation in the trafficking of NIS to the plasma membrane. Immunofluorescence or subcellular fractionation

analyses comparing the subcellular localisations of WT and mutant NIS when expressed alone and in combination may provide useful insight to explore this hypothesis.

Furthermore, PLA signal and corrected FRET for WT NIS was distributed across the whole cell, not just at the plasma membrane. Altogether, these data suggest that the role of dimerisation may be to ensure the normal trafficking of NIS to the plasma membrane, where it is functional. As dimerisation has been shown to be important for the membrane protein trafficking of GPCRs (Salahpour et al., 2004, Zhou et al., 2006, Dorsch et al., 2009), it is particularly interesting that this is also the proposed role for dimerisation in NIS, given that both GPCRs and NIS are multi-pass membrane proteins. To investigate whether dimerisation does occur during the trafficking process, it may be beneficial to conduct whole-cell dimerisation studies in the presence of an endocytosis inhibitor, as detecting intracellular dimerisation under these conditions would demonstrate that dimerisation occurs prior to expression at the plasma membrane.

7.6 Critical evaluation and future directions

While the FRET method developed in this thesis provided valuable information into NIS dimerisation and the interactions involved, the data analysis required proved more extensive than initially anticipated. Future investigations into NIS dimerisation may benefit from utilising bimolecular fluorescence complementation (BiFC), where two truncated halves of a fluorophore are individually conjugated onto the NIS C-terminus. As fluorescence is only observed when the two halves of the fluorophore are brought together, complications arising from the spectral overlap between the two fluorophores used in FRET are no longer present, thus obviating the need for the corrections discussed in this thesis. It is important to note that this technique was not used at the outset because false-positives are more likely to occur

with BiFC than FRET, as BiFC can occur at larger distances than FRET, therefore a negative control which cannot dimerise is essential for BiFC studies (Miller et al., 2015), which was not available at the start of these studies. However, the mutant combinations which significantly reduced FRET could be utilised as a negative control for future BiFC studies.

Co-expression has been a vital component of many of these studies, but with co-transfecting two plasmids, it is unlikely that cells will express equal quantities of both proteins. This can have implications for subsequent experiments, particularly for FRET studies, as deviations from the ideal 1:1 fluorophore stoichiometry negatively impacts the FRET signal (Stanley, 2003, Piston and Kremers, 2007). Consequently, these studies may be improved from utilising plasmids expressing multiple proteins, so-called multicistronic vectors (Fan, 2014), as this would enable 1:1 co-expression of two plasmids from transfection with just one plasmid. There are two commonly used methods to co-express two proteins from one plasmid: internal ribosome entry site (IRES) and 2A peptides. Introducing an IRES element between the two genes enables the recruitment of a second ribosome during translation, thereby initiating translation of the second protein and resulting in co-expression of the two proteins (Figure 7-1A (Fan, 2014)). The presence of a 2A peptide (between 18-22 residues) between two genes causes the ribosome to skip synthesis during translation. This 'cleaves' between the glycine and proline residues at the end of the 2A peptide and generates co-expression of two distinct proteins, each left expressing part of the 2A peptide (Figure 7-1B (Liu et al., 2017, Fan, 2014)). Although both techniques are valuable, they also have some disadvantages. IRES is known to have reduced expression of the downstream protein, resulting in an uneven ratio between the two proteins. While 2A peptides give a 1:1 stoichiometry, the ribosome skipping can fail, thus generating a fusion protein (Chan et al.,

2011). Consequently, the 2A peptide method would be the most appropriate method for future NIS dimerisation studies, as equal expression levels are required for these studies.

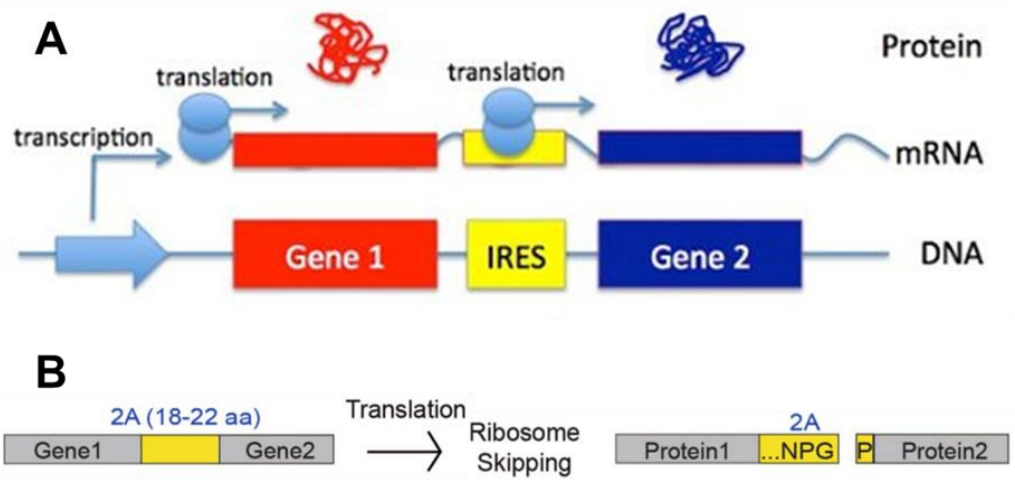

Figure 7-1 – Methods for co-expressing two proteins in one plasmid. A) An internal ribosome entry site (IRES) between two genes recruits a second ribosome to enable translation of two separate proteins. B) Expression of a 2A peptide between two genes results in ribosome skipping, which cleaves between C-terminal glycine (G) and proline (P) residues of the peptide and results in two distinct proteins. Image adapted from Fan, 2014 (A) and Liu et al., 2017 (B).

Although a comprehensive study is described in this thesis, the main limitation is the sole reliance on an exogenous system. However, endogenous dimerisation is extremely difficult to measure, given the need to conclusively prove that two monomers are interacting. This is achievable with differentially-tagged variants, but much more challenging in an endogenous system, such as normal or cancerous thyroid tissue. Nevertheless, it is possible to utilise the PLA method to study endogenous protein dimerisation. This involves differentially-labelling two populations of the same monoclonal antibody (mAb) against the protein of interest with either the PLUS oligo or the MINUS oligo (Sigma-Aldrich, 2018c). Monomers would only be labelled with one mAb, and so only one oligo, thus identifying dimerisation between endogenous monomers. However, the concerns that PLA results could be false-positives still remain. Furthermore, the protocol dictates a required mAb concentration of 1mg/ml in a buffer free of amine, carrier and preservative (Sigma-Aldrich, 2018c). This is a substantial barrier to conducting these studies, as this is an uncommon antibody formulation and buffer

exchange procedures often result in loss of antibody. Consequently, it may prove more attainable to perform a transfection titration and repeating these experiments to see if similar results are achieved with more physiologically-relevant expression levels of NIS.

7.7 Concluding statements

The research presented in this thesis has successfully demonstrated that NIS does dimerise, which had only been hypothesised previously. Although it was revealed that putative dimerisation motifs in the NIS sequence were unlikely to be involved in dimerisation, these data proposed a role for these motifs in NIS protein folding. This led to the development of a novel homology model of NIS dimerisation which identified the residues forming a putative dimerisation interface. Of these residues, interactions between three key residues (Q471, Y242 and T243) were shown to be crucial for NIS dimerisation to occur. While extensive further study is required to fully elucidate the importance of dimerisation for NIS function, the data described here indicate that dimerisation occurs during the protein trafficking pathway and therefore suggests a potential role for dimerisation in the trafficking of NIS to the plasma membrane, where it is functional. However, as the majority of mutants presented in this thesis retained dimerisation but were non-functional, possibly due to misfolding, it is unlikely that dimerisation is solely responsible for trafficking to the membrane.

This work has provided novel insight into NIS biology which may have wider implications, particularly for the clinical application of NIS. If future work confirms dimerisation is important for NIS trafficking to the plasma membrane, this could lead to the development of a novel gene therapy in which dimerised NIS is expressed in tumour cells to increase NIS expression at the plasma membrane and subsequently enhance radioiodide uptake of the tumour cells. This could improve treatment efficacy and, hence, outcome for the patient.

CHAPTER 8 - REFERENCES

ABD ALLA, J., REECK, K., LANGER, A., STREICHERT, T. & QUITTERER, U. 2009. Calreticulin enhances B2 bradykinin receptor maturation and heterodimerization. *Biochem Biophys Res Commun,* 387**,** 186-90.

ABRAMSON, J. & WRIGHT, E. M. 2009. Structure and function of Na(+)-symporters with inverted repeats. *Curr Opin Struct Biol,* 19**,** 425-32.

AL-KARADAGHI, S. 2017. *Structural bioinformatics, protein crystallography, sequence analysis & homolog modelling.* [Online]. Available: https://proteinstructures.com/Modeling/homology-modeling.html [Accessed 11th March 2018].

ALTORJAY, A., DOHAN, O., SZILAGYI, A., PARODER, M., WAPNIR, I. L. & CARRASCO, N. 2007. Expression of the Na+/I- symporter (NIS) is markedly decreased or absent in gastric cancer and intestinal metaplastic mucosa of Barrett esophagus. *BMC Cancer,* 7**,** 5.

ANGERS, S., SALAHPOUR, A., JOLY, E., HILAIRET, S., CHELSKY, D., DENNIS, M. & BOUVIER, M. 2000. Detection of beta 2-adrenergic receptor dimerization in living cells using bioluminescence resonance energy transfer (BRET). *Proc Natl Acad Sci U S A,* 97**,** 3684-9.

BART, G., VICO, N. O., HASSINEN, A., PUJOL, F. M., DEEN, A. J., RUUSALA, A., TAMMI, R. H., SQUIRE, A., HELDIN, P., KELLOKUMPU, S. & TAMMI, M. I. 2015. Fluorescence resonance energy transfer (FRET) and proximity ligation assays reveal functionally relevant homo- and heteromeric complexes among hyaluronan synthases HAS1, HAS2, and HAS3. *J Biol Chem,* 290**,** 11479-90.

BARTON, K. N., STRICKER, H., ELSHAIKH, M. A., PEGG, J., CHENG, J., ZHANG, Y., KARVELIS, K. C., LU, M., MOVSAS, B. & FREYTAG, S. O. 2011. Feasibility of adenovirus-mediated hNIS gene transfer and 131I radioiodine therapy as a definitive treatment for localized prostate cancer. *Mol Ther,* 19**,** 1353-9.

BAUMANN, E. 1896. Uber das Thyrojodin. *Munch Med Wschr.***,** 309-312.

BERDELOU, A., LAMARTINA, L., KLAIN, M., LEBOULLEUX, S. & SCHLUMBERGER, M. 2018. Treatment of refractory thyroid cancer. *Endocr Relat Cancer,* 25**,** R209-R223.

BERMAN, H. M., WESTBROOK, J., FENG, Z., GILLILAND, G., BHAT, T. N., WEISSIG, H., SHINDYALOV, I. N. & BOURNE, P. E. 2000. The Protein Data Bank. *Nucleic Acids Res,* 28**,** 235-42.

BIDART, J. M., LACROIX, L., EVAIN-BRION, D., CAILLOU, B., LAZAR, V., FRYDMAN, R., BELLET, D., FILETTI, S. & SCHLUMBERGER, M. 2000. Expression of Na+/I- symporter and Pendred syndrome genes in trophoblast cells. *J Clin Endocrinol Metab,* 85**,** 4367-72.

BOCHAROV, E. V., MAYZEL, M. L., VOLYNSKY, P. E., GONCHARUK, M. V., ERMOLYUK, Y. S., SCHULGA, A. A., ARTEMENKO, E. O., EFREMOV, R. G. & ARSENIEV, A. S. 2008a. Spatial structure and pH-dependent conformational diversity of dimeric transmembrane domain of the receptor tyrosine kinase EphA1. *J Biol Chem,* 283**,** 29385-95.

BOCHAROV, E. V., MINEEV, K. S., VOLYNSKY, P. E., ERMOLYUK, Y. S., TKACH, E. N., SOBOL, A. G., CHUPIN, V. V., KIRPICHNIKOV, M. P., EFREMOV, R. G. & ARSENIEV, A. S. 2008b. Spatial structure of the dimeric transmembrane domain of the growth factor receptor ErbB2 presumably corresponding to the receptor active state. *J Biol Chem,* 283**,** 6950-6.

BOYER, S. B. & SLESINGER, P. A. 2010. Probing novel GPCR interactions using a combination of FRET and TIRF. *Commun Integr Biol,* 3**,** 343-6.

BRAVERMAN, L. E. & INGBAR, S. H. 1963. CHANGES IN THYROIDAL FUNCTION DURING ADAPTATION TO LARGE DOSES OF IODIDE. *J Clin Invest,* 42**,** 1216-31.

BRITISH THYROID FOUNDATION. 2015. *Thyroid function tests* [Online]. Available: http://www.btf-thyroid.org/information/leaflets/34-thyroid-function-tests-guide [Accessed 31st March 2018].

BROSE, M. S., NUTTING, C. M., JARZAB, B., ELISEI, R., SIENA, S., BASTHOLT, L., DE LA FOUCHARDIERE, C., PACINI, F., PASCHKE, R., SHONG, Y. K., SHERMAN, S. I., SMIT, J. W., CHUNG, J., KAPPELER, C., PENA, C., MOLNAR, I. & SCHLUMBERGER, M. J. 2014. Sorafenib in radioactive iodine-refractory, locally advanced or metastatic differentiated thyroid cancer: a randomised, double-blind, phase 3 trial. *Lancet,* 384**,** 319-28.

BROUSSARD, J. A., RAPPAZ, B., WEBB, D. J. & BROWN, C. M. 2013. Fluorescence resonance energy transfer microscopy as demonstrated by measuring the activation of the serine/threonine kinase Akt. *Nat Protoc,* 8**,** 265-81.

CANCER RESEARCH UK. 2016. *Thyroid cancer incidence statistics* [Online]. Available: http://www.cancerresearchuk.org/health-professional/cancer-statistics/statistics-by-cancer-type/thyroid-cancer/incidence#heading-Three [Accessed 9th April 2018].

CASTRO, M. R., BERGERT, E. R., BEITO, T. G., ROCHE, P. C., ZIESMER, S. C., JHIANG, S. M., GOELLNER, J. R. & MORRIS, J. C. 1999. Monoclonal antibodies against the human sodium iodide symporter: utility for immunocytochemistry of thyroid cancer. *J Endocrinol,* 163**,** 495-504.

CENGIC, N., BAKER, C. H., SCHUTZ, M., GOKE, B., MORRIS, J. C. & SPITZWEG, C. 2005. A novel therapeutic strategy for medullary thyroid cancer based on radioiodine therapy following tissue-specific sodium iodide symporter gene expression. *J Clin Endocrinol Metab,* 90**,** 4457-64.

CHAN, H. Y., V, S., XING, X., KRAUS, P., YAP, S. P., NG, P., LIM, S. L. & LUFKIN, T. 2011. Comparison of IRES and F2A-based locus-specific multicistronic expression in stable mouse lines. *PLoS One,* 6**,** e28885.

CHEMISTRY-LIBRETEXTS. 2018a. *Covalent bond distance, radius and Van der Waals radius* [Online]. Available: https://chem.libretexts.org/Core/Physical_and_Theoretical_Chemistry/Chemical_Bonding/Fundamentals_of_Chemical_Bonding/Covalent_Bond_Distance%2C_Radius_and_van_der_Waals_Radius [Accessed 10th March 2018].

CHEMISTRY-LIBRETEXTS. 2018b. *Van der Waals interactions* [Online]. Available: https://chem.libretexts.org/Core/Physical_and_Theoretical_Chemistry/Physical_Properties_of_Matter/Atomic_and_Molecular_Properties/Intermolecular_Forces/Specific_Interactions/Van_Der_Waals_Interactions [Accessed 10th March 2018].

CLAROS, M. G. & VON HEIJNE, G. 1994. TopPred II: an improved software for membrane protein structure predictions. *Comput Appl Biosci,* 10**,** 685-6.

COSTAMAGNA, E., GARCIA, B. & SANTISTEBAN, P. 2004. The functional interaction between the paired domain transcription factor Pax8 and Smad3 is involved in transforming growth factor-beta repression of the sodium/iodide symporter gene. *J Biol Chem,* 279**,** 3439-46.

COTE, G. J., GRUBBS, E. G. & HOFMANN, M. C. 2015. Thyroid C-Cell Biology and Oncogenic Transformation. *Recent Results Cancer Res,* 204**,** 1-39.

DAI, G., LEVY, O. & CARRASCO, N. 1996. Cloning and characterization of the thyroid iodide transporter. *Nature,* 379**,** 458-60.

DARROUZET, E., LINDENTHAL, S., MARCELLIN, D., PELLEQUER, J. L. & POURCHER, T. 2014. The sodium/iodide symporter: state of the art of its molecular characterization. *Biochim Biophys Acta,* 1838**,** 244-53.

DAVIDSON, M. & PISTON, D. *unpublished*. *Michael Davidson Lab: Empty Backbones* [Online]. Available: https://www.addgene.org/browse/article/8501/ [Accessed 01.08.16].

DAY, R. N. & DAVIDSON, M. W. 2009. The fluorescent protein palette: tools for cellular imaging. *Chem Soc Rev,* 38**,** 2887-921.

DAYEM, M., BASQUIN, C., NAVARRO, V., CARRIER, P., MARSAULT, R., CHANG, P., HUC, S., DARROUZET, E., LINDENTHAL, S. & POURCHER, T. 2008. Comparison of expressed human and mouse sodium/iodide symporters reveals differences in transport properties and subcellular localization. *J Endocrinol,* 197**,** 95-109.

DE LA VIEJA, A., DOHAN, O., LEVY, O. & CARRASCO, N. 2000. Molecular analysis of the sodium/iodide symporter: impact on thyroid and extrathyroid pathophysiology. *Physiol Rev,* 80**,** 1083-105.

DE LA VIEJA, A., GINTER, C. S. & CARRASCO, N. 2004. The Q267E mutation in the sodium/iodide symporter (NIS) causes congenital iodide transport defect (ITD) by decreasing the NIS turnover number. *J Cell Sci,* 117**,** 677-87.

DE LA VIEJA, A., GINTER, C. S. & CARRASCO, N. 2005. Molecular analysis of a congenital iodide transport defect: G543E impairs maturation and trafficking of the Na+/I- symporter. *Mol Endocrinol,* 19**,** 2847-58.

DE LA VIEJA, A., REED, M. D., GINTER, C. S. & CARRASCO, N. 2007. Amino acid residues in transmembrane segment IX of the Na+/I- symporter play a role in its Na+ dependence and are critical for transport activity. *J Biol Chem,* 282**,** 25290-8.

DE LA VIEJA, A. & SANTISTEBAN, P. 2018. Role of iodide metabolism in physiology and cancer. *Endocr Relat Cancer*.

DEVUYST, O., GOLSTEIN, P. E., SANCHES, M. V., PIONTEK, K., WILSON, P. D., GUGGINO, W. B., DUMONT, J. E. & BEAUWENS, R. 1997. Expression of CFTR in human and bovine thyroid epithelium. *Am J Physiol,* 272**,** C1299-308.

DI JESO, B. & ARVAN, P. 2016. Thyroglobulin From Molecular and Cellular Biology to Clinical Endocrinology. *Endocr Rev,* 37**,** 2-36.

DOHAN, O., GAVRIELIDES, M. V., GINTER, C., AMZEL, L. M. & CARRASCO, N. 2002. Na(+)/I(-) symporter activity requires a small and uncharged amino acid residue at position 395. *Mol Endocrinol,* 16**,** 1893-902.

DOHAN, O., PORTULANO, C., BASQUIN, C., REYNA-NEYRA, A., AMZEL, L. M. & CARRASCO, N. 2007. The Na+/I symporter (NIS) mediates electroneutral active transport of the environmental pollutant perchlorate. *Proc Natl Acad Sci U S A,* 104**,** 20250-5.

DORION, D. 2017. *Thyroid Anatomy* [Online]. Medscape. Available: https://reference.medscape.com/article/835535-overview#showall [Accessed 30th March 2018].

DORSCH, S., KLOTZ, K. N., ENGELHARDT, S., LOHSE, M. J. & BUNEMANN, M. 2009. Analysis of receptor oligomerization by FRAP microscopy. *Nat Methods,* 6**,** 225-30.

DURANTE, C., HADDY, N., BAUDIN, E., LEBOULLEUX, S., HARTL, D., TRAVAGLI, J. P., CAILLOU, B., RICARD, M., LUMBROSO, J. D., DE VATHAIRE, F. & SCHLUMBERGER, M. 2006. Long-term outcome of 444 patients with distant metastases from papillary and follicular thyroid carcinoma: benefits and limits of radioiodine therapy. *J Clin Endocrinol Metab,* 91**,** 2892-9.

DWYER, R. M., BERGERT, E. R., O'CONNOR M, K., GENDLER, S. J. & MORRIS, J. C. 2005. In vivo radioiodide imaging and treatment of breast cancer xenografts after MUC1-driven expression of the sodium iodide symporter. *Clin Cancer Res,* 11**,** 1483-9.

ELISEI, R., ROMEI, C., VORONTSOVA, T., COSCI, B., VEREMEYCHIK, V., KUCHINSKAYA, E., BASOLO, F., DEMIDCHIK, E. P., MICCOLI, P., PINCHERA, A. & PACINI, F. 2001. RET/PTC rearrangements in thyroid nodules: studies in irradiated and not irradiated, malignant and benign thyroid lesions in children and adults. *J Clin Endocrinol Metab,* 86**,** 3211-6.

ENG, P. H., CARDONA, G. R., FANG, S. L., PREVITI, M., ALEX, S., CARRASCO, N., CHIN, W. W. & BRAVERMAN, L. E. 1999. Escape from the acute Wolff-Chaikoff effect is associated with a decrease in thyroid sodium/iodide symporter messenger ribonucleic acid and protein. *Endocrinology,* 140**,** 3404-10.

ENG, P. H., CARDONA, G. R., PREVITI, M. C., CHIN, W. W. & BRAVERMAN, L. E. 2001. Regulation of the sodium iodide symporter by iodide in FRTL-5 cells. *Eur J Endocrinol,* 144**,** 139-44.

ESAPA, C. T., JOHNSON, S. J., KENDALL-TAYLOR, P., LENNARD, T. W. & HARRIS, P. E. 1999. Prevalence of Ras mutations in thyroid neoplasia. *Clin Endocrinol (Oxf),* 50**,** 529-35.

ESKANDARI, S., LOO, D. D., DAI, G., LEVY, O., WRIGHT, E. M. & CARRASCO, N. 1997. Thyroid Na+/I- symporter. Mechanism, stoichiometry, and specificity. *J Biol Chem,* 272**,** 27230-8.

FAGIN, J. A., MATSUO, K., KARMAKAR, A., CHEN, D. L., TANG, S. H. & KOEFFLER, H. P. 1993. High prevalence of mutations of the p53 gene in poorly differentiated human thyroid carcinomas. *J Clin Invest,* 91**,** 179-84.

FAHAM, S., WATANABE, A., BESSERER, G. M., CASCIO, D., SPECHT, A., HIRAYAMA, B. A., WRIGHT, E. M. & ABRAMSON, J. 2008. The crystal structure of a sodium galactose transporter reveals mechanistic insights into Na+/sugar symport. *Science,* 321**,** 810-4.

FAIVRE, J., CLERC, J., GEROLAMI, R., HERVE, J., LONGUET, M., LIU, B., ROUX, J., MOAL, F., PERRICAUDET, M. & BRECHOT, C. 2004. Long-term radioiodine retention and regression of liver cancer after sodium iodide symporter gene transfer in wistar rats. *Cancer Res,* 64**,** 8045-51.

FAN, M. 2014. *Plasmids 101: Multicistronic Vectors* [Online]. Available: https://blog.addgene.org/plasmids-101-multicistronic-vectors [Accessed 25/7/18].

FANG, Y., JAYARAM, H., SHANE, T., KOLMAKOVA-PARTENSKY, L., WU, F., WILLIAMS, C., XIONG, Y. & MILLER, C. 2009. Structure of a prokaryotic virtual proton pump at 3.2 A resolution. *Nature,* 460**,** 1040-3.

FERRANDINO, G., NICOLA, J. P., SANCHEZ, Y. E., ECHEVERRIA, I., LIU, Y., AMZEL, L. M. & CARRASCO, N. 2016. Na+ coordination at the Na2 site of the Na+/I- symporter. *Proc Natl Acad Sci U S A.*

FISCHER, A. J., LENNEMANN, N. J., KRISHNAMURTHY, S., POCZA, P., DURAIRAJ, L., LAUNSPACH, J. L., RHEIN, B. A., WOHLFORD-LENANE, C., LORENTZEN, D., BANFI, B. & MCCRAY, P. B., JR. 2011. Enhancement of respiratory mucosal antiviral defenses by the oxidation of iodide. *Am J Respir Cell Mol Biol,* 45**,** 874-81.

FISCHER, J., KLEINAU, G., MULLER, A., KUHNEN, P., ZWANZIGER, D., KINNE, A., REHDERS, M., MOELLER, L. C., FUHRER, D., GRUTERS, A., KRUDE, H., BRIX, K. & BIEBERMANN, H. 2015. Modulation of monocarboxylate transporter 8 oligomerization by specific pathogenic mutations. *J Mol Endocrinol,* 54**,** 39-50.

FORTUNATI, N., CATALANO, M. G., ARENA, K., BRIGNARDELLO, E., PIOVESAN, A. & BOCCUZZI, G. 2004. Valproic acid induces the expression of the Na+/I- symporter and iodine uptake in poorly differentiated thyroid cancer cells. *J Clin Endocrinol Metab,* 89**,** 1006-9.

FOTIADIS, D., JASTRZEBSKA, B., PHILIPPSEN, A., MULLER, D. J., PALCZEWSKI, K. & ENGEL, A. 2006. Structure of the rhodopsin dimer: a working model for G-protein-coupled receptors. *Curr Opin Struct Biol,* 16**,** 252-9.

FREDRIKSSON, S., GULLBERG, M., JARVIUS, J., OLSSON, C., PIETRAS, K., GUSTAFSDOTTIR, S. M., OSTMAN, A. & LANDEGREN, U. 2002. Protein detection using proximity-dependent DNA ligation assays. *Nat Biotechnol,* 20**,** 473-7.

FROHLICH, E., MACHICAO, F. & WAHL, R. 2005. Action of thiazolidinediones on differentiation, proliferation and apoptosis of normal and transformed thyrocytes in culture. *Endocr Relat Cancer,* 12**,** 291-303.

FUXE, K., MARCELLINO, D., LEO, G. & AGNATI, L. F. 2010. Molecular integration via allosteric interactions in receptor heteromers. A working hypothesis. *Curr Opin Pharmacol,* 10**,** 14-22.

GAJADHAR, A. & GUHA, A. 2010. A proximity ligation assay using transiently transfected, epitope-tagged proteins: application for in situ detection of dimerized receptor tyrosine kinases. *Biotechniques,* 48**,** 145-52.

GAO, X., LU, F., ZHOU, L., DANG, S., SUN, L., LI, X., WANG, J. & SHI, Y. 2009. Structure and mechanism of an amino acid antiporter. *Science,* 324**,** 1565-8.

GARCIA, B. & SANTISTEBAN, P. 2002. PI3K is involved in the IGF-I inhibition of TSH-induced sodium/iodide symporter gene expression. *Mol Endocrinol,* 16**,** 342-52.

GENSCRIPT. 2018. *ELISA - Principles, Formats and Optimization* [Online]. Available: https://www.genscript.com/ELISA-Principles-Formats-and-Optimization.html [Accessed 03.06.18].

GOMES, I., SIERRA, S. & DEVI, L. A. 2016. Detection of Receptor Heteromerization Using In Situ Proximity Ligation Assay. *Curr Protoc Pharmacol,* 75**,** 2 16 1-2 16 31.

GRASBERGER, B., MINTON, A. P., DELISI, C. & METZGER, H. 1986. Interaction between proteins localized in membranes. *Proc Natl Acad Sci U S A,* 83**,** 6258-62.

GRIESBECK, O., BAIRD, G. S., CAMPBELL, R. E., ZACHARIAS, D. A. & TSIEN, R. Y. 2001. Reducing the environmental sensitivity of yellow fluorescent protein. Mechanism and applications. *J Biol Chem,* 276**,** 29188-94.

HAKOSHIMA, T. 2005. Leucine Zippers. *Encylopedia of Life Sciences*.

HEBERT, T. E. & BOUVIER, M. 1998. Structural and functional aspects of G protein-coupled receptor oligomerization. *Biochem Cell Biol,* 76**,** 1-11.

HERTZ, S. & ROBERTS, A. 1942. RADIOACTIVE IODINE AS AN INDICATOR IN THYROID PHYSIOLOGY. V. THE USE OF RADIOACTIVE IODINE IN THE DIFFERENTIAL DIAGNOSIS OF TWO TYPES OF GRAVES' DISEASE. *J Clin Invest,* 21**,** 31-2.

HINGORANI, M., SPITZWEG, C., VASSAUX, G., NEWBOLD, K., MELCHER, A., PANDHA, H., VILE, R. & HARRINGTON, K. 2010. The biology of the sodium iodide symporter and its potential for targeted gene delivery. *Curr Cancer Drug Targets,* 10**,** 242-67.

HOFFMAN, K. & STOFFEL, W. 1993. TMbase - A database of membrane spanning proteins segments. *Biological Chemistry Hoppe-Seyler,* 374.

HONG, C. M. & AHN, B. C. 2017. Redifferentiation of Radioiodine Refractory Differentiated Thyroid Cancer for Reapplication of I-131 Therapy. *Front Endocrinol (Lausanne),* 8**,** 260.

HOPPE, A., CHRISTENSEN, K. & SWANSON, J. A. 2002. Fluorescence resonance energy transfer-based stoichiometry in living cells. *Biophys J,* 83**,** 3652-64.

HOU, P., BOJDANI, E. & XING, M. 2010. Induction of thyroid gene expression and radioiodine uptake in thyroid cancer cells by targeting major signaling pathways. *J Clin Endocrinol Metab,* 95**,** 820-8.

HUBBARD, S. R. & TILL, J. H. 2000. Protein tyrosine kinase structure and function. *Annu Rev Biochem,* 69**,** 373-98.

HUC-BRANDT, S., MARCELLIN, D., GRASLIN, F., AVERSENG, O., BELLANGER, L., HIVIN, P., QUEMENEUR, E., BASQUIN, C., NAVARRO, V., POURCHER, T. & DARROUZET, E. 2011. Characterisation of the purified human sodium/iodide symporter reveals that the protein is mainly present in a dimeric form and permits the detailed study of a native C-terminal fragment. *Biochim Biophys Acta,* 1808**,** 65-77.

JENA, B. P. 2008. Intracellular organelle dynamics at nm resolution. *Methods Cell Biol,* 90**,** 19-37.

JUNG, H. 2002. The sodium/substrate symporter family: structural and functional features. *FEBS Lett,* 529**,** 73-7.

KANG, D. Y., LEE, H. W., CHOI, P. J., LEE, K. E. & ROH, M. S. 2009. Sodium/iodide symporter expression in primary lung cancer and comparison with glucose transporter 1 expression. *Pathol Int,* 59**,** 73-9.

KARPOWICH, N. K. & WANG, D. N. 2008. Structural biology. Symmetric transporters for asymmetric transport. *Science,* 321**,** 781-2.

KELLEY, L. A. & STERNBERG, M. J. 2009. Protein structure prediction on the Web: a case study using the Phyre server. *Nat Protoc.* England.

KIM, S., JEON, T. J., OBERAI, A., YANG, D., SCHMIDT, J. J. & BOWIE, J. U. 2005. Transmembrane glycine zippers: physiological and pathological roles in membrane proteins. *Proc Natl Acad Sci U S A,* 102**,** 14278-83.

KIM, W. G., KIM, E. Y., KIM, T. Y., RYU, J. S., HONG, S. J., KIM, W. B. & SHONG, Y. K. 2009. Redifferentiation therapy with 13-cis retinoic acids in radioiodine-resistant thyroid cancer. *Endocr J,* 56**,** 105-12.

KIMURA, E. T., NIKIFOROVA, M. N., ZHU, Z., KNAUF, J. A., NIKIFOROV, Y. E. & FAGIN, J. A. 2003. High prevalence of BRAF mutations in thyroid cancer: genetic evidence for constitutive activation of the RET/PTC-RAS-BRAF signaling pathway in papillary thyroid carcinoma. *Cancer Res,* 63**,** 1454-7.

KITAZONO, M., ROBEY, R., ZHAN, Z., SARLIS, N. J., SKARULIS, M. C., AIKOU, T., BATES, S. & FOJO, T. 2001. Low concentrations of the histone deacetylase inhibitor, depsipeptide (FR901228), increase expression of the Na(+)/I(-) symporter and iodine accumulation in poorly differentiated thyroid carcinoma cells. *J Clin Endocrinol Metab,* 86**,** 3430-5.

KOGAI, T., ENDO, T., SAITO, T., MIYAZAKI, A., KAWAGUCHI, A. & ONAYA, T. 1997. Regulation by thyroid-stimulating hormone of sodium/iodide symporter gene expression and protein levels in FRTL-5 cells. *Endocrinology,* 138**,** 2227-32.

KRIEGER, E. & VRIEND, G. 2014. YASARA View—molecular graphics for all devices—from smartphones to workstations. *Bioinformatics,* 30**,** 2981-2982.

KRISHNAMURTHY, H., PISCITELLI, C. L. & GOUAUX, E. 2009. Unlocking the molecular secrets of sodium-coupled transporters. *Nature,* 459**,** 347-55.

KROGH, A., LARSSON, B., VON HEIJNE, G. & SONNHAMMER, E. L. 2001. Predicting transmembrane protein topology with a hidden Markov model: application to complete genomes. *J Mol Biol,* 305**,** 567-80.

KROLL, T. G., SARRAF, P., PECCIARINI, L., CHEN, C. J., MUELLER, E., SPIEGELMAN, B. M. & FLETCHER, J. A. 2000. PAX8-PPARgamma1 fusion oncogene in human thyroid carcinoma [corrected]. *Science,* 289**,** 1357-60.

KRYLOV, D. & VINSON, C. R. 2001. Leucine Zipper. *Encyclopedia of Life Sciences*.

KUSZAK, A. J., PITCHIAYA, S., ANAND, J. P., MOSBERG, H. I., WALTER, N. G. & SUNAHARA, R. K. 2009. Purification and functional reconstitution of monomeric mu-opioid receptors: allosteric modulation of agonist binding by Gi2. *J Biol Chem,* 284**,** 26732-41.

LA PERLE, K. M., KIM, D. C., HALL, N. C., BOBBEY, A., SHEN, D. H., NAGY, R. S., WAKELY, P. E., JR., LEHMAN, A., JARJOURA, D. & JHIANG, S. M. 2013. Modulation of sodium/iodide symporter expression in the salivary gland. *Thyroid,* 23**,** 1029-36.

LAMOND, A. I. 2014. FRET measurement between CFP and YFP. Centre for Gene Regulation and Expression, University of Dundee.

LAN, L., BASOURAKOS, S., CUI, D., ZUO, X., DENG, W., HUO, L., CHEN, H., ZHANG, G., DENG, L., SHI, B. & LUO, Y. 2017. ATRA increases iodine uptake and inhibits the proliferation and invasiveness of human anaplastic thyroid carcinoma SW1736 cells: Involvement of beta-catenin phosphorylation inhibition. *Oncol Lett,* 14**,** 7733-7738.

LANDA, I., GANLY, I., CHAN, T. A., MITSUTAKE, N., MATSUSE, M., IBRAHIMPASIC, T., GHOSSEIN, R. A. & FAGIN, J. A. 2013. Frequent somatic TERT promoter mutations in thyroid cancer: higher prevalence in advanced forms of the disease. *J Clin Endocrinol Metab,* 98**,** E1562-6.

LANDA, I., IBRAHIMPASIC, T., BOUCAI, L., SINHA, R., KNAUF, J. A., SHAH, R. H., DOGAN, S., RICARTE-FILHO, J. C., KRISHNAMOORTHY, G. P., XU, B., SCHULTZ, N., BERGER, M. F., SANDER, C., TAYLOR, B. S., GHOSSEIN, R., GANLY, I. & FAGIN, J. A. 2016. Genomic and transcriptomic hallmarks of poorly differentiated and anaplastic thyroid cancers. *J Clin Invest,* 126**,** 1052-66.

LEE, C. 2007. Coimmunoprecipitation assay. *Methods Mol Biol,* 362**,** 401-6.

LEE, J. H. & ANZAI, Y. 2013. Imaging of thyroid and parathyroid glands. *Semin Roentgenol,* 48**,** 87-104.

LEONI, S. G., KIMURA, E. T., SANTISTEBAN, P. & DE LA VIEJA, A. 2011. Regulation of thyroid oxidative state by thioredoxin reductase has a crucial role in thyroid responses to iodide excess. *Mol Endocrinol,* 25**,** 1924-35.

LEVY, O., DAI, G., RIEDEL, C., GINTER, C. S., PAUL, E. M., LEBOWITZ, A. N. & CARRASCO, N. 1997. Characterization of the thyroid Na+/I- symporter with an anti-COOH terminus antibody. *Proc Natl Acad Sci U S A,* 94**,** 5568-73.

LEVY, O., DE LA VIEJA, A., GINTER, C. S., RIEDEL, C., DAI, G. & CARRASCO, N. 1998a. N-linked glycosylation of the thyroid Na+/I- symporter (NIS). Implications for its secondary structure model. *J Biol Chem,* 273**,** 22657-63.

LEVY, O., GINTER, C. S., DE LA VIEJA, A., LEVY, D. & CARRASCO, N. 1998b. Identification of a structural requirement for thyroid Na+/I- symporter (NIS) function from analysis of a mutation that causes human congenital hypothyroidism. *FEBS Lett,* 429**,** 36-40.

LI, E. & HRISTOVA, K. 2006. Role of receptor tyrosine kinase transmembrane domains in cell signaling and human pathologies. *Biochemistry,* 45**,** 6241-51.

LI, E. & HRISTOVA, K. 2010. Receptor tyrosine kinase transmembrane domains: Function, dimer structure and dimerization energetics. *Cell Adh Migr,* 4**,** 249-54.

LI, E., YOU, M. & HRISTOVA, K. 2005. Sodium dodecyl sulfate-polyacrylamide gel electrophoresis and forster resonance energy transfer suggest weak interactions between fibroblast growth factor receptor 3 (FGFR3) transmembrane domains in the absence of extracellular domains and ligands. *Biochemistry,* 44**,** 352-60.

LI, W., NICOLA, J. P., AMZEL, L. M. & CARRASCO, N. 2013. Asn441 plays a key role in folding and function of the Na+/I- symporter (NIS). *FASEB J,* 27**,** 3229-38.

LI, X., JAYACHANDRAN, S., NGUYEN, H.-H. T. & CHAN, M. K. 2007. Structure of the *Nitrosomonas europaea* Rh protein. *Proceedings of the National Academy of Sciences,* 104**,** 19279-19284.

LIU, X., BISHOP, J., SHAN, Y., PAI, S., LIU, D., MURUGAN, A. K., SUN, H., EL-NAGGAR, A. K. & XING, M. 2013. Highly prevalent TERT promoter mutations in aggressive thyroid cancers. *Endocr Relat Cancer,* 20**,** 603-10.

LIU, Z., CHEN, O., WALL, J. B. J., ZHENG, M., ZHOU, Y., WANG, L., RUTH VASEGHI, H., QIAN, L. & LIU, J. 2017. Systematic comparison of 2A peptides for cloning multi-genes in a polycistronic vector. *Sci Rep,* 7**,** 2193.

MARUYAMA, I. N. 2015. Activation of transmembrane cell-surface receptors via a common mechanism? The "rotation model". *Bioessays,* 37**,** 959-67.

MAUREL, D., COMPS-AGRAR, L., BROCK, C., RIVES, M. L., BOURRIER, E., AYOUB, M. A., BAZIN, H., TINEL, N., DURROUX, T., PREZEAU, L., TRINQUET, E. & PIN, J. P. 2008. Cell-surface protein-protein interaction analysis with time-resolved FRET and snap-tag technologies: application to GPCR oligomerization. *Nat Methods,* 5**,** 561-7.

MENDROLA, J. M., BERGER, M. B., KING, M. C. & LEMMON, M. A. 2002. The single transmembrane domains of ErbB receptors self-associate in cell membranes. *J Biol Chem,* 277**,** 4704-12.

MILLER, K. E., KIM, Y., HUH, W. K. & PARK, H. O. 2015. Bimolecular Fluorescence Complementation (BiFC) Analysis: Advances and Recent Applications for Genome-Wide Interaction Studies. *J Mol Biol,* 427**,** 2039-2055.

MILLIGAN, G. 2010. The role of dimerisation in the cellular trafficking of G-protein-coupled receptors. *Current Opinions in Pharmacology,* 10**,** 23-9.

MORENO, J. C. & VISSER, T. J. 2010. Genetics and phenomics of hypothyroidism and goiter due to iodotyrosine deiodinase (DEHAL1) gene mutations. *Mol Cell Endocrinol,* 322**,** 91-8.

MOTHERSILL, C. & SEYMOUR, C. B. 2004. Radiation-induced bystander effects--implications for cancer. *Nat Rev Cancer,* 4**,** 158-64.

NICOLA, J. P., BASQUIN, C., PORTULANO, C., REYNA-NEYRA, A., PARODER, M. & CARRASCO, N. 2009. The Na+/I- symporter mediates active iodide uptake in the intestine. *Am J Physiol Cell Physiol,* 296**,** C654-62.

NICOLA, J. P., REYNA-NEYRA, A., SAENGER, P., RODRIGUEZ-BURITICA, D. F., GODOY, J. D., MUZUMDAR, R., AMZEL, L. M. & CARRASCO, N. 2015. The sodium/iodide symporter mutant V270E causes stunted growth but no cognitive deficiency. *J Clin Endocrinol Metab***,** jc20151824.

NIKIFOROV, Y. E., ROWLAND, J. M., BOVE, K. E., MONFORTE-MUNOZ, H. & FAGIN, J. A. 1997. Distinct pattern of ret oncogene rearrangements in morphological variants of radiation-induced and sporadic thyroid papillary carcinomas in children. *Cancer Res,* 57**,** 1690-4.

NIKIFOROVA, M. N., KIMURA, E. T., GANDHI, M., BIDDINGER, P. W., KNAUF, J. A., BASOLO, F., ZHU, Z., GIANNINI, R., SALVATORE, G., FUSCO, A., SANTORO, M., FAGIN, J. A. & NIKIFOROV, Y. E. 2003. BRAF mutations in thyroid tumors are restricted to papillary carcinomas and anaplastic or poorly differentiated carcinomas arising from papillary carcinomas. *J Clin Endocrinol Metab,* 88**,** 5399-404.

NIKOLAEV, V. O., BUNEMANN, M., HEIN, L., HANNAWACKER, A. & LOHSE, M. J. 2004. Novel single chain cAMP sensors for receptor-induced signal propagation. *J Biol Chem,* 279**,** 37215-8.

OKUDA, T., OSAWA, C., YAMADA, H., HAYASHI, K., NISHIKAWA, S., USHIO, T., KUBO, Y., SATOU, M., OGAWA, H. & HAGA, T. 2012. Transmembrane topology and oligomeric structure of the high-affinity choline transporter. *J Biol Chem,* 287**,** 42826-34.

ORTIGA-CARVALHO, T. M., CHIAMOLERA, M. I., PAZOS-MOURA, C. C. & WONDISFORD, F. E. 2016. Hypothalamus-Pituitary-Thyroid Axis. *Compr Physiol,* 6**,** 1387-428.

PARODER, V., NICOLA, J. P., GINTER, C. S. & CARRASCO, N. 2013. The iodide-transport-defect-causing mutation R124H: a delta-amino group at position 124 is critical for maturation and trafficking of the Na+/I- symporter. *J Cell Sci.* England.

PARODER-BELENITSKY, M., MAESTAS, M. J., DOHAN, O., NICOLA, J. P., REYNA-NEYRA, A., FOLLENZI, A., DADACHOVA, E., ESKANDARI, S., AMZEL, L. M. & CARRASCO, N. 2011. Mechanism of anion selectivity and stoichiometry of the Na+/I- symporter (NIS). *Proc Natl Acad Sci U S A,* 108**,** 17933-8.

PEER, W. A. 2011. Plasma membrane protein trafficking. *In:* MURPHY, A. S., PEER, W. A. & SCHULZ, B. (eds.) *The Plant Plasma Membrane.* 1 ed.: Springer-Verlag Berlin Heidelberg.

PHIZICKY, E. M. & FIELDS, S. 1995. Protein-protein interactions: methods for detection and analysis. *Microbiol Rev,* 59**,** 94-123.

PISTON, D. W. & KREMERS, G. J. 2007. Fluorescent protein FRET: the good, the bad and the ugly. *Trends Biochem Sci,* 32**,** 407-14.

PLACZKOWSKI, K. A., REDDI, H. V., GREBE, S. K., EBERHARDT, N. L. & MCIVER, B. 2008. The Role of the PAX8/PPARgamma Fusion Oncogene in Thyroid Cancer. *PPAR Res,* 2008**,** 672829.

PORTULANO, C., PARODER-BELENITSKY, M. & CARRASCO, N. 2014. The Na+/I- symporter (NIS): mechanism and medical impact. *Endocr Rev,* 35**,** 106-49.

PUPPIN, C., D'AURIZIO, F., D'ELIA, A. V., CESARATTO, L., TELL, G., RUSSO, D., FILETTI, S., FERRETTI, E., TOSI, E., MATTEI, T., PIANTA, A., PELLIZZARI, L. & DAMANTE, G. 2005. Effects of histone acetylation on sodium iodide symporter promoter and expression of thyroid-specific transcription factors. *Endocrinology,* 146**,** 3967-74.

RAUE, F. & FRANK-RAUE, K. 2016. Thyroid Cancer: Risk-Stratified Management and Individualized Therapy. *Clin Cancer Res,* 22**,** 5012-5021.

RAVERA, S., REYNA-NEYRA, A., FERRANDINO, G., AMZEL, L. M. & CARRASCO, N. 2017. The Sodium/Iodide Symporter (NIS): Molecular Physiology and Preclinical and Clinical Applications. *Annu Rev Physiol,* 79**,** 261-289.

REED-TSUR, M. D., DE LA VIEJA, A., GINTER, C. S. & CARRASCO, N. 2008. Molecular characterization of V59E NIS, a Na+/I- symporter mutant that causes congenital I- transport defect. *Endocrinology,* 149**,** 3077-84.

RESSL, S., TERWISSCHA VAN SCHELTINGA, A. C., VONRHEIN, C., OTT, V. & ZIEGLER, C. 2009. Molecular basis of transport and regulation in the Na(+)/betaine symporter BetP. *Nature,* 458**,** 47-52.

RICE, P., LONGDEN, I. & BLEASBY, A. 2000. EMBOSS: the European Molecular Biology Open Software Suite. *Trends Genet,* 16**,** 276-7.

RIEDEL, C., LEVY, O. & CARRASCO, N. 2001. Post-transcriptional regulation of the sodium/iodide symporter by thyrotropin. *J Biol Chem,* 276**,** 21458-63.

RIESCO-EIZAGUIRRE, G., LEONI, S. G., MENDIOLA, M., ESTEVEZ-CEBRERO, M. A., GALLEGO, M. I., REDONDO, A., HARDISSON, D., SANTISTEBAN, P. & DE LA VIEJA, A. 2014. NIS mediates iodide uptake in the female reproductive tract and is a poor prognostic factor in ovarian cancer. *J Clin Endocrinol Metab,* 99**,** E1199-208.

RIZZO, M. A., SPRINGER, G. H., GRANADA, B. & PISTON, D. W. 2004. An improved cyan fluorescent protein variant useful for FRET. *Nat Biotechnol.* United States.

ROBINSON, D. R., WU, Y. M. & LIN, S. F. 2000. The protein tyrosine kinase family of the human genome. *Oncogene,* 19**,** 5548-57.

RODRIGUEZ, A. M., PERRON, B., LACROIX, L., CAILLOU, B., LEBLANC, G., SCHLUMBERGER, M., BIDART, J. M. & POURCHER, T. 2002. Identification and characterization of a putative human iodide transporter located at the apical membrane of thyrocytes. *J Clin Endocrinol Metab,* 87**,** 3500-3.

ROST, B., YACHDAV, G. & LIU, J. 2004. The PredictProtein server. *Nucleic Acids Res,* 32**,** W321-6.

RUSS, W. P. & ENGELMAN, D. M. 1999. TOXCAT: a measure of transmembrane helix association in a biological membrane. *Proc Natl Acad Sci U S A,* 96**,** 863-8.

RUSS, W. P. & ENGELMAN, D. M. 2000. The GxxxG motif: a framework for transmembrane helix-helix association. *J Mol Biol,* 296**,** 911-9.

RYU, K. Y., TONG, Q. & JHIANG, S. M. 1998. Promoter characterization of the human Na+/I- symporter. *J Clin Endocrinol Metab,* 83**,** 3247-51.

SALAHPOUR, A., ANGERS, S., MERCIER, J. F., LAGACE, M., MARULLO, S. & BOUVIER, M. 2004. Homodimerization of the beta2-adrenergic receptor as a prerequisite for cell surface targeting. *J Biol Chem,* 279**,** 33390-7.

SALIM, K., FENTON, T., BACHA, J., URIEN-RODRIGUEZ, H., BONNERT, T., SKYNNER, H. A., WATTS, E., KERBY, J., HEALD, A., BEER, M., MCALLISTER, G. & GUEST, P. C. 2002. Oligomerization of G-protein-coupled receptors shown by selective co-immunoprecipitation. *J Biol Chem,* 277**,** 15482-5.

SARABIPOUR, S., DEL PICCOLO, N. & HRISTOVA, K. 2015. Characterization of membrane protein interactions in plasma membrane derived vesicles with quantitative imaging Forster resonance energy transfer. *Acc Chem Res,* 48**,** 2262-9.

SCHLESSINGER, J. 2000. Cell signaling by receptor tyrosine kinases. *Cell,* 103**,** 211-25.

SCHLUMBERGER, M., TAHARA, M., WIRTH, L. J., ROBINSON, B., BROSE, M. S., ELISEI, R., HABRA, M. A., NEWBOLD, K., SHAH, M. H., HOFF, A. O., GIANOUKAKIS, A. G., KIYOTA, N., TAYLOR, M. H., KIM, S. B., KRZYZANOWSKA, M. K., DUTCUS, C. E., DE LAS HERAS, B., ZHU, J. & SHERMAN, S. I. 2015. Lenvatinib versus placebo in radioiodine-refractory thyroid cancer. *N Engl J Med,* 372**,** 621-30.

SCHMUTZLER, C., SCHMITT, T. L., GLASER, F., LOOS, U. & KOHRLE, J. 2002. The promoter of the human sodium/iodide-symporter gene responds to retinoic acid. *Mol Cell Endocrinol,* 189**,** 145-55.

SCHULZE, S., KOSTER, S., GELDMACHER, U., TERWISSCHA VAN SCHELTINGA, A. C. & KUHLBRANDT, W. 2010. Structural basis of Na(+)-independent and cooperative substrate/product antiport in CaiT. *Nature,* 467**,** 233-6.

SCOTT, D. A., WANG, R., KREMAN, T. M., SHEFFIELD, V. C. & KARNISKI, L. P. 1999. The Pendred syndrome gene encodes a chloride-iodide transport protein. *Nat Genet,* 21**,** 440-3.

SEIDLIN, S. M., OSHRY, E. & YALOW, A. A. 1948. Spontaneous and experimentally induced uptake of radioactive iodine in metastases from thyroid carcinoma; a preliminary report. *J Clin Endocrinol Metab,* 8**,** 423-32.

SENES, A., ENGEL, D. E. & DEGRADO, W. F. 2004. Folding of helical membrane proteins: the role of polar, GxxxG-like and proline motifs. *Curr Opin Struct Biol,* 14**,** 465-79.

SENES, A., GERSTEIN, M. & ENGELMAN, D. M. 2000. Statistical analysis of amino acid patterns in transmembrane helices: the GxxxG motif occurs frequently and in association with beta-branched residues at neighboring positions. *J Mol Biol,* 296**,** 921-36.

SERRANO-NASCIMENTO, C., CALIL-SILVEIRA, J. & NUNES, M. T. 2010. Posttranscriptional regulation of sodium-iodide symporter mRNA expression in the rat thyroid gland by acute iodide administration. *Am J Physiol Cell Physiol,* 298**,** C893-9.

SERRANO-NASCIMENTO, C., NICOLA, J. P., TEIXEIRA SDA, S., POYARES, L. L., LELLIS-SANTOS, C., BORDIN, S., MASINI-REPISO, A. M. & NUNES, M. T. 2016. Excess iodide downregulates Na(+)/I(-) symporter gene transcription through activation of PI3K/Akt pathway. *Mol Cell Endocrinol,* 426**,** 73-90.

SIEGER, S., JIANG, S., SCHONSIEGEL, F., ESKERSKI, H., KUBLER, W., ALTMANN, A. & HABERKORN, U. 2003. Tumour-specific activation of the sodium/iodide symporter gene under control of the glucose transporter gene 1 promoter (GTI-1.3). *Eur J Nucl Med Mol Imaging,* 30**,** 748-56.

SIGMA-ALDRICH. 2018a. *Duolink® PLA Fluorescence Protocol* [Online]. Available: https://www.sigmaaldrich.com/technical-documents/protocols/biology/duolink-fluorescence-user-manual.html [Accessed 03.06.2018].

SIGMA-ALDRICH. 2018b. *Duolink® PLA Troubleshooting Guide* [Online]. Available: https://www.sigmaaldrich.com/technical-documents/protocols/biology/duolink-troubleshooting-guide.html#faq [Accessed 03.06.18].

SIGMA-ALDRICH. 2018c. *Duolink® PLAProbemaker Guide* [Online]. Available: https://www.sigmaaldrich.com/technical-documents/protocols/biology/duolink-probemaker-user-manual.html [Accessed 23/07/2018].

SIMON, D., KOEHRLE, J., REINERS, C., BOERNER, A. R., SCHMUTZLER, C., MAINZ, K., GORETZKI, P. E. & ROEHER, H. D. 1998. Redifferentiation therapy with retinoids: therapeutic option for advanced follicular and papillary thyroid carcinoma. *World J Surg,* 22**,** 569-74.

SMANIK, P. A., LIU, Q., FURMINGER, T. L., RYU, K., XING, S., MAZZAFERRI, E. L. & JHIANG, S. M. 1996. Cloning of the human sodium lodide symporter. *Biochem Biophys Res Commun,* 226**,** 339-45.

SMITH, V. E., READ, M. L., TURNELL, A. S., WATKINS, R. J., WATKINSON, J. C., LEWY, G. D., FONG, J. C., JAMES, S. R., EGGO, M. C., BOELAERT, K., FRANKLYN, J. A. & MCCABE, C. J. 2009. A novel mechanism of sodium iodide symporter repression in differentiated thyroid cancer. *J Cell Sci,* 122**,** 3393-402.

SPARROW, L. G., MCKERN, N. M., GORMAN, J. J., STRIKE, P. M., ROBINSON, C. P., BENTLEY, J. D. & WARD, C. W. 1997. The disulfide bonds in the C-terminal domains of the human insulin receptor ectodomain. *J Biol Chem,* 272**,** 29460-7.

SPITZWEG, C., DIETZ, A. B., O'CONNOR, M. K., BERGERT, E. R., TINDALL, D. J., YOUNG, C. Y. & MORRIS, J. C. 2001a. In vivo sodium iodide symporter gene therapy of prostate cancer. *Gene Ther,* 8**,** 1524-31.

SPITZWEG, C., DUTTON, C. M., CASTRO, M. R., BERGERT, E. R., GOELLNER, J. R., HEUFELDER, A. E. & MORRIS, J. C. 2001b. Expression of the sodium iodide symporter in human kidney. *Kidney Int,* 59**,** 1013-23.

SPITZWEG, C., JOBA, W., MORRIS, J. C. & HEUFELDER, A. E. 1999a. Regulation of sodium iodide symporter gene expression in FRTL-5 rat thyroid cells. *Thyroid,* 9**,** 821-30.

SPITZWEG, C., JOBA, W., SCHRIEVER, K., GOELLNER, J. R., MORRIS, J. C. & HEUFELDER, A. E. 1999b. Analysis of human sodium iodide symporter immunoreactivity in human exocrine glands. *J Clin Endocrinol Metab,* 84**,** 4178-84.

SPITZWEG, C., O'CONNOR, M. K., BERGERT, E. R., TINDALL, D. J., YOUNG, C. Y. & MORRIS, J. C. 2000. Treatment of prostate cancer by radioiodine therapy after tissue-specific expression of the sodium iodide symporter. *Cancer Res,* 60**,** 6526-30.

SPITZWEG, C., ZHANG, S., BERGERT, E. R., CASTRO, M. R., MCIVER, B., HEUFELDER, A. E., TINDALL, D. J., YOUNG, C. Y. & MORRIS, J. C. 1999c. Prostate-specific antigen (PSA) promoter-driven androgen-inducible expression of sodium iodide symporter in prostate cancer cell lines. *Cancer Res,* 59**,** 2136-41.

STANLEY, M. 2003. An Introduction to FRET, with and Emphasis on the Optics Involved. *Chroma Technology Corp.,* Application Notes.

STER, J., DE BOCK, F., GUERINEAU, N. C., JANOSSY, A., BARRERE-LEMAIRE, S., BOS, J. L., BOCKAERT, J. & FAGNI, L. 2007. Exchange protein activated by cAMP (Epac) mediates cAMP activation of p38 MAPK and modulation of Ca2+-dependent K+ channels in cerebellar neurons. *Proc Natl Acad Sci U S A,* 104**,** 2519-24.

SUN, Y., DAY, R. N. & PERIASAMY, A. 2011. Investigating protein-protein interactions in living cells using fluorescence lifetime imaging microscopy. *Nat Protoc,* 6**,** 1324-40.

TAKI, K., KOGAI, T., KANAMOTO, Y., HERSHMAN, J. M. & BRENT, G. A. 2002. A thyroid-specific far-upstream enhancer in the human sodium/iodide symporter gene requires Pax-8 binding and cyclic adenosine 3',5'-monophosphate response element-like sequence binding proteins for full activity and is differentially regulated in normal and thyroid cancer cells. *Mol Endocrinol,* 16**,** 2266-82.

TAZEBAY, U. H., WAPNIR, I. L., LEVY, O., DOHAN, O., ZUCKIER, L. S., ZHAO, Q. H., DENG, H. F., AMENTA, P. S., FINEBERG, S., PESTELL, R. G. & CARRASCO, N. 2000. The mammary gland iodide transporter is expressed during lactation and in breast cancer. *Nat Med,* 6**,** 871-8.

TEESE, M. G. & LANGOSCH, D. 2015. Role of GxxxG Motifs in Transmembrane Domain Interactions. *Biochemistry,* 54**,** 5125-35.

THERMO FISCHER SCIENTIFIC. 2018. *Spectra Viewer* [Online]. Available: https://www.thermofisher.com/order/spectra-viewer [Accessed 09.06.18].

THEUNIPROTCONSORTIUM 2017. UniProt: the universal protein knowledgebase. *Nucleic Acids Research,* 45**,** D158-D169.

TUSNÁDY, G. E. & SIMON, I. 2001. The HMMTOP transmembrane topology prediction server. *Bioinformatics,* 17**,** 849-850.

TWYFFELS, L., STRICKAERT, A., VIRREIRA, M., MASSART, C., VAN SANDE, J., WAUQUIER, C., BEAUWENS, R., DUMONT, J. E., GALIETTA, L. J., BOOM, A. & KRUYS, V. 2014. Anoctamin-1/TMEM16A is the major apical iodide channel of the thyrocyte. *Am J Physiol Cell Physiol,* 307**,** C1102-12.

ULMSCHNEIDER, M. B. & SANSOM, M. S. 2001. Amino acid distributions in integral membrane protein structures. *Biochim Biophys Acta,* 1512**,** 1-14.

UYTTERSPROT, N., PELGRIMS, N., CARRASCO, N., GERVY, C., MAENHAUT, C., DUMONT, J. E. & MIOT, F. 1997. Moderate doses of iodide in vivo inhibit cell proliferation and the expression of thyroperoxidase and Na+/I- symporter mRNAs in dog thyroid. *Mol Cell Endocrinol,* 131**,** 195-203.

VAN DER GEER, P. 2014. Analysis of protein-protein interactions by coimmunoprecipitation. *Methods Enzymol,* 541**,** 35-47.

VERGARA-JAQUE, A., FONG, P. & COMER, J. 2017. Iodide Binding in Sodium-Coupled Cotransporters. *J Chem Inf Model*.

VIDI, P. A., CHEN, J., IRUDAYARAJ, J. M. & WATTS, V. J. 2008. Adenosine A(2A) receptors assemble into higher-order oligomers at the plasma membrane. *FEBS Lett,* 582**,** 3985-90.

VIOLA, D., VALERIO, L., MOLINARO, E., AGATE, L., BOTTICI, V., BIAGINI, A., LORUSSO, L., CAPPAGLI, V., PIERUZZI, L., GIANI, C., SABINI, E., PASSANNATI, P., PULEO, L., MATRONE, A., PONTILLO-CONTILLO, B., BATTAGLIA, V., MAZZEO, S., VITTI, P. & ELISEI, R. 2016. Treatment of advanced thyroid cancer with targeted therapies: ten years of experience. *Endocr Relat Cancer,* 23**,** R185-205.

VISSER, W. E., FRIESEMA, E. C. & VISSER, T. J. 2011. Minireview: thyroid hormone transporters: the knowns and the unknowns. *Mol Endocrinol,* 25**,** 1-14.

VISSER, W. E., PHILP, N. J., VAN DIJK, T. B., KLOOTWIJK, W., FRIESEMA, E. C., JANSEN, J., BEESLEY, P. W., IANCULESCU, A. G. & VISSER, T. J. 2009. Evidence for a homodimeric structure of human monocarboxylate transporter 8. *Endocrinology,* 150**,** 5163-70.

WAPNIR, I. L., VAN DE RIJN, M., NOWELS, K., AMENTA, P. S., WALTON, K., MONTGOMERY, K., GRECO, R. S., DOHAN, O. & CARRASCO, N. 2003. Immunohistochemical profile of the sodium/iodide symporter in thyroid, breast, and other carcinomas using high density tissue microarrays and conventional sections. *J Clin Endocrinol Metab,* 88**,** 1880-8.

WATANABE, A., CHOE, S., CHAPTAL, V., ROSENBERG, J. M., WRIGHT, E. M., GRABE, M. & ABRAMSON, J. 2010. The mechanism of sodium and substrate release from the binding pocket of vSGLT. *Nature,* 468**,** 988-91.

WEBELEMENTS. 2018. *Iodine: the essentials* [Online]. Available: https://www.webelements.com/iodine/index.html [Accessed 14/06/18].

WEIBRECHT, I., LEUCHOWIUS, K. J., CLAUSSON, C. M., CONZE, T., JARVIUS, M., HOWELL, W. M., KAMALI-MOGHADDAM, M. & SODERBERG, O. 2010. Proximity ligation assays: a recent addition to the proteomics toolbox. *Expert Rev Proteomics,* 7**,** 401-9.

WEYAND, S., SHIMAMURA, T., YAJIMA, S., SUZUKI, S., MIRZA, O., KRUSONG, K., CARPENTER, E. P., RUTHERFORD, N. G., HADDEN, J. M., O'REILLY, J., MA, P., SAIDIJAM, M., PATCHING, S. G., HOPE, R. J., NORBERTCZAK, H. T., ROACH, P. C., IWATA, S., HENDERSON, P. J. & CAMERON, A. D. 2008. Structure and molecular mechanism of a nucleobase-cation-symport-1 family transporter. *Science,* 322**,** 709-13.

WHORTON, M. R., BOKOCH, M. P., RASMUSSEN, S. G., HUANG, B., ZARE, R. N., KOBILKA, B. & SUNAHARA, R. K. 2007. A monomeric G protein-coupled receptor isolated in a high-density lipoprotein particle efficiently activates its G protein. *Proc Natl Acad Sci U S A,* 104**,** 7682-7.

WILSON, S., WILKINSON, G. & MILLIGAN, G. 2005. The CXCR1 and CXCR2 receptors form constitutive homo- and heterodimers selectively and with equal apparent affinities. *J Biol Chem,* 280**,** 28663-74.

WOLFF, J. & CHAIKOFF, I. L. 1948. Plasma inorganic iodide as a homeostatic regulator of thyroid function. *J Biol Chem,* 174**,** 555-64.

WOLFF, J., CHAIKOFF, I. L. & ET AL. 1949. The temporary nature of the inhibitory action of excess iodine on organic iodine synthesis in the normal thyroid. *Endocrinology,* 45**,** 504-13, illust.

WRIGHT, E. M. & TURK, E. 2004. The sodium/glucose cotransport family SLC5. *Pflugers Arch,* 447**,** 510-8.

XIE, Q., SOUTTO, M., XU, X., ZHANG, Y. & JOHNSON, C. H. 2011. Bioluminescence resonance energy transfer (BRET) imaging in plant seedlings and mammalian cells. *Methods Mol Biol,* 680**,** 3-28.

XIE, Z., TURK, E. & WRIGHT, E. M. 2000. Characterization of the Vibrio parahaemolyticus Na+/Glucose cotransporter. A bacterial member of the sodium/glucose transporter (SGLT) family. *J Biol Chem,* 275**,** 25959-64.

YAMASHITA, A., SINGH, S. K., KAWATE, T., JIN, Y. & GOUAUX, E. 2005. Crystal structure of a bacterial homologue of Na+/Cl--dependent neurotransmitter transporters. *Nature,* 437**,** 215-23.

ZABALLOS, M. A., GARCIA, B. & SANTISTEBAN, P. 2008. Gbetagamma dimers released in response to thyrotropin activate phosphoinositide 3-kinase and regulate gene expression in thyroid cells. *Mol Endocrinol,* 22**,** 1183-99.

ZABALLOS, M. A. & SANTISTEBAN, P. 2017. Key signaling pathways in thyroid cancer. *J Endocrinol,* 235**,** R43-R61.

ZARNEGAR, R., BRUNAUD, L., KANAUCHI, H., WONG, M., FUNG, M., GINZINGER, D., DUH, Q. Y. & CLARK, O. H. 2002. Increasing the effectiveness of radioactive iodine therapy in the treatment of

thyroid cancer using Trichostatin A, a histone deacetylase inhibitor. *Surgery,* 132**,** 984-90; discussion 990.

ZHOU, F., FILIPEANU, C. M., DUVERNAY, M. T. & WU, G. 2006. Cell-surface targeting of alpha2-adrenergic receptors -- inhibition by a transport deficient mutant through dimerization. *Cell Signal,* 18**,** 318-27.

ZHU, Z., GANDHI, M., NIKIFOROVA, M. N., FISCHER, A. H. & NIKIFOROV, Y. E. 2003. Molecular profile and clinical-pathologic features of the follicular variant of papillary thyroid carcinoma. An unusually high prevalence of ras mutations. *Am J Clin Pathol,* 120**,** 71-7.

CHAPTER 9 - APPENDIX

9.1 NIS coding sequence

The following figure shows the NIS coding sequence and the resultant amino acid sequence, with the residue numbers stated at the start of each row. Residues mutated in this thesis are indicated in red.

```
    ATG GAG GCC GTG GAG ACC GGG GAA CGG CCC ACC TTC GGA GCC TGG GAC TAC GGG GTC TTT
1     M   E   A   V   E   T   G   E   R   P   T   F   G   A   W   D   Y   G   V   F

    GCC CTC ATG CTC CTG GTG TCC ACT GGC ATC GGG CTG TGG GTC GGG CTG GCT CGG GGC GGG
21    A   L   M   L   L   V   S   T   G   I   G   L   W   V   G   L   A   R   G   G

    CAG CGC AGC GCT GAG GAC TTC TTC ACC GGG GGC CGG CGC CTG GCG GCC CTG CCC GTG GGC
41    Q   R   S   A   E   D   F   F   T   G   G   R   R   L   A   A   L   P   V   G

    CTG TCG CTG TCT GCC AGC TTC ATG TCG GCC GTG CAG GTG CTG GGC GTG CCG TCG GAG GCC
61    L   S   L   S   A   S   F   M   S   A   V   Q   V   L   G   V   P   S   E   A

    TAT CGC TAT GGC CTC AAG TTC CTC TGG ATG TGC CTG GGC CAG CTT CTG AAC TCG GTC CTC
81    Y   R   Y   G   L   K   F   L   W   M   C   L   G   Q   L   L   N   S   V   L

    ACC GCC CTG CTC TTC ATG CCC GTC TTC TAC CGC CTG GGC CTC ACC AGC ACC TAC GAG TAC
101   T   A   L   L   F   M   P   V   F   Y   R   L   G   L   T   S   T   Y   E   Y

    CTG GAG ATG CGC TTC AGC CGC GCA GTG CGG CTC TGC GGG ACT TTG CAG TAC ATT GTA GCC
121   L   E   M   R   F   S   R   A   V   R   L   C   G   T   L   Q   Y   I   V   A

    ACG ATG CTG TAC ACC GGC ATC GTA ATC TAC GCA CCG GCC CTC ATC CTG AAC CAA GTG ACC
141   T   M   L   Y   T   G   I   V   I   Y   A   P   A   L   I   L   N   Q   V   T

    GGG CTG GAC ATC TGG GCG TCG CTC CTG TCC ACC GGA ATT ATC TGC ACC TTC TAC ACG GCT
161   G   L   D   I   W   A   S   L   L   S   T   G   I   I   C   T   F   Y   T   A

    GTG GGC GGC ATG AAG GCT GTG GTC TGG ACT GAT GTG TTC CAG GTC GTG GTG ATG CTA AGT
181   V   G   G   M   K   A   V   V   W   T   D   V   F   Q   V   V   V   M   L   S

    GGC TTC TGG GTT GTC CTG GCA CGC GGT GTC ATG CTT GTG GGC GGG CCC CGC CAG GTG CTC
201   G   F   W   V   V   L   A   R   G   V   M   L   V   G   G   P   R   Q   V   L

    ACG CTG GCC CAG AAC CAC TCC CGG ATC AAC CTC ATG GAC TTT AAC CCT GAC CCG AGG AGC
221   T   L   A   Q   N   H   S   R   I   N   L   M   D   F   N   P   D   P   R   S

    CGC TAT ACA TTC TGG ACT TTT GTG GTG GGT GGC ACG TTG GTG TGG CTC TCC ATG TAT GGC
241   R   Y   T   F   W   T   F   V   V   G   G   T   L   V   W   L   S   M   Y   G

    GTG AAC CAG GCG CAG GTG CAG CGC TAC GTG GCT TGC CGC ACA GAG AAG CAG GCC AAG CTG
261   V   N   Q   A   Q   V   Q   R   Y   V   A   C   R   T   E   K   Q   A   K   L

    GCC CTG CTC ATC AAC CAG GTC GGC CTG TTC CTG ATC GTG TCC AGC GCT GCC TGC TGT GGC
281   A   L   L   I   N   Q   V   G   L   F   L   I   V   S   S   A   A   C   C   G

    ATC GTC ATG TTT GTG TTC TAC ACT GAC TGC GAC CCT CTC CTC CTG GGG CGC ATC TCT GCC
301   I   V   M   F   V   F   Y   T   D   C   D   P   L   L   L   G   R   I   S   A

    CCA GAC CAG TAC ATG CCT CTG CTG GTG CTG GAC ATC TTC GAA GAT CTG CCT GGA GTC CCC
321   P   D   Q   Y   M   P   L   L   V   L   D   I   F   E   D   L   P   G   V   P

    GGG CTT TTC CTG GCC TGT GCT TAC AGT GGC ACC CTC AGC ACA GCA TCC ACC AGC ATC AAT
341   G   L   F   L   A   C   A   Y   S   G   T   L   S   T   A   S   T   S   I   N

    GCT ATG GCT GCA GTC ACT GTA GAA GAC CTC ATC AAA CCT CGG CTG CGG AGC CTG GCA CCC
361   A   M   A   A   V   T   V   E   D   L   I   K   P   R   L   R   S   L   A   P

    AGG AAA CTC GTG ATT ATC TCC AAG GGG CTC TCA CTC ATC TAC GGA TCG GCC TGT CTC ACC
381   R   K   L   V   I   I   S   K   G   L   S   L   I   Y   G   S   A   C   L   T
```

```
    GTG GCA GCC CTG TCC TCA CTG CTC GGA GGA GGT GTC CTT CAG GGC TCC TTC ACC GTC ATG
401  V   A   A   L   S   S   L   L   G   G   G   V   L   Q   G   S   F   T   V   M

    GGA GTC ATC AGC GGC CCC CTG CTG GGA GCC TTC ATC TTG GGA ATG TTC CTG CCG GCC TGC
421  G   V   I   S   G   P   L   L   G   A   F   I   L   G   M   F   L   P   A   C

    AAC ACA CCG GGC GTC CTC GCG GGA CTA GGC GCG GGC TTG GCG CTG TCG CTG TGG GTG GCC
441  N   T   P   G   V   L   A   G   L   G   A   G   L   A   L   S   L   W   V   A

    TTG GGC GCC ACG CTG TAC CCA CCC AGC GAG CAG ACC ATG AGG GTC CTG CCA TCG TCG GCT
461  L   G   A   T   L   Y   P   P   S   E   Q   T   M   R   V   L   P   S   S   A

    GCC CGC TGC GTG GCT CTC TCA GTC AAC GCC TCT GGC CTC CTG GAC CCG GCT CTC CTC CCT
481  A   R   C   V   A   L   S   V   N   A   S   G   L   L   D   P   A   L   L   P

    GCT AAC GAC TCC AGC AGG GCC CCC AGC TCA GGA ATG GAC GCC AGC CGA CCC GCC TTA GCT
501  A   N   D   S   S   R   A   P   S   S   G   M   D   A   S   R   P   A   L   A

    GAC AGC TTC TAT GCC ATC TCC TAT CTC TAT TAC GGT GCC CTG GGC ACG CTG ACC ACT GTG
521  D   S   F   Y   A   I   S   Y   L   Y   Y   G   A   L   G   T   L   T   T   V

    CTG TGC GGA GCC CTC ATC AGC TGC CTG ACA GGC CCC ACC AAG CGC AGC ACC CTG GCC CCG
541  L   C   G   A   L   I   S   C   L   T   G   P   T   K   R   S   T   L   A   P

    GGA TTG TTG TGG TGG GAC CTC GCA CGG CAG ACA GCA TCA GTG GCC CCC AAG GAA GAA GTG
561  G   L   L   W   W   D   L   A   R   Q   T   A   S   V   A   P   K   E   E   V

    GCC ATC CTG GAT GAC AAC TTG GTC AAG GGT CCT GAA GAA CTC CCC ACT GGA AAC AAG AAG
581  A   I   L   D   D   N   L   V   K   G   P   E   E   L   P   T   G   N   K   K

    CCC CCT GGC TTC CTG CCC ACC AAT GAG GAT CGT CTG TTT TTC TTG GGG CAG AAG GAG CTG
601  P   P   G   F   L   P   T   N   E   D   R   L   F   F   L   G   Q   K   E   L

    GAG GGG GCT GGC TCT TGG ACC CCC TGT GTT GGA CAT GAT GGT GGT CGA GAC CAG CAG GAG
621  E   G   A   G   S   W   T   P   C   V   G   H   D   G   G   R   D   Q   Q   E

    ACA AAC CTC TGA
641  T   N   L  STOP        643
```

9.2 Site-directed mutagenesis sequencing analysis

The following figures show the sequencing analysis for all mutants made during this thesis.

Mutant sequence is shown below the WT, and mutated bases are indicated by arrows.

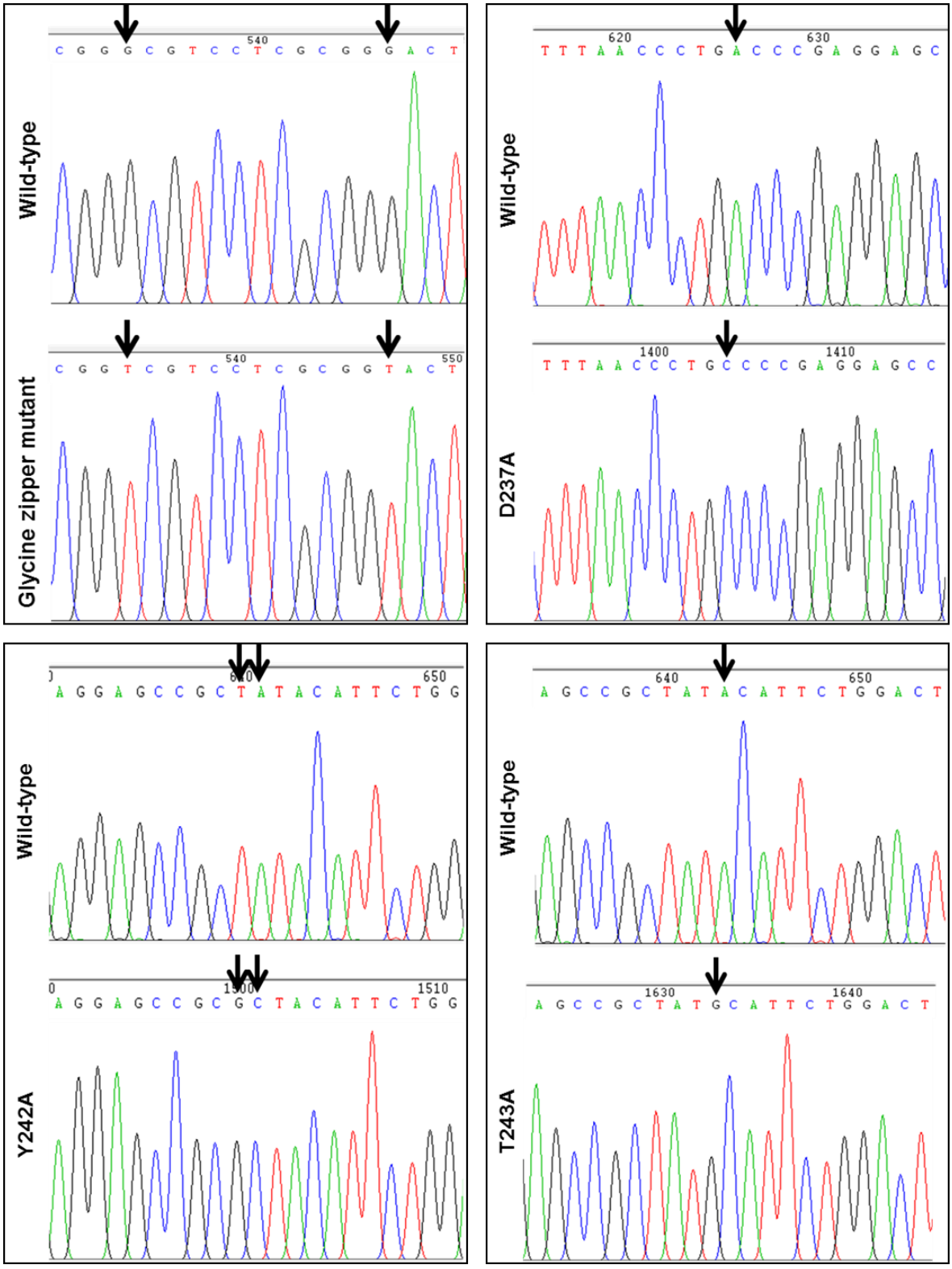
Wild-type
Glycine zipper mutant
Wild-type
D237A
Wild-type
Y242A
Wild-type
T243A

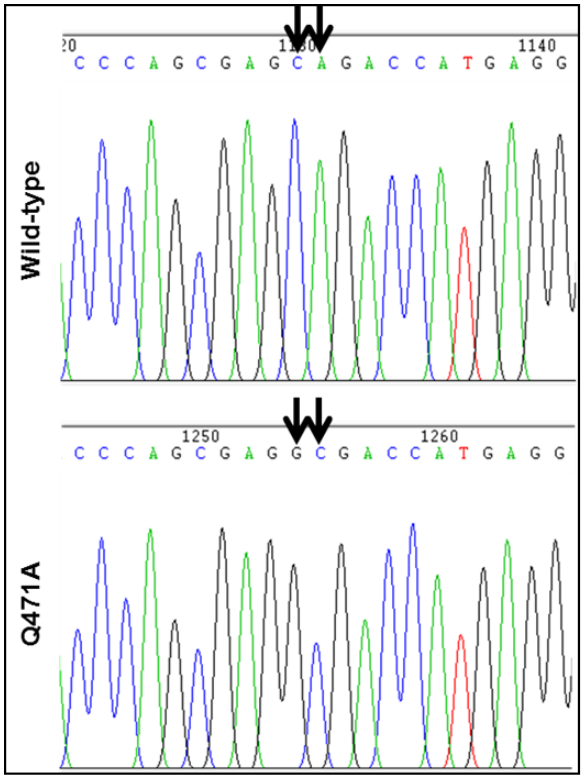
Wild-type
Q471A

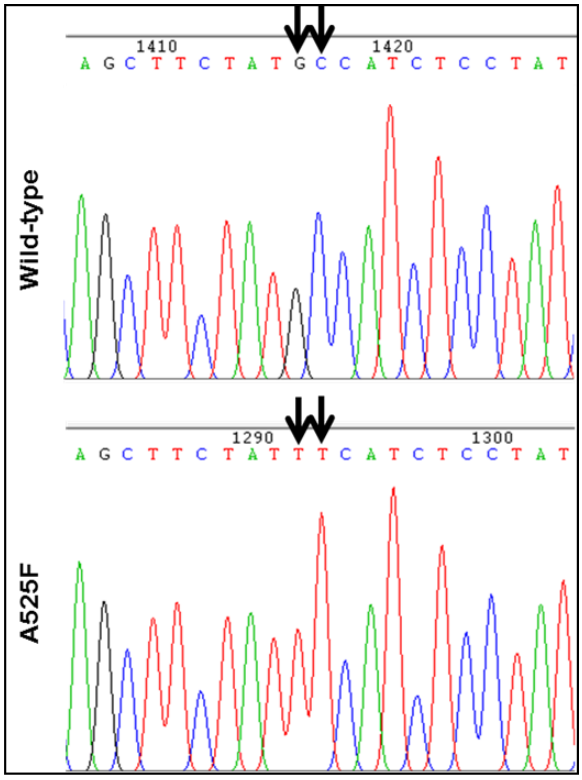
Wild-type
A525F

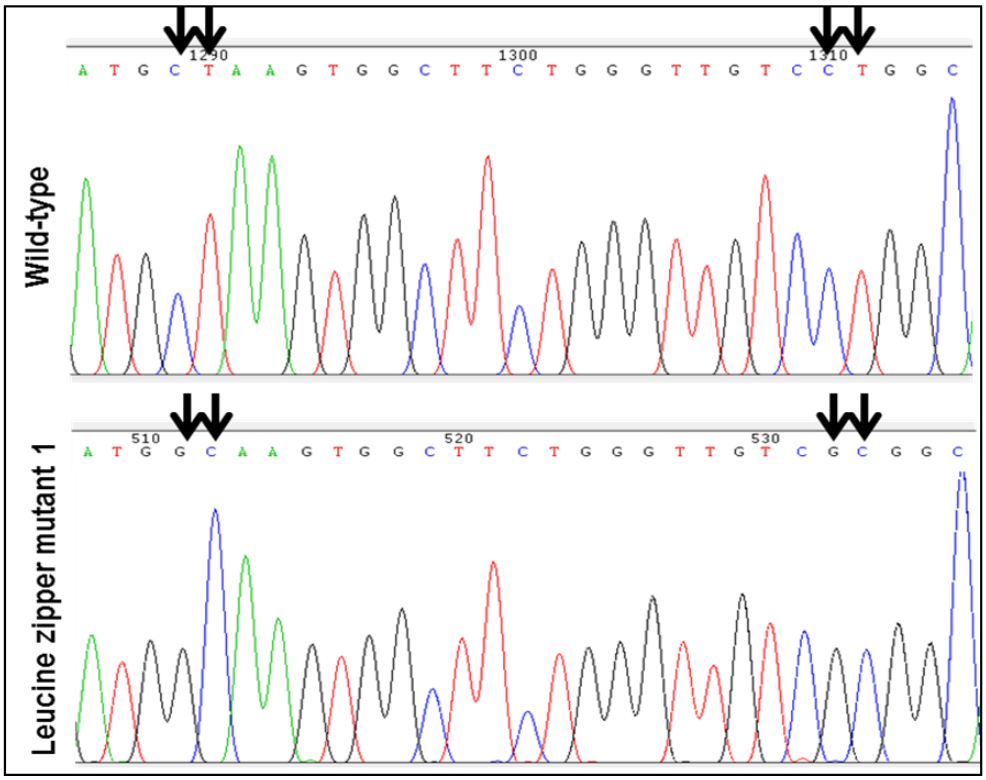
Wild-type
Leucine zipper mutant 1

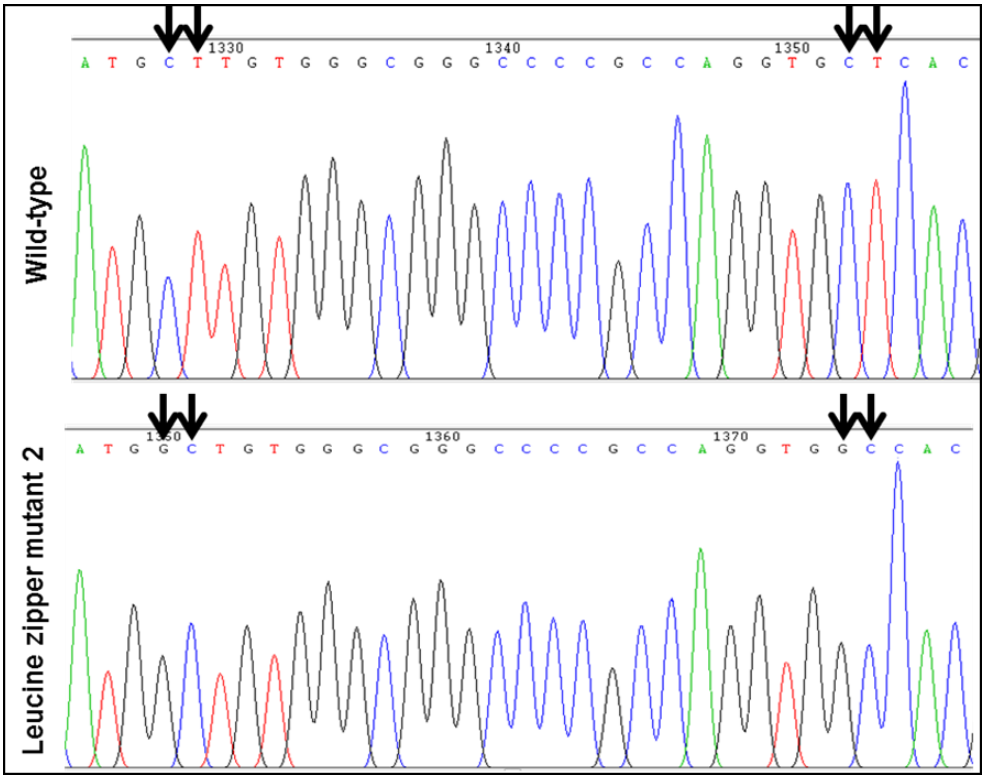
Wild-type
1330
1340
1350
A T G C T T G T G G G C G G G C C C C G C C A G G T G C T C A C
Leucine zipper mutant 2
1360
1370
A T G G C T G T G G G C G G G C C C C G C C A G G T G G C C A C

9.3 MYC and HA tags

The figure below shows the coding sequence and corresponding chromatograph for the MYC and HA tags, alongside the amino acid sequences.

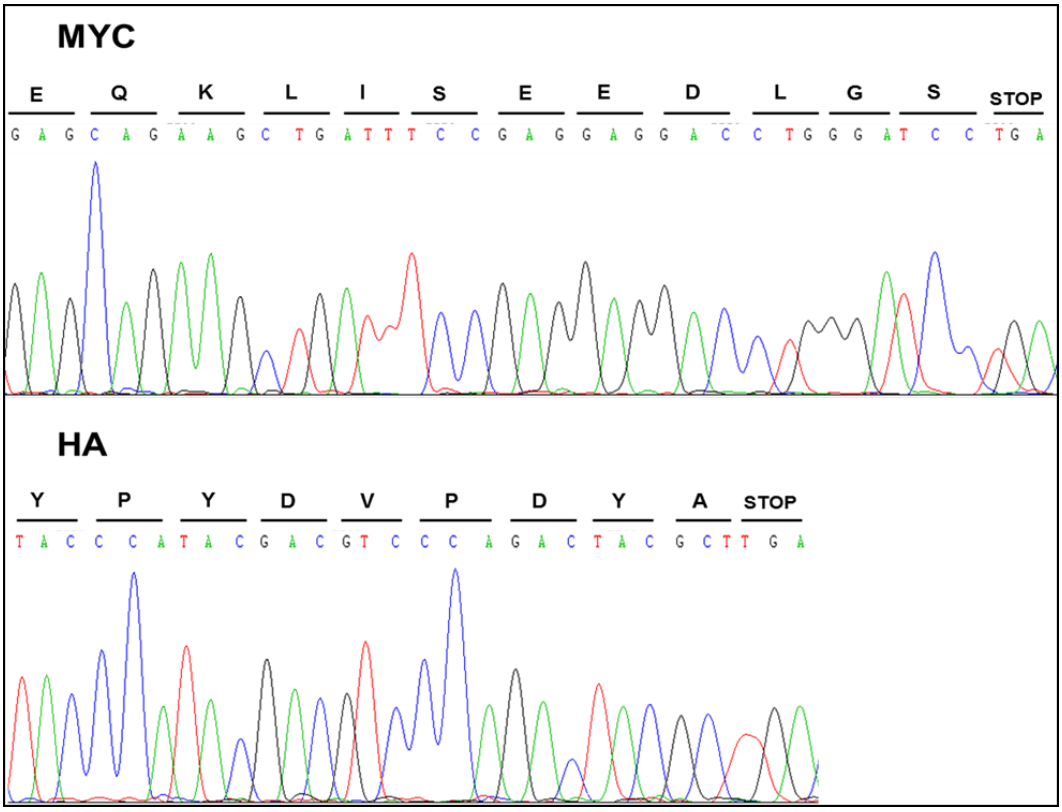

9.4 Cerulean and Citrine

The figure below shows the coding sequences for the Cerulean and Citrine fluorophores. Residues involved in the chromophore are highlighted in yellow, with start codons highlighted in grey and stop codons in red. Also shown is the coding sequence and corresponding amino acid sequence for the Cerulean-Citrine Linker created in this thesis.

ATGGTGATG - Cerulean Sequence (717 Nucleotides - 239 Amino Acids)
ACCTGGGGC - Cerulean Chromophore (TWG); A206 = GCC
ATG - Methionine Start Codon
TAG TAA TGA - Stop Codons

```
ATGGTGAGCAAGGGCGAGGAGCTGTTCACCGGGGTGGTGCCCATCCTGGTCGAGCTGGACGGCGACGTAAACGGC
CACAAGTTCAGCGTGTCCGGCGAGGGCGAGGGCGATGCCACCTACGGCAAGCTGACCCTGAAGTTCATCTGCACC
ACCGGCAAGCTGCCCGTGCCCTGGCCCACCCTCGTGACCACCCTGACCTGGGGCGTGCAGTGCTTCGCCCGCTAC
CCCGACCACATGAAGCAGCACGACTTCTTCAAGTCCGCCATGCCCGAAGGCTACGTCCAGGAGCGCACCATCTTC
TTCAAGGACGACGGCAACTACAAGACCCGCGCCGAGGTGAAGTTCGAGGGCGACACCCTGGTGAACCGCATCGAG
CTGAAGGGCATCGACTTCAAGGAGGACGGCAACATCCTGGGGCACAAGCTGGAGTACAACGCCATCAGCGACAAC
GTCTATATCACCGCCGACAAGCAGAAGAACGGCATCAAGGCCAACTTCAAGATCCGCCACAACATCGAGGACGGC
AGCGTGCAGCTCGCCGACCACTACCAGCAGAACACCCCCATCGGCGACGGCCCCGTGCTGCTGCCCGACAACCAC
TACCTGAGCACCCAGTCCGCCCTGAGCAAAGACCCCAACGAGAAGCGCGATCACATGGTCCTGCTGGAGTTCGTG
ACCGCCGCCGGGATCACTCTCGGCATGGACGAGCTGTACAAGTAA
```

GTGAGCAAG - Citrine Sequence (717 Nucleotides - 239 Amino Acids)
GGCTACGGC - Citrine Chromophore (GYG)
ATG - Methionine Start Codon
TAG TAA TGA - Stop Codons

```
ATGGTGAGCAAGGGCGAGGAGCTGTTCACCGGGGTGGTGCCCATCCTGGTCGAGCTGGACGGCGACGTAAACGGC
CACAAGTTCAGCGTGTCCGGCGAGGGCGAGGGCGATGCCACCTACGGCAAGCTGACCCTGAAGTTCATCTGCACC
ACCGGCAAGCTGCCCGTGCCCTGGCCCACCCTCGTGACCACCTTCGGCTACGGCCTGATGTGCTTCGCCCGCTAC
CCCGACCACATGAAGCAGCACGACTTCTTCAAGTCCGCCATGCCCGAAGGCTACGTCCAGGAGCGCACCATCTTC
TTCAAGGACGACGGCAACTACAAGACCCGCGCCGAGGTGAAGTTCGAGGGCGACACCCTGGTGAACCGCATCGAG
CTGAAGGGCATCGACTTCAAGGAGGACGGCAACATCCTGGGGCACAAGCTGGAGTACAACTACAACAGCCACAAC
GTCTATATCATGGCCGACAAGCAGAAGAACGGCATCAAGGTGAACTTCAAGATCCGCCACAACATCGAGGACGGC
AGCGTGCAGCTCGCCGACCACTACCAGCAGAACACCCCCATCGGCGACGGCCCCGTGCTGCTGCCCGACAACCAC
TACCTGAGCTACCAGTCCGCCCTGAGCAAAGACCCCAACGAGAAGCGCGATCACATGGTCCTGCTGGAGTTCGTG
ACCGCCGCCGGGATCACTCTCGGCATGGACGAGCTGTACAAGTAA
```

```
    CERULEAN                    LINKER                        CITRINE
      Y    K    S    G    L    R    S    R    A    Q    A    L    V    S
5′ - TAC AAG TCC GGA CTC AGA TCT CGA GCT CAA GCT TTG GTG AGC – 3′
```

CHAPTER 10 - BIBLIOGRAPHY

10.1 Presentations relating to this thesis

1) Poster presentation at the British Thyroid Association meeting in 2017 – won Best Basic Science poster prize

2) Oral presentation at the European Thyroid Association meeting in 2017

3) Poster presentation at the American Thyroid Association meeting in 2017 – entered into poster competition as one of the top 30 highest-scoring abstracts submitted by trainee scientists

4) Oral presentation at the British Endocrine Society meeting in 2017 – won Highly Commended Early Career oral communication prize and the British Thyroid Association Award for the highest-scoring abstract in the thyroid field

5) Oral presentation at the British Thyroid Association meeting in 2018 – won Best Basic Science oral communication prize

10.2 Publications relating to thesis

Read, M. L., Fong, J. C., Modasia, B., Fletcher, A., Imruetaicharoenchoke, W., Thompson, R. J., Nieto, H., Reynolds, J. J., Bacon, A., Mallick, U., Hackshaw, A., Watkinson, J. C., Boelaert, K., Turnell, A. S., Smith, V. E. & McCabe, C. J. 2017. Elevated PTTG and PBF predicts poor patient outcome and modulates DNA damage response genes in thyroid cancer. *Oncogene,* 36**,** 5296-5308.

Imruetaicharoenchoke, W., Fletcher, A., Lu, W., Watkins, R. J., Modasia, B., Poole, V. L., Nieto, H. R., Thompson, R. J., Boelaert, K., Read, M. L., Smith, V. E. & McCabe, C. J. 2017. Functional consequences of the first reported mutations of the proto-oncogene PTTG1IP/PBF. *Endocr Relat Cancer,* 24**,** 459-474.

Read, M. L., Modasia, B., Fletcher, A., Thompson, R. J., Baker, K., Rae, P., Nieto, H. R., Poole, V. L., Campbell, M., Boelaert, K., Turnell, A., Smith, V. E., Mehanna, H. & McCabe, C. J. 2018. PTTG and PBF functionally interact with p53 and predict overall survival in head and neck cancer. Cancer Research. **– *under revision***

Fletcher, A., Poole, V. L., Modasia, B., Imruetaicharoenchoke, W., Thompson, R. J., Sharma, N., Nieto, H. R., Read, M. L., Turnell, A., Boelaert, K., Smith, V. E. & McCabe, C. J. Identification of novel sodium iodide symporter (NIS) interactors which modulate iodide uptake. **– *in preparation***

Thompson, R. J., Fine, N. H. F., Baker, K., Fletcher, A., Nieto, H. R., Alshahrani, M., Thornton, C., Mueller, J. W., Hodson, D. J., Read, M. L., Boelaert, K., Smith, V. E. & McCabe, C. J. An investigation into sodium-iodide symporter (NIS) dimerisation. **– *in preparation***